The Dynamics of Magnetised Warped Discs

Joseph Benjamin Paris

Trinity College
Department of Applied Mathematics and Theoretical Physics
University of Cambridge

supervised by
Professor Gordon Ogilvie

This dissertation is submitted for the degree of Doctor of Philosophy

December 2018

Statement of Originality

This dissertation is the result of my own work and includes nothing which is the outcome of work done in collaboration except as declared in the Preface and specified in the text.

It is not substantially the same as any that I have submitted, or, is being concurrently submitted for a degree or diploma or other qualification at the University of Cambridge or any other University or similar institution except as declared in the Preface and specified in the text. I further state that no substantial part of my dissertation has already been submitted, or, is being concurrently submitted for any such degree, diploma or other qualification at the University of Cambridge or any other University or similar institution except as declared in the Preface and specified in the text. It does not exceed the prescribed word limit for the relevant Degree Committee.

The Dynamics of Magnetised Warped Discs

Joseph Benjamin Paris

ABSTRACT

The study of warped discs and the study of magnetised discs have generally been performed in relative isolation, and comparatively little attention has been given to the complex interplay between these two aspects of accretion disc physics. This thesis aims to provide a synthesis of these disparate areas of research and explore the effects of a mean magnetic field on warp evolution.

Using a coordinate system based upon tilted spheres, a series of self-similar solutions are presented for the global structure of a potential magnetic field beyond a warped disc. Warped discs threaded by a mean magnetic field are investigated numerically and semi-analytically in both a warped shearing box and a corrugated disc model. An asymptotic analysis is used to demonstrate the relation between these distinct local perspectives. Interactions between the warp and what we have called 'Alfvénic-epicyclic' oscillation modes, the magnetic analogues to epicyclic oscillations, are found to have potentially profound and hitherto unexplored consequences for the evolution of the warp. Resonances between the vertical oscillation mode and the Alfvénic-epicyclic modes imbue magnetised discs with a rich and subtle structure compared to their hydrodynamic counterparts. Notably the anomalous rapid propagation of the warp in Keplerian inviscid discs is suppressed, while warp propagation in non-Keplerian discs may be considerably enhanced. Non-local angular momentum transport via the external magnetic field may also provide an additional important contribution to the warp evolution. The practical application of these results to numerical simulations is discussed.

Acknowledgements

There are many people who have, in big ways and small, contributed to the completion of this thesis. In fact there are too many to name in this section, but I shall try to do so regardless.

First and foremost I would like to thank my supervisor Gordon Ogilvie. It was only his remarkable insight, support, patience and kindness that have made this thesis possible. I am immensely grateful for the advice he has provided, and have been truly honoured to be his student.

I would also like to thank everyone in the DAMTP astro group for their enlightening discussion, friendship and keen wit over the past several years. I thank Trinity College and the University of Cambridge for accepting me into what has become almost a second home. I am honoured to have Dr. Nixon and Henrik act as examiners for this thesis; I wish to thank both of them for their time and insightful comments.

I would not be half the man I am without my friends, new and old, whose companionship I treasure. I wish to express my deepest gratitude to Oliver, Mike, James and Steph, Jonathan, Martin, Adam, Rosalyn, and all the unnamed others who brighten my life, from A to Z.

My family has always been close to my heart, and I would like to thank them - my mother, my father, Tanya, Sam, Ruby and my wonderful new sister-in-law Michelle - for their constant support, wisdom and strength. It is a gratitude I cannot express. I dedicate this thesis to my grandparents; in particular, I dedicate it to my grandfather Clifford Carter, who not only was a man of science but, more importantly, a man of great warmth, humour, kindness and nobility.

The Dynamics of Magnetised Warped Discs

Joseph Benjamin Paris

ABSTRACT

The study of warped discs and the study of magnetised discs have generally been performed in relative isolation, and comparatively little attention has been given to the complex interplay between these two aspects of accretion disc physics. This thesis aims to provide a synthesis of these disparate areas of research and explore the effects of a mean magnetic field on warp evolution.

Using a coordinate system based upon tilted spheres, a series of self-similar solutions are presented for the global structure of a potential magnetic field beyond a warped disc. Warped discs threaded by a mean magnetic field are investigated numerically and semi-analytically in both a warped shearing box and a corrugated disc model. An asymptotic analysis is used to demonstrate the relation between these distinct local perspectives. Interactions between the warp and what we have called 'Alfvénic-epicyclic' oscillation modes, the magnetic analogues to epicyclic oscillations, are found to have potentially profound and hitherto unexplored consequences for the evolution of the warp. Resonances between the vertical oscillation mode and the Alfvénic-epicyclic modes imbue magnetised discs with a rich and subtle structure compared to their hydrodynamic counterparts. Notably the anomalous rapid propagation of the warp in Keplerian inviscid discs is suppressed, while warp propagation in non-Keplerian discs may be considerably enhanced. Non-local angular momentum transport via the external magnetic field may also provide an additional important contribution to the warp evolution. The practical application of these results to numerical simulations is discussed.

CONTENTS

1. INTRODUCTION

1.1 General Background

Accretion discs are discs of diffuse matter in orbit around a central body and may be formed in an extremely wide variety of physical scenarios, from relatively cool protoplanetary discs orbiting Sun-like stars to the massive ultraluminous hot discs orbiting supermassive black holes. The dynamics of accretion discs are intimately related to a wealth of fascinating and often poorly understood physical phenomena, such as planet formation, the development of astrophysical jets travelling near the speed of light and the extreme luminosities that characterise active galactic nuclei. Consequently the study of accretion discs has become a cornerstone of modern astrophysical research.

At a coarse level of description, accretion discs may form from the gravitational attraction of diffuse matter towards a central object. The diffuse matter typically has its own initial angular momentum that must be conserved. Thus the gravitational collapse of the diffuse matter eventually results in a disc oriented perpendicularly to the average angular momentum vector of the gas. The disc angular momentum may, through a variety of mechanisms, be slowly removed from the inner part of the disc on a time-scale that is typically long relative to the orbital time-scale of the disc, leading to the slow inflow of material and the eponymous accretion of disc material onto the central object.

The modern study of accretion discs began with what must be described as a prescient paper by Kuiper (1941), who correctly intuited that in some circumstances, the close contact of two binary stars must result in a stream of matter passing between them. Of particular note was the ‘curious result’,

as he described it, that the accreting matter formed a ring around the larger star. Prendergast & Burbidge (1968) and Pringle & Rees (1972) created the first models of an accretion disc, assuming the disc to be flat, hydrodynamic and viscous. This influential and comparatively simple model has, unfortunately, failed to match the variety and multifarious splendour of the natural phenomena observed in our Universe. It has been the work of theorists for the past half-century to amend and refine their perspective of accretion discs in line with observations.

One such amendment came from the discovery that accretion discs need not be flat. Indeed, in almost any scenario where there is misalignment between the orbital plane of the disc and some other nearby astrophysical object it is possible for the disc to suffer some form of distortion. Examples include discs orbiting misaligned Kerr black holes (i.e. spin orbit misalignment) which experience Lense-Thirring torques due to frame-dragging, inclined discs in X-ray binaries subjected to radiative-driven warping, or misaligned protoplanetary discs in binary systems that deform due to tidal torques from the binary companion. The hydrodynamics of these discs and evolution of the 'warp', or geometrical disturbance, have been studied with great interest over the preceding half century. Advances in the theoretical understanding of the warp evolution process have provided invaluable aid in the interpretation of both observations and simulations.

The importance of magnetic fields in astrophysics has long been recognised, and a tremendous amount of effort has been made in trying to understand how the magnetic field affects the development and evolution of accretion discs. Magnetically driven turbulence is now thought to be the primary driver of accretion, superseding the role of viscosity in earlier models. Magnetic fields also play a crucial role in the generation and collimation of vast jets, streams of matter emitted perpendicular to the disc, potentially responsible for ejecting angular momentum from the disc and driving the accretion process. Certainly there are mysteries yet to be resolved, and many of the finer details of these

processes have yet to come into focus; however there is a consensus, at the very least, that a purely hydrodynamic understanding of accretion discs is often insufficient.

While the physics of magnetised discs and warped discs have both been studied in great detail, they have unfortunately often been studied in relative isolation. The aim of this thesis is to reconcile and synthesise these two somewhat disparate areas of research and develop a coherent local picture of magnetised warped discs. In the process we will highlight those unique aspects of magnetised warped discs that distinguish them from their hydrodynamic counterparts.

The structure of the introduction is as follows. In section 1.2 we will give a brief account of the observational history of warps in discs. In section 1.3 we will provide a historical overview of the development of hydrodynamic warped disc theory. In section 1.4 we will attempt to provide a single coherent mathematical framework that will provide sufficient theoretical background for the remainder of the thesis. We discuss the general role of magnetism in accretion disc theory with particular emphasis on preceding research of magnetised warped discs in section 1.5. A broad overview of the computational research performed on warped discs (both magnetised and hydrodynamic) will be presented in section 1.6. In section 1.7 we will outline the current research and rationale behind the use of local models in warped disc dynamics. Finally in section 1.8 a brief overview of the thesis in its entirety will be presented.

1.2 A Brief Observational History

The study of warped discs could be said to have begun with the discovery of the binary neutron star X-ray source Her X-1 (Tananbaum et al., 1972) in the constellation Hercules. For some years the observational data posed an interminable puzzle to early theorists. Most notably, while a clear 1.24-s period neutron star rotational period and a 1.7-d neutron star orbital period

were inferred from the observational data, an additional unexplained 35-d periodicity in the luminosity was also observed.

Shakura (1972) and Katz (1973) were the first to proffer the idea of a warped or precessing disc surrounding the neutron star and out of the plane of the binary star system. However, it was Gerend & Boynton (1976) who first subjected this idea to rigorous analysis. They postulated that the relatively complex patterns of luminosity could be best understood by considering the relative orientations of the binary pair with the observer's line of sight and the precessing (and, by their suggestion, tilted) disc. Petterson (1977) quickly provided a similar analysis, finding in Her X-1 an unexpected application for his 'twisted disc' theory he had developed while considering a wholly different class of systems - namely Kerr black holes. As observational capacity has improved, Her X-1 has come to be seen less as a unique phenomenon and more as the prototypical system of a class of 'superperiodic' X-ray binaries. Petterson's suggestion of radiation driven warping, later developed in greater detail by Wijers & Pringle (1999) and Ogilvie & Dubus (2001), remains popular as a explanation for the behaviour of many of these systems (Clarkson et al. (2003), Kotze & Charles (2012)).

Superperiodic X-ray binaries are far from the only systems in which disc warping or tilting has been observed. The asymmetric jets of microquasar GROJ1655-40 (Hjellming & Rupen (1995), Martin, Tout & Pringle (2008)) have been taken as indicators of disc warping, in this case explained by Lense-Thirring torques due to disc-quasar misalignment. Warps have been observed in the water maser emissions of NGC4258 (Herrnstein, Greenhill & Moran (1996), Miyoshi et al. (1995)) (see Figure 1.2). Distinct asymmetries that could perhaps be best explained through disc warping were observed by the HST in the young binary HK Tau (Stapelfeldt, Krist, Ménard, Bouvier, Padgett & Burrows, 1998). Warps in young protostellar binaries such as HK Tau have been explained via the tidal interaction between the binary system and the misaligned disc (Lubow & Ogilvie, 2000). Optical and near-IR photome-

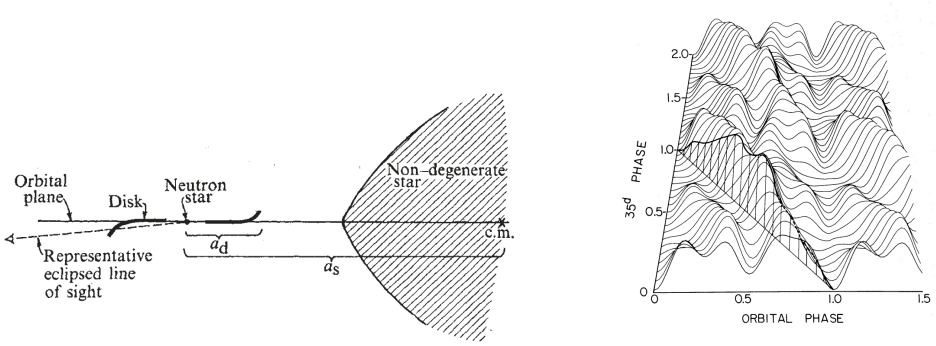

(a) The model of Her X-1 proposed by Katz (1973) (figure taken from that work).

(b) Optical data expressed as a function of both the orbital phase and 35^d phase, taken from Gerend & Boynton (1976). The diagonal cut represents a locus of constant disc-star configuration.

Fig. 1.1: The first observational evidence of a warped disc, found in the spectra of Her X-1.

try and spectroscopy in the protostellar disc of the young low-mass star AA Tau (Bouvier, Grankin, Ellerbroek, Bouy & Barrado, 2013) strongly suggest the disc in this system may be warped. More recently observations have been made of warped protoplanetary discs (Marino, Perez & Casassus, 2015) as well as transition discs (Casassus, 2016; 2017).

Recent observations from the Atacama Large Millimeter Array (ALMA) have revealed the presence of warped dics in a variety of systems, such as in the protostellar disc around T Tauri star TW Hya (Rosenfeld, et al., 2012), the Herbig Fe star system HD 142527 (Christiaens, et al, 2018) or in the DoAr 44 T Tauri transition disc (Casassus, et al., 2018). The continuous discovery of new and better-resolved warped discs in an ever-expanding array of distinct scenarios lends a renewed urgency to the search for a more comprehensive theoretical understanding of warped disc dynamics.

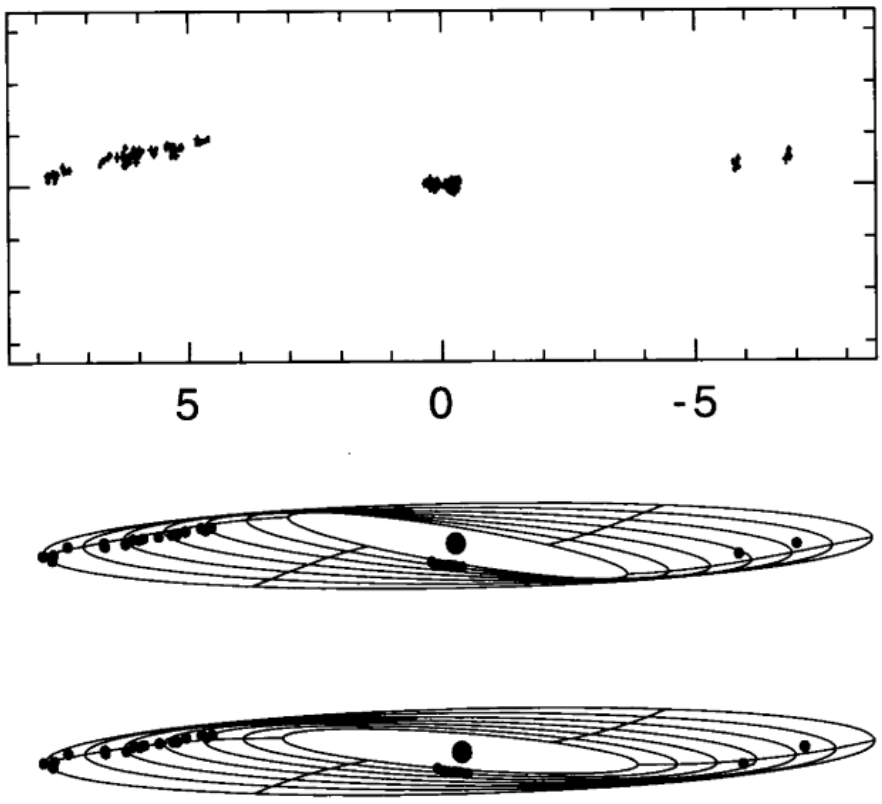

Fig. 1.2: The distribution of water masers in NGC 4258 (top), accompanied by two explanatory warped disc models. Figure taken from Herrnstein, Greenhill & Moran (1996).

1.3 Warped Disc Hydrodynamic Theory

The hydrodynamics of warped discs has been studied and re-evaluated several times from the mid-seventies until the present, each iteration evolving or contradicting the ideas of previous iterations. In this section we will endeavour to provide a brief historical sketch of the development of the fundamental theory of hydrodynamic warped discs.

Bardeen & Petterson (1975) were the first to attempt to build a physical model for disc warping. Their motivation was largely theoretical in nature; it had been known for some time that a rotating (Kerr) black hole drags the inertial frame in what is known as the Lense-Thirring effect. One particularly notable effect is the precession of a test particle's orbital plane about the rotation axis of the Kerr black hole. Bardeen & Petterson (1975) were curious as to how this result extended from test particles to continuous fluid discs, and in pursuit of this question constructed the mathematical foundations for the study of warped discs.

This relatively short paper was primarily concerned with the static equilibrium shape of the accretion disc in the misaligned Kerr gravitational potential rather than the dynamics of the warped disc. However Petterson expanded on these ideas and derived what might be called the first full hydrodynamic theory of warped disc dynamics in a trilogy of papers published between 1977 and 1978. (Petterson, 1977a, 1977b, 1978).

From Petterson's perspective a thin disc could be thought of as distinct thin interacting rings of matter. A warped disc is distinguished from a flat disc only by the relative orientation of the orbital planes of each of these rings; in flat discs all rings lie within the same orbital plane, while in warped discs the orbital plane may vary with radius and in time. The inclination of the orbital plane at different radii can hence be described by a single vector $\boldsymbol{l}(r,t)$ defined to be perpendicular to the local orbital plane.

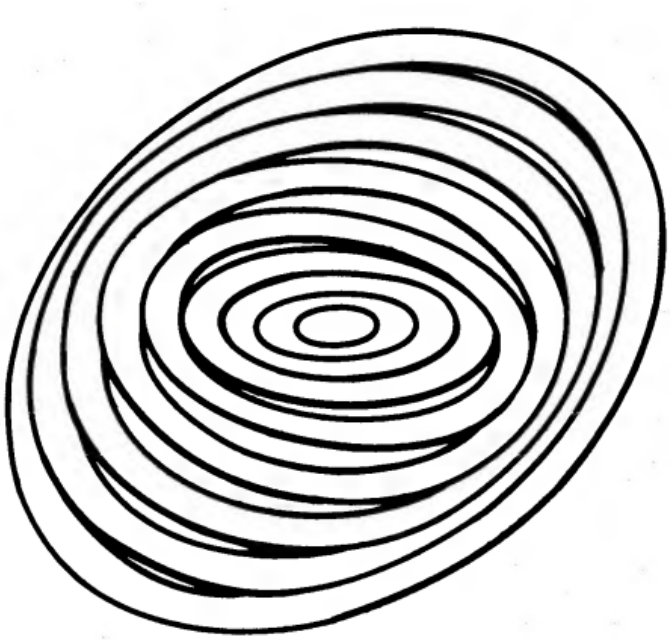

Fig. 1.3: Petterson's 'tilted rings' picture of warped accretion discs. Figure taken from Petterson (1977).

Informed by this perspective, Petterson constructed a coordinate system similar to the standard cylindrical coordinate system but where the $\widehat{z}$ coordinate vector was defined to be parallel to $\boldsymbol{l}$, or equivalently the $x-y$ plane is at each radius coincident with the orbital plane. Eulerian angles $\beta(r,t)$ and $\gamma(r,t)$ could be used (see Figure 1.3) to define the orientation of the orbital plane at different radii. Petterson set out to find a set of evolutionary equations for $\beta(r,t)$ and $\gamma(r,t)$, which in turn would determine the evolution of the shape of the disc itself. While some of the details of Petterson's approach have been improved upon, many of the fundamentals ideas – notably the notion of using a tilt vector $\boldsymbol{\ell}(r,t)$ and Eulerian angles β and γ to describe the shape of a warped disc – have remained in common use.

The physical assumptions of the Petterson model are, at face value, quite reasonable. Besides several relatively benign assumptions regarding disc thinness ($H \ll R$), the standard linear functional form of the viscosity and the

dominance of gravitational forces over pressure and viscous forces, he assumes that the chief driver of the warp is either external torques (Lense-Thirring in the case of Bardeen & Petterson (1975), radiative in the case of Petterson (1977)), or the viscous shear of neighbouring rings. The action of the internal torque generated by neighbouring rings serves to diffuse or smoothe the warp on a timescale $t_\nu \sim \alpha^{-1}(R/H)^2\Omega^{-1}$, where α is the Shakura-Sunyaev viscosity parameter and all other terms have their usual meanings. It is worthy of note that his model also assumes the warp to be small, a defect that called into question much of its applicability to real warps.

It was not long before contradictions were found within Petterson's model. Notably the 'twist equations' – the equations governing the Eulerian angles β and γ – were found to differ between Bardeen & Petterson (1975) and Petterson (1978). An investigation by Hatchett, Begelman, & Sarazin (1981) into these discrepancies found that most of the errors were due to the subtleties of working within Petterson's warped coordinate system. They produced a more accurate set of twist equations, yet left in place many of the fundamental assumptions of Petterson's model.

A more qualitative change in understanding followed the work of Papaloizou & Pringle (1983), who largely abandoned the differential geometric framework of Petterson. They demonstrated how the set of prima facie reasonable assumptions used by Petterson and Hatchett et al. led to evolutionary equations that did not conserve angular momentum and were consequently fundamentally flawed. The key physical insight of Papaloizou & Pringle (1983) was the recognition that the warp itself creates oscillatory radial pressure gradients in the frame of the fluid, resonantly driving horizontal fluid motions. The amplitude and phase of these motions are, in the case of a Keplerian disc (in which the orbital frequency matches the epicyclic frequency), constrained only by the viscosity. Angular momentum is radially advected, providing a far more efficient method of angular momentum exchange than viscous torquing. Two immediate consequences arise from their analysis. Firstly, the diffusion

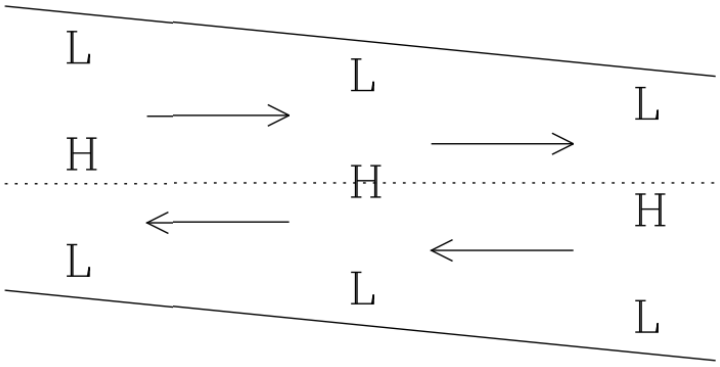

Fig. 1.4: A simple illustration of internal flows and regions of high (H) and low (L) pressure in a warped disc. The hydrostratic vertical pressure gradient creates an unbalanced radial force. Viewed from the local fluid frame, the horizontal pressure gradients oscillate at the orbital frequency. Figure taken from Ogilvie & Latter (2013a).

of the warp was found to occur on a timescale $t \sim \alpha^2 t_R$, a factor of α^2 faster than proposed by Hatchett, Begelman, & Sarazin (1981). Secondly, it was realised that the diffusive interpretation of warp dynamics was only valid when $\alpha > H/R$, what was to be called the 'diffusive regime'. The authors speculated that for $\alpha < H/R$, the warp would enter a 'bending wave' regime, where the warp would propagate radially in a wave-like manner.

Papaloizou & Lin (1995) returned to the problem of the bending wave regime some years after its initial speculation. They presented a simultaneous numerical and theoretical exploration of this low-viscosity limit, in both self-gravitating and non-self-gravitating discs. It was found that, for non-self-gravitating nearly inviscid Keplerian discs, the warp travels as a non-dispersive wave at roughly half the sound speed. The mechanism for this process is similar to the mechanism described above - horizontal velocities are resonantly forced by the warped geometry leading to the efficient and rapid transport of angular momentum. For non self-gravitating discs that are either viscous (yet still within the bending wave regime) or non-Keplerian, the warp obeys a dispersive wave equation. Self-gravitating discs allow for the non-local transport of angular momentum via gravitational interaction. In real space this involves

the integral over rings of different radii, with a kernel of the form $\frac{1}{|r-r'|}$. In Fourier space this implies a $|k|$ term in the dispersion relation. Indeed the authors report that the frequency of waves in nearly Keplerian self-gravitating discs in the long wavelength limit satisfies

$$\omega = \frac{\pi G \Sigma}{\Omega}|k|, \tag{1.1}$$

and hence waves in self-gravitating discs travel without dispersion at the speed $\pi G\Sigma/\Omega$.

Motivated by the idea that the simpler model of Hatchett, Begelman, & Sarazin (1981) failed because it did not conserve angular momentum, one might wonder whether a simpler picture of warp propagation might be obtained directly via the conservation equations themselves. Pringle (1992) took just this approach and, based on the conservation of mass and angular momentum as derived in Papaloizou & Pringle (1983), formulated a set of equations for the (vertically integrated) evolution of the disc (see Figure 1.5). The equations used by Pringle relating to the conservation of mass and angular momentum are given by

$$\frac{\partial \Sigma}{\partial t} + \frac{1}{r}\frac{\partial}{\partial r}(r\Sigma v_r) = 0, \tag{1.2}$$

$$\frac{\partial}{\partial t}(\Sigma r^2 \Omega \boldsymbol{l}) + \frac{1}{r}\frac{\partial}{\partial r}(\Sigma v_r r^3 \Omega \boldsymbol{l}) = \frac{1}{r}\frac{\partial}{\partial r}(\nu_1 \Sigma r^3 \frac{\partial \Omega}{\partial r}\boldsymbol{l}) + \frac{1}{r}\frac{\partial}{\partial r}(\frac{1}{2}\nu_2 \Sigma r^3 \Omega \frac{\partial \boldsymbol{l}}{\partial r}), \tag{1.3}$$

where $v_r(r,t)$ is the radial velocity in the disc, ν_1 is the viscosity corresponding to azimuthal shear, ν_2 is the viscosity corresponding to vertical shear and all other terms have their usual definition.

The simplicity of this one-dimensional model relative to the three-dimensional analysis of Papaloizou & Pringle (1983) made it extremely mathematically tractable. Moreover it required no assumption of small warping for its validity, and in this respect Pringle's approach represented clear progress over

previous models of warp dynamics. However this somewhat heuristic approach left some questions unanswered, most notably regarding the internal dynamics of non-linear warped discs and the interpretation or physical origin of the viscous parameters ν_1 and ν_2.

Ogilvie (1999) developed a fully three-dimensional non-linear model of warped discs, partly in an attempt to reconcile the linear three-dimensional hydrodynamic model of Papaloizou & Pringle (1983) with the simplified non-linear one-dimensional framework of Pringle (1992). In analogy to Petterson's warped cylindrical coordinate system, Ogilvie created a similar warped spherical coordinate system that better suited the geometry of a warped disc. Using this adapted coordinate system, Ogilvie was able to derive a non-linear theory of warped disc hydrodynamics in the diffusive regime ($\alpha > H/R$) that in the limit of small warps reduced to the linear model of Papaloizou & Pringle (1983) and, for discs that are not both Keplerian and inviscid, largely supported the one-dimensional approach of Pringle (1992). However it was clear from his analysis (and indeed from the work of Papaloizou & Pringle (1983)) that the 'viscosities' ν_1 and ν_2 of the Pringle angular momentum equation (1.3) should not be interpreted as true microscopic viscosities but rather as coefficients representing the general exchange of angular momentum, which in turn was more likely due to the induced horizontal flows than a simple viscous interaction. Ogilvie's generalization was expressed as

$$\frac{\partial}{\partial t}(\Sigma r^2 \Omega \boldsymbol{l}) + \frac{1}{r}\frac{\partial}{\partial r}(\Sigma v_r r^3 \Omega \boldsymbol{l}) = \frac{1}{r}\frac{\partial}{\partial r}(Q_1 \mathcal{J} r^2 \Omega^2 \boldsymbol{l}) + \frac{1}{r}\frac{\partial}{\partial r}\left(Q_2 \mathcal{J} r^3 \Omega^2 \frac{\partial \boldsymbol{l}}{\partial r}\right) + \frac{1}{r}\frac{\partial}{\partial r}\left(Q_3 \mathcal{J} r^3 \Omega^2 \boldsymbol{l} \times \frac{\partial \boldsymbol{l}}{\partial r}\right) + \mathcal{T} \tag{1.4}$$

where $\mathcal{J}$ is the azimuthally averaged second vertical moment of the density, $\mathcal{T}$ represents any generic external torque and Q_1, Q_2 and Q_3 are dimensionless coefficients describing the internal torques acting within the disc and are dependent upon the detailed dynamics of the disc. Q_1 represents a torque

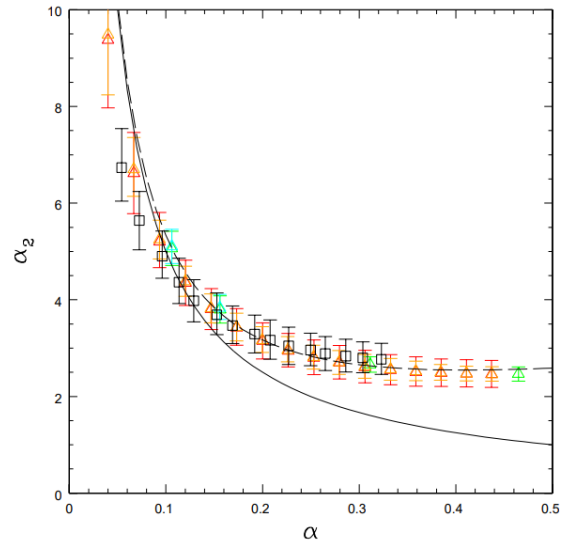

(a) Small warps. The solid black line corresponds to the relation $\alpha_2 = 1/(2\alpha)$ as predicted by Papaloizou and Pringle (1983), while the dashed line includes non-linear corrections.

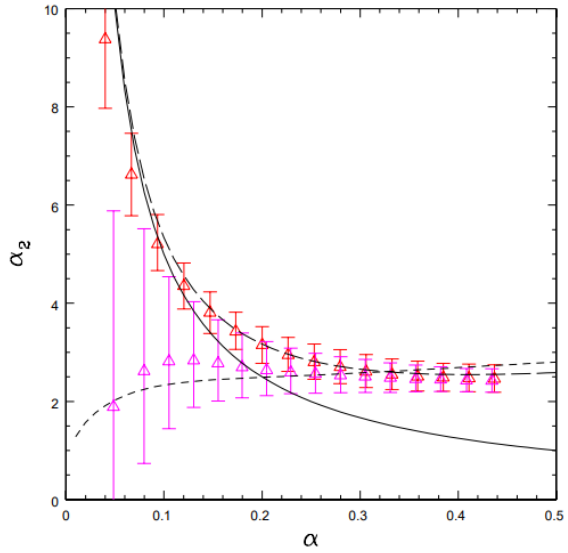

(b) Large warps (shown in pink). An additional short-dashed line corresponding to the non-linear theory of Ogilvie (1999), is shown.

Fig. 1.5: A comparison between the reduced 1-D description of Pringle (1992) (amended to include the Q_3 term of Ogilvie (1999)) and 3-D smoothed particle hydrodynamics (SPH) simulations by Lodato & Price (2010) for large and small warps. The relation between the warp diffusion coefficient α_2 and the viscosity parameter α are compared to various theoretical curves for both small and large warps. Figures taken from Lodato & Price (2010)

spinning up or spinning down the disc, while Q_2 represents the flattening or smoothing of the disc. Q_3 did not appear in the theory of Pringle (1992) and represents a torque forcing the ring to precess, leading to the wave-like dispersive propagation of the warp.

Taylor series of the Q coefficients were presented for both inviscid non-Keplerian discs and viscous Keplerian discs. Most notably in the context of this thesis, for an inviscid non-Keplerian disc one derives the dispersive wave equation

$$\Sigma r^2 \Omega \frac{\partial \boldsymbol{\ell}}{\partial t} = \frac{1}{r}\frac{\partial}{\partial r}\left(Q_3 \mathcal{J} r^3 \Omega^2 \boldsymbol{\ell} \times \frac{\partial \boldsymbol{\ell}}{\partial r} \right) \tag{1.5}$$

and

$$Q_3 = \frac{1}{2(1-\tilde{\kappa}^2)} + \frac{6+\Gamma}{4(3-\Gamma)(1-\tilde{\kappa}^2)^2}|\psi|^2 + O(|\psi|^4) \tag{1.6}$$

where $|\psi| = r|\frac{\partial \boldsymbol{\ell}}{\partial r}|$ is a measure of the degree of warping, $\tilde{\kappa}$ is the ratio of the epicyclic frequency to the orbital frequency and Γ is the adiabatic index. In the short-wavelength limit (more explicitly $|kr| \gg 1$ where k is the wavenumber) for an isothermal disc this expression implies

$$\frac{\omega(k)}{\Omega} = \pm\frac{1}{2}\left(\frac{\Omega^2}{\Omega^2 - \kappa^2}\right)(kH)^2 + O\left[(kH)^4\right], \tag{1.7}$$

consistent with a previous analysis by Lubow and Pringle (1993).

Lubow & Ogilvie (2000) investigated the dynamics of a protostellar disc initially tilted to the orbit of a binary companion, discovering that under certain circumstances such a disc may become warped. While the details of this paper are beyond the scope of this introduction, Lubow & Ogilvie (2000) also presented a reduced description of linear bending waves that is perhaps the most readily interpretable and will form the basis of the mathematical summary of warped disc hydrodynamics presented in the following section.

Ogilvie (1999) explicitly did not probe the case of Keplerian inviscid discs, restraining his analysis to either inviscid non-Keplerian or viscous Keplerian discs. As had been shown by previous authors, notably Papaloizou & Lin (1995), in a Keplerian inviscid disc the horizontal flows are resonantly driven by the warp due to the coincidence of the orbital and epicyclic frequencies. Consequently the Keplerian inviscid disc is in some sense analogous to the resonant forcing of an undamped pendulum and requires a distinct mathematical analysis. Rather than satisfying a dispersive wave equation, the bending waves in this regime qualitatively change their character and satisfy a dispersionless wave equation, travelling at half the sound speed. Ogilvie (2006) explored this resonant case for non-linear warps and found that the nature of the non-linear effects is intimately related to the adiabatic index Γ, in some cases broadening and in some cases steepening travelling waves.

We note for completeness that the radial flows induced within a warped disc may be subject to a linear hydrodynamic instability related to the parametric resonance of inertial waves as described by Gammie, Goodman & Ogilvie (2000), Ogilvie & Latter (2013b) and Paardekooper and Ogilvie (2019).

Having arrived at a coherent theory of hydrodynamic warped discs, research focus largely shifted towards either numerical simulations of warped discs in a variety of systems or tentative theoretical advancement in the addition of magnetic fields to these hydrodynamic models. We will briefly discuss both of these areas in turn.

1.4 Mathematical Background to Warped Disc Theory

Here we provide a mathematical introduction to the theory of warped disc dynamics with particular emphasis on the physical mechanisms and the application to low-viscosity bending waves. It is hoped that, in conjuction with section 1.7 and the more qualitative previous section, this section will provide sufficient mathematical context to understand the work of this thesis. As

discussed earlier, the hydrodynamics of warped discs have been formulated multiple times with several different conventions. We will be loosely following the convention of Ogilvie (1999) and especially the discussion in section 2 of Lubow & Ogilvie (2000). For a fuller and more thorough analysis, the reader is referred to these works.

1.4.1 Derivation

Consider a thin non-self-gravitating disc in an axisymmetric external potential $\Phi(r, z)$, where (r, ϕ, z) are cylindrical coordinates. There are fundamentally three frequencies of note: the orbital frequency Ω, vertical oscillation frequency Ω_z and epicyclic frequency κ given by

$$\Omega^2 = \frac{1}{r}\frac{\partial \Phi}{\partial r}\bigg|_{z=0}, \tag{1.8}$$

$$\kappa^2 = 4\Omega^2 + 2r\Omega\frac{d\Omega}{dr}, \tag{1.9}$$

$$\Omega_z^2 = \frac{\partial^2 \Phi}{\partial z^2}\bigg|_{z=0}. \tag{1.10}$$

The derivation of these frequencies is a part of standard accretion disc theory. Expression (1.8) may be derived by considering the forces upon a point particle in a circular orbit with a centrifugal force balanced by the gravitational force. (1.9) and (1.10) may be derived by considering a small horizontal or vertical perturbation to a point particle in a circular orbit respectively.

We may write out the fluid dynamical equations for the velocity in a reference frame rotating with angular velocity $\Omega \mathbf{e}_z$ as

$$\rho\left(\frac{D\mathbf{u}}{Dt} + 2\Omega\mathbf{e}_z \wedge \mathbf{u}\right) = \nabla \cdot T_{visc} - \rho\nabla\Phi - \nabla p + \mathbf{J} \wedge \mathbf{B}, \tag{1.11}$$

along with mass continuity

$$\frac{\partial \rho}{\partial t} + \nabla \cdot (\rho \mathbf{u}) = 0 \tag{1.12}$$

where D/Dt is the Lagrangian derivative, ρ is the fluid density, $\mathbf{u}$ is the fluid velocity, T_{visc} is the viscous stress tensor, Φ is the effective potential, p is the fluid pressure, $\mathbf{J}$ is the electric current density and $\mathbf{B}$ is the magnetic field. On the left hand side are the fluid acceleration and the correction due to the rotating frame of reference. On the right hand side are the viscous, gravitational, pressure and Lorentz forces respectively.

A small warp may be expressed as an $m = 1$ Eulerian perturbation to a flat disc. The sinusoidal variation of the disc mid-plane with azimuthal angle ϕ at a given radius is, from a global perspective, equivalent to a rigid tilt of the disc itself. This equivalence between $m = 1$ Eulerian perturbations and disc tilting will recur many times throughout this thesis in various forms and is worthy of some emphasis. In the context of this introductory problem, we introduce a warp through a general perturbation of all physical variables of the form

$$u(r, z, \phi, t) = \Re[u'(r, z, t)e^{-i\phi}]. \tag{1.13}$$

One may with great care solve for these perturbations, the details of which are beyond the scope of this introduction and may be found in the Appendix of Lubow & Ogilvie (2000). Their general method of approach as outlined here – solving for linear warping perturbations to an equilibrium state – will be reprised in this thesis, though with particular attention paid to magnetised discs (see Chapter 4). If we assume that the disc is nearly Keplerian and almost inviscid, more precisely defined by

$$\left|\frac{\kappa^2 - \Omega^2}{\Omega^2}\right| \lesssim \epsilon, \tag{1.14}$$

$$\left|\frac{\Omega_z^2 - \Omega^2}{\Omega^2}\right| \lesssim \epsilon, \tag{1.15}$$

$$\alpha \lesssim \epsilon. \tag{1.16}$$

where $\epsilon = H/R$ and the viscosity $\nu = \alpha c_s H$ follows the Shakura-Sunyaev

prescription (Shakura & Sunyaev, 1973), then we may derive a pair of evolutionary equations

$$\Sigma r^2 \Omega \frac{\partial \boldsymbol{\ell}}{\partial t} = \frac{1}{r}\frac{\partial \boldsymbol{G}}{\partial r} + \boldsymbol{T} \tag{1.17}$$

and

$$\frac{\partial \boldsymbol{G}}{\partial t} + \left(\frac{\kappa^2 - \Omega^2}{\Omega^2}\right)\frac{\Omega}{2}\boldsymbol{e}_z \times \boldsymbol{G} + \alpha\Omega\boldsymbol{G} = \frac{\mathcal{J} r^3 \Omega^3}{4}\frac{\partial \boldsymbol{\ell}}{\partial r} \tag{1.18}$$

where $2\pi\boldsymbol{G}$ is the internal torque, $\boldsymbol{T}$ is the external torque per unit area and $\mathcal{J} = \int \rho z^2 dz$ is the second vertical moment of the density. In this context the 'internal torque' is the torque acting on the fluid disc directly by the disc itself, whether that be through advection of angular momentum or by viscous stresses. Conversely the 'external torque' corresponds to non-local torquing due to some external source. These external torques might be Lense-Thirring, tidal or radiative in nature dependent on the physical context.

1.4.2 Discussion

The pair of equations (1.17)–(1.18) are the primary result of this section and their physical interpretations are to be emphasised. The first of these equations, (1.17), has a clear interpretation: the time evolution of the warp is driven by the radial derivative of the internal torque (which could be thought of as the differential torque between neighbouring rings of the disc) as well as the action of some generic external torque. An interpretation of (1.18) might be that the time evolution of the internal torque is driven by the differential tilting or warp of the disc (the term on the RHS). The viscosity, here represented in the third term of (1.18), acts to reduce the internal torque and is qualitatively not dissimilar to damping in a harmonic oscillator. The second term is responsible for the precession of the internal torque and in some sense represents a form of detuning; when the epicyclic modes are in resonance with the orbital frequency, this term vanishes. Its physical origin is related to the precession of radially displaced orbits when the epicyclic frequency does not

equal the orbital frequency.

One aspect of warp dynamics that is of particular importance is the distinction between the resonant (Keplerian inviscid) case and the non-Keplerian or viscous cases. The distinction between these cases may be understood quite well through a brief and somewhat informal analysis of (1.17)–(1.18).

Let us, without loss of generality, consider a system of units such that the orbital velocity Ω, r and Σ are all of unit order. The second moment of density, $\mathcal{J}$, is then of order of the square of the scale height (or equivalently $O(\epsilon^2)$). The size of precession and viscous terms in (1.18) are parameters of the disc itself and must be imposed. Additionally the wavelength of the warp itself λ_{warp} may be prescribed; this implies the existence of a dimensionless number, kH, where k is the wavenumber of the warp. For ease of comprehension it will be convenient to use the shorthand

$$\delta = \left(\frac{\kappa^2 - \Omega^2}{2\Omega^2} \right) \tag{1.19}$$

in which case (1.18) becomes

$$\frac{\partial \boldsymbol{G}}{\partial t} + \delta \Omega \boldsymbol{e}_z \times \boldsymbol{G} + \alpha \Omega \boldsymbol{G} = \frac{\mathcal{J} r^3 \Omega^3}{4} \frac{\partial \boldsymbol{\ell}}{\partial r}. \tag{1.20}$$

Note that this problem has four distinct potentially small and independently tunable dimensionless parameters: the viscous coefficient α , the non-Keplerian precession term δ, the disc aspect ratio ϵ, and the normalised wavenumber kH. The qualitatively distinct regimes of warped disc evolution may be understood through the mutual interaction and competition of these four terms. We discuss this in more detail below.

Inviscid, Keplerian

If the disc were perfectly Keplerian and inviscid, the dominant terms of (1.17) –(1.18) would be

$$\Sigma r^2 \Omega \frac{\partial \boldsymbol{\ell}}{\partial t} = \frac{1}{r}\frac{\partial \boldsymbol{G}}{\partial r} \tag{1.21}$$

and

$$\frac{\partial \boldsymbol{G}}{\partial t} = \frac{\mathcal{J} r^3 \Omega^3}{4}\frac{\partial \boldsymbol{\ell}}{\partial r}. \tag{1.22}$$

In this case the warp takes the form of a non-dispersive wave, and a cursory order-of-magnitude analysis implies that $\omega \sim O(kH)$ and $\boldsymbol{G} \sim O(\epsilon)$. In physical terms, the warp induces internal flows within the disc resulting in an internal torque of order ϵ. This in turn allows for the evolution of the warp on a time-scale of order $O(\epsilon^{-1}\Omega^{-1}) \approx r/c_s$, of order of the radial sound crossing time and longer than the orbital time ($O(1)$) but shorter than the viscous evolution time-scale ($O(\alpha^{-1}\epsilon^{-2})$). This is but another reflection of the famous result, first found by Papaloizou & Pringle (1983), that the warp can evolve far quicker than would be predicted by simple viscous evolution.

The neglected terms, $\delta\Omega \boldsymbol{e}_z \times \boldsymbol{G}$ and $\alpha\Omega\boldsymbol{G}$, may be treated as sub-dominant if $\alpha, \delta \ll kH$. Bending waves of this form were investigated by Papaloizou & Lin (1995) and Ogilvie (2006). The dispersion relation for these bending waves is

$$\frac{\omega(k)}{\Omega} = \pm\frac{c_s}{2\Omega}k \tag{1.23}$$

in an inertial reference frame. To ensure consistency with the work of this thesis, it will be convenient to formulate the dispersion relation in a reference frame co-rotating with the fluid at the orbital frequency. In this case, the frequency-shifted dispersion relation may be given as

$$\frac{\widehat{\omega}(k)}{\Omega} = 1 \pm \frac{c_s}{2\Omega}k \tag{1.24}$$

where $\widehat{\omega}$ is the wave frequency in the local frame.

Inviscid, Non-Keplerian

Let us now consider the case where the disc is inviscid but significantly non-Keplerian such that the precession term is dominant. A similar order-of-magnitude analysis plays out differently in this case:

$$\Sigma r^2 \Omega \frac{\partial \boldsymbol{\ell}}{\partial t} = \frac{1}{r}\frac{\partial \boldsymbol{G}}{\partial r} \tag{1.25}$$

and

$$\delta \Omega \boldsymbol{e}_z \times \boldsymbol{G} = \frac{\mathcal{J} r^3 \Omega^3}{4}\frac{\partial \boldsymbol{\ell}}{\partial r} \tag{1.26}$$

where $\boldsymbol{G} \sim O(\epsilon kH/\delta)$ and $\omega \sim O((kH)^2/\delta)$. Here we see that the disc again evolves on a time-scale considerably longer than the orbital time-scale ($O(1)$) and yet shorter than the viscous time-scale ($O(\alpha^{-1}\epsilon^{-2})$). The warp now satisfies a dispersive wave equation – indeed the warp evolution in this case can easily be seen to be equivalent to equation (1.5).

Note that we are able to perform something of a separation of scales analysis in this case. (1.26) has no time derivative, so for a given warp amplitude $\psi = r\frac{\partial \boldsymbol{\ell}}{\partial r}$ we may solve explicitly for the instantaneous internal torque within the disc $\boldsymbol{G}$. The time evolution of $\boldsymbol{\ell}$ may then be found from (1.25). Precisely this strategy is employed by Ogilvie & Latter (2013a) for hydrodynamic discs and in section 3 of this thesis for a magnetised disc. The precise details of the internal dynamics can be abstracted into the Q coefficients as discussed in the context of equation (1.5). More explicitly, bending waves will have the form:

$$\frac{\widehat{\omega}(k)}{\Omega} = 1 + Q_3 \frac{c_s^2}{\Omega^2} k^2 \tag{1.27}$$

The neglected term $\frac{\partial \boldsymbol{G}}{\partial t}$ is smaller than the dominant terms by a factor of $(kH)^2/\delta^2$, and hence can be reasonably neglected if $|\delta| \gg kH$. If one were to naively let δ tend to zero without consideration of this neglected term, the scalings above imply that the resonantly driven internal flows would increase without limit, and consequently internal torque $\boldsymbol{G}$ as well as torque coefficient Q_3 would diverge as $1/\delta$. This seemingly unphysical result is not a failure of

the theory but rather merely an indication that some physical assumption, namely the assumption that the neglected term $\frac{\partial \boldsymbol{G}}{\partial t}$ is sub-dominant, has failed.

Viscous, Keplerian

The viscous Keplerian case is mathematically very similar to the above inviscid non-Keplerian case, and a cursory inspection finds that the internal torque is of order $\boldsymbol{G} \sim O(\epsilon k H/\alpha)$ and $\omega \sim O((kH)^2/\alpha)$. The distinction between the two cases comes only from their geometric forms: while the non-Keplerian inviscid disc acts to precess the warp, the viscous Keplerian disc acts to diffuse the warp. From the perspective of Ogilvie (1999), this scenario corresponds to a non-zero Q_2 coefficient rather than a non-zero Q_3 coefficient.

Analysis of the neglected terms implies that the viscous term is dominant if $\delta \ll \alpha$ and $\alpha \gg kH$. If this condition holds, we are formally in what is described in the literature as the 'diffusive' regime discussed by Papaloizou & Pringle (1983). If one assumes that the characteristic radial wavelength of the warp is of the order of the radial lengthscale, $k \sim O(1)$, then the above scaling relation implies that the warp will diffusively evolve on a time-scale $t \sim (\alpha/\epsilon^2)$. Compared to the viscous evolution timescale of Hatchett, Begelman, & Sarazin (1981), $t \sim (1/\alpha\epsilon^2)$, one does indeed rederive the result from Papaloizou & Pringle (1983) that the warp evolves on a timescale shorter than the viscous timescale by a factor of α^2.

The Transition to Resonance

One may wonder how the two inviscid regimes - the resonant and non-resonant inviscid regime outlined above - are related. The transition from non-resonant to resonant behaviour will be a recurring theme throughout this thesis and is therefore worthy of especial attention.

The principal idea to be conveyed in this section is that the transition

between resonant and non-resonant behaviour is **wavelength-dependent**. As is clear from the above analysis, the internal torque evolution term is dominant when $kH \gg |\delta|$, resulting in (for an inviscid disc) the non-dispersive wave behaviour travelling at the sound speed. Conversely, the precession term is dominant when $kH \ll |\delta|$, resulting in the dispersive evolution of the warp. The transition between the two regimes occurs when $|\delta| \sim kH$, or equivalently when the ratio of the disc thickness to the warp radial extent is of the order of the frequency difference δ:

$$\frac{H}{\lambda_{warp}} \sim \frac{\kappa^2 - \Omega^2}{\Omega^2}. \tag{1.28}$$

More formally, one may seek a wave solution to

$$\Sigma r^2 \Omega \frac{\partial \boldsymbol{\ell}}{\partial t} = \frac{1}{r}\frac{\partial \boldsymbol{G}}{\partial r} \tag{1.29}$$

and

$$\frac{\partial \boldsymbol{G}}{\partial t} + \delta\Omega \boldsymbol{e}_z \times \boldsymbol{G} = \frac{\mathcal{J} r^3 \Omega^3}{4}\frac{\partial \boldsymbol{\ell}}{\partial r} \tag{1.30}$$

Without going into too much detail and defining the disc scale height such that $\mathcal{J} = \Sigma H^2$, one derives the solution

$$\widehat{\omega}(k) = \Omega - \frac{\delta\Omega}{2} \pm \frac{\delta\Omega}{2}\sqrt{1 + \frac{H^2k^2}{\delta^2}} \tag{1.31}$$

At small k the familiar non-resonant condition is easily obtained

$$\widehat{\omega}(k) \approx \Omega + \frac{\Omega}{4\delta}(kH)^2 \tag{1.32}$$

whilst at large k the dispersionless bending wave at half the sound speed

$$\widehat{\omega}(k) \approx \Omega \pm \frac{\Omega}{2}kH \tag{1.33}$$

may be found.

Graphical Interpretation

An alternative perspective on the transition to resonance may be gained by a brief examination of the dispersion curve solutions to equation (1.31), $\omega(k)$, at various values of δ as shown by Fig 1.6. The first thing to note is that there are two distinct branches of the dispersion curve, namely the warping mode and the epicyclic mode. The warping mode corresponds to a predominantly vertical oscillation at the orbital frequency, corresponding to a static warp in a non-rotating reference frame. To understand the origin of the purely epicyclic mode, note that while equations (1.17)–(1.18) were derived with the intention of studying warp dynamics, they also allow an epicyclic solution with absolutely no warp character when $k = 0$.

The transition to resonance described in the previous section thus has a graphical interpretation as an avoided crossing between the epicyclic dispersion curve branch and the vertical oscillation branch (or warping branch) of the dispersion curve.

Whether the dispersion curve may be accurately described as quadratic or linear (or equivalently whether the warp travels as a dispersionless wave at half the sound speed or not) depends on the range of wavelengths under consideration and how closely the vertical oscillation and epicyclic frequency match. An example of this is shown in Figure 1.6. Looking at the third row one can see that when the relative difference between the vertical oscillation frequency and the epicyclic frequency is roughly 0.005, the dispersion curve is linear for virtually all the wavenumbers under consideration (corresponding to a warp that roughly ten to one hundred scale-heights in radial extent). Yet as one moves further from resonance, as shown in the first row of Figure 1.6 where $|(\kappa-\Omega)/\Omega| = 0.05$, the interpretation is much more subtle. Warps with a radial wavelength of roughly fifty scale heights will still travel in a dispersionless manner at half the sound speed; however longer warps (of the order of a five hundred scale heights or more) will travel at a far slower speed and in the dispersive manner characteristic of non-Keplerian discs.

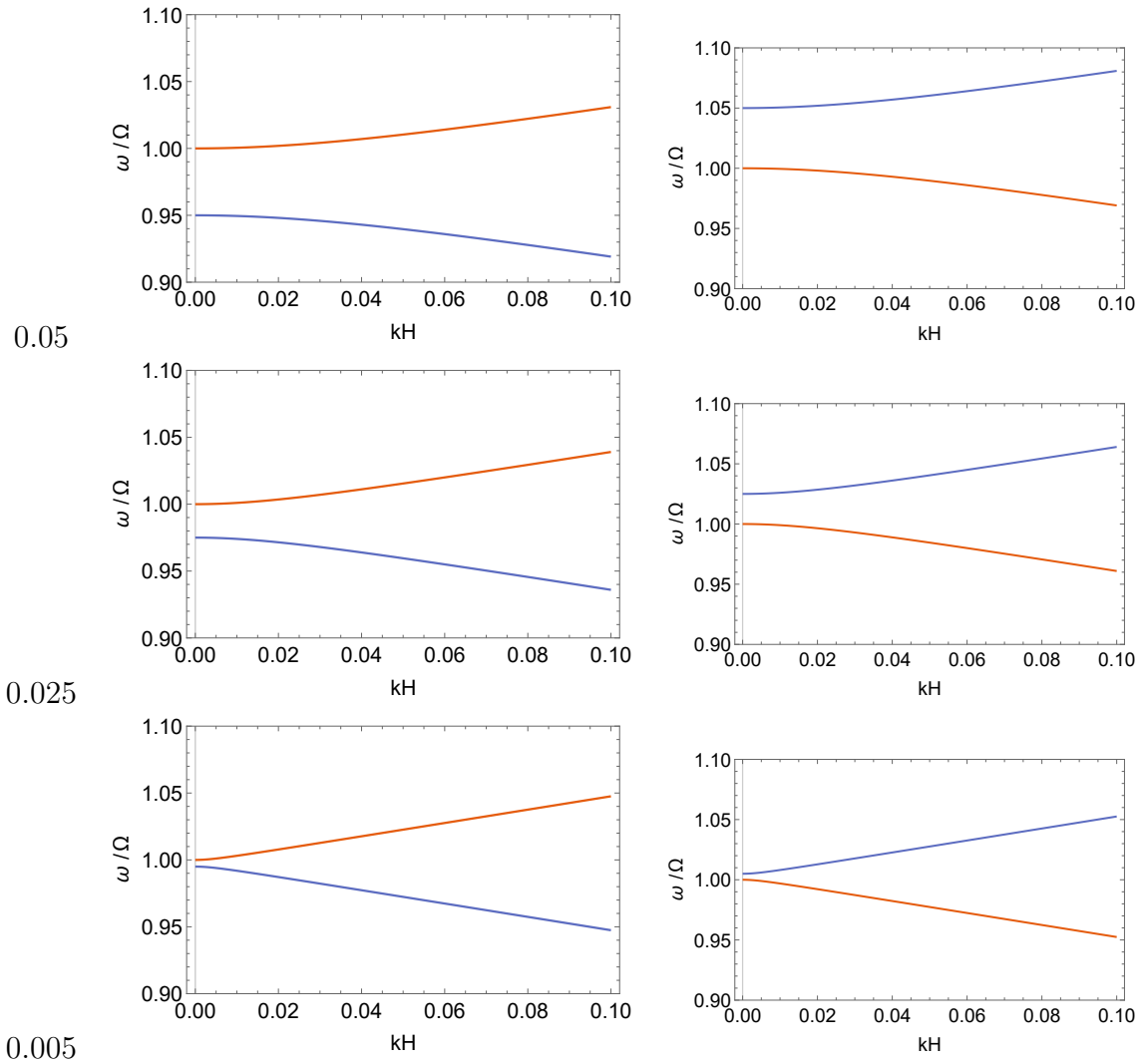

Fig. 1.6: Dispersion branches of an isothermal hydrodynamic warped disc. The epicyclic mode is shown in blue while the bending wave mode is shown in yellow. These are the solutions of equation (1.31).

This example serves to illustrate that when considering the physical significance of the hydrodynamic resonance (and its magnetic analogues as discussed later in this thesis), one should not ask how finely the disc parameters need be tuned in order to achieve resonance; rather, one should ask how finely tuned the disc parameters must be in order to achieve resonance on whatever length-scale is of interest. Generally speaking longer wavelength bending waves require more precise tuning in order for the resonant effects to be physically significant.

1.4.3 Summary

In this section we briefly described the derivation of the warp evolution equations (1.17)–(1.18) as well as exposited on their physical interpretation. The implications of this pair of equations for viscous and inviscid Keplerian and non-Keplerian discs was discussed in some detail, and particular emphasis was placed on the transition between resonant and non-resonant behaviour. A graphical interpretation of the resonance between the epicyclic and warping oscillation modes was presented, where the transition between resonant and non-resonant behaviour could be interpreted as an avoided crossing between the epicyclic and warping dispersion curve branches.

It is my hope that this introduction has provided some mathematical background to aid in the understanding of warp dynamics in hydrodynamic discs. Yet magnetised discs differ in several important ways. Notably, the single epicyclic oscillation mode is replaced by a series of distinct oscillation modes, each with their own distinct natural frequency and each independently capable of interacting with the vertical oscillation mode. Secondly, the ability of the magnetic field to non-locally transport angular momentum along the field lines creates complications that may fundamentally alter the dynamics of the warp. This thesis aims to investigate these issues and present analogous results for magnetised discs.

1.5 Magnetic Fields in Accretion Discs

1.5.1 The Structure of the Magnetic Field

Magnetic fields in astrophysics may come in a variety of complex and distinct geometric and topological structures. The precise form a magnetic field takes in a given system is dependent on the mechanism by which the field is generated. Let us briefly consider these mechanisms with the aim of motivating the various models for the magnetic field that have been studied by various authors.

The first such mechanism places the source of the magnetic field with the accreting stellar object (or possibly some perturbing binary companion). Although such a stellar field may be relatively chaotic, the dipole component typically dominates sufficiently far from the stellar surface and serves as an adequate approximation for the field as a whole. Within the magnetosphere the stellar object may enforce isorotation in the disc. Further out the magnetic field, to the extent that it threads the disc, becomes progressively twisted due to the differential rotation between the disc and the stellar object, generating a toroidal field. Such a scenario is inherently untenable and kink instabilities may set in if the toroidal field becomes significantly greater in strength than the seeding poloidal field. It has been suggested that some combination of this instability and plasma flow from the disc into the magnetosphere will 'blow' the field lines open beyond the magnetosphere (see Lovelace, Romanova & Bisnovatyi-Kogan (1995) and the references therein). The interaction between the stellar (dipole) field and the disc have been the subject of considerable analysis (Pringle & Rees (1972), Ghosh & Lamb (1979), Aly (1980)) and models of this type have dominated the majority of the literature surrounding magnetically-driven warps.

Several aspects of this model remain somewhat unclear. Perhaps most

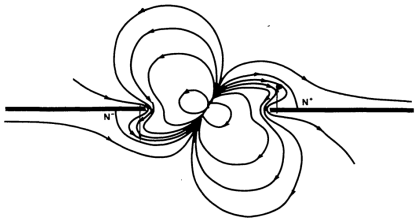

(a) A tilted magnetic dipole around a diamagnetic disc. Figure taken from Aly (1980).

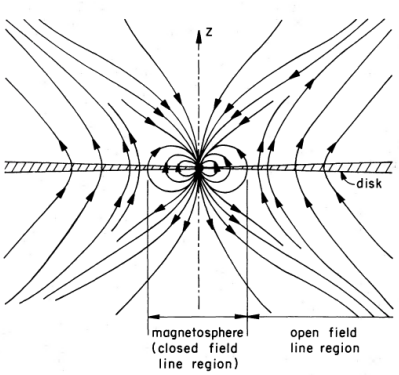

(b) A dipole field 'blown open' beyond the magnetosphere. Figure taken from Lovelace, Romanova & Bisnovatyi-Kogan (1995).

Fig. 1.7: Dipole-disc field models

notably, it is unknown to what extent the magnetic field is able to thread the disc as opposed to being screened by diamagnetic currents, as well as whether the magnetic field threading the disc remains closed (either connected to the central object or another part of the disc) or opens.

Conversely, one may consider a magnetic field originating from the disc itself. Generally speaking there are two distinct mechanisms capable of producing a magnetic field anchored within the disc. If the disc is formed by the gravitational collapse of some low-density gas initially threaded by a weak magnetic field, the collapse and accretion process will accumulate the flux within the inner portion of the disc. In equilibrium, the inward advection of the field is thought to be balanced by outward magnetic diffusion. For low-diffusivity discs the accretion process may result in the formation of a strong poloidal field anchored within the disc, though turbulent diffusion is thought to be effective in preventing advection. Disc dynamos have been proposed as an alternative route by which a macroscopic field may be anchored within the disc, though the feasibility of such a process is unclear (see the discussion of Spruit (2010)).

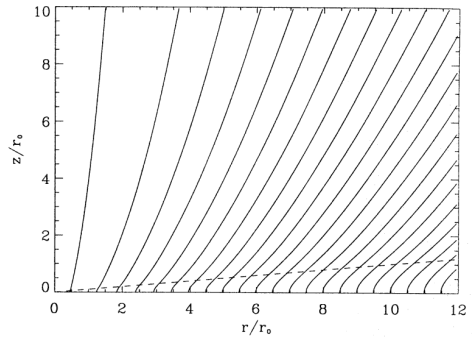

(a) Model field in a disc of finite thickness($H/R = 0.1$). Figure taken from Cao & Spruit (1994).

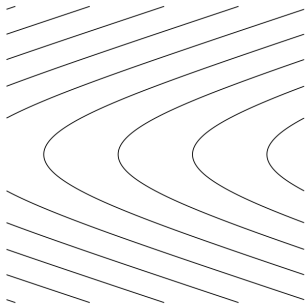

(b) A schematic of the local field structure near the disc. Figure taken from Ogilvie (2012).

Fig. 1.8: Magnetic field used in axisymmetric wind models

Early studies of the field diffusion process (Lubow, Papaloizou & Pringle (1994), Heyvaerts, Priest & Bardou (1996)) suggested that an initially seeded poloidal field would deviate from the vertical only very slightly ($B_r/B_z \sim \mathcal{P}(H/R)$ where $\mathcal{P}$ is the effective magnetic Prandtl number, expected to be of order unity in a turbulent disc). This presented an issue for disc/jet models, as the magnetic field must be inclined by at least 30° to the vertical in order to generate an outflow by a Blandford-Payne magnetocentrifugal mechanism (see section 1.5.4). However, further investigation by Guilet & Ogilvie (2012) found that vertical variation within the disc allows significantly bent poloidal magnetic field configurations to be formed via advection without the use of unexpectedly large Prandtl numbers. Hence the field accretion model provides a physical mechanism though which a class of bending field solutions could be found, some of which allow for the development of jets and winds. An archetypal poloidal bending field configuration is shown in Fig 1.8.

What magnetic field strengths are relevant when formulating disc models? The answer varies widely between different systems. Contemporary MRI simulations typically use values of mid-plane plasma beta (the ratio of gas pressure to magnetic pressure) from $\beta \sim 10^5 - 10^1$ (Salvesen et al., 2016), though wind and jet studies often allow for considerably stronger fields such

that $\beta < 1$ (Ogilvie & Livio (2001), Moll (2012)).

1.5.2 The MRI

Perhaps the simplest yet most profound question one may ask of accretion discs is: what causes them to accrete? While standard shear viscosity might appear to offer a compelling answer to this problem, mathematical models of the accretion process using microscopic viscosities have failed to account for the unexpectedly efficient accretion observed in discs. Perhaps some form of turbulent flow within the disc might result in a greater effective viscosity; if so, what drives the turbulent flow? The preceding few decades have seen a plethora of proposals for the source of disc turbulence, and precisely which mechanism is dominant in what regime remains subject to debate.

One of the most promising candidates is the magnetorotational instablity (MRI), a robust mechanism for the development and sustenance of turbulence originally promoted by Balbus & Hawley (1991). While a very lucid and complete treatment may be found in the review article Balbus & Hawley (1998), we satisfy ourselves here with a brief summary of the physical mechanism. Consider two point mass particles, initially very close to one another, linked via a massless spring and in some orbit. Let the two masses be perturbed radially such that one mass, m_o, find itself at some larger radius r_o while the other mass, m_i, finds itself at some inner radius, r_i. Due to the differential rotation of the disc, the angular velocity of the inner mass m_i is greater than that of the outer mass m_o. The consequent shearing increases the distance between the two masses and stretches the connecting spring. The spring acts to pull the two particles together, robbing m_i of angular momentum in the process and transferring that momentum to m_o; yet this frustrated effort only forces m_i to fall further within the disc, while m_o is flung further outward. The increased distance between the particles strengthens the tension, in turn driving greater separation and thus an instability is established. Here the spring represents the effects of a magnetic field threading the disc and con-

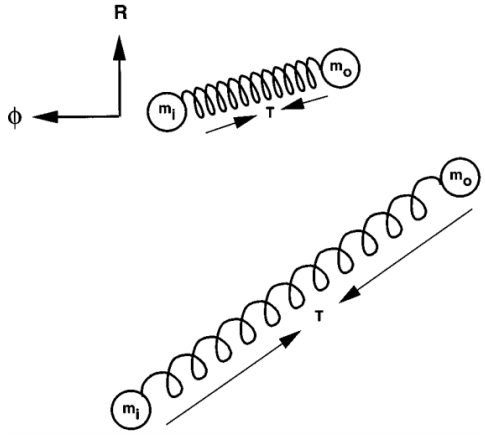

Fig. 1.9: The magneto-rotational instability (MRI) represented by two masses connected with a spring. As m_i and m_o move radially inward and outward respectively, shearing increases their separation. The tension in the spring redistributes angular momentum, further separating the two. Figure taken from Balbus & Hawley (1998).

necting various fluid elements.

The discovery of the MRI sparked a flurry of research, the details of which are sadly beyond the scope of this introduction. A tremendous amount of effort has been invested into both global (Hawley (2000), Parkin & Bicknell (2013)) and local simulations of the MRI, attempting to discern some predicated value of α – if indeed such a description is valid. Studies of stratified (Brandenburg, Nordlund, Stein & Torkelsson (1995), Simon, Beckwith & Armitage (2012)) and unstratified shearing boxes (Hawley, Gammie & Balbus (1995), Latter & Papaloizou (2012)), both with and without net flux (Fromang & Papaloizou, 2007), have proven to be somewhat divergent in their predictions. With the MRI being by nature a turbulent process, many questions about numerical resolution, convergence (Fromang & Papaloizou, 2007), and physical interpretation of these simulations remain open. In addition, the effect of both the magnetic field strength (Salvesen et al. (2016), Bai & Stone (2013), Lesur, Ferreira & Ogilvie (2013)) and the equilibrium field geometry in these scenarios remain contentious.

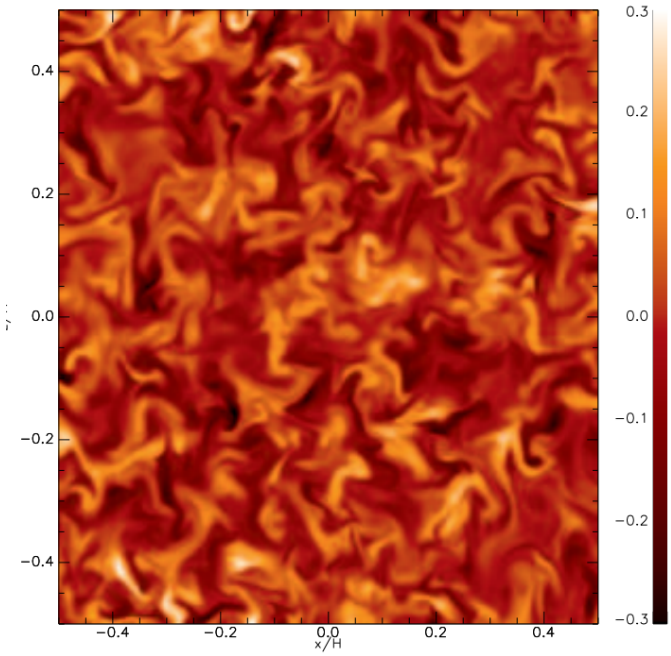

Fig. 1.10: A demonstration of the MRI turbulence in a zero net flux shearing box. The y-component of the magnetic field is shown. Figure taken from Fromang & Papaloizou (2007).

While we refrain from a full discussion of the topic, we note for context some of the salient details. Zero net flux simulations generally imply a value of $\alpha \sim 0.01$ while those with net vertical flux show considerably more efficient angular momentum transport, with associated values of α reportedly as large as $\alpha \sim 1$ (Bai & Stone, 2013) when the field approaches a mid-plane value of $\beta = 10^2$. When the magnetic field is sufficiently strong, the 'spring' becomes effectively too stiff for the MRI to function, creating distinct MRI stable/unstable regimes. The precise MRI stability boundary in the presence of different field geometries remains unknown, though as a rule of thumb, the MRI is suppressed when plasma $\beta \lesssim 1$.

Though the aim of this thesis is not a direct investigation of the MRI, there is a surprising correspondence between the content of this thesis and an early theoretical investigation of the MRI in a vertically stratified local

model by Gammie & Balbus (1994). They considered small perturbations to an axisymmetric radially homogenous isothermal disc threaded by a vertical magnetic field, seeking an exponentially growing solution corresponding to an unstable MRI mode. The coupled radial and toroidal equations of motion each involve a second order operator of Sturm-Liouville form. Solution by semi-analytical methods gives a spectrum of MRI modes, of which the lowest order mode takes prominence as the fastest growing and most unstable. Most notably, they find that the transition to MRI-stability occurs when

$$V_{a0}^2 > 2q\Omega_0^2 H^2/E_1, \tag{1.34}$$

where E_1 is the lowest eigenvalue of a particular differential operator ($E_1 = 1.34$ for an isothermal disc), V_{a0} is the mid-plane Alvén speed, q is the orbital shear rate (3/2 for a Keplerian disc) and all other terms have their usual meanings.

The work of Gammie & Balbus (1994) is somewhat similar to that of section 3 of this thesis. Indeed, there is a direct correspondence between the MRI modes of Gammie & Balbus (1994) and the Alfvénic-epicyclic modes discussed in this thesis; it is only in the physical interpretation that the two truly differ. From the perspective of Gammie & Balbus (1994), the horizontal epicyclic-magnetic modes are of interest when they are exponentially growing, allowing the spontaneous development of turbulence when their frequency (or complex growth rate) $\omega_n^2 < 0$. From the perspective of our thesis, these very same modes may, when stable, become resonant with the vertical oscillation frequency Ω_z when $\omega_n^2 = \Omega_z^2$, modifying or enhancing the warp in a manner akin to that of Papaloizou & Pringle (1983).

1.5.3 Jet Launching

The very existence of vast astrophysical jets (Curtis, 1918) hurtling into the great blackness would seemingly provide sufficient motivation to study their origins. Yet over the years they have been recognized not only for their fantastical appearance but for their profound dynamical consequences on the

accretion discs from which they are generated. While traditionally accretion discs were viewed as a 'sink' into which mass falls as angular momentum is expelled, propagating outward due to viscous/magnetic torques or some form of turbulence, jets provide an alternative mechanism by which angular momentum might be efficiently removed from the disc. The existence of these jets leads to several questions. In the context of this thesis, the most pertinent are: how are these jets created, and what do they imply about the structure of the magnetic field?

Blandford & Payne (1982) proposed a conceptually simple mechanism to explain at least part of the jet formation process (see Fig 1.11). Consider the magnetically dominated region of the disc some number of scale heights above the mid-plane. The magnetic field, assumed to be anchored within the disc, rotates at the orbital frequency of its footpoint in the disc. Due to the low density of this region, each fluid element is forced to follow the dynamically dominant field 'like beads on a string', as phrased by the original authors. Let us consider the stability of a small fluid element in this region originally at radius r_0 and assumed to remain corotating with the field at the Keplerian orbital frequency $\omega_0 = \sqrt{GM/r_0^3}$. In a corotating frame of reference there are two contributions to the effective potential of the fluid Φ - the first centrifugal and the second gravitational in origin - giving

$$\Phi(r,z) = -\frac{GM}{r_0}\left[\frac{1}{2}(\frac{r}{r_0})^2 + \frac{r_0}{(r^2+z^2)^{1/2}}\right].$$

If we consider small radial and vertical perturbations δr and δz from the element's original position at $r = r_0$, it can be shown that the fluid element is stable iff $(\delta z/\delta r)^2 > 3$. The vertical and horizontal perturbations are not independent, but are rather fixed by the condition that the fluid is constrained to travel along the magnetic field line. More specifically, if the field lines form an angle with the vector perpendicular to the disc surface in excess of 30°, the system is unstable and material is evacuated from the disc magnetosphere. While other questions remain, notably regarding the global field geometry and the collimation of the jet far from the disc (Heyvaerts & Norman, 1989), the

Blandford-Payne mechanism provides a simple criterion for the development of a jet outflow from the accretion disc surface.

Improvements in computational resources have spurred the development of numerous numerical investigations into the nature of jet formation, beginning with Uchida & Shibata (1985). For a more complete background on astrophysical jets, see the review articles by Spruit (1996) and Pudritz, Ouyed, Fendt & Brandenburg (2007) as well as the references therein. Speaking broadly, theorists have been attempting to gain a better understanding of how the disc parameters influence both the jet outflow and the resultant magnetic field structure. More recently, following a series of simulations displaying unsteady outflows driven by MRI turbulence (Bai & Stone (2013), Fromang, Latter, Lesur & Ogilvie (2013), Riols, Ogilvie, Latter & Ross (2016)), the interaction between the MRI and disc jets/winds has been gaining greater attention.

In the context of this thesis, the axisymmetric model of the interior of a thin disc threaded by a poloidal field of dipolar symmetry presented by Ogilvie & Livio (2001) is of greatest relevance. While previous jet models had treated the disc as a boundary capable of loading mass at a specified rate upon the magnetic field lines, the model of Ogilvie & Livio (2001) allowed the mass-loss rate to vary dependent on the disc and field parameters. The mass-loss rate was found to be sensitive to both the strength of the magnetic field and, critically, the inclination angle of the poloidal field with the disc surface (see also Cao & Spruit (1994)). For example, a 10 degree change in inclination angle in a disc that is marginally MRI stable may easily result in a change of several orders of magnitude in mass-loss rate. The impact of disc warping on this sensitive process remains largely unexplored and motivates a better understanding of magnetised warped discs with a jet-launching magnetic field geometry.

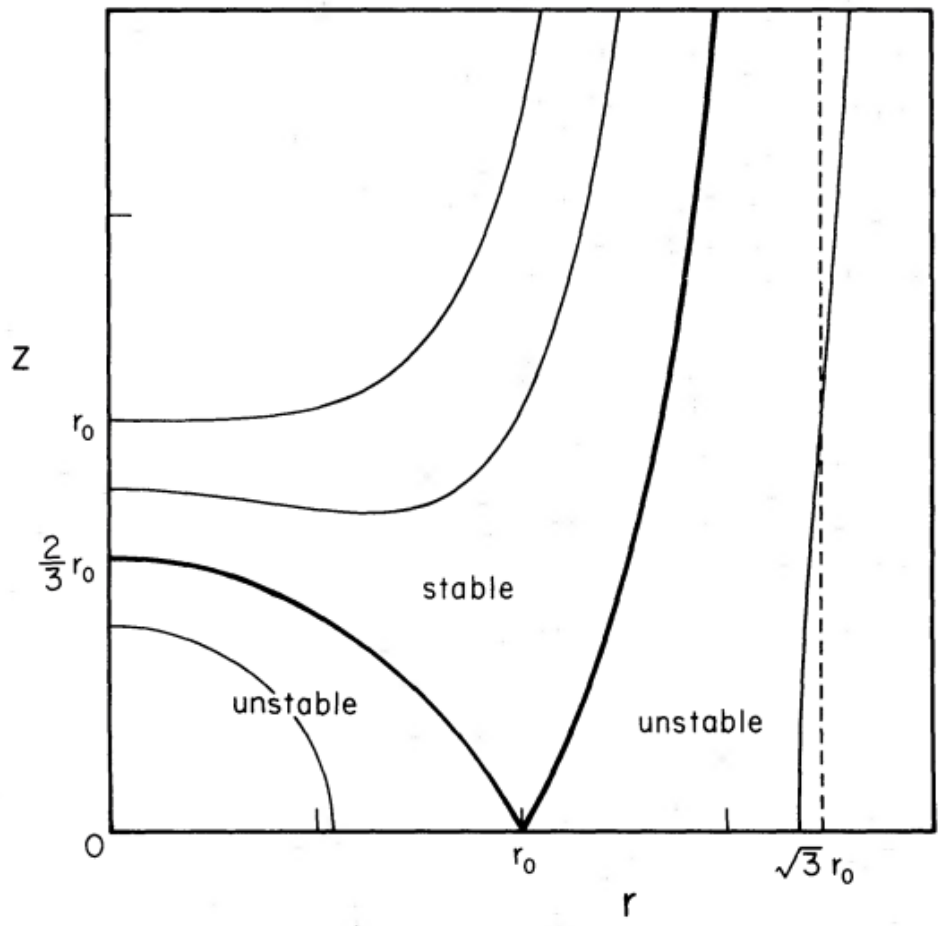

Fig. 1.11: Equipotential surfaces for a bead on a wire, corotating at a Keplerian angular velocity at radius r_0 within a gravitational potential. If the wire is inclined at less than 30° to the vertical, the bead is stable. If the wire is incline at greater than 30° to the vertical, the equilibrium at r_0 is unstable. Figure taken from Blandford & Payne (1982).

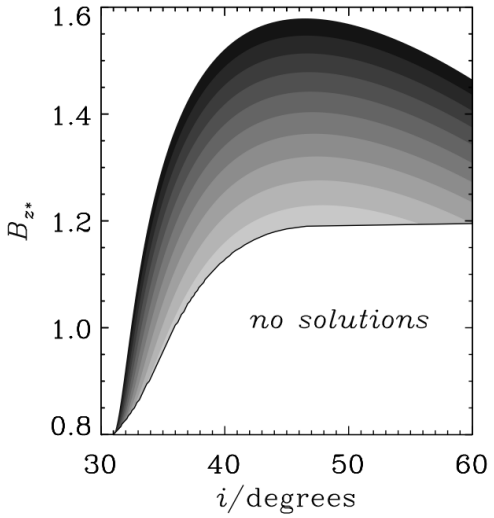

Fig. 1.12: Mass loss rate via jet outflow as a function of the strength and inclination of the magnetic field. Contours of $\log_{10}(m/\Sigma\Omega)$ range from -14 (lightest) to -4 (darkest) with unit spacing. Figure taken from Ogilvie & Livio (2001).

1.5.4 Magnetised Warped Disc Theory

While this thesis presents an analysis of warp dynamics in magnetised discs, it is important to acknowledge that in this respect it is not totally unique. However, the work of this thesis is distinguished from previous attempts primarily by the structure of the magnetic field under consideration and the emphasis on the warp dynamics. The aim of this section is to provide an overview of prior research on magnetised warped disc theory.

In a somewhat prescient paper, Aly (1980) considered the structure of a magnetic dipole inclined with respect to a diamagnetic disc and determined that the resultant magnetic pressure imbalance above and below the disc would generate a torque. This core idea would be substantially amended by both Lai (1999) and Terquem & Papaloizou (2000). In the first of these works, Lai (1999) investigates a dipole-disc model in which the stellar rotation axis, the magnetic dipole moment and disc angular momentum may indepen-

dently be misaligned. He considers both a perfectly diamagnetic disc and a magnetically threaded disc. In the diamagnetic case, the induced azimuthal screening current interacts with the radial stellar field to induce a tilt within the disc. In the magnetically threaded case, the twisting of the vertical threading field generates a discontinuity in the azimuthal magnetic field across the disc, implying the existence of a radial surface current. This current interacts with the azimuthal stellar field to again produce a tilting force. While not given a full mathematical treatment, Lai takes care to highlight the potential resonance between the magnetically driven warping with either the vertical oscillation mode or the epicyclic modes. In this respect, much of the work of this thesis may be considered an expansion of this general idea.

Terquem & Papaloizou (2000) provide a similar analysis but distinguish their work in several critical ways. Like Lai (1999), Terquem & Papaloizou (2000) consider the interaction between a disc and a misaligned dipole. Yet the scope of their analysis was somewhat more restrained, limiting themselves to perfectly diamagnetic discs in analogy to the models of Aly (1980) and Low (1986) and situations in which the disc and stellar rotational axes are aligned (though misaligned with the stellar magnetic dipole). Terquem & Papaloizou (2000) also lack a toroidal field threading the disc; this component is likely generated by the twisting of vertical field lines in the model of Lai (1999), and hence is unnecessary in a wholly diamagnetic scenario. Terquem & Papaloizou (2000) however note that the model of Lai (1999) did not include the potentially crucial effects of disc warping on the disc response. As an explicit example of this, Terquem & Papaloizou (2000) considered a sinusoidal vertical perturbation to their thin disc. These perturbations distort the surrounding magnetic field, inducing a magnetic restoring force on the disc surface. The dispersion relation of these waves are given as

$$(\omega - \Omega_K)^2 = \Omega_K^2 + \frac{2(B_r^+)^2}{\mu_0 \Sigma}|k| \tag{1.35}$$

where Ω_K is the Keplerian frequency, B_r^+ is the value of the radial bending field at the upper surface, and k is the wavenumber of the disturbance. This

result is consistent with equation (4.19) of this thesis. These propagating waves appear in the numerical results of Terquem & Papaloizou (2000), potentially forming a smooth warp if the viscosity is sufficiently large.

A discussion of the theory of magnetised discs would be incomplete without mention of Agapitou, Papaloizou, & Terquem (1997), in which global bending modes of an aligned disc-dipole system are analysed in some detail. In contrast to the previous two models, the disc is permitted to have some assumed internal/self-generated field in addition to the background dipole field. A magnetic bending instability is presented which could perhaps be best understood, as suggested by the authors, as due to the competition between a stabilising gravitational potential acting on a current loop and the release of magnetic energy due to the loop-dipole interaction. Alternatively, a more general form of (1.35)

$$(\omega + m\Omega)^2 = \Omega_K^2 + \frac{2B_r^+}{\Sigma}\frac{\partial B_z}{\partial r} + \frac{2(B_r^+)^2}{\Sigma}|k| \tag{1.36}$$

indicates that instability is possible if $\Omega_K^2 + \frac{2B_r^+}{\Sigma}\frac{\partial B_z}{\partial r} < 0$. This may be satisfied if the vertical magnetic field threading the disc is both very strong and very rapidly decreasing with radius; a condition that is likely to hold only close to the magnetosphere where the field lines are linked with the central dipole.

As we end this discussion of previous studies of magnetised warped discs, it may be helpful to clarify to how the work of this thesis differs from the prior research presented above.

The first difference lies in physical context. Many of these works have sought to understand warp genesis and propagation primarily through the effects of an external stellar field. While this is well-justified in many scenarios, especially in a disc with a weak intrinsic magnetic field close to the magnetosphere, there are situations in which this approach is not valid. As discussed in 1.5.2, the accretion of magnetic flux or disc dynamos might present situations in which, at least beyond some radii, the field is anchored within the disc

itself. Even when the stellar dipole initially dominates, the 'blowing open' of the field lines may again result in an open configuration for the majority of the disc; in these cases, prior research offers little understanding of the warp dynamics.

A second related difference lies in the treatment of the internal torque in the warp propagation process. Papaloizou & Pringle (1983) and many other since have convincingly demonstrated that hydrodynamic warps are often primarily communicated by internal flows driven by a radial pressure gradient. Yet all the analytical models discussed above treat the disc in a vertically integrated manner, entirely ignoring the presence of these internal flows. From their perspective, warp propagation only proceeds by the non-local transfer of angular momentum via the external magnetic field. In the case of Lai (1999), the warping of the disc itself provides no feedback, and is entirely driven by the external field. Terquem & Papaloizou (2000) are correct in identifying the potential magnetic contribution to the propagation of the warp due to the warping itself, yet still do not consider the internal flows of the disc. Due to this omission, scant effort has been made to synthesise our understanding of warp propagation in magnetised discs with the corresponding hydrodynamic theory.

Neglecting the internal flows of the disc may be permissible if the field is sufficiently strong and the disc sufficiently viscous to render the internal torque negligible – this may perhaps be the case very close to the magnetosphere. Yet the total neglect of the internal flows in magnetised warped disc models remains a worry; a worry made especially acute by the development of MHD warped disc simulations capable of resolving these flows.

This thesis aims to investigate generic warp propagation in a disc threaded by an open magnetic field. The models presented in this work are local, rather than global, so that we may resolve the critical internal flows of the disc and better situate ourselves in the context of the well-established hydrodynamic

theory. Whereas the previous theories are of greatest relevance close to the stellar magnetosphere, where coupling to the stellar object dominates the angular momentum transport, the work of this thesis is of greatest relevance to systems with an open field geometry, where internal torques may provide a substantial contribution to the warp propagation.

1.6 Warped Disc Simulations: A Survey of the Field

1.6.1 General Comments

Driven by the rapid advance of computing power, the previous two decades have seen a gradual shift of emphasis from analytic models of warp propagation towards global simulation. Before embarking on a discussion of the various simulations that have formed the landscape that theory must now navigate, it may be informative to briefly consider the inherent difficulties in resolving warped discs numerically via global simulations.

Let us briefly consider the physics from the perspective of a fluid element within a thin disc. The warp induces radial pressure gradients oscillating at the orbital frequency (in the local fluid frame; in the static global frame, this is merely a static $m = 1$ azimuthal perturbation). Consequently the relevant motion we wish to resolve occurs within the disc and on the orbital time-scale. The warp, on the other hand, evolves on a timescale that may be an order of R/H slower for Keplerian inviscid discs, $(R^2/H^2)\frac{\Omega^2}{\kappa^2-\Omega^2}$ for non-Keplerian inviscid discs or $(\alpha R^2/H^2)$ for Keplerian viscous discs. Furthermore even in the Keplerian inviscid case, one is often interested in the long-term steady behaviour of the warp which will be resolved on a slower time-scale related to the viscosity. To perform a satisfactory global simulation one must therefore resolve the interior of a thin disc globally with a time-step that captures the orbital time-scales, yet runs long enough to make meaningful statements on the vastly larger warp evolution timescales.

Spatial resolution may also severely constrain the performance of certain warped disc simulations. To achieve true fidelity to many of the most physically interesting or relevant systems, a simulation must simultaneously resolve the internal flows within a thin disc (including those on the turbulence length-scale) while also simulating an appropriately large radial region of the disc to comment on the large-scale warp evolution. Attempts to circumvent these restrictions in practice – by, for example, increasing the disc aspect ratio or unnaturally truncating the disc outer radius – are common. These contrivances, though often necessary, may have dramatic and unintended consequences. If the aspect ratio is artificially increased then the fundamental bending wave/diffusive behaviour may be significantly altered (see the discussion of section 1.4). If the disc is radially truncated, propagating bending waves may reflect off the outer radial boundary and artificially induce a global rigid precession of the disc where none ought to exist (Nixon and King, 2013). Computational physicists investigating warp propagation are therefore confronted with the tremendous challenge of producing technically feasible and physically reliable results.

Many of these concerns led to the adoption of Smoothed Particle Hydrodynamics (SPH) (Gingold & Monaghan (1977), Lucy (1977)) for the majority of hydrodynamic simulations of warps. Rather than a Eulerian grid-based approach to fluid dynamics, SPH takes a Lagrangian approach; speaking loosely, SPH tracks the motion and interactions of a finite number of representative particles from which the general fluid flow is extracted. While this meshfree method has some difficulty when imposing certain boundary conditions such as walls, it is well-suited to dynamic flow geometries and free boundaries. Further, SPH methods tend to preserve conservation relations and dynamically resolve higher density regions. In the context of a warped disc, dealing with multiple time-scales, large disparities between high and low-density regions and flexible geometries, SPH perhaps not unexpectedly became the method of choice of computational physicists. SPH is not without its downsides; grid-based methods may offer tighter control of the viscosity (e.g. Fragner & Nelson

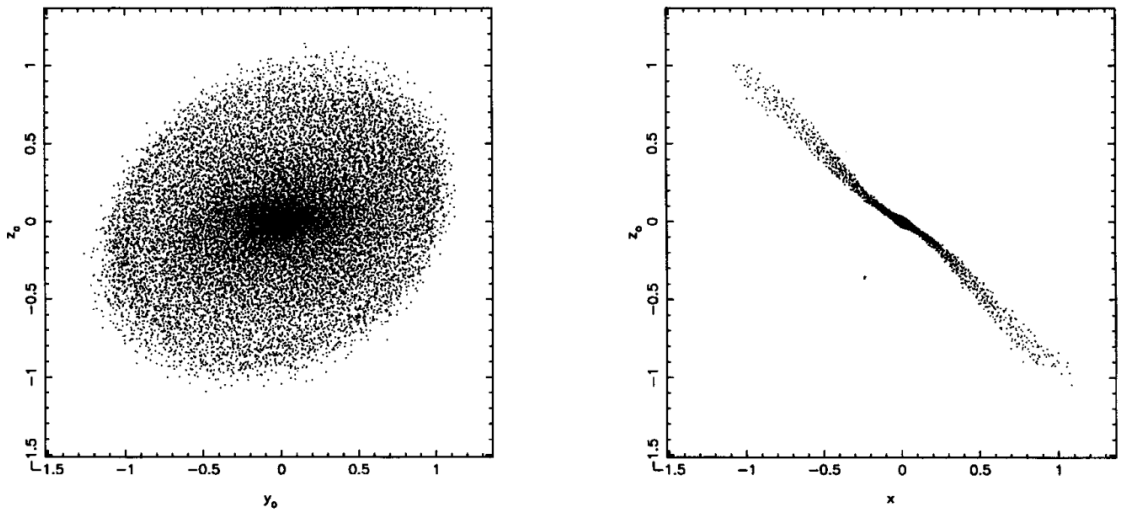

Fig. 1.13: An early smoothed particle hydrodynamics simulation discerning the presence of a tidally-induced disc warp. Figure taken from Larwood, Nelson, Papaloizou & Terquem (1996).

(2010)) and tend to be easier to extend to MHD.

Owing to the great number of simulations that have been performed and the limited space available in this introduction, it is necessary to only highlight a small selection. Nevertheless we hope to provide an overview of the spectrum of scenarios that have been investigated by computational astrophysicists, indicate those papers that are most significant in the context of this thesis, and highlight the outstanding problems that the work within this thesis hopes to, if not directly address, at least inform.

1.6.2 Hydrodynamics

Larwood et al. (1996, 1997) presented the first global simulations of a hydrodynamic warped disc using an SPH code developed previously by Nelson and Papaloizou (1994, 1996) with 17500 particles. Their model investigated the warp stimulated by the presence of a misaligned binary system. Under their choice of parameters the disc was well within the bending-wave regime,

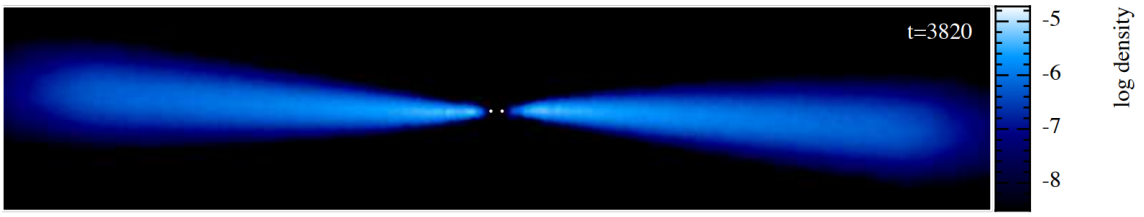

Fig. 1.14: Smoothed particle hydrodynamics simulation of a disc initially inclined to the plane of the central binary system. The relevant parameters for this simulation are $H/R \sim 0.1$, $\alpha = 0.05$ and the disc at the outer radius is inclined at an angle of 5° to the binary plane. Figure taken from Facchini, Lodato & Price (2013).

leading to the efficient transfer of angular momentum and the nearly rigid-body precession of the disc, resulting in the formation of only a modest warp. However, much of the emphasis was placed on the tidal truncation of such binary discs rather than the dynamics of the warp, and the parameter space under investigation did not provide tremendous clarity in the verification or contradiction of the hydrodynamic warp models presented in section 1.4.

Their work was followed up with a pair of papers (Nelson & Papaloizou (1999)(2000)) that provided a much clearer comparison of simulation to hydrodynamic theory. With a resolution of 20000-100000 particles, $H/R \sim 0.1$, they were able to reproduce the distinct bending wave and diffusive regimes predicted by Papaloizou & Pringle (1983) as well as resolve the expected horizontal internal flows so critical to the warp dynamics. The non-linear regime was found to be more dissipative than expected, largely due to the formation of shocks resulting from the collision of oppositely directed internal flows. The second of the two papers investigated the Bardeen-Petterson effect through the use of a pseudo-Newtonian approximation for the Kerr black hole with an added gravitomagnetic force. Notably they found that due to the enhanced warp evolution driven by the internal flows of the disc (as described in Papaloizou & Pringle (1983)), the transition radius was substantially smaller than originally predicted by Bardeen and Petterson.

Generic radiation-driven hydrodynamic warped discs were studied via 3D SPH simulations by Foulkes, Haswell & Murray (2006), with an extension to super-periodic X-ray binaries such as Her X-1 produced several years later (Foulkes, Haswell & Murray, 2010). While the details of their results are beyond the scope of this introduction, we note that rather gratifyingly they strongly concluded, at long last, that the super-orbital behaviour of Her X-1 – the stimulus for the development of warped disc theory nearly half a century prior – was indeed likely caused by irradiation-driven warping of the surrounding disc.

A wealth of hydrodynamic global simulations that placed greater emphasis on warp dynamics rather than the specifics of a particular system (akin in spirit to Nelson & Papaloizou (1999)) proved the hydrodynamic theory of warps to be remarkably successful. Although an initial hydrodynamic SPH simulation by Lodato & Pringle (2007) appeared inconsistent with the theory of Ogilvie (1999), this disagreement was later found to be due to a slight error in the implementation of the zero-torque inner boundary condition. Lodato & Price (2010), improving upon the work of Lodato & Pringle (2007), used the SPH implementation in PHANTOM (Price et al., 2017) with up to 20 million particles to run a suite of simulations probing the diffusive regime at a variety of resolutions, warp amplitudes and viscous prescriptions. Both the diffusion coefficients and precession were found the be in very good agreement with theory (see Figure 1.5). Facchini, Lodato & Price (2013) provided a similar analysis, again using PHANTOM, to probe both the diffusive regime, the bending wave regime with $\alpha = 0.01$ and a nearly inviscid case $\alpha \approx 0$. A comparison of their 3D simulation to a reduced 1D model similar to that of Pringle (1992), (equations (1.2)–(1.3)), lent credence to the notion that 3D warp dynamics could be accurately approximated by the 1D analytic models developed in section 1.4. A suite of hydrodynamic simulations of misaligned binaries performed in the grid-based code NIRVANA by Fragner & Nelson (2010) found again that thick inviscid discs communicate the warp efficiently and precess as rigid bodies, while thin viscous discs may develop significant

twists and warps, consistent with the bending-diffusive regime dichotomy.

It has been suggested that under certain circumstances – namely larger, non-linear warps in thin discs with small viscosities – the disc may be subject to fragmentation and breaking into distinct, non-parallel discs. While this dramatic outcome has been observed in several simulations stretching back to Larwood & Papaloizou (1997) (and indeed was a theoretical implication of Ogilvie (1999)), the idea has gained renewed interest following a series of grid-based 1D simulations (the validity of which had been confirmed in prior works by Lodato et al.) by Nixon & King (2012). It was found that for constant values of α, Lense-Thirring torques may cause the fragmentation of the disc for sufficiently large inclination angles. Moreover, non-linear warping effects may further exacerbate the fragmentation process at larger viscosities and smaller inclinations. Although this phenomenon is not directly relevant to the work of this thesis, we note that this remains an active area of research (Doğan, Nixon, King & Price (2015), Nealon et al., (2016)).

Hydrodynamic warped disc simulations in recent years have largely shifted focus from the study of the fundamental warp evolution process to the study of specific theoretical or observational contexts in which warps may arise. A handful of recent examples might be the case of misaligned disc-planet orbits (Xiang-Gruess & Papaloizou, 2013), single stellar flybys (Cuello, et al. (2018), Xiang-Gruess (2016)), tidal disruptions (Ivanov, Zhuravlev & Papaloizou (2018), Xiang-Gruess, Ivanov & Papaloizou (2016)), the interaction of two separate proto-planetary discs during a close encounter in a stellar cluster (Xiang-Gruess & Kroupa, 2017). However, as per our discussion in section 1.5, the ubiquitous presence of magnetic fields in many astrophysical contexts and the importance of magnetic turbulence to the accretion process imply that one must be conscious of the limits of purely hydrodynamic simulations. To that end we now turn our attention to magnetohydrodynamic simulations of warps in discs.

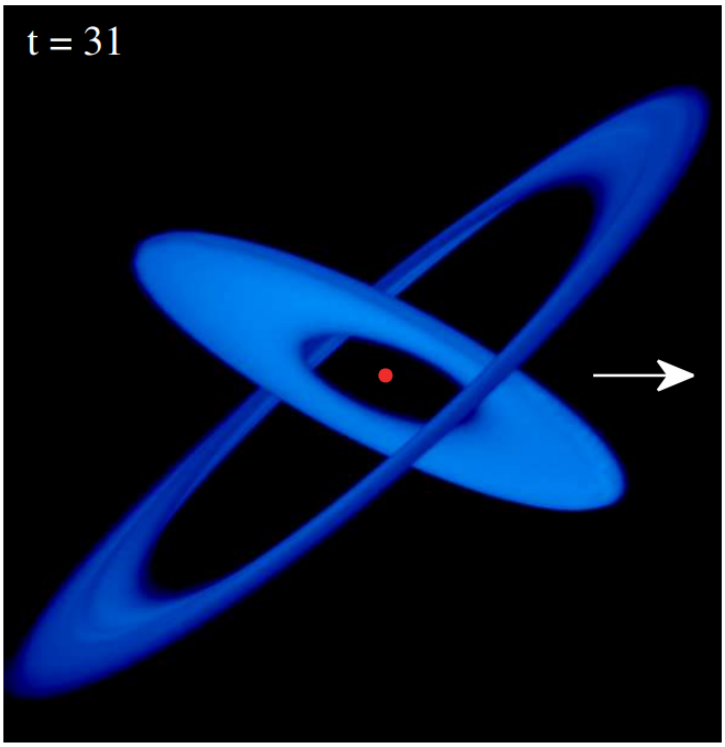

Fig. 1.15: An SPH simulation of a highly inclined disc (45°) orbiting a binary system. After 31 binary orbits, the initially unwarped disc has fragmented into a distinct inner and outer disc. Figure taken from Doğan, Nixon, King & Price (2015).

1.6.3 Magnetohydrodynamics

While the hydrodynamics of warped discs have been somewhat thoroughly explored, the study of equivalent magnetohydrodynamic problems remains in its relative infancy. Computational limitations are largely to blame for this; the presence of a magnetic field complicates the implementation of SPH, introduces ambiguities in the appropriate flux distribution or field structure upon initialisation, allows for the existence of significant outflows, introduces turbulence via the MRI and severely restricts the necessary time-step due to the large Alfvén speeds in low density regions. Yet the recent advent of newer grid-based MHD simulations has rendered the once impossible possible and likely heralds the beginning of a new era in the numerical study of warped discs. With it will certainly come new challenges for theorists, who must amend their hydrodynamic models to accommodate the effects of small-scale and large-scale magnetic structures.

Motivated by the problem of magnetically-driven warping as expounded by Terquem & Papaloizou (2000) and Lai (1999), Murray et al. (2002) used SPH to investigate a misaligned cataclysmic variable in which the donor is magnetised, thereby inducing a warp. While the structure of the magnetic field in their problem is qualitatively different to that of this thesis (see section 1.5), this paper remains notable for being the first to simulate warping in the presence of a magnetic field, the first to exhibit the development of a warp from an initially flat disc, and for the rather large jump in resolution to 500000 particles. It could be argued that this was not a true MHD simulation, as indeed a magnetic force term was added by hand to an essentially hydrodynamic code.

Fragile & Anninos (2005) eschewed the use of SPH, electing to use 'Cosmos', a grid-based parallel code suitable for relativistic MHD to simulate a warped magnetised disc near to a misaligned black hole. They cleverly sidestepped many of the computational difficulties inherent in grid-based warped disc simulations by initialising the disc along the computational grid while

misaligning the black hole metric. Having presented the first fully relativistic hydrodynamic warped disc simulations (albeit for relatively thick discs), they used an updated version of their code, 'Cosmos++', to present analogous GRMHD simulations with a magnetic beta $\beta \gtrsim 10$ (Fragile et al., 2007). Though a triumph in the field of black hole simulation (soon to be followed by a similar simulation that better resolved the poles, allowing greater investigation of jets (Fragile, Lindner, Anninos & Salmonson, 2009)), from a warp dynamical perspective the results are rather plain. Due to the thickness of the discs in use, $\alpha \leq H/R$ and the warp evolves as a bending wave rather than diffusively as is the case for standard Bardeen-Petterson alignment. However, the wavelength of the warp is considerably longer than the radial extent of the disc itself, leading to uniform precession and very modest (though physically significant) warping.

Morales Teixeira, Fragile, Zhuravlev & Ivanov (2014) revisited the Bardeen-Petterson effect using a newer, fully conservative implementation of Cosmos++ which boasted the ability to better resolve shocks. Through the introduction of an ad hoc cooling function, they were able to reduce the scale height of the disc to $H/R = 0.08$, significantly smaller than their thick disc counterparts of Fragile et al. (2007). Prograde discs were not found to align with the black hole spin, in contrast to the prediction of Bardeen and Petterson, but rather became further misaligned, leading to the tentative conclusion that the authors remain in the bending wave regime. Some alignment was, however observed in an analogous retrograde simulation. Much like the preceding work, emphasis was placed on the full general relativistic treatment and the specifics of Bardeen-Petterson alignment close to the black hole rather than the evolutionary mechanism of the warp. McKinney, Tchekhovskoy & Blandford (2013) utilised the GRMHD code HARM in relatively thick discs ($H/R \sim 0.3 - 0.6$) to investigate Bardeen-Petterson alignment in magnetically saturated discs (minimum plasma $\beta \approx 40$); this stands in contrast to Morales Teixeira, Fragile, Zhuravlev & Ivanov (2014), whose model did not include sufficient magnetic flux to produce a magnetically-arrested state by

the end of their simulation. Their results suggest that the inner section of a magnetically saturated disc and its jet may orient themselves with the black hole spin due to EM forces in what the authors describe as a 'magneto-spin alignment mechanism.'

The first explicit investigations into the effects of MHD itself on warp propagation were performed by Sorathia, Krolik & Hawley (2013a, 2013b) and Krolik & Hawley (2015) in somewhat thick discs ($H/R \simeq 0.1 - 0.2$) using the 3D finite-difference MHD code Zeus. Interestingly the authors sought to not only compare and contrast the warp evolution of hydrodynamic and MHD discs but also overturn many of the foundational principles of hydrodynamic warp theory. This re-evaluation of hydrodynamic warped theory and the inclusion of MHD is no coincidence, and much of the issue lies at heart with the interpretation of α. In its initial conception α was a scaling for the $r - \phi$ component of the stress tensor. In the earliest models of disc warping α was used, more out of necessity than by rigorous argument, to parametrise the size of some assumed microscopic viscosity within the disc. Later this interpretation was revised to reflect a generic viscous-like behaviour, likely due to small-scale turbulence (most often attributed to the MRI). Hydrodynamic models, requiring some proxy for this turbulence, substituted it with an artificial tunable viscosity. The introduction of global simulations capable of directly modelling the MRI renders an artificial viscosity unnecessary and might call into question the validity of using an artificial isotropic viscosity to represent the anisotropic effects of MRI turbulence. In particular Sorathia, Krolik, & Hawley (2013a, 2013b) contended that the MHD turbulence induced by the magnetic field did not behave in a manner similar to that of an α viscosity but rather disrupted the coherence of bending waves without damping them. Further, they call into question the interpretation of a 'bending wave' or 'diffusive' regime, citing the great importance of shocks and non-linearities to the warp evolution process, leading to what they describe as a characteristic 'slip-stick' behaviour.

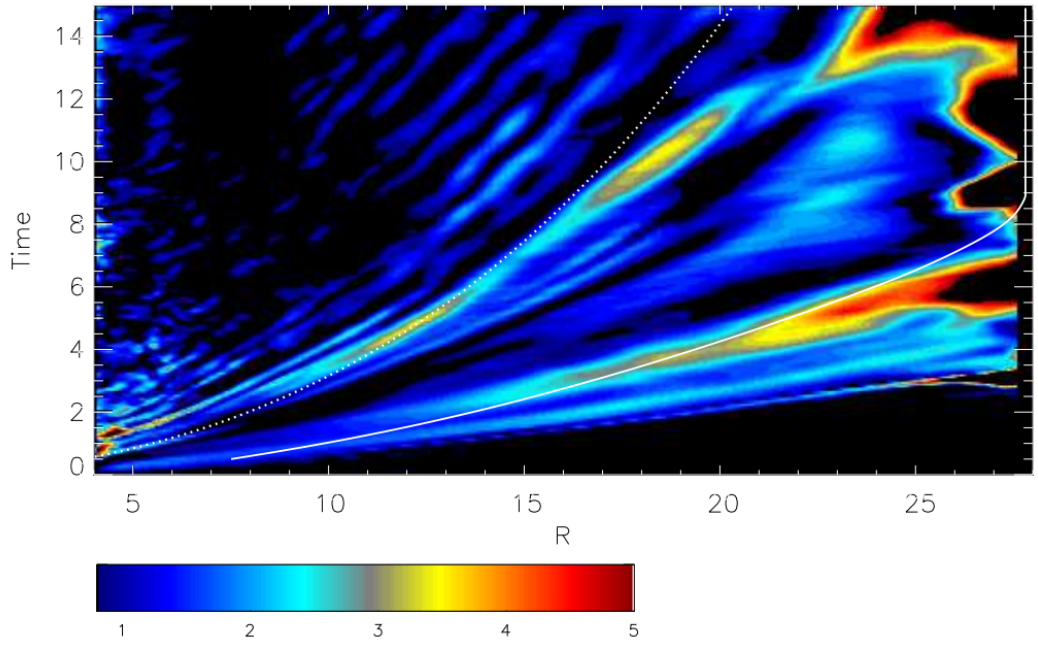

(a) Hydrodynamic

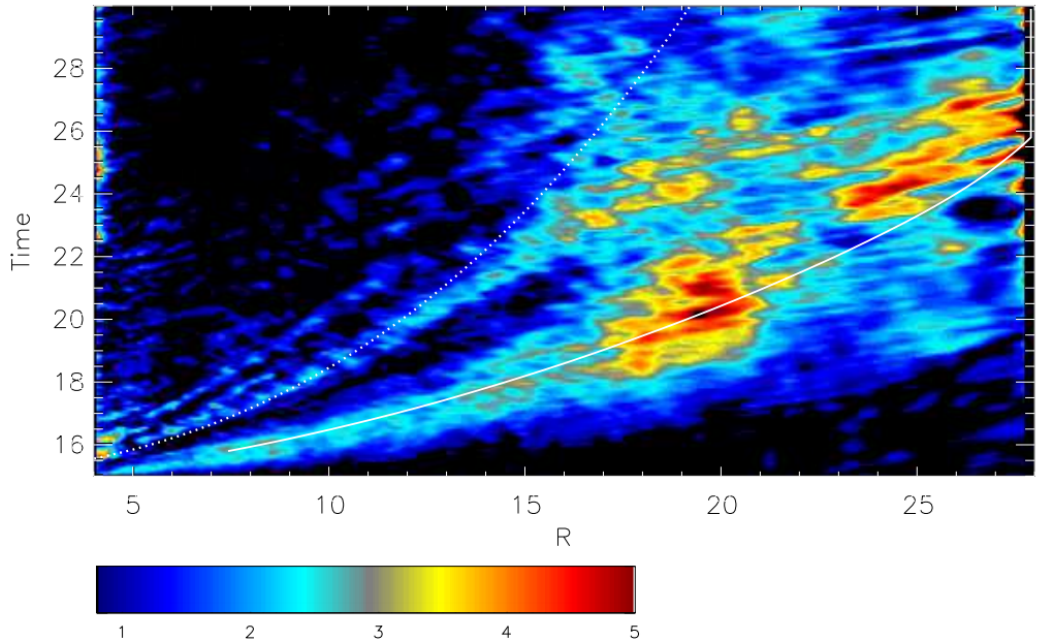

(b) Magnetohydrodynamic

Fig. 1.16: Colour contours of warp amplitude $\widehat{\psi} = \psi R/H$ in hydrodynamic and MHD discs. The warp is initially generated by Lense-Thirring torques and propagated outward. The solid line describes the bending wave front as predicted by hydrodynamic theory. Figure taken from Sorathia, Krolik, & Hawley (2013).

Several challenges have been levelled at many of these conclusions. Nixon (2015) argued that observational evidence from Her X-1 tightly constrains the anisotropy of α, contradicting the assertion that MHD turbulence is highly anisotropic. Nealon et al. (2016) took this idea further, directly comparing the MHD output of Krolik & Hawley (2015) to an analogous hydrodynamic alpha model in SPH. Relatively little difference was observed between the two cases, seemingly suggesting that an isotropic alpha prescription provides a suitable approximation for MHD turbulence. These results are consistent with earlier numerical (Torkelsson et al., 2000) and theoretical (Ogilvie, 2003) investigations into the anisotropy of α in MRI-turbulent discs. Without delving much deeper into this particular issue, we briefly note that the isotropy of α has been widely discussed in many contexts beyond the scope of this discussion while debate on the nature of hydrodynamic warping and the role of α continues (Hawley & Krolik, 2018).

In warped disc simulations the magnetic field has largely been cast in the role of a (arguably anistropic) turbulence source, a mere background upon which hydrodynamic warp evolution acts. Rarely are the tenets of hydrodynamic warp theory, predicated upon the subtle and intimate internal dynamics of the disc itself, questioned in the presence of a mean magnetic field. Certainly in the studies described above, where $\beta \approx 1000$, this may be permissible. Yet these only constitute the vanguard of a new generation of warped MHD simulations, and inevitably theorists will be called upon to interpret simulations of thinner warped discs threaded by dynamically important magnetic fields. Such considerations indicate the necessity for a magnetohydrodynamic extension to the mathematical formulation of warped disc dynamics set out in section 1.4 and have motivated the work of this thesis.

1.7 Local Models of Warped Discs

The preceding discussion of warped disc hydrodynamics in sections 1.3 and 1.4 indicate that the propagation of a warp is, by its nature, a local phenomenon

(in radius) and can often be understood via reduced 1D descriptions. Conversely, the previous section has emphasised many of the difficulties inherent in studying warp propagation in magnetised thin discs via global simulations. Consequently, while most have sought to understand and interpret warp dynamics via intensive global simulations, perhaps a simpler and fuller understanding may be gained via a local perspective.

The hydrodynamics of warped discs from a local perspective has been explored numerically using the classic shearing box by Torkelsson et al. (2000) and Gammie, Goodman & Ogilvie (2000). The warp in these cases was effectively represented by an artificial vertically stratified epicyclic oscillation, similar in form to what would be induced by a warp. Attempts were later made to develop local models that more directly represented the presence of a warp.

Two local models of warped discs are of particular interest and, though similar, each approaches warp evolution with a slightly different set of assumptions. While both are described in greater mathematical detail in their relevant chapters, I hope here to present a rationale for their usage and explain the contexts in which they have already been used.

1.7.1 The Warped Shearing Box

It was noted in section 1.4.2 that, provided that the disc was sufficiently non-Keplerian or viscous, one could neglect the $\frac{\partial \boldsymbol{G}}{\partial t}$ term in equation (1.18). Devoid of any explicit time dependence, one could then solve for the internal torque $\boldsymbol{G}$ instantaneously given only a particular warp profile $r\frac{\partial \boldsymbol{\ell}}{\partial r}$ via equation (1.25). Physically we are following a separation of scales argument; we may consider the warp to be effectively static on the orbital time-scale, allowing us to solve for the internal torque. The internal torque may then be used (via equation (1.17)) to solve for the warp evolution on a longer time-scale.

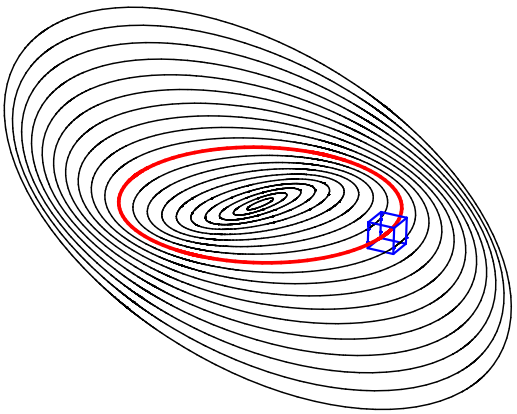

Fig. 1.17: An untwisted self-similar warped disc, viewed as a series of tilted rings. A co-rotating local Cartesian model may be constructed at some reference orbit as represented by the blue box. This Cartesian frame forms the basis of the warped shearing box. Figure taken from Ogilvie & Latter (2013a).

This insight suggests it may be possible to develop a local model in which a static warp is effectively imposed, driving internal flows and generating an internal torque. The warped shearing box (WSB) model developed by Ogilvie & Latter (2013a) does precisely this, integrating a background warping motion into the classic shearing box of Goldreich & Lynden-Bell (1965). This integration is achieved in an analogous manner to how the shear itself is incorporated into the shearing box model. Consider a standard Cartesian reference frame centered on a fluid element at the disc mid-plane. Owing to the differential rotation of the fluid, the azimuthal coordinate (or y-coordinate) between two nearby radially displaced fluid elements will naturally drift apart due to the shear. The background shearing is incorporated into the coordinate system by imposing a coordinate transformation that follows the shear flow,

$$y' = y + q\Omega t x. \tag{1.37}$$

Similarly in a warped disc the differential warping in the local frame implies that nearby radially displaced fluid elements will experience a natural relative vertical velocity, oscillating at the orbital frequency. Like the background shear flow, this motion may be incorporated into the coordinate system via a coordinate transformation

$$z' = z + |\psi| \cos(\Omega t) x \tag{1.38}$$

where $|\psi| = r \left|\frac{\partial \boldsymbol{\ell}}{\partial r}\right|$ is the measure of the differential change in orbital inclination with radius, or 'warp amplitude'. The radial dependence of ψ is in theory arbitrary, though in practice it is often easiest to allow ψ to be independent of radius. This can be justified by either assuming the warped shearing box is sufficiently small to ignore the radial variation in ψ or by assuming the disc to be (at least within some region of applicability) self-similar. The warped shearing box is horizontally homogenous and admits periodic boundary conditions, and is therefore suitable for use in 3-D or 2-D simulations. Alternatively one may seek solutions that are independent of azimuth or radius (x' or y'), reducing the internal dynamics to a 1-D problem. This is appropriate if the warp varies on a radial length-scale far greater than the height of the disc and

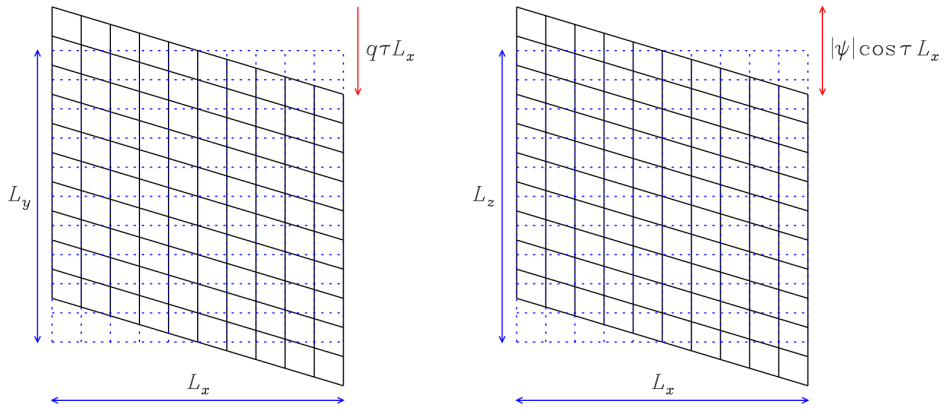

Fig. 1.18: A representation of the warped shearing coordinate system. The dotted blue line represents the local Cartestian coordinates used in the usual shearing box, while the black grid represents the warped shearing coordinate system. Figure taken from Ogilvie & Latter (2013a).

on time-scales far longer than the orbital time-scale – conditions that are generally quite easily satisfied. Ogilvie & Latter (2013a) showed that this local perspective was absolutely compatible with the non-linear theory of Ogilvie (1999), offering a new and relatively simple framework with which one could investigate warped disc dynamics. In chapter 3 we use the warped shearing box to investigate the evolution of magnetised warped discs.

As discussed previously, it's important to note that the separation of scales that allows for $\frac{\partial \boldsymbol{G}}{\partial t}$ to be neglected (and is implicitly built into the warped shearing box formalism) may not always be valid. Notably, resonances in inviscid discs may produce arbitrarily large internal flows and torques. This should be clearly understood as merely representing a transition in the character of the warp evolution that cannot be captured by the warped shearing box, as discussed in section 1.4.

1.7.2 The Corrugated Disc Model

The corrugated disc model models offers an alternative and complementary perspective on the internal dynamics of warped discs. Consider a radially in-

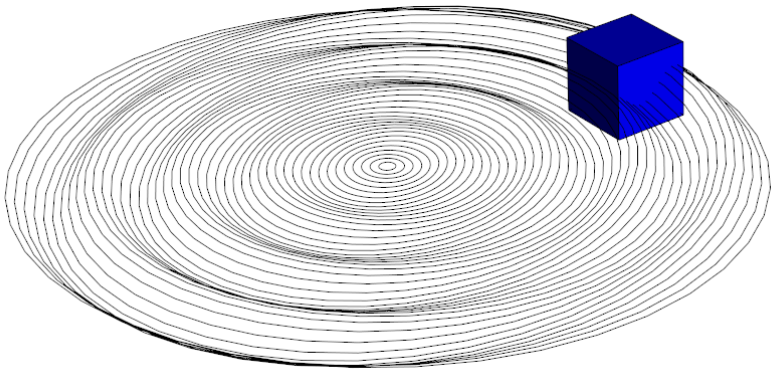

Fig. 1.19: An untwisted warped disc, viewed as a collection of tilted rings subjected to a sinusoidal corrugation. A co-rotating local Cartesian model may be constructed at some reference orbit as represented by the blue box.

finite vertically stratified disc in which the tilt vector $\boldsymbol{\ell}(r,t)$ varies sinusoidally with radius, corresponding to a 'corrugation' of the disc surface. Alternatively this could be formulated as a radially oscillating Lagrangian vertical displacement to an initially flat disc, or (at least for small warps) a Fourier decomposition of a more arbitrary warp profile. A local Cartesian model co-rotating with the fluid, assumed to be small compared to the radial length-scale of the disc but large enough to capture some features of the corrugation, may be constructed. This forms the basis of the corrugated disc model (see Chapter 4).

The differences between the two models are to be emphasised. While both are local perspectives, the warp of the WSB is defined by a single parameter, the warp amplitude ψ. In contrast the corrugated disc is defined by both the wave-number of the corrugation and the amplitude of the corrugation. In the WSB, the warp amplitude is effectively static unless the long-term evolution of the warp is added manually; in contrast the corrugated disc allows for the time evolution of the corrugation, thereby capturing both the resonant and non-resonant regimes.

While hydrodynamic warp propagation has been studied in both of these

models, the MHD case remains as of yet completely unexplored. Further, the relation between these two models remains somewhat unclear. The work of this thesis aims to resolve both of these outstanding issues.

1.8 Structure of the Thesis

The outline for this thesis is as follows. In chapter 2 we discuss the role of the global magnetic field structure on the warp evolution. Utilizing the warped spherical coordinate system defined in Ogilvie (1999), we generate a series of self-similar models for the magnetic field exterior to the disc. The physical feasibility of these models, their relevance to the local disc models discussed in later chapters and their implications for jet formation are discussed.

In chapter 3 we employ the warped shearing box model developed by Ogilvie & Latter (2013a) and discussed in section 1.7 to express the fully non-linear local ideal MHD equations. We consider the one-dimensional laminar solutions to these equations, and by expanding linearly in warp amplitude about an equilibrium solution, a system of first-order differential equations is found for the internal structure of the disc. A semi-analytical solution is found for the special case of a warped disc threaded by a magnetic field perpendicular to the disc midplane.

In chapter 4 we define an alternative 'corrugated disc' model of warp dynamics. Using this model, we find the free wave modes of magnetised warped discs and the corresponding dispersion curves. The connection between the warped shearing box model of chapter 3 and the corrugated disc model are discussed in greater detail. Finally, applications to MRI stability are considered.

Chapter 5 contains an in-depth semi-analytical treatment of the long-wavelength disc modes in the vertical field case, paying particular attention to the physical interpretation of these wave modes and the resonance between

the warp and the horizontal Alfvénic-epicyclic modes. This analysis is used to interpret the numerical results of the corrugated disc model for bending field configurations.

In chapter 6 we attempt to demonstrate, both in theory and in practice, how an understanding of these wave modes can be used to inform our understanding of warped disc dynamics in simulations. We compare our theoretical analysis to the output of a series of Athena++ simulations, demonstrating the practical validity of the ideas outlined in this thesis.

In chapter 7 the results of the work outlined in this thesis, its shortcomings and implications for future work are briefly discussed.

2. A SELF-SIMILAR EXTERNAL MAGNETIC FIELD MODEL

2.1 Preamble - The Role of the External Magnetic Field in Local Models

The study of magnetised accretion discs necessarily encompasses a vast array of distinct physical scenarios and limits; indeed, there are certainly more discs in the heavens than are dreamt of in our philosophy. We therefore must begin by restricting the scope of our investigation to a reasonable subset of magnetised accretion disc models. One of the most important of these restrictions, and the subject of this chapter, is a condition on the form and structure of the magnetic field.

The magnetic field can be responsible for the non-local transport of angular momentum between footpoints of a magnetic field line and hence appears, at first glance, to be antithetical to the notion of a local model for warp propagation within a magnetic field. Certainly there are scenarios in which this is true. For example, if the magnetic field threading an annulus of the disc were connected to a central object, such as a black hole or the surface of a star, the differential rotation between the central object and the disc at various radii would lead to a shearing of the magnetic field lines on the orbital timescale, the exchange of angular momentum between the disc and the central object and the formation of a relatively chaotic magnetic field structure. Such a model is not particularly amenable to theoretical analysis.

Let us briefly and very roughly consider how this appears from a local

perspective. Let us follow a fluid element of the disc as it traces an orbit. The flow of angular momentum through its boundaries is a well-defined local quantity, yet the fluid element is non-locally exchanging angular momentum with the central object through the magnetic field. From the perspective of the fluid element this exchange of angular momentum appears as a time-varying boundary condition on the magnetic field. This time-variation is related to the global structure of the magnetic field and hence cannot be determined by purely local considerations. This stands in sharp contrast to hydrodynamic warp propagation, where all fluxes of angular momentum are locally determined and measurable.

Warp propagation in magnetised discs is thus immediately distinct from its hydrodynamic analogy precisely because of this non-local character introduced by the magnetic field. In principle - and according to the current convention - the only way in which one may analyse warp propagation in magnetised discs is through an entirely global perspective. Computationally this introduces a number of restrictions on the discs that may be investigated, as well as serious issues related to resolution. From a theoretical perspective attempts have been made to reduce the disc to an effectively 2D sheet. However while these works manage to make the problem somewhat tractable, they inevitably suffer by lacking the internal flows that have been shown to be critical in warp propagation in certain situations.

Yet perhaps we need not give up entirely on a local perspective. The considerations of the previous paragraph suggest a conceptual division. A local model may be used to understand the internal structure of the disc, including the fluxes of angular momentum that are critical to understanding the nature of warp propagation, subject to particular magnetic boundary conditions. Simultaneously a global model for the magnetic field may be found external to the disc, subject to boundary conditions imposed on the disc surface that are informed by the local analysis. Rather than a single global problem we may solve these two related problems in a self-consistent manner. This approach

allows us to capture the internal local dynamics with an unprecedented level of detail.

The majority of this thesis is focused primarily on the local aspect of this problem. This chapter stands in contrast as a brief and tentative investigation into the global magnetic field structure beyond the disc itself. The models we develop not only illustrate some of the possible relatively simple magnetic field configurations valid far from the midplane of a warped disc, but will also help inform our choice of boundary conditions when we come to investigate local models in the subsequent chapters.

2.2 A Self-Similar Magnetic Field Model

In this section we elaborate on the type of external magnetic field models we wish to investigate as well as provide a broad overview of our approach. In this context, 'external' refers to the region of space several scale heights above the disc midplane (typically roughly five or six scale-heights in numerical calculations) such that the plasma beta is very low and the magnetic field is effectively force-free. Magnetised accretion discs may be subject to outflows in the form of winds and jets (Blandford & Payne, 1982), in which case this notion of 'external' becomes rather muddy; we thus restrict ourselves to discs that are stable to jet outflows. What this means in practice will be discussed later in the chapter.

We restrict ourselves further, for the sake of simplicity, to current free or potential fields, mathematically defined by

$$\nabla \times \mathbf{B} = \mathbf{0} \tag{2.1}$$

which implies the magnetic field may be expressed as the gradient of a magnetic potential

$$\mathbf{B} \equiv \nabla\Phi. \tag{2.2}$$

The vanishing divergence of the magnetic field thus implies

$$\nabla^2\Phi = 0. \tag{2.3}$$

We see that the magnetic potential exterior to the disc may be found by solving Laplace's equation separately in the region above and below the disc.

In order to solve Laplace's equation, we must specify two things. Firstly we must specify the shape of the disc, which of course will be dependent on the warp profile of the disc. Secondly we must define the normal component of the magnetic field everywhere on the disc surface (a Neumann boundary condition), which is equivalent to specifying a magnetic flux distribution everywhere on the disc surface. In practice this process is greatly simplified through the use of a warped coordinate system, the details of which are discussed in section 2.3 and 2.4.

What warp profile and magnetic flux distribution should be used? In principle this could be arbitrary. We seek solutions that are somewhat realistic, relatively simple to investigate and consistent with a local approach to warp propagation. We choose to restrict our attention to self-similar discs; these are not only particularly simple to work with, but also often function well as intermediate asymptotic solutions far from the disc boundaries in extended systems. Our choice of flux distribution is discussed in more detail in sections 2.5 and 2.6.

By this stage the problem is clearly defined; to make further progress, in sections 2.7 and 2.8 we perform a perturbation analysis of an initially unwarped disc that should be suitable for small warps. In section 2.9 we present a brief analysis of the prospective relationship between warps and outflows.

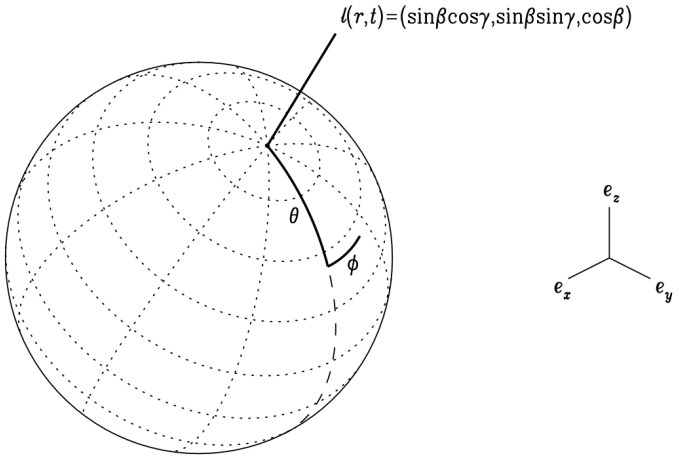

Fig. 2.1: Warped spherical coordinates defined for a sphere of radius r. Angular coordinates are defined with respect to a tilt vector $\boldsymbol{\ell}(r,t)$. (Figure taken with permission from Ogilvie (1999)).

2.3 Global Warped Coordinates

In order to define the warped disc surface it will be convenient to use the set of warped coordinated defined by Ogilvie (1999). Although this set of coordinates is not original research, it will be instructive for the remainder of this chapter to begin with a brief review. The warped coordinate system can be seen in Figure 2.1 and is in some sense a spherical analogue to the 'tilted rings' warped cylindrical coordinate system of Petterson (1977) (see Figure 1.3). Consider a traditional spherical coordinate system. On each sphere of constant radius r, let (θ,ϕ) be defined as usual but with respect to an axis that, rather than being oriented in the direction $\mathbf{e}_z$, is oriented in the direction of the so-called tilt vector $\boldsymbol{\ell}(r,t)$. In terms of Euler angles $\beta(r,t)$ and $\gamma(r,t)$ the tilt vector may be written as

$$\boldsymbol{\ell}(r,t) = \sin\beta\cos\gamma\ \mathbf{e}_x + \sin\beta\sin\gamma\ \mathbf{e}_y + \cos\beta\ \mathbf{e}_z \tag{2.4}$$

The transformation from Cartesian coordinates to this set of adapted

spherical coordinates is given by

$$\begin{pmatrix} x \\ y \\ z \end{pmatrix} = \mathbf{M}(r,\theta,\phi,t) \begin{pmatrix} r \\ 0 \\ 0 \end{pmatrix} \tag{2.5}$$

where

$$\mathbf{M}(r,\theta,\phi,t) = \begin{bmatrix} \cos\gamma & -\sin\gamma & 0 \\ \sin\gamma & \cos\gamma & 0 \\ 0 & 0 & 1 \end{bmatrix} \begin{bmatrix} \cos\beta & 0 & \sin\beta \\ 0 & 1 & 0 \\ -\sin\beta & 0 & \cos\beta \end{bmatrix} \begin{bmatrix} \cos\phi & -\sin\phi & 0 \\ \sin\phi & \cos\phi & 0 \\ 0 & 0 & 1 \end{bmatrix} \begin{bmatrix} \sin\theta & \cos\theta & 0 \\ 0 & 0 & 1 \\ \cos\theta & -\sin\theta & 0 \end{bmatrix} \tag{2.6}$$

This coordinate system could be motivated in the following way. From one perspective, a thin (non-eccentric) accretion disc may be viewed as a series of distinct circular rings at different radii. In a flat disc, every such ring is oriented such that the plane of each ring is perpendicular to a particular unit vector $\boldsymbol{\ell}$ which defines the orientation of the ring in 3D space. In a warped disc, these rings need not all lie in the same plane but rather may be tilted with respect to neighbouring rings. Consequently the vector $\boldsymbol{\ell}$ defining the orientation of these rings becomes a function of radius (and time, if the shape is evolving), $\boldsymbol{\ell} = \boldsymbol{\ell}(r,t)$.

This perspective of disc warping naturally leads to a set of warped spherical coordinates such that the polar axis is allowed to vary with radius following the tilt vector $\boldsymbol{\ell}$. In these warped coordintes the disc is by definition defined to be on (or more precisely very near) the surface $\theta = \pi/2$. Ogilvie (1999) also defines an orthonormal basis $\{\mathbf{e_r},\mathbf{e}_\theta,\mathbf{e}_\phi\}$, identical to its spherical analogue at fixed radius, but varying in orientation with the coordinate system. Details of the vector algebra of this coordinate system can be found in that paper and will largely be omitted from this chapter.

The Euler angle β is a measure of the magnitude of the tilt vector angular

displacement from an initial reference axis. Radial variation of β hence corresponds to an untwisted warping of the disc. Variation of γ with radius does not change the magnitude of the angular displacement but rather changes the orientation of the tilt vector corresponding to a 'twisting' of the disc warp. For the sake of simplicity, we only consider non-twisted warps for the remainder of this section and hence set $\gamma = 0$.

To define an untwisted warp we require a warp profile, which may be a function of the form $\beta(r)$, to specify the profile of the disc. From the perspective of local dynamics the absolute value of $\beta(r)$ is not of greatest relevance; rather it is the differential of the tilt vector between adjacent disc rings, $\frac{\partial \boldsymbol{\ell}}{\partial r}$, that governs the local disc dynamics. To that end we define the warp amplitude

$$\psi(r,t) = r\left|\frac{\partial \boldsymbol{\ell}(r,t)}{\partial r}\right| \tag{2.7}$$

as a scale-free measure of the degree of warping at any given point in the disc. A function $\psi(r)$ must be prescribed in order to define the initial shape of the warped disc. Due to our assumption of self-similarity, the entirety of the warp may be easily described by a single radially invariant variable ψ. Sketches of self-similar discs at various values of ψ are shown in Figure 2.2.

Recall that in the previous section we found that we needed to solve Laplace's equation for the magnetic potential Φ defined in the region external to the disc. In order to satisfactorily define the problem, the normal component of the magnetic field must be satisfied on the warped disc surface. As the warped coordinate system defined in this section has the pleasant property that the disc midplane lies on the surface $\theta = \pi/2$, the warping of the disc surface has in some sense been transferred into a warping of the coordinate system itself, resulting in an extremely simple expression for the disc surface. This will allow us to apply the appropriate boundary conditions on Φ far more easily. However, such trickery brings its own complications. While the boundary condition has been simplified considerably, by using an adapted

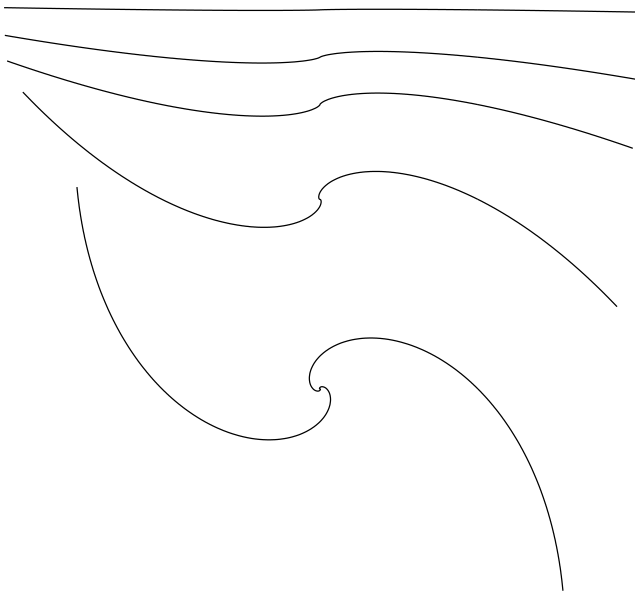

Fig. 2.2: A side-on view of untwisted self-similar warps with (radially invariant) warp amplitudes $\psi = 0.01$(top), 0.1, 0.2, 0.5, and 1(bottom). Figure taken with permission from Ogilvie & Latter (2013a).

coordinate system we have changed the form of the Laplacian operator ∇^2. Finding the form of the Laplacian in these warped coordinates is the subject of the next section.

2.4 Finding the Laplacian in the Warped Coordinates

While Ogilvie (1999) provides a very thorough exposition of the mathematical properties of the warped coordinate system, it does not provide a simple closed form expression for the Laplacian operator in those coordinates. In this section we address this deficiency using a more differential geometric approach.

The Jacobian of the warped coordinate system is given in Ogilvie (1999) as

$$\mathbf{J} = \mathbf{M} \begin{bmatrix} 1 & 0 & 0 \\ r\beta' \cos\phi + r\gamma' \sin\phi & r & 0 \\ -r\beta' \cos\theta \sin\phi + r\gamma'(\cos\beta \sin\theta + \sin\beta \cos\theta \cos\phi) & 0 & r\sin\theta \end{bmatrix}. \tag{2.8}$$

where a prime denotes a radial derivative. By considering the matrix $\mathbf{J}^T\mathbf{J}$ and noting that $\mathbf{M}$ is an orthogonal matrix (not surprising given that it is simply a series of successive rotations), one may derive that the metric of the coordinate system is given by

$$g_{ij} = \mathbf{J}^T\mathbf{J} \tag{2.9}$$

with components

$$g_{rr} = 1 + (r\beta' \cos\phi + r\gamma' \sin\phi)^2 + (-r\beta' \cos\theta \sin\phi + r\gamma'(\cos\beta \sin\theta + \sin\beta \cos\theta \cos\phi))^2 \tag{2.10}$$

$$g_{r\theta} = r^2\beta' \cos\phi + r^2\gamma' \sin\phi \tag{2.11}$$

$$g_{r\phi} = r\sin\theta(-r\beta' \cos\theta \sin\phi + r\gamma'(\cos\beta \sin\theta + \sin\beta \cos\theta \cos\phi)) \tag{2.12}$$

$$g_{\theta\theta} = r^2 \tag{2.13}$$

$$g_{\theta\phi} = 0 \tag{2.14}$$

$$g_{\phi\phi} = r^2 \sin^2\theta \tag{2.15}$$

I include this full form for the sake of completeness. However, in the context of the current problem we are only interested in the untwisted disc case with a warp of constant amplitude as discussed in the previous section. Recalling the definition of warp amplitude ψ and setting γ' to zero the above set of equations becomes

$$g_{ij} = \begin{pmatrix} 1+\psi(\cos^2\theta+\cos^2\phi-\frac{1}{2}\cos^2\theta\cos^2\phi) & \psi r\cos\phi & -\psi r\cos\theta\sin\theta\sin\phi \\ \psi r\cos\phi & r^2 & 0 \\ -\psi r\cos\theta\sin\theta\sin\phi & 0 & r^2\sin^2\theta \end{pmatrix} \tag{2.16}$$

which has determinant $g = \det(g_{ij}) = r^4\sin^2\theta$, identical to that of standard spherical polar coordinates. The inverse of the metric is

$$g^{ij} = \begin{pmatrix} 1 & -\frac{\psi}{r}\cos\phi & \frac{\psi}{r}\cot\theta\sin\phi \\ -\frac{\psi}{r}\cos\phi & \frac{1}{r^2}+(\frac{\psi}{r})^2\cos^2\phi & -(\frac{\psi}{r})^2\sin\phi\cot\theta\cos\phi \\ \frac{\psi}{r}\cot\theta\sin\phi & -(\frac{\psi}{r})^2\sin\phi\cot\theta\cos\phi & \frac{1}{r^2\sin^2\theta}+(\frac{\psi}{r})^2\cot^2\theta\sin^2\phi \end{pmatrix}. \tag{2.17}$$

Using the standard relation

$$\nabla^2\Phi = \frac{1}{\sqrt{g}}\frac{\partial}{\partial u^j}\left(\sqrt{g}g^{jk}\frac{\partial\Phi}{\partial u^k}\right) \tag{2.18}$$

where u^i defines a general coordinate basis, we can therefore find an expression for the Laplacian in this coordinate system. Note that as the Laplacian is a scalar quantity, it is independent of the vector basis used.

The Laplacian may be expressed in orders of ψ. To zeroth order in ψ, we recover the traditional Laplacian for spherical coordinates, which will be denoted as ∇_0^2. To first order in ψ, there is a contribution to the Laplacian ∇_1^2 given by:

$$\nabla_1^2\Phi = -\frac{\psi}{r^2\sin\theta}\frac{\partial}{\partial r}\left(r\sin\theta\cos\phi\,\frac{\partial\Phi}{\partial\theta}\right)+\frac{\psi}{r^2\sin\theta}\frac{\partial}{\partial r}\left(r\cos\theta\sin\phi\,\frac{\partial\Phi}{\partial\phi}\right)$$

$$-\frac{\psi}{r^2\sin\theta}\frac{\partial}{\partial\theta}\left(r\sin\theta\cos\phi\,\frac{\partial\Phi}{\partial r}\right)+\frac{\psi}{r^2\sin\theta}\frac{\partial}{\partial\phi}\left(r\cos\theta\sin\phi\,\frac{\partial\Phi}{\partial r}\right) \tag{2.19}$$

and to second order we have

$$\nabla_2^2\Phi = \frac{\psi^2}{r^2\sin\theta}\frac{\partial}{\partial\theta}\left(\sin\theta\cos^2\phi\frac{\partial\Phi}{\partial\theta}\right) - \frac{\psi^2}{r^2\sin\theta}\frac{\partial}{\partial\theta}\left(\sin\phi\cos\phi\cos\theta\frac{\partial\Phi}{\partial\phi}\right)$$

$$-\frac{\psi^2}{r^2\sin\theta}\frac{\partial}{\partial\phi}\left(\sin\phi\cos\phi\cos\theta\frac{\partial\Phi}{\partial\theta}\right) + \frac{\psi^2}{r^2\sin\theta}\frac{\partial}{\partial\phi}\left(\cot\theta\cos\theta\sin^2\phi\,\frac{\partial\Phi}{\partial\phi}\right) \tag{2.20}$$

In summary, we have derived an expression for the disc surface and the Laplacian operator using a warped coordinate system. All that remains is to specify an appropriate boundary condition on the magnetic field along the disc surface.

2.5 Implications from the Induction Equation

Before we specify a flux function, it will be illustrative to consider what components of the magnetic field are relevant for the solution of Laplace's equation and how each component of the magnetic field is advected along an orbit. As per the discussion at the start of this chapter, the external field problem must be solved in a manner consistent with the advection of flux within the disc.

The magnetic field component B_θ (with the θ component defined according to Ogilvie (1999)) is perpendicular to the orbital plane at $\theta \approx \pi/2$. However, this is **not** the component of the magnetic field perpendicular to the disc surface. Rather unintuitively, the orbital plane at a given radius is not equivalent to the disc surface in a warped disc. This is perhaps most easily understood visually in Figure 2.3, illustrating a 2-D cut through a small section of a warped accretion disc. The central object is indicated by a small circle centered about the point **O**, while **P** and **Q** indicate two nearby points

in a small radial section of a warped disc, drawn in red (in general the disc would have some curved radial profile between point **P** and **Q**; we assume we are looking at a small enough section of the disc such that the disc profile is approximately linear. This can always be done as long as the disc is assumed to have a smooth profile.) The orbital plane at **P** (defined by normal unit vector $\mathbf{z}_P$) is not coincident with the orbital plane at point **Q** (defined by normal unit vector $\mathbf{z}_Q$), and both are distinct from the disc surface (defined by normal vector $\mathbf{e}_\perp$). 2-D cuts of the 'tilted spheres' defining the coordinate system of Ogilvie (1999) are shown in dotted-dashed lines through points **P** and **Q**, with polar vectors parallel $\mathbf{z}_P$ and $\mathbf{z}_Q$ at radii $r = |OP|$ and $r = |OQ|$ respectively. One can clearly see that $\mathbf{e}_\theta \neq \mathbf{e}_\perp$ at point **P** unless the disc is aligned with the orbital plane.

By considering two adjacent rings of the disc with different orientations signified by tilt vectors $\boldsymbol{\ell}(r)$ and $\boldsymbol{\ell}(r + dr)$, we may derive that the normal component of the magnetic field to the disc surface is

$$B_\perp = \frac{-B_\theta + \psi \cos\phi \; B_r}{\sqrt{1 + \psi^2 \cos^2\phi}}. \tag{2.21}$$

The element of magnetic flux threading the disc is equal to the product of the normal magnetic field $B_\perp$ and the area of the disc surface element. The warping of the disc increases the effective area of the disc, leading to a geometric factor of $\sqrt{1 + \psi^2 \cos^2\phi}$. Hence the flux element of a disc annulus is given by:

$$\mathbf{B} \cdot d\mathbf{S} = (-B_\theta + \psi \cos\phi \; B_r) r dr d\phi \tag{2.22}$$

It should be noted that the deviation of the geometric normalisation factor from unity is of order ψ^2, and for small warps can be effectively neglected.

Thus far in this analysis we have not made any reference to the fact that we are dealing not with a stationary deformed sheet, but rather a thin disc of fluid. From the perspective of the external field problem, the greatest

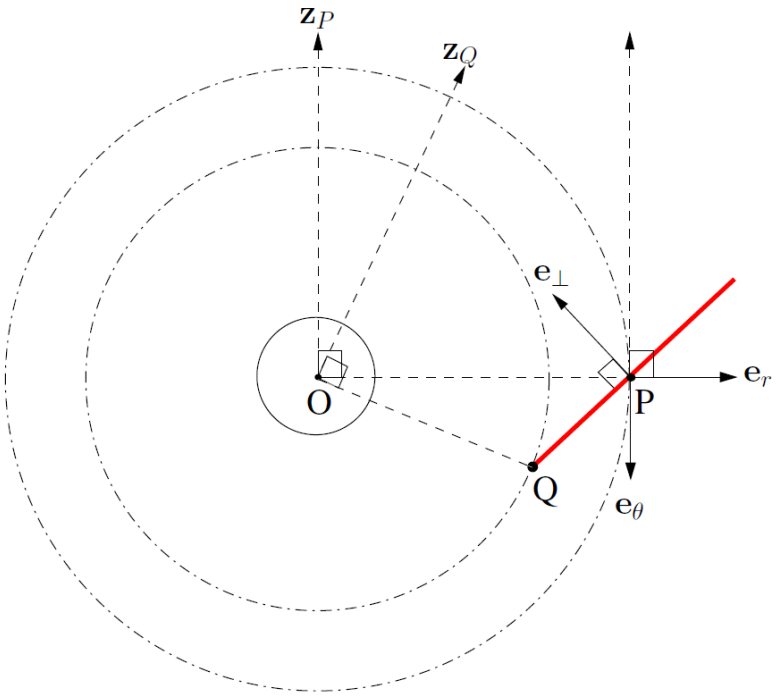

Fig. 2.3: A 2-D illustration of the warped coordinate system along with relative vector orientations at the disc surface. A thin cross-section of the disc is shown in red centered about the point P, while the central object is illustrated at the point O. At radius $r = |OP|$ the coordinate system corresponds to traditional spherical polars with the z-axis aligned normal to the orbital plane as indicated by $\mathbf{z}_P$. Note that the normal vector to the disc surface $\mathbf{e}_\perp$ is not parallel to $\mathbf{e}_\theta$ in a warped disc. At $r = |OQ|$, the warped coordinate system again corresponds to traditional spherical polars, but with z-axis oriented parallel to $\mathbf{z}_Q$.

significance of the fluid motion is the advection and distortion of the magnetic field footpoints. Let us assume that the primary motion of the disc is an axisymmetric azimuthal velocity or

$$\mathbf{u} \approx u_\phi(r)\mathbf{e}_\phi = r\sin\theta\Omega(r)\mathbf{e}_\phi \tag{2.23}$$

corresponding to the orbital motion of the disc (this condition will be relaxed and discussed in greater detail in the following chapter). A word of caution – here 'axisymmetric' is, at a given radius, defined relative to the axis of the

tilted sphere at that radius. While in an unwarped disc the effect of this motion on the Lagrangian derivative of the magnetic field is fairly obvious, the problem is made considerably more complex by the warped geometry. Using the geometrical results from Ogilvie (1999), one can show that the ideal induction equation takes the form

$$\frac{DB_r}{Dt} = 0 \tag{2.24}$$

$$\frac{DB_\theta}{Dt} = -\psi\Omega \sin\phi B_r \tag{2.25}$$

$$\frac{DB_\phi}{Dt} = B_r r \frac{\partial\Omega}{\partial r} \tag{2.26}$$

The first equation tells us that the radial component of the field is advected with the fluid. We will see in the following section that this is modified somewhat by radial or vertical internal flows. The final relation will likely not be of much use, but is still of physical interest – we see that an azimuthal field can be generated by non-solid body rotation of the disc. The condition on B_θ is not too illuminating on its own but may be recast as

$$\frac{D}{Dt}(-B_\theta + \psi\cos\phi\ B_r) = 0. \tag{2.27}$$

This relationship is of great importance to this thesis and turns out to hold true even when poloidal velocity fluctuations are considered under certain assumptions (see chapter 3). This conserved quantity, $-B_\theta + \psi\cos(\phi)B_r$, has a special physical significance – it is proportional to the magnetic field component normal to the disc surface (see equation 2.22). Therefore this relation has a straightforward physical interpretation; the magnetic flux normal to the disc is advected by the motion or, in the local frame of the fluid element (see chapter 3), remains a constant. This is a form of flux conservation, not unexpected in the context of ideal MHD but obfuscated somewhat by the warped geometry. This means that, as long as the disc flow remains toroidal, an initially axisymmetric boundary condition on the magnetic flux will remain axisymmetric.

We are therefore free to prescribe an axisymmetric distribution of magnetic flux on the disc surface, safe in the knowledge that the orbital motion will not distort the magnetic field lines. This preserved axisymmetry is of critical importance as we attempt to solve for the exterior field; it effectively allows us to treat the problem as static. For although the fluid disc may be in constant motion, the only relevant component when solving Laplace's equation for the external field is the magnetic flux at the disc surface. Hence as long as the flux is axisymmetric and advected with the fluid, our hearts may rest easy as we solve for the magnetic potential in a time-independent manner.

2.6 The Flux Distribution

Thus far we have specified a warp profile for the disc and deduced that we may select an axisymmetric function for the magnetic flux distribution. In principle we have a great deal of freedom, even under these constraints. Using our assumption of self-similarity, the functional form of the magnetic potential can be written as

$$\Phi \propto r^{-\alpha}. \tag{2.28}$$

A value of self-similarity parameter $\alpha = 2$ (and consequently $\mathbf{B} \propto r^{-3}$) corresponds to a dipole field where every magnetic field line through the disc has, in theory, a footpoint at the origin and the electric current is effectively constrained to the origin. Conversely a value of $\alpha = -1$ corresponds to a uniform magnetic field generated by a current loop at a radius far larger than the disc. In a physically reasonable scenario the electric current would be distributed throughout the disc; consequently a reasonable self-similarity parameter would fall within the range $-1 < \alpha < 2$. A standard choice in the literature (e.g. Blandford & Payne (1982)) that will provide us with a helpful reference is $\alpha = 1/4$, or $\mathbf{B} \propto r^{-5/4}$.

Finally we are now in a position to write down the boundary conditions

on the magnetic potential Φ. The magnetic flux should be axisymmetric as discussed in the previous section and fall off as $r^{-\alpha-1}$ on the disc surface. This surface is, in the warped coordinate system, simply defined by $\theta = \pi/2$. We also require regularity at the pole $\theta = 0$ in order to restrict ourselves to physically meaningful solutions of Φ. Thus equipped, we proceed to solve for Φ in various scenarios.

2.7 The Equilibrium Field

Having set out our assumptions on the magnetic field, we may now set about solving for the magnetic potential Φ and consequently for the entire magnetic field external to the disc. We begin by solving for the field in the simple case of an unwarped disc ($\psi = 0$). The warped coordinate system reduces to standard polar coordinates and the disc surface is coplanar with the orbital plane.

Solving Laplace's equation in spherical polar coordinates is a standard problem. It is relatively straightforward to show that the only axisymmetric unwarped magnetic potential is given by

$$\Phi_0(r, \theta) = Ar^{-\alpha} P_{-\alpha}(\cos\theta), \tag{2.29}$$

where A is a constant and P_ν is the Legendre function of order ν. We note that the second Legendre function $Q_{-\alpha}(\cos\theta)$ solution is excluded due to the regularity condition at the pole $\theta = 0$. Differentiation leads to an expression for the magnetic field

$$\mathbf{B} = Ar^{-\alpha-1}(-\alpha P_{-\alpha}(\cos\theta)\mathbf{e}_r + P^1_{-\alpha}(\cos\theta)\mathbf{e}_\theta). \tag{2.30}$$

This magnetic field is plotted for several values of self-similarity parameter α (Figure 2.4). We may deduce that the magnetic field is inclined to the normal vector of the orbital plane (or equivalently the disc surface, as the disc is unwarped) at an angle of θ_m given by

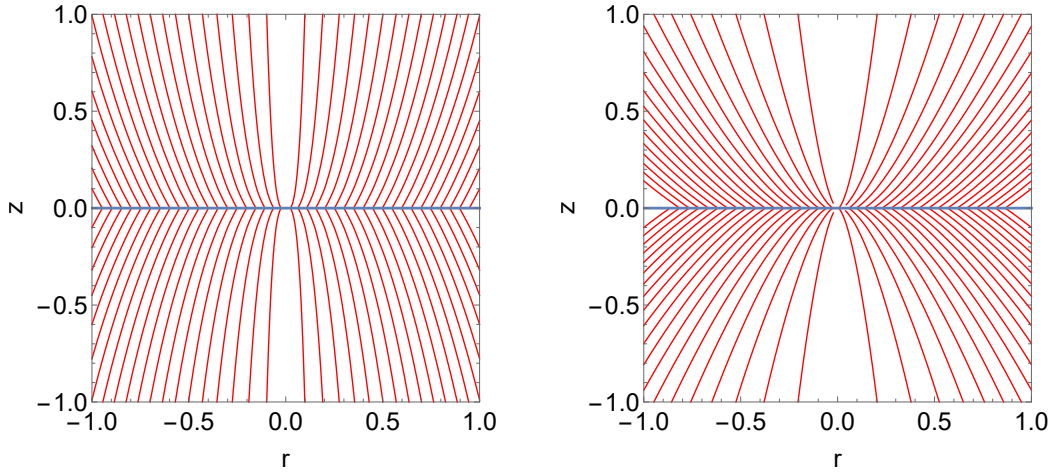

(a) $\alpha = -0.4$ (b) $\alpha = 1/4$

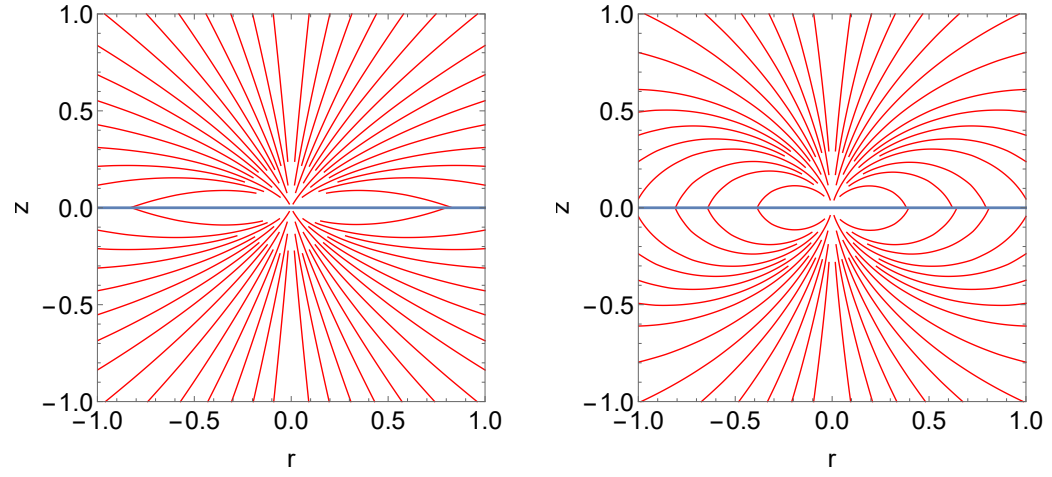

(c) $\alpha = 1.3$ (d) $\alpha = 1.8$

Fig. 2.4: Magnetic field external to a self-similar unwarped disc for a variety of model parameters α.

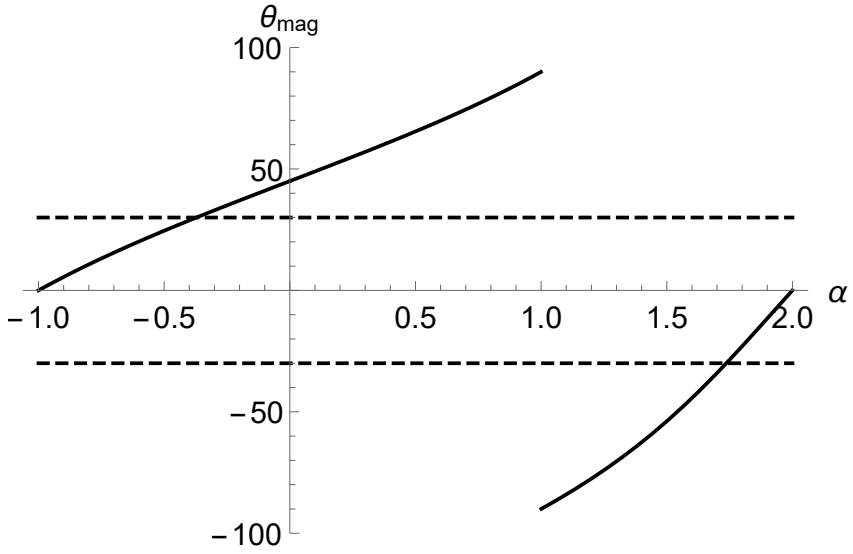

Fig. 2.5: Inclination angle of the equilibrium field plotted against self-similarity parameter α. The region between the two black lines indicate where the disc is stable to outflows via the Blandford and Payne criterion, $-30^\circ < \theta_{mag} < 30^\circ$.

$$\theta_{mag}(\alpha) = \arctan \frac{-B_r}{B_\theta} = \arctan \left(\frac{\alpha P_{-\alpha}(0)}{P^1_{-\alpha}(0)} \right). \tag{2.31}$$

The variation of θ_{mag} with self-similarity parameter α can be seen in Figure 2.5. The majority of self-similar models are subject to Blandford and Payne outflows ($|\theta_{mag}| > 30^\circ$); only a narrow range of α ($\alpha < -0.4$ and $\alpha > 1.7$) allows for models that do not exhibit any outflow. Further, the solutions with self-similarity parameter $\alpha > 1.7$ are not consistent with the notion of an open field geometry (see Figure 6.7c). Hence the models with $\alpha < -0.4$ are of greatest relevance should one seek open magnetic field geometries without outflows. It should be noted that these models, for example Figure 6.7a, are comparable to the disc wind magnetic field geometries shown in Figure 1.8 and the flux accretion models of Lubow, Papaloizou & Pringle (1994).

2.8 The First Order Magnetic Perturbation

While solving for the magnetic potential Φ is non-trivial, we may perform a perturbation expansion in orders of the dimensionless warp amplitude ψ to find the approximate magnetic field in the case of small warps. Consider the following expansion of the magnetic potential in orders of ψ:

$$\Phi = \Phi_0 + \Phi_1\psi + \Phi_2\psi^2 + \cdots \tag{2.32}$$

To zeroth order in warp amplitude ψ, Laplace's equation is

$$\nabla_0^2\Phi_0 = 0. \tag{2.33}$$

Recalling that ∇_0^2 is simply the Laplacian operator in normal spherical coordinates, we see that this is simply the equilibrium field discussed in the previous section. The first order equation may be written as

$$\nabla_0^2\Phi_1 = -\nabla_1^2\Phi_0 \tag{2.34}$$

subject to appropriate boundary conditions.

We have already found expressions for the operator ∇_1^2 and Φ_0, namely (2.19) and (2.29). Consequently the above expression may be written as

$$\nabla_0^2\Phi_1 = -(2\alpha - 1)A\psi r^{-\alpha-2}P^1_{-\alpha}(\cos\theta)\cos\phi. \tag{2.35}$$

By performing this perturbation expansion, we find that the problem of solving Laplace's equation in warped coordinates has been transformed into the solution of Poisson's equation in spherical coordinates – the warped geometry appears as a source term.

In order to preserve self-similarity and match the form of the forcing term, we require $\Phi_1 \propto r^{-\alpha}$. Further, by comparing the oddness and evenness of both sides, we conclude that Φ_1 must be odd in θ, thus forcing $\Phi_1(\theta = 0) = 0$. We now apply our boundary conditions. Looking at the induction equation

(2.27), to first order in warp amplitude ψ we have

$$\frac{D}{Dt}\left((B_\theta)_1 - \psi\cos\phi(B_r)_0\right) = 0, \tag{2.36}$$

where $(B_i)_j$ is defined as the i component of the magnetic field of order j in ψ – we are simply matching the order of the two terms. As the second term is proportional to $\cos\phi$, in order for the above relationship to be satisfied at all ϕ we require that $(B_\theta)_1 \propto \cos\phi$. This in turn implies that $\Phi_1 \propto \cos\phi$.

As a result of these considerations, we can now reduce this problem to an ODE in θ. If we express Φ_1 as:

$$\Phi_1(r,\theta,\phi) = A\psi r^{-\alpha}\cos(\phi) f_\alpha(\theta) \tag{2.37}$$

then the induction equation gives:

$$\frac{D}{Dt}(Ar^{-\alpha-1}\cos(\phi)\{f'_\alpha(\theta) + \alpha P_{-\alpha}(\cos\theta)\}) = 0 \tag{2.38}$$

implying that at the disc surface the function f_α must satisfy:

$$f'_\alpha(\pi/2) = -\alpha P_{-\alpha}(0) \tag{2.39}$$

which will be one of the boundary conditions to our problem. Poisson's equation can therefore be reduced to an ODE in θ

$$f''_\alpha + \cot\theta f'_\alpha - \left((\alpha(1-\alpha) + \frac{1}{\sin^2\theta}\right) f_\alpha = -(2\alpha-1)P^1_{-\alpha}(\cos\theta) \tag{2.40}$$

We note that the LHS of this equation is simply the associated Legendre equation for $m = 1, l = -\alpha$ or $l = \alpha - 1$ (the two l cases being degenerate/identical).

The complementary functions associated with this second order ODE are the associated Legendre functions $P^1_{-\alpha}(\cos\theta)$ and $Q^1_{-\alpha}(\cos\theta)$. However $Q^1_{-\alpha}(\cos\theta)$ diverges as $\theta \to 0$, which violates our boundary condition at $\theta = 0$. Therefore we only have a single suitable complementary function $P^1_{-\alpha}(\cos\theta)$.

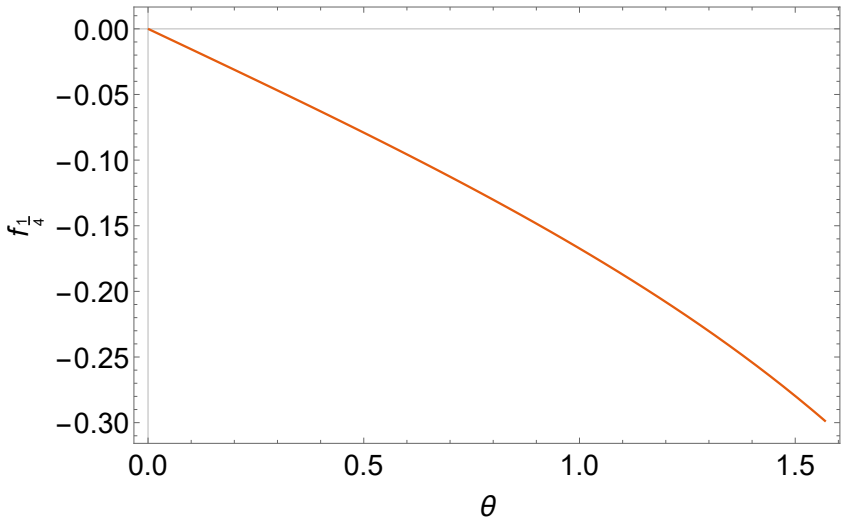

Fig. 2.6: The function $f_{1/4}(\theta)$, calculated numerically.

Let us define the normalised complementary function

$$y_{CF}(\theta) = \frac{2}{\alpha(1-\alpha)} P^1_{-\alpha}(\cos\theta) \tag{2.41}$$

such that $y_{CF}(0) = 0$, $y'_{CF}(0) = 1$. We numerically solve for the particular integral y_{PI} subject to the first boundary condition $y_{PI}(0) = y'_{PI}(0) = 0$. Our general solution may now be written as:

$$f_\alpha(\theta) = y_{PI} + \lambda_\alpha y_{CF} \tag{2.42}$$

We find the value of the constant λ_α by imposing the final boundary condition, namely that

$$f'_\alpha(\pi/2) = y'_{PI}(\pi/2) + \lambda_\alpha y'_{CF}(\pi/2) = -\alpha P_{-\alpha}(0). \tag{2.43}$$

The function f_α is plotted for the case of $\alpha = 1/4$ in Figure 2.6.

The magnetic potential and field to first order in warp amplitude is plotted for a series of self-similar models below. We note that the first order solution is divergent if $\alpha = -1$ (a uniform vertical field configuration), $\alpha = 1$ (a split

monopole field configuration) or $\alpha = 2$ (a dipole field configuration). From a mathematical perspective the cause is very simple; for these integer values of α, $y'_{CF}(\pi/2) = 0$. The value of λ_α is divergent in the region of these values of α.

The magnetic field at various values of self-similarity parameter α and warp magnitude ψ are shown in Figure 2.7. The plot omits the region close to the origin to avoid divergences - given the self-similar nature of the solutions, no information is lost by this omission. The region below the disc too is omitted. Note that θ_{mag}, the inclination of the magnetic field to the disc normal, is independent of disc radius – this is a natural consequence of self-similarity. Also note that this angle may vary significantly as the warp amplitude is increased.

2.9 The Effect of Disc Warping on Jet Formation

The model we have outlined in this chapter is by design relatively simple and certainly does not provide the appropriate framework for studying jet outflows in great detail. However this work may have some implications for jet outflows that should be mentioned.

We begin by asking how the Blandford and Payne model of jet formation is impacted by the presence of the warp. According to Blandford and Payne, a jet may be formed when the atmosphere of the disc in the magnetically dominant regions near the disc surface is unstable to outflow along the magnetic field lines. This may happen if the magnetic field is inclined too sharply with regards to the orbital plane; more precisely, if $|\theta_{mag}| > 30^\circ$ or equivalently $|B_\theta/B_r| > 1/\sqrt{3}$, the disc atmosphere will be flung out along the field lines, eventually becoming a jet.

Note that it is the angle that the magnetic field makes with the **orbital plane** that is relevant to jet formation and not the inclination of the magnetic field with respect to the disc surface (see Figure 2.8). This can be shown more formally but there is a relatively simple intuitive explanation: the jet launch-

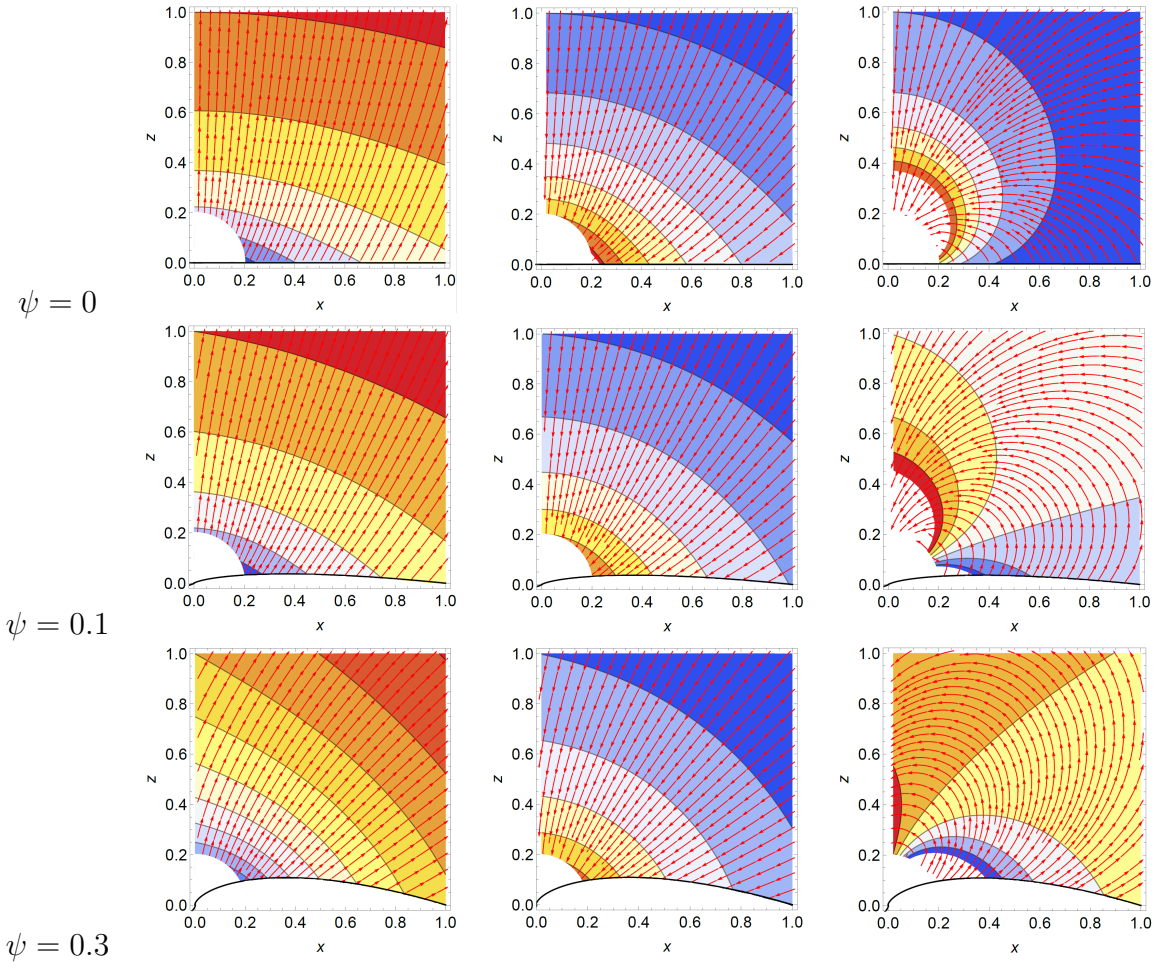

Fig. 2.7: A two-dimensional cut of an untwisted self-similar warped disc in the azimuthal direction of greatest warping ($\phi = 0$) along with a contour plot of the magnetic potential Φ plotted at various values of warp amplitude. The magnetic field lines are shown in red. The region $r < 0.2$ and the region below the disc surface are not shown. Note that the angle between the magnetic field and the disc surface is the same at all points along the disc (a consequence of self-similarity) but varies with warp amplitude.

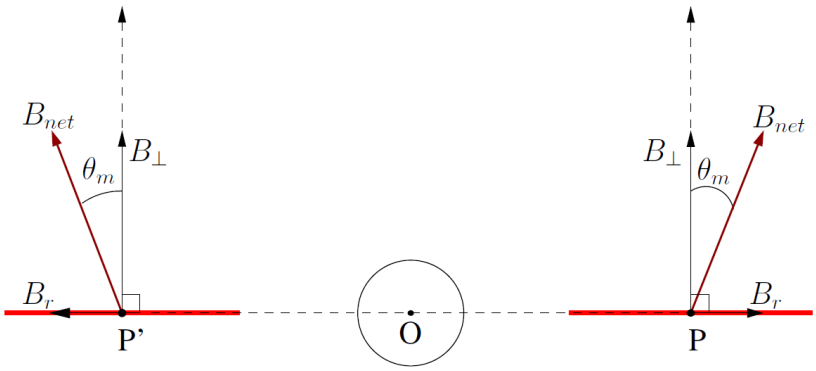

Fig. 2.8: An exaggerated sketch of small region of an unwarped disc (shown in red) surrounding a point P, including its orientation relative to the central stellar object O (not shown to scale). Also shown is a region of the same disc phase shifted by π along its orbit from P, labelled as P'. The magnetic field (mauve) as well as the directions of the magnetic field component directions B_r and $B_\perp$ are shown at P and P'. Both B_r and $B_\perp$ are advected by the flow and, under axisymmetric initial conditions, remain constant. The inclination of the magnetic field to the normal of the orbital plane θ_m consequently remains unchanged.

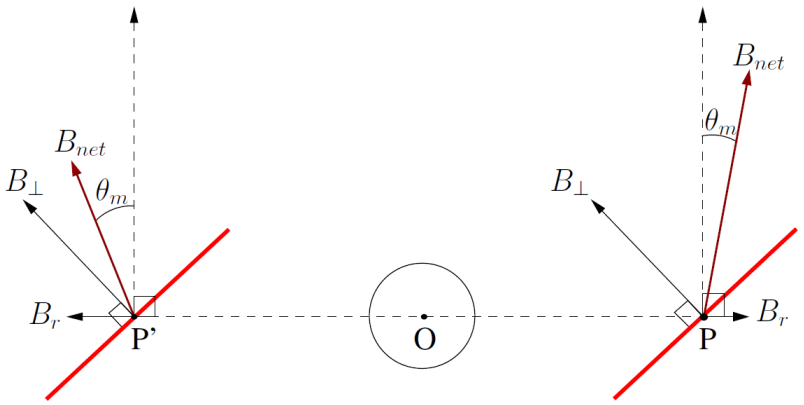

Fig. 2.9: A similar sketch of small region of a warped disc (shown in red) surrounding a point P. $B_\perp$ is advected by the flow and is a constant of the motion; consequently the projection of B_{net} onto $B_\perp$ is unchanged over an orbit. B_r is however subject to oscillatory perturbations imposed by the global external field solution. The relative orientation of these two vectors and the orbital plane results in the variation of θ_{mag} over an orbit.

ing mechanism is fundamentally a consequence of the centrifugal apparent force due to the orbital motion, thus it is the magnetic field inclination with respect to the orbital plane that is relevant.

In an unwarped axisymmetric disc the orbital motion of the fluid advects the poloidal magnetic field and there is no change in the inclination angle between the orbital plane and the magnetic field over an orbit. In a warped disc the magnetic field perpendicular to the disc surface is preserved, but the radial component is not – this is a consequence of the global solution for the magnetic field. Further, as the disc surface is not parallel to the orbital plane, the relative orientation of these vectors changes across an orbit. As a result the inclination angle of the magnetic field with respect to the orbital plane – and by extension the susceptibility of the fluid to jet formation – may vary considerably along a given orbit (Figure 2.9).

While this phenomenon as described is quite generic and no notion of self-similarity is necessary to derive it, it can be clearly seen in our self-similar model. If we look at the magnetic field to first order in warp amplitude,

$$\mathbf{B} = \mathbf{B}_0 + \mathbf{B}_1 = \nabla_0\Phi_0 + \psi(\nabla_1\Phi_0 + \nabla_0\Phi_1) \tag{2.44}$$

(Note that we must include the term $\nabla_1\Phi_0$ – this is due to the fact that ∇ in warped coordinates contains a term proportional to ψ, and therefore must be taken into account). At the disc surface, which we recall is at $\theta \approx \pi/2$, the components of the field are given by:

$$B_r/(Ar^{-\alpha-1}) = -(\alpha a + (b + \alpha c)\psi\cos\phi) \tag{2.45}$$

$$B_\theta/(Ar^{-\alpha-1}) = b + d\psi\cos\phi \tag{2.46}$$

$$B_\phi/(Ar^{-\alpha-1}) = -c\psi\sin\phi \tag{2.47}$$

where the numbers a, b, c, and d are dependent on α and given by:

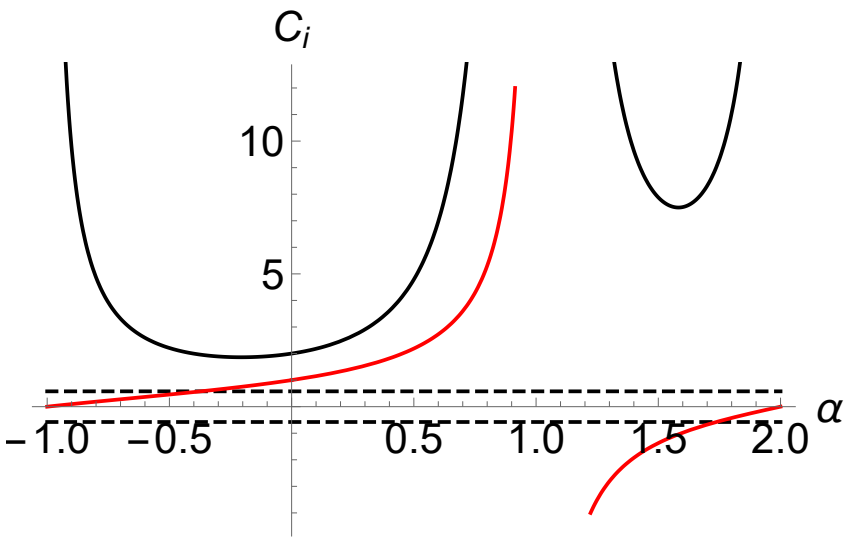

Fig. 2.10: The coefficients C_0 and C_1, drawn in red and black respectively.

$$a = P_{-\alpha}(0); b = P'_{-\alpha}(0); c = f_\alpha(\pi/2); d = f'_\alpha(\pi/2) \tag{2.48}$$

Hence we find that the relevant angle between the orbital plane of the particle and the poloidal magnetic field threading the disc is:

$$\tan\theta_{mag} = -B_r/B_\theta = C_0(\alpha) + C_1(\alpha)\psi\cos\phi + O(\psi^2) \tag{2.49}$$

where $C_0(\alpha) = \alpha a/b$ and $C_1(\alpha) = 1 + \alpha c/b - \alpha a d/b^2$.

If the magnetic field normal to disc is conserved throughout the motion while the radial component varies by an amount proportional to $\psi\cos\phi$ as determined by the solution for the global magnetic field, the relative orientation of the magnetic field and orbital plane should be expected to vary. The variation of $\tan\theta_{mag}$ should in turn be expected to have an amplitude proportional to the degree of warping and to vary sinusoidally with ϕ.

One can speculate about the effects that this variation would cause (see Table 2.1). The most immediate consequence might be the formation of asymmetric jets, jets where the majority of the outflow is launched from within a

α	θ_0	ψ	θ_{min}	θ_{max}	Status
-0.8	10.7°	0	10.7°	10.7°	No outflow
-0.8	10.7°	0.05	−3.1°	23.4°	No outflow
-0.8	10.7°	0.1	−16.6°	34.0°	Partial outflow
-0.4	28.8°	0	28.8°	28.8°	No outflow
-0.4	28.8°	0.05	24.2°	33.0°	Partial outflow
-0.4	28.8°	0.1	19.3°	36.9°	Partial outflow
-1/4	35.0°	0	35.0°	35.0°	Outflow at all ϕ
-1/4	35.0°	0.05	31.3°	38.4°	Outflow at all ϕ
-1/4	35.0°	0.1	27.2°	41.6°	Partial outflow
1/4	55.0°	0	55.0°	55.0°	Outflow at all ϕ
1/4	55.0°	0.05	52.3°	57.4°	Outflow at all ϕ
1/4	55.0°	0.1	49.3°	59.5°	Outflow at all ϕ
0.5	65.0°	0	65.0°	65.0°	Outflow at all ϕ
0.5	65.0°	0.05	62.8°	67.6°	Outflow at all ϕ
0.5	65.0°	0.1	59.7°	69.4°	Outflow at all ϕ
1.8	−23.0°	0	−23.0°	−23.0°	No outflow
1.8	−23.0°	0.05	−44.3°	7.3°	Partial outflow
1.8	−23.0°	0.1	−56.8°	34.2°	Partial outflow

Tab. 2.1: A table illustrating the variation of θ_{mag}, the inclination of the magnetic field to the disc surface, to first order in ψ along a single orbit for a variety of self-similarity parameters α and warp magnitudes ψ. θ_0 is the value of θ_{mag} in the unwarped case. As the warp amplitude is increased, the magnitude of θ_{mag} oscillates over a single orbit; the maximum and minimum values of θ_{mag} are shown in each case. The nature of the outflow as predicted by the Blandford and Payne criterion is also presented for each case.

very narrow band of azimuthal angles corresponding to a maximal $|\theta_{mag}|$. Unwarped discs with no outflow may form jets if a warp is introduced. Unwarped discs susceptible to jet outflows have been shown to be highly sensitive to inclination angle (e.g. Ogilvie & Livio (2001)), and hence may qualitatively alter their behaviour upon the introduction of a relatively modest warp. This interaction between disc warping and asymmetrical jet formation could potentially be linked to jet abnormalities in systems such as SS433 (Fabian & Rees, 1979). Yet we admit wholly that this remains speculation, and a fuller investigation is required to probe the significance of disc warping on jet formation. The magnetic field found in these simple models assumes, in addition to self-similarity, the lack of any significant outflow, and we cannot have confidence in the validity of these models in the presence of an outflow. Yet we believe the mechanism we have outlined by which a warped disc might vary its inclination angle with azimuthal angle merits further study.

2.10 Summary

In this chapter we have used the warped coordinates of Ogilvie (1999) to express the equation for the magnetic potential in the force-free region above a warped disc in the form of a modified Laplacian. Explicit solutions were found for the linearised problem, relevant when the warp amplitude ψ is small. The magnetic field perpendicular to the disc surface was found to be a conserved quantity if the flow is purely toroidal. Using the Blandford and Payne criterion we find that the susceptibility of warped discs to jet formation varies with orbital phase and may have interesting physical consequences.

From one perspective, the topic of this chapter has been the response of the external magnetic field to a deformation of the disc. Yet what drives, propagates, or dampens the warp itself? To answer these questions our attention now turns from the disc exterior to the disc interior. In the following chapter we present a local model for the interior structure of a magnetised disc, for which the work of this chapter will provide useful context.

3. THE WARPED SHEARING BOX MODEL

3.1 Introduction

Warps in magnetised discs have either been studied through vast global simulations or via theoretical methods that make no attempt to model the internal structure of the disc or account for their potentially critical internal flows. A number of fundamental questions have yet to be satisfactorily answered: Does the presence of a mean magnetic field enhance or retard the exchange of angular momentum in a warped disc? Does the vertical structure of a magnetised disc share many of the same properties as its hydrodynamic counterpart? What of the resonance between the epicyclic and vertical oscillation frequencies that, in hydrodynamic discs, leads to the rapid propagation of the warp at half the sound speed? To answer these questions we require a framework in which we may resolve the internal torques and flows within the disc.

Ogilvie & Latter (2013a) showed that the nonlinear hydrodynamic theory of Ogilvie (1999) can be derived by separating the global and local aspects of a warped thin disc. The global evolution of the mass distribution and the shape of the disc can be deduced from the (vectorial) conservation of angular momentum, provided that the internal torque is known. The internal torque can be calculated from time-averaged quantities in a local model, which is constructed around a reference point that follows a circular orbit through a warped disc and experiences a geometry that oscillates at the orbital frequency, thereby generalizing the well known shearing sheet or box. The simplest solutions in the warped shearing box are laminar internal flows that oscillate at the orbital frequency; these are driven by a radial pressure gradient that arises from the warped geometry and the vertical stratification

of the disc. Owing to the coincidence of the orbital and epicyclic frequency in a Keplerian disc, this forcing may result in fast internal flows for even comparatively small warps. Such flows generate correspondingly large internal torques, leading to the rapid propagation of the warp.

In this chapter we extend the work of Ogilvie & Latter (2013a) and present the first local study of magnetised warped discs utilizing the warped shearing box formalism, thereby addressing some of the pressing questions presented at the start of this chapter.

In the following section we employ the warped shearing box model to express the fully non-linear local ideal MHD equations in a reference frame comoving with a fluid element in the warped disc midplane. In section 3.3 we consider one-dimensional laminar solutions to these equations, and by expanding linearly in warp amplitude about an equilibrium solution, a system of first-order differential equations is found for the internal structure of the disc.

In section 3.4 we consider the special case of a disc threaded by a magnetic field perpendicular to the disc midplane. A solution to this particular case is found via a spectral method. The unique features of magnetised warped disc dynamics are discussed. In section 3.5 we outline two numerical procedures that are used to check the results of the spectral method. The results of this chapter are then discussed and summarised in section 3.6.

3.2 The Warped Shearing Box

3.2.1 Definition of the Warped Shearing Box

We restrict ourselves to circular warped discs (as opposed to elliptical discs) due to their relative simplicity. Ogilvie (1999) showed that a circular warped disc may be mathematically described by a radially dependent vector $\mathbf{l}(r,t)$

defined to be perpendicular to the orbital plane of the fluid at radius r. The radial dependence of the orbital plane causes a warping in the disc geometry, as can be seen in Figure 3.1. For this class of accretion disc, only the dimensionless warp amplitude ψ defined by $\psi = r|\frac{\partial \mathbf{l}}{\partial r}|$ is necessary to specify the local geometry of the warped disc. The physical significance of the warping parameter ψ can be clearly seen in Figure 2.2.

Local models of unwarped accretion discs are typically constructed around a reference point in the midplane of the disc co-orbiting with the surrounding fluid. A Cartesian coordinate system can be imposed with the origin at this reference point and the axes rotating at the orbital frequency such that the x-direction is radial, the y-direction is azimuthal and the z-direction is perpendicular to the disc midplane. There is a shearing flow within the box due the differential rotation of the disc; consequently such models are often called 'shearing box' models.

An analogous construction is the 'warped shearing box', introduced in Ogilvie & Latter (2013a) and effectively utilised by Ogilvie & Latter (2013b) and Paardekooper & Ogilvie (2019) to investigate the parametric instability of hydrodynamic warped discs. In the warped shearing box a Cartesian coordinate system is constructed around a reference point in the mid-plane of a warped accretion disc as shown in Figure 1. The warped shearing box is represented by the non-orthogonal primed coordinates (t', x', y', z') chosen to compensate for the local geometry of the warped disc. These are related to the Cartesian coordinate system (t, x, y, z) comoving with the fluid via expressions (3.1)–(3.4) below, where $q \equiv -\frac{d\ln\Omega}{d\ln r}$ is the orbital shear rate of the disc in question and Ω is the orbital frequency at the reference radius.

We define z' such that the surface $z' = 0$ corresponds to the midplane of the warped disc and the z'-axis is normal to the disc midplane rather than normal to the orbital plane. The definition of y' simply takes into account the shear due to the differential rotation, where q is assumed to be 3/2 for a Ke-

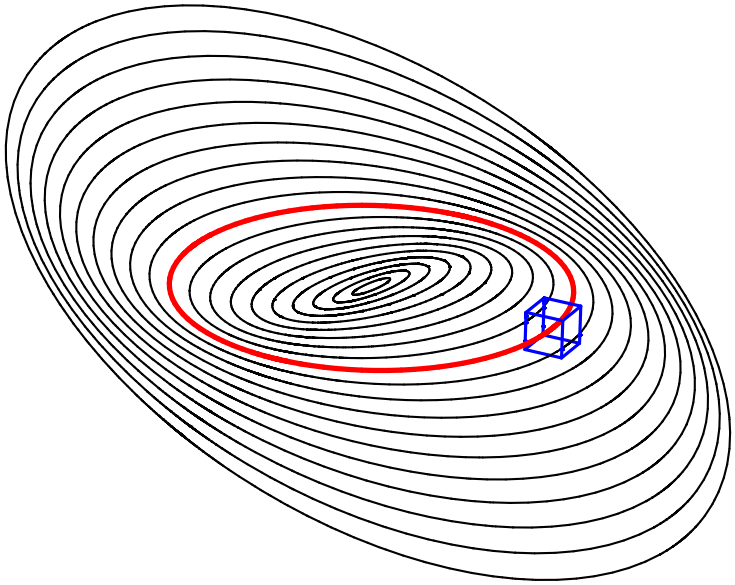

Fig. 3.1: A warped disc, viewed as a collection of tilted rings. As discussed in Section 3.2.1, a local frame (the blue box) is centred on a point that follows the red reference orbit. Figure taken from Ogilvie and Latter (2013).

plerian disc. The relative velocities $\mathbf{v}$ are constructed to remove the expected azimuthal velocity changes due to shear or the vertical velocity changes due to the warped geometry of the disc.

$$t' = t, \tag{3.1}$$

$$x' = x, \tag{3.2}$$

$$y' = y + q\Omega t x, \tag{3.3}$$

$$z' = z + \psi x \cos(\Omega t). \tag{3.4}$$

In such coordinates, it is important to note that

$$\partial_t = \partial_{t'} + q\Omega x \partial_{y'} - \psi \Omega x \sin(\Omega t) \partial_{z'}, \tag{3.5}$$

$$\partial_x = \partial_{x'} + q\Omega t \partial_{y'} + \psi \cos(\Omega t) \partial_{z'}, \tag{3.6}$$

$$\partial_y = \partial_{y'}, \tag{3.7}$$

$$\partial_z = \partial_{z'}, \tag{3.8}$$

and relative velocities are defined such that

$$v_x = u_x, \tag{3.9}$$

$$v_y = u_y + q\Omega x, \tag{3.10}$$

$$v_z = u_z - \psi \Omega x \sin(\Omega t). \tag{3.11}$$

3.2.2 The Non-Linear MHD equations in a Warped Disc

Having defined the coordinate system of the warped shearing box, we may now express the full non-linear local MHD equations in these coordinates.

The physical equations

The momentum equation expressed in a coordinate system corotating with the reference orbit is

$$\rho\left(\frac{D\mathbf{u}}{Dt}+2\Omega\mathbf{e}_z\wedge\mathbf{u}\right)=-\rho\nabla\Phi-\nabla p+\mathbf{J}\wedge\mathbf{B}, \tag{3.12}$$

where the effective potential due to a central gravitational force and the rotating frame is given by

$$\Phi=\frac{1}{2}\Omega^2(z^2-2qx^2) \tag{3.13}$$

and the Lorentz force in ideal MHD is expressed as

$$\mathbf{J}\wedge\mathbf{B}=\frac{1}{\mu_0}(\mathbf{B}\cdot\nabla)\mathbf{B}-\frac{1}{2\mu_0}\nabla\mathbf{B}^2. \tag{3.14}$$

The induction equation in ideal MHD is given by

$$\frac{\partial\mathbf{B}}{\partial t}=\nabla\wedge(\mathbf{u}\wedge\mathbf{B})=\mathbf{B}\cdot\nabla\mathbf{u}-\mathbf{u}\cdot\nabla\mathbf{B}-\mathbf{B}(\nabla\cdot\mathbf{u}), \tag{3.15}$$

while the continuity equation gives

$$\frac{\partial\rho}{\partial t}+\nabla\cdot(\rho\mathbf{u})=0. \tag{3.16}$$

For simplicity the disc is assumed to be isothermal with uniform sound speed c_s, implying

$$p=c_s^2\rho. \tag{3.17}$$

Rather than expressing the full MHD equations in terms of the vector components perpendicular to the orbital plane, such as v_z and B_z, it will be more convenient to consider the vector components perpendicular to the disc midplane as defined by $v_{z'}=v_z+\psi\cos(\Omega t)v_x$, $B_{z'}=B_z+\psi\cos(\Omega t)B_x$ (in fact, these are contravariant vector components in the warped shearing coordinate system). The full non-linear MHD equations are then given by

$$\frac{Dv_x}{Dt'} - 2\Omega v_y = -\frac{1}{\rho}[\partial_{x'} + q\Omega t'\partial_{y'} + \psi\cos(\Omega t')\partial_{z'}]\Pi + \frac{1}{\mu_0\rho}(\mathbf{B}'\cdot\nabla)B_x, \tag{3.18}$$

$$\frac{Dv_y}{Dt'} + (2-q)\Omega v_x = -\frac{1}{\rho}\partial_{y'}\Pi + \frac{1}{\mu_0\rho}(\mathbf{B}'\cdot\nabla)B_y, \tag{3.19}$$

$$\frac{Dv_{z'}}{Dt'} = -2\psi\Omega\sin(\Omega t')v_x - \Omega^2 z' + 2\Omega\psi\cos(\Omega t')v_y - \frac{\gamma^2}{\rho}\partial_{z'}\Pi - \frac{1}{\rho}\psi\cos(\Omega t')(\partial_{x'} + q\Omega t'\partial_{y'})\Pi + \frac{1}{\mu_0\rho}(\mathbf{B}'\cdot\nabla)B_{z'}, \tag{3.20}$$

$$\frac{\partial B_x}{\partial t'} = \mathbf{B}'\cdot\nabla v_x - (\nabla\cdot\mathbf{v}')B_x - \mathbf{v}'\cdot\nabla B_x, \tag{3.21}$$

$$\frac{\partial B_y}{\partial t'} = -q\Omega B_x + \mathbf{B}'\cdot\nabla v_y - (\nabla\cdot\mathbf{v}')B_y - \mathbf{v}'\cdot\nabla B_y, \tag{3.22}$$

$$\frac{\partial B_{z'}}{\partial t'} = \mathbf{B}'\cdot\nabla v_{z'} - (\nabla\cdot\mathbf{v}')B_{z'} - \mathbf{v}'\cdot\nabla B_{z'}, \tag{3.23}$$

$$\nabla\cdot\mathbf{B}' = 0, \tag{3.24}$$

$$\partial_{t'}\rho + \rho(\nabla\cdot\mathbf{v}') + \mathbf{v}'\cdot\nabla\rho = 0, \tag{3.25}$$

where

$$\frac{D}{Dt'} = \partial_{t'} + \mathbf{v}'\cdot\nabla, \tag{3.26}$$

$$\mathbf{v}'\cdot\nabla = v_x\partial_{x'} + (v_y + q\Omega t' v_x)\partial_{y'} + v_{z'}\partial_{z'}, \tag{3.27}$$

$$\nabla \cdot \mathbf{v}' = \partial_{x'} v_x + \partial_{y'}(v_y + q\Omega t' v_x) + \partial_{z'} v_{z'}, \tag{3.28}$$

$$\mathbf{B}' \cdot \nabla = B_x \partial_{x'} + (B_y + q\Omega t' B_x)\partial_{y'} + B_{z'}\partial_{z'}, \tag{3.29}$$

$$\nabla \cdot \mathbf{B}' = \partial_{x'} B_x + \partial_{y'}(B_y + q\Omega t' B_x) + \partial_{z'} B_{z'}, \tag{3.30}$$

total pressure $\Pi \equiv c_s^2 \rho + \frac{\mathbf{B}^2}{2\mu_0}$ and $\gamma^2 \equiv 1 + \psi^2 \cos^2(\Omega t')$.

This system of equations is horizontally homogeneous as it does not refer explicitly to x' or y', and so is compatible with periodic horizontal boundary conditions. In order to solve this system of equations, boundary conditions far from the disc midplane must be imposed. More specifically limiting magnetic field values, along with a condition on material inflow/outflow, must be prescribed.

The validity of the local model

It is imperative that we keep track of the assumptions made to derive these equations. Firstly, we have assumed an isothermal gas for simplicity. Perhaps more subtly there is also an implicit separation of scales in the formulation of these equations. The warp, expressed by the warp amplitude ψ, is assumed to be independent of time. This reflects the assumption that the warp propagates on a timescale far longer than the orbital timescale ($|\frac{d\psi}{dt}| \ll \Omega\psi$).

At first glance it may seem curious that the warp amplitude is a fixed parameter given that this model is intended partly for the study of warp propagation. However, there is no contradiction here. The warp amplitude determines the internal dynamics of the disc on the fast orbital timescale. An internal torque is generated by the internal flows driven by the warp (as discussed in section 3.4.2), which can be calculated. In principle the warp could then be allowed to vary on a slower timescale in a manner consistent

with the torques acting upon that annulus of the disc. In practice, however, we can deduce the evolution of the warp from the calculated internal torque and the conservation of angular momentum. In this way, warp propagation may be investigated in the local model without an explicitly time-dependent warp amplitude. Ogilvie & Latter (2013a) displayed that the hydrodynamic warped shearing box is indeed capable of replicating the results of the global asymptotic theory of warped discs (Ogilvie, 1999), validating the local approach.

Other challenges may be levelled at this approach to warped disc dynamics. If one were to investigate solutions to these equations that are either one-dimensional or have periodic radial boundaries, one would require the structure of the warp to vary on a length scale much greater than the radial excursion of fluid elements over the period of an orbit. If this were not the case, then the radial variation of the warp amplitude would affect the internal structure of the disc and it would be impossible to characterise a region of the disc by a single value for the warp amplitude. Hence the warped shearing box would be unable to appropriately model a disc with extreme radial variations in warp amplitude. If the warp varies on the length scale of the disc radius this condition simplifies to $|\mathbf{v}| \ll \Omega R$, or equivalently the relative velocity must be much less than the orbital velocity.

Additionally, the presence of a global magnetic field implies that in some sense the transport of angular momentum may not be truly local as is the case for hydrodynamic discs, but rather angular momentum may be communicated non-locally via magnetic stresses to other parts of the disc. This issue enters the local model via several unspecified boundary terms (see section 3.2.2). This topic is discussed in greater detail in the following chapter.

3.3 One-Dimensional Solutions

3.3.1 Non-linear 1D MHD Equations

Having derived the fully non-linear local MHD equations we proceed by looking for the simplest solutions for the disc structure. The warped shearing box was designed such that the MHD equations do not explicitly contain x' or y', and are hence horizontally homogeneous. We therefore start by seeking solutions that are independent of x' and y'. All physical quantities are taken to be functions of z' and t' alone, and the MHD equations reduce to a set of 1D equations. Recall that the oscillatory time-dependence of quantities in the local model corresponds to their azimuthal dependence in a global description (see Fig. 1). We note that such a laminar flow excludes the possibility of turbulence, most notably MRI turbulence.

Scaling

$B_{z'}$, as shown in the following section, is a constant of the motion and therefore can be used as a scaling parameter. Using this convention the above set of equations (3.18)–(3.30) can be made dimensionless via the following scaling relations:

$$\widehat{t} = \Omega t, \tag{3.31}$$

$$\widehat{z'} = \frac{z'\Omega}{c_s}, \tag{3.32}$$

$$\widehat{v_i} = v_i/c_s, \tag{3.33}$$

$$\widehat{\rho} = \frac{\rho c_s}{\Sigma\Omega}, \tag{3.34}$$

$$\widehat{B}_{z'} = \frac{B_{z'}}{\sqrt{\mu_0 \Sigma c_s \Omega}}, \tag{3.35}$$

$$\widehat{B}_x = \frac{B_x}{B_{z'}}, \tag{3.36}$$

where c_s is the isothermal sound speed, Σ is the vertically integrated surface density of the disc, and all other terms maintain their previous definitions.

From this point onwards all physical quantities will be scaled as shown above and the circumflexes will be removed. The one dimensional non-linear MHD equations are hence given by:

$$\begin{aligned}\frac{Dv_x}{Dt'} - 2v_y = &-\frac{\psi\cos(t')}{\rho}\partial_{z'}\rho + \frac{B_{z'}^2}{\rho}\{\gamma^2[\partial_{z'}B_x \\ &-\psi\cos(t')B_x\partial_{z'}B_x] - \psi\cos(t')B_y\partial_{z'}B_y\},\end{aligned} \tag{3.37}$$

$$\frac{Dv_y}{Dt'} = -(2-q)v_x + \frac{B_{z'}^2}{\rho}\partial_{z'}B_y, \tag{3.38}$$

$$\begin{aligned}\frac{Dv_{z'}}{Dt'} = &-2\psi\sin(t')v_x - z' + 2\psi\cos(t')v_y - \frac{\gamma^2}{\rho}\partial_{z'}\rho \\ &+\frac{B_{z'}^2\gamma^2}{\rho}[-\gamma^2 B_x\partial_{z'}B_x + \psi\cos(t')\partial_{z'}B_x - B_y\partial_{z'}B_y],\end{aligned} \tag{3.39}$$

$$\frac{\partial\rho}{\partial t'} + \partial_{z'}(\rho v_{z'}) = 0, \tag{3.40}$$

$$\frac{\partial B_x}{\partial t'} = \partial_{z'}v_x - v_{z'}\partial_{z'}B_x - B_x\partial_{z'}v_{z'}, \tag{3.41}$$

$$\frac{\partial B_y}{\partial t'} = \partial_{z'}v_y - qB_x - v_{z'}\partial_{z'}B_y - B_y\partial_{z'}v_{z'}, \tag{3.42}$$

$$\frac{\partial B_{z'}}{\partial t'} = 0, \tag{3.43}$$

$$\frac{\partial B_{z'}}{\partial z'} = 0, \tag{3.44}$$

where $\frac{D}{Dt'} = \partial_{t'} + v_{z'}\partial_{z'}$ and $\gamma^2 \equiv 1 + \psi^2 \cos^2(t')$.

Properties of the non-linear 1D MHD equations

Some general comments can be made at this stage. The final two equations (3.43)–(3.44) reveal an important property of warped magnetized accretion discs. The magnetic field component perpendicular to the disc midplane, $B_{z'}$, is independent of both time and height above the midplane. This is a consequence of magnetic flux conservation under the assumption of horizontal uniformity. The magnetic field perpendicular to the disc midplane is therefore advected with the fluid and a constant of the motion, while the other magnetic field components are not. Thus the use of $B_{z'}$ as a scaling parameter is justified. We had encountered this result from another perspective in the previous chapter assuming that the flow was purely toroidal in the local plane(see equation (2.27) and note that $B_\theta = -B_z$ near the disc midplane). We have now demonstrated that this result holds true in the presence of vertically stratified internal flows.

In a standard unwarped accretion disc there is an azimuthal symmetry present in the equations of motion. With suitable boundary conditions and in the absence of a symmetry-breaking process, there is therefore an azimuthal symmetry in all physical quantities. Although this axisymmetry is broken in a warped disc, equations (3.37)–(3.44) reveal that a point symmetry still exists. This point symmetry could be described as a reflection in the local disc midplane followed by a rotation by π radians. For example, for a scalar quantity $f(z', t')$ this transformation can be represented by the operator $\widehat{T}$ such that

$$\widehat{T} f(z', t') = f(-z', t' + \pi). \tag{3.45}$$

For vector quantities, the vector components parallel to the disc plane are invariant under transformation $\widehat{T}$ and the vector components perpendicular to the disc surface are inverted. For pseudovectors, the opposite is true;

pseudovector components parallel to the disc surface are inverted, while pseudovector components perpendicular to the disc surface are invariant.

This symmetry can be proven by making the appropriate simultaneous transformation in the warped disc MHD equations: $\{z' \to -z', t' \to t'+\pi, \rho \to \rho, v_x \to v_x, v_y \to v_y, v_{z'} \to -v_{z'}, B_x \to -B_x, B_y \to -B_y, B_{z'} \to B_{z'}\}$. This transformation leaves equations (3.37)–(3.44) invariant, and is therefore a symmetry of the system. The existence of this symmetry is not only of physical interest but is of practical use in the numerical work described in sections 4 and 5.

3.3.2 *Perturbation Analysis of the Warped Disc MHD equations*

In the previous section we found a set of one-dimensional MHD equations for the vertical structure of a magnetised warped disc. We proceed by linearising these equations with respect to the warp amplitude ψ. The solutions found by this method will be valid only for small warps ($\psi \ll 1$).

The unwarped solution

The equilibrium state is chosen to be an unwarped disc such that $B_y = v_x = v_{z'} = 0$ and there is no jet outflow for simplicity (Ogilvie, 1997). This represents an unwarped accretion disc with a poloidal magnetic field and a purely azimuthal velocity. The unwarped disc is described by three variables $\{\rho_0, B_{x0}, v_{y0}\}$ which satisfy the following set of equations:

$$2v_{y0} + \frac{B_{z'}^2}{\rho_0} d_{z'} B_{x0} = 0, \tag{3.46}$$

$$z' + \frac{1}{\rho_0} d_{z'} \rho_0 + \frac{B_{z'}^2}{\rho_0} B_{x0} d_{z'} B_{x0} = 0, \tag{3.47}$$

$$d_{z'} v_{y0} - q B_{x0} = 0. \tag{3.48}$$

The following three associated boundary conditions must also be satisfied:

$$B_{x0}|_{z'\to\infty} = \tan i, \tag{3.49}$$

$$B_{x0}(0) = 0, \tag{3.50}$$

and

$$\int_{-\infty}^{\infty} \rho_0(z')dz' = 1. \tag{3.51}$$

The first condition states that the inclination angle i of the poloidal magnetic field has to be specified at large z'. We only consider $i < 30°$, as an inclination angle in excess of this value produces a jet outflow (Blandford & Payne, 1982). The second condition is a result of the odd symmetry of B_{x0} in z', and the final condition normalizes the surface density of the disc.

The MHD equations to first order

Through inspection of equations (3.37)–(3.44) and comparison with the hydrodynamic solutions found by Ogilvie & Latter (2013a), all first-order physical quantities can be expected to vary sinusoidally throughout the orbit. More specifically, the following time-dependence is consistent with the MHD equations (3.37)–(3.44) to first order in warp amplitude ψ: $\{v_{x1} \sim \sin(t'), v_{y1} \sim \cos(t'), B_{x1} \sim \cos(t'), B_{y1} \sim \sin(t'), \rho_1 \sim \cos(t'), v_{z1'} \sim \sin(t')\}$.

We now assume the above time-dependence for all six variables and remove the relevant factors of $\sin(t')$ or $\cos(t')$ from the linear equations. Eliminating the time-dependence in this way, the first-order MHD equations reduce to a set of six interrelated first-order ordinary differential equations for the vertical structure of the disc:

$$v_{x1} - 2v_{y1} = -\frac{1}{\rho_0} d_{z'}\rho_0 + \frac{B_{z'}^2}{\rho_0}\left(d_{z'}B_{x1} - \frac{\rho_1}{\rho_0} d_{z'}B_{x0} - B_{x0}d_{z'}B_{x0}\right), \tag{3.52}$$

$$-v_{y1} = -(2-q)v_{x1} + \frac{B_{z'}^2}{\rho_0} d_{z'}B_{y1} - v_{z1'}d_{z'}v_{y0}, \tag{3.53}$$

$$\begin{aligned} v_{z1'} = 2v_{y0} - \frac{1}{\rho_0} d_{z'}\rho_1 + \frac{\rho_1}{\rho_0^2} d_{z'}\rho_0 + \frac{B_{z'}^2}{\rho_0}\Bigg(&-B_{x0}d_{z'}B_{x1} \\ &-B_{x1}d_{z'}B_{x0} + B_{x0}d_{z'}B_{x0}\frac{\rho_1}{\rho_0} + d_{z'}B_{x0}\Bigg), \end{aligned} \tag{3.54}$$

$$-\rho_1 + d_{z'}(\rho_0 v_{z1'}) = 0, \tag{3.55}$$

$$-B_{x1} = d_{z'}v_{x1} - v_{z1'}d_{z'}B_{x0} - B_{x0}d_{z'}v_{z1'}, \tag{3.56}$$

$$B_{y1} = d_{z'}v_{y1} - qB_{x1}. \tag{3.57}$$

The symmetry properties of the first-order problem can be found by the following considerations. It was shown in section 3.1.2 that all physical quantities have a symmetry under the transformation $\{t' \to t'+\pi, z' \to -z'\}$. Given that the zeroth-order terms have no time-dependence and the first-order terms have a sinusoidal dependence, one can deduce whether each variable is an even or odd function of z'. For example $\rho_1(-z', t'+\pi) = \rho_1(z', t')$ from the point symmetry of the warped disc, but the sinusoidal time-dependence of ρ_1 implies that $\rho_1(z', t'+\pi) = -\rho_1(z', t')$. We may thus conclude that $\rho_1(-z', t') = -\rho_1(z', t')$, or ρ_1 is an odd function of z'. In summary, $\{\rho_0, v_{y0}, v_{z1'}, B_{x1}, B_{y1}\}$ are even functions of z', while $\{B_{x0}, \rho_1, v_{x1}, v_{y1}\}$ are odd functions of z'. These symmetry considerations lead to boundary conditions (3.58)–(3.63).

Equations (3.52)–(3.57) specify six first-order differential equations with one free dimensionless parameter, $B_{z'}$, which fixes the strength of the magnetic

field. Note that $B_{z'}$ as defined in equation (3.35) is the same dimensionless parameter used in the study of jet launching from isothermal discs by Ogilvie (2012). In addition we require six boundary conditions in order to construct a numerical solution for the vertical structure of the disc. Symmetry considerations imply that the equations need only be solved above the midplane and immediately fix three boundary conditions at the midplane. The magnetic field at the upper surface must be prescribed, leading to a further two boundary conditions (3.58)–(3.59).

We chose to impose a rigid lid on the upper disc surface corresponding to the final boundary condition (3.63). An analysis of the far-field solution of equations (3.52)–(3.57) implied that the high-density region of the disc is insensitive to any reasonable boundary condition on the disc outflow at sufficiently large z'. Numerical tests (see section 3.5.1) confirmed this result, validating our choice of boundary condition.

In summary the boundary conditions on the problem are:

$$B_{x1}(\infty) = A, \tag{3.58}$$

$$B_{y1}(\infty) = B, \tag{3.59}$$

$$\rho_1(0) = 0, \tag{3.60}$$

$$v_{x1}(0) = 0, \tag{3.61}$$

$$v_{y1}(0) = 0, \tag{3.62}$$

$$v_{z1}(\infty) = 0, \tag{3.63}$$

where A and B are the limiting values of the radial and toroidal field far above

the disc mid-plane. In the context of this model, A and B are free parameters. Physically, A and B need to be determined by solving for the global magnetic field in the force-free region far above and below the disc and solving for the disc's internal structure in a self-consistent manner. If the length-scale of the warp is much smaller than the lengthscale of the disc, it may be possible to determine these coefficients. We discuss this in the following chapter.

3.3.3 The Magnetic Field and Physical Relevance

Having reduced the MHD equations to a set of linear one-dimensional equations, it is informative to step back and consider the structure of the magnetic field described by this model. Due to the time dependence we have assigned to the magnetic field, the field must be anchored within the disc. Were the magnetic field not anchored within the disc, the differential rotation would inevitably lead to far more complex magnetic field configurations. Beyond being anchored in the disc, we have chosen to model the equilibrium magnetic field as purely poloidal. This assumption is made for mathematical simplicity and also to eliminate the transport of angular momentum by either an outflow or an exchange of magnetic torques. The extent to which the magnetic field bends is a free parameter of the model. A similar magnetic field structure can be found in Guilet & Ogilvie (2012)

If the dimensionless magnetic field strength $B_{z'} \lesssim 1$ we are no longer justified in neglecting the MRI. While a more detailed discussion of the MRI is given in section 3.4.4, we briefly mention that due to the neglect of the MRI, this model is of greatest relevance at plasma betas of order unity where the MRI is suppressed. Magnetic fields of this strength are often invoked to explain observed jet emissions (for examples see Moll (2012), Ogilvie (2012), Cao & Spruit (2013), and Campbell (2010)).

Recent studies of protostellar disc formation from molecular cloud core collapse by Lewis, Bate, & Price (2015), Lewis & Bate (2017) indicate that

protostellar discs may form with plasma betas of order unity. In addition, the continued study of magnetically arrested discs (Narayan, Igumenshchev, & Abramowicz, 2003) around black holes further motivates the study of strongly magnetised warped disc dynamics. It is in this strong regime that the results of this thesis are most applicable.

3.4 The Special Case of the Purely Vertical Magnetic Field

3.4.1 Solution via a Spectral Method

The simplest magnetised warped disc model is one in which the inclination angle $\tan i$ of the magnetic field at the disc boundary is zero, implying the magnetic field above and below the disc is perpendicular to the disc surface. This corresponds to setting boundary conditions (3.49), (3.58) and (3.59) to zero. This model is relatively easy to analyse, yet demonstrates many of the qualitative differences between purely hydrodynamic and magnetised warped discs.

Under these conditions, the unwarped density profile is given by

$$\rho_0(z') = \frac{1}{\sqrt{2\pi}} e^{-z'^2/2} \tag{3.64}$$

and the first-order equations reduce to

$$\frac{d^2 v_{x1}}{dz'^2} = -\frac{\rho_0}{B_{z'}^2}(v_{x1} - 2v_{y1} - z'), \tag{3.65}$$

$$\frac{d^2 v_{y1}}{dz'^2} = \frac{\rho_0}{B_{z'}^2}(2v_{x1} - (1+2q)v_{y1} - qz'). \tag{3.66}$$

The coupled pair of differential equations (3.65) and (3.66) were solved via a spectral method as outlined below.

Using the set of basis functions $\{y_n(z') = P_{2n-1}(\tanh z')\}$, the first twelve eigenvalues and eigenfunctions of the following Sturm-Liouville problem were

found via a combined Rayleigh-Ritz and Gram-Schmidt procedure:

$$\frac{d^2u}{dz'^2} + \mu\rho_0 u = 0, \tag{3.67}$$

where we impose the boundary conditions $u(0) = 0$ and $\frac{dv}{dz'} = 0$ at large z'. Let this eigenfunction basis be $\{u_i\}$, with associated eigenvalues $\mu_i = \{3.363, 22.30, 57.12, 107.8, \dots\}$. The eigenfunctions u_i are plotted in Figure 3.2 (see also Latter, Fromang, & Gressel (2010)).

Equations (3.41) and (3.42) together with a vanishingly small magnetic field perturbation at large z' imply that velocity perturbations v_{x1} and v_{y1} must have a vanishingly small derivative at the upper boundary. Through symmetry arguments one can deduce that v_{x1} and v_{y1} are odd in z' and so vanish at $z' = 0$. Therefore, v_{x1} and v_{y1} satisfy the same boundary conditions as the eigenfunctions u_i. Let us project the velocity perturbations v_{x1}, v_{y1} and the function $f(z') = z'$ onto this basis in the following way:

$$v_{x1}(z') = \sum_i a_i u_i(z'), \tag{3.68}$$

$$v_{y1}(z') = \sum_i b_i u_i(z'), \tag{3.69}$$

$$z' = \sum_i c_i u_i(z'). \tag{3.70}$$

Projecting the function z' onto the eigenfunction basis $\{u_i\}$ requires some consideration, as this function does not satisfy the appropriate boundary conditions far from the midplane. However, beyond a few scale heights the density becomes vanishingly small and the error in approximating z' via the set of eigenfunctions $\{u_i\}$ is negligible.

If we let $\lambda_i = \mu_i B_{z'}^2$, the MHD equations (3.65)–(3.66) give

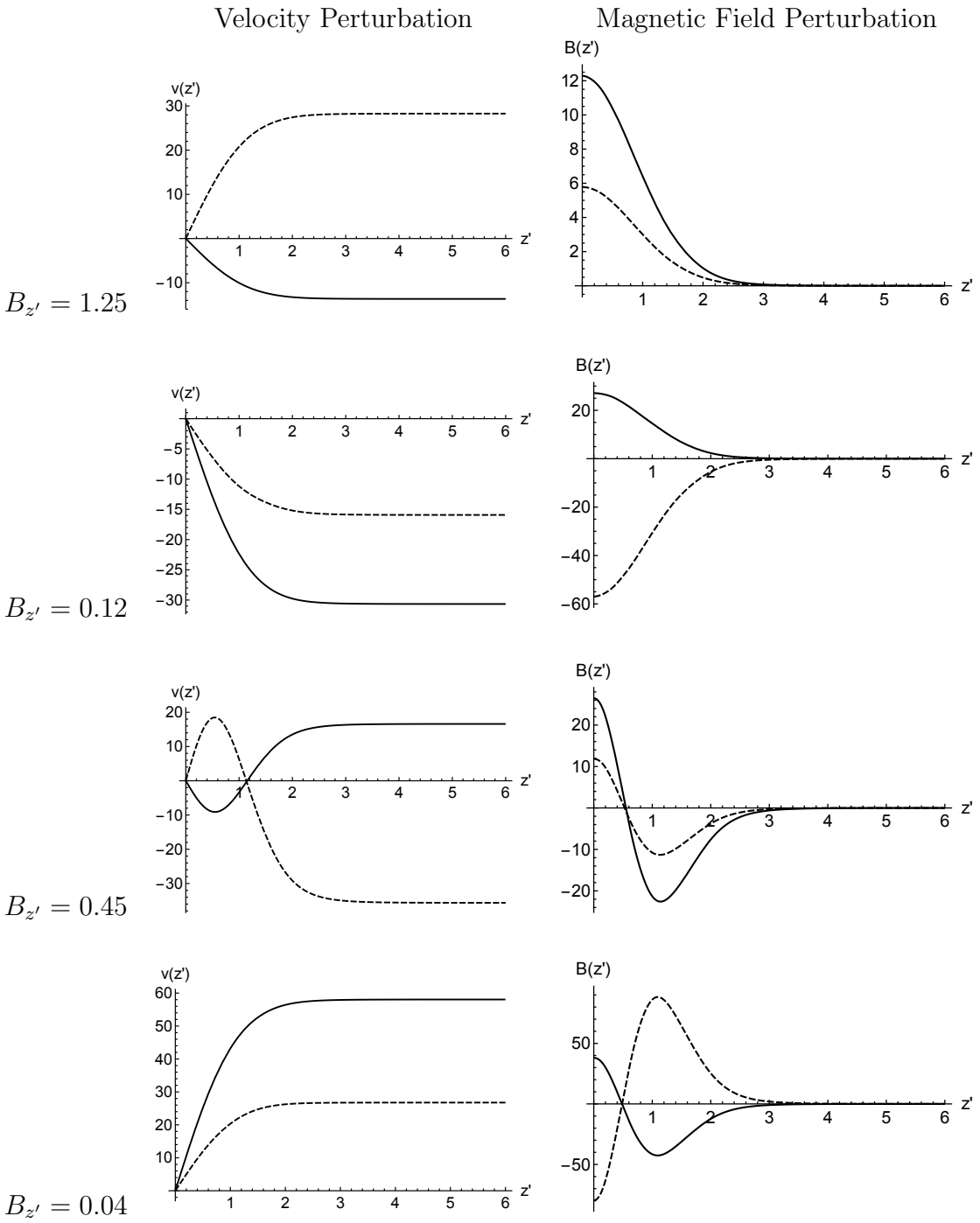

Tab. 3.1: The vertical structure of the first two Alfvénic-epicyclic fast and slow modes. The radial and toroidal velocity perturbations v_{x1} and v_{y1} are represented in the left hand column by the solid and dashed lines respectively. The magnetic field perturbations B_{x1} and B_{y1} are represented in the right hand column by the solid and dashed lines respectively. In all cases $q = 1.6$ and the magnetic field is varied to be close to the resonant points of the first two Alfvénic-epicyclic fast and slow modes. Referencing from the top row down, the resonances shown correspond to the first slow mode, the first fast mode, the second slow mode, and the second fast mode. The associated magnetic field strengths are shown on the left of each row.

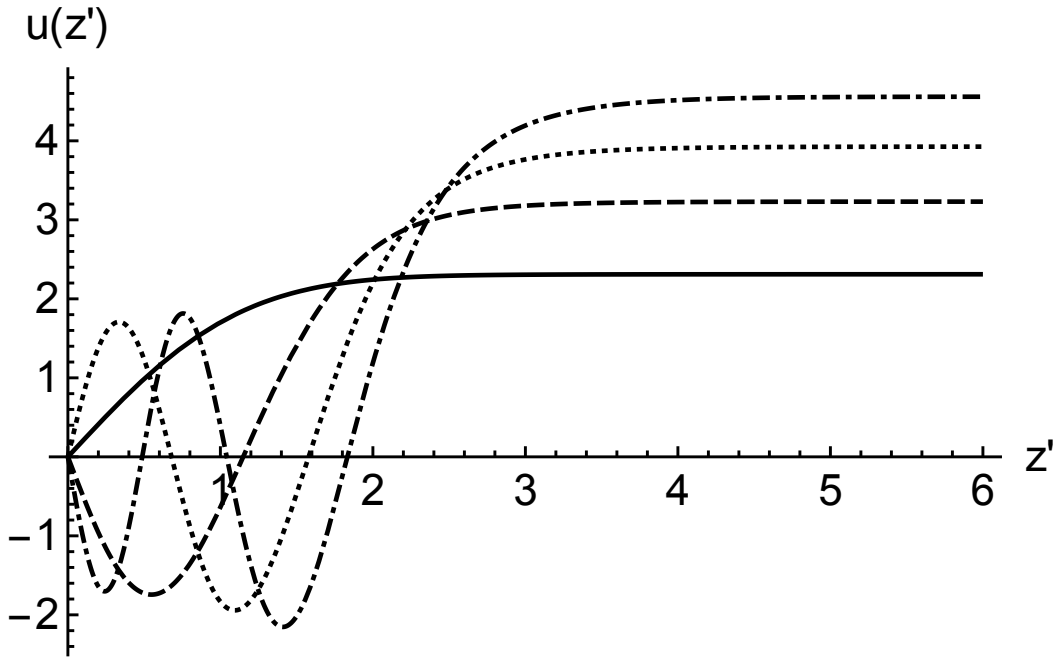

Fig. 3.2: The first four eigenfunctions of equation (3.67), u_1,u_2,u_3,u_4. The velocities of the Alfvénic-epicyclic modes are proportional to these eigenfunctions.

$$a_i = -\frac{\lambda_i - 1}{\lambda_i^2 - 2(1+q)\lambda_i + (2q-3)} c_i, \tag{3.71}$$

$$b_i = \frac{\lambda_i q + 2 - q}{\lambda_i^2 - 2(1+q)\lambda_i + (2q-3)} c_i, \tag{3.72}$$

where

$$c_i = \int_0^\infty z' \rho_0(z') u_i(z') dz'. \tag{3.73}$$

The critical aspect of this set of equations is the dependence of the denominator on the magnetic field strength and the shear rate q associated with the disc. Resonances will occur whenever either of the following conditions holds for any eigenvalue μ:

$$B_{z'}^2 \mu = 1 + q + \sqrt{4 + q^2}, \tag{3.74}$$

$$B_{z'}^2\mu = 1 + q - \sqrt{4 + q^2}. \tag{3.75}$$

These resonances result in arbitrarily large velocities, magnetic fields and internal torques acting within the disc. More generally equations (3.71)–(3.73) imply the existence of a set of modes, henceforth called Alfvénic-epicyclic modes, in this magnetised warped disc. They are the result of a coupling between the magnetic field and the epicyclic modes. Each of these modes is associated with its own distinct vertical structure and a natural frequency given by

$$\omega_{i(fast)}^2 = \lambda_i + 2 - q + \sqrt{4\lambda_i + (2-q)^2} \tag{3.76}$$

and

$$\omega_{i(slow)}^2 = \lambda_i + 2 - q - \sqrt{4\lambda_i + (2-q)^2}. \tag{3.77}$$

Whenever there is a coincidence between the natural frequency of a particular Alfvénic-epicyclic mode and the orbital frequency ($\omega = 1$ in scaled units), a resonance will occur and that mode will dominate the solution.

The Alfvénic-epicyclic mode velocities are proportional to their respective eigenfunction u_i, while the magnetic field strengths associated with each mode are proportional to the derivatives of the respective eigenfunction $\frac{du_i}{dz'}$. The radial and azimuthal velocities for the first and second Alfvénic-epicyclic modes are shown in Table 3.1. The absolute magnitude of these velocities becomes arbitrarily high as a resonance is approached, leading to a breakdown of the linear formalism outlined here. An investigation into the fully non-linear theory would be required to explore the behaviour near resonance.

In the Keplerian case (q=3/2), which is the case of greatest physical interest, equations (3.74)–(3.75) reduce to:

$$B_{z'}^2\mu_i = 5, \tag{3.78}$$

$$B_{z'}^2 \mu_i = 0, \tag{3.79}$$

implying that the fast modes are all resonant iff $B_{z'} = 0$. This corresponds to the hydrodynamic resonance familiar from earlier work. On the other hand, if the strength of the magnetic field is non-zero this resonance will be lifted and, provided the orbital frequency does not coincide with the natural frequency of a slow Alfvénic-epicyclic mode, well-behaved solutions are obtained. The magnetic field strengths associated with these resonances of the slow modes are at $B_{z'} = \{1.22, 0.473, 0.296, 0.215, \dots\}$, the resonances becoming more and more closely spaced as the magnetic field strength approaches zero.

3.4.2 The Internal Torque

The internal structure of a magnetised disc with an external magnetic field oriented normal to the disc surface was found in the previous section. The torque acting on the disc can now be calculated. As found in Ogilvie & Latter (2013a) , the torque acting within the disc may be written in the following way:

$$\mathbf{G} = -2\pi\Sigma c_s^2 r^2 \left(Q_1 \mathbf{l} + Q_2 r \frac{\partial \mathbf{l}}{\partial r} + Q_3 r \mathbf{l} \wedge \frac{\partial \mathbf{l}}{\partial r} \right), \tag{3.80}$$

where Q_1,Q_2, and Q_3 are dimensionless coefficients given by

$$-Q_1 \Sigma c_s^2 = \left\langle \int (\rho v_x v_y - T_{xy}) dz' \right\rangle_{t'}, \tag{3.81}$$

$$-Q_4 \psi \Sigma c_s^2 = \left\langle e^{it'} \int [\rho v_x (-\Omega z' - i v_z) + i T_{xz}] dz' \right\rangle_{t'}, \tag{3.82}$$

where $Q_4 = Q_2 + iQ_3$. The angular brackets denote that the quantities inside the brackets are time-averaged. Q_1 is similar to the usual accretion disc torque, while Q_2 corresponds to diffusion of the warp and Q_3 causes a dispersive wave-like propagation of the warp.

Torque coefficients Q_1 and Q_2 are related to dissipation. This model does

not include viscosity or resistivity, implying both of these coefficients will vanish and only Q_3 need be considered. We note that this can be also be proven by considering the symmetry properties of the system as discussed in section 3.1.2.

Equation (3.82) suggests that a radial magnetic stress T_{xz} will contribute to Q_3; for a vertical equilibrium field configuration however, this radial stress is exactly balanced by a magnetic stress difference above and below the disc surface. The contribution to the torque from magnetic stresses therefore vanishes to first order and only the radial flux of angular momentum need be considered, implying that

$$Q_3 = \frac{1}{2\pi}\int_0^{2\pi}\int \rho_0 v_{x1} z' \sin^2 t' dz' dt' + O(\psi^2). \tag{3.83}$$

Projecting v_{x1} and z' onto the eigenfunction basis $\{u_i\}$ described above in (3.67) and using the orthogonality relationships of the eigenfunction basis, equation (3.83) simplifies to

$$Q_3 = \sum_i \frac{(1-\lambda_i)}{\lambda_i^2 - 2(1+q)\lambda_i + (2q-3)} c_i^2, \tag{3.84}$$

where $\lambda_i = \mu_i B_{z'}^2$. In the hydrodynamic limit, recalling that normalization of density implies $\sum c_i^2 = 1/2$, we find

$$Q_3 = \frac{1}{2(2q-3)} + O(\psi^2, B^2), \tag{3.85}$$

which is consistent with the result found by Ogilvie & Latter (2013a) for a hydrodynamic warped disc.

The internal torque coefficient Q_3, as can be seen by the denominator of equation (3.84), also diverges near an Alfvénic-epicyclic resonance. The dependence of Q_3 on the magnetic field strength $B_{z'}$ and shear rate q is shown in Figures 3.3, 3.4 and 3.5. The Alfvénic-epicyclic resonances as functions of q and $B_{z'}$ are shown in figure 3.6 for comparison.

It is worthy of note that in the strong-field limit $B_{z'}^2 \gg 1$, $Q_3 \approx \frac{-c_1^2}{\mu_1 B_{z'}^2}$. At very large magnetic field strengths the increasing stiffness imbued by the magnetic flux dampens the disc response. Consequently the induced internal flows lower in amplitude and warp propagation slows as the magnetic field strength is increased.

The weak field limit is far more subtle. Since the model presented in this paper is concerned with mean-field effects, it is reasonable to expect that at weaker field strengths the hydrodynamic limit for Q_3 is recovered. It can be seen in Figure 3.3(a) that this holds true at all points except those very near to an Alfvénic-epicyclic resonance. At these resonances the warp structure and propagation properties may be quite sensitive to the magnetic field strength and even a relatively weak magnetic field may have significant consequences for the warp evolution. This has special physical relevance in light of the fact that a hydrodynamic Keplerian disc is precisely at one such resonance (or alternatively, the resonance of a Keplerian hydrodynamic disc could be considered as the pile-up of fast Alfvénic-epicyclic modes as the magnetic strength falls to zero as shown in Figure 3.5). We explore this concept in greater detail in chapter 5. Warp propagation in a Keplerian low-viscosity disc may therefore be quite sensitive to the introduction of even a weak magnetic field. In the Keplerian weak-field limit $B_{z'}^2 \ll 1$, the case of most physical interest, we note that $Q_3 \approx \frac{-c_1^2}{5\mu_1 B_{z'}^2}$.

In a more realistic model one might expect the mean-field effects described above to compete with viscous effects including those that might arise from MRI turbulence. In some circumstances, these non-ideal effects may eliminate any distinction between the MHD model presented here and the corresponding hydrodynamic model. Further investigation is required to determine what factors influence warp propagation in a weakly magnetised disc.

Although viscosity has not been included in any of the derivations thus far,

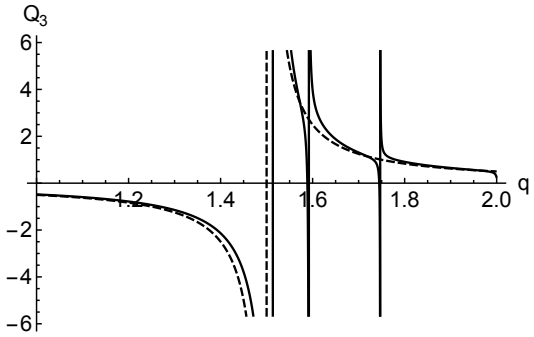

(a) $B_{z'} = 0.04$. The discontinuities at $q > 1.5$ correspond to resonances of fast Alfvénic-epicyclic modes.

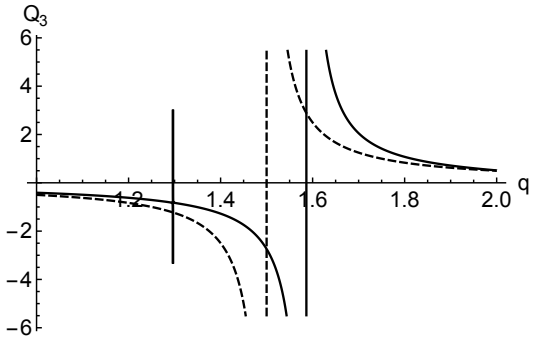

(b) $B_{z'} = 0.1$. The central discontinuity originally at $q = 1.5$ has been displaced rightward, lifting the hydrodynamic resonance at q=1.5.

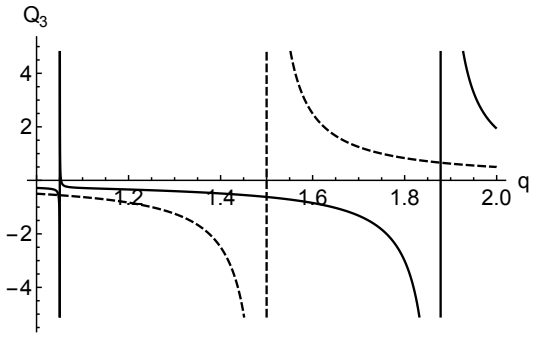

(c) $B_{z'} = 0.2$. The central discontinuity has moved well past $q = 1.5$. Near $q = 1.0$ there is a discontinuity associated with a slow Alfvénic-epicyclic mode.

Fig. 3.3: The internal torque coefficient Q_3 as a function of q at various values of magnetic field strength $B_{z'}$. The dotted line shows Q_3 for a hydrodynamic disc.

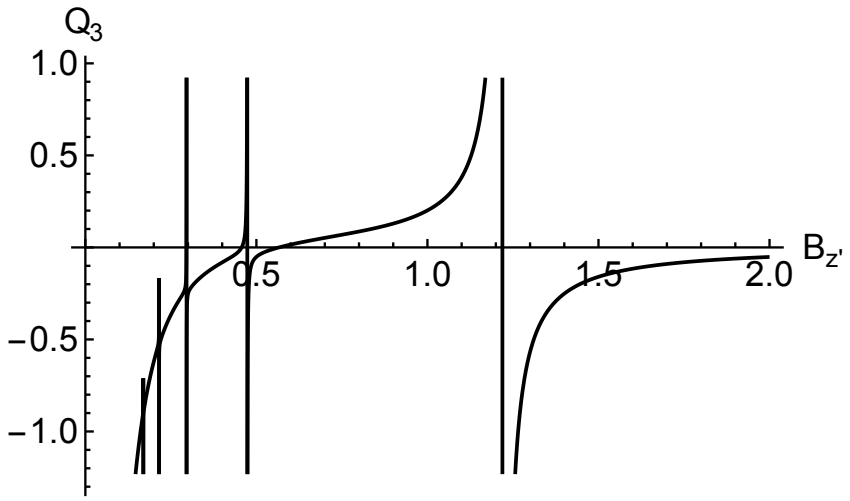

Fig. 3.4: The internal torque coefficient Q_3 as a function of magnetic field strength $B_{z'}$ in scaled units for a Keplerian disc. The most significant resonance occurs at $B_{z'} = 1.22$, corresponding the ground state Alfvénic-epicyclic mode.

let us consider the effect of a magnetic field on the internal torque coefficient Q_2. It was found in Ogilvie & Latter (2013a) that the torque coefficient Q_2 in a Keplerian disc grows inversely with viscosity as the hydrodynamic resonance is approached. It is expected, subject to further analysis, that the presence of a magnetic field will lift the resonance of a Keplerian hydrodynamic disc and therefore remove the divergence in torque coefficient Q_2, reducing the anomalously quick diffusion of the warp in this case.

We would like to emphasise for completeness that it is only for the vertical equilibrium field configuration that there is no explicit magnetic contribution to the torque. Warp propagation in discs with a 'bending' field ($B_{x0} \neq 0$) differs from the vertical field case in several respects. Notably, the magnetic field can potentially play a greater role in the transport of angular momentum through the disc; warp propagation in more general magnetic field configurations will be considered in the following chapters.

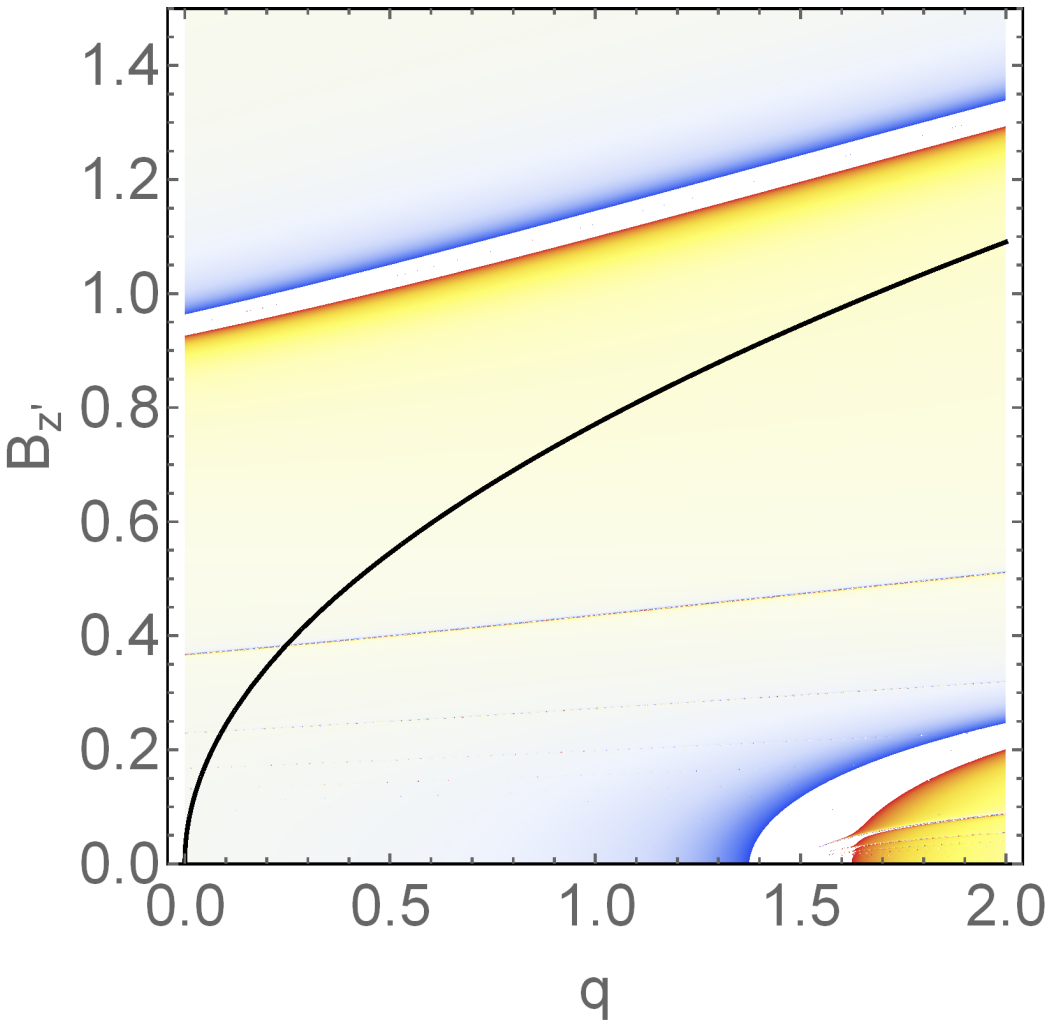

Fig. 3.5: Torque coefficient Q_3 as a function of shear rate q and magnetic field strength $B_{z'}$. White regions indicate large torques that fall beyond the plot range. Due to poor resolution, many of the higher order resonances are not clearly visible. Large values of Q_3 can be observed near the first slow mode resonance where $B_{z'} \approx 1$ and near the first fast mode resonance. The fast mode resonance is responsible for the anomalous behaviour of Keplerian hydrodynamic warped discs. The MRI stability curve is shown in black.

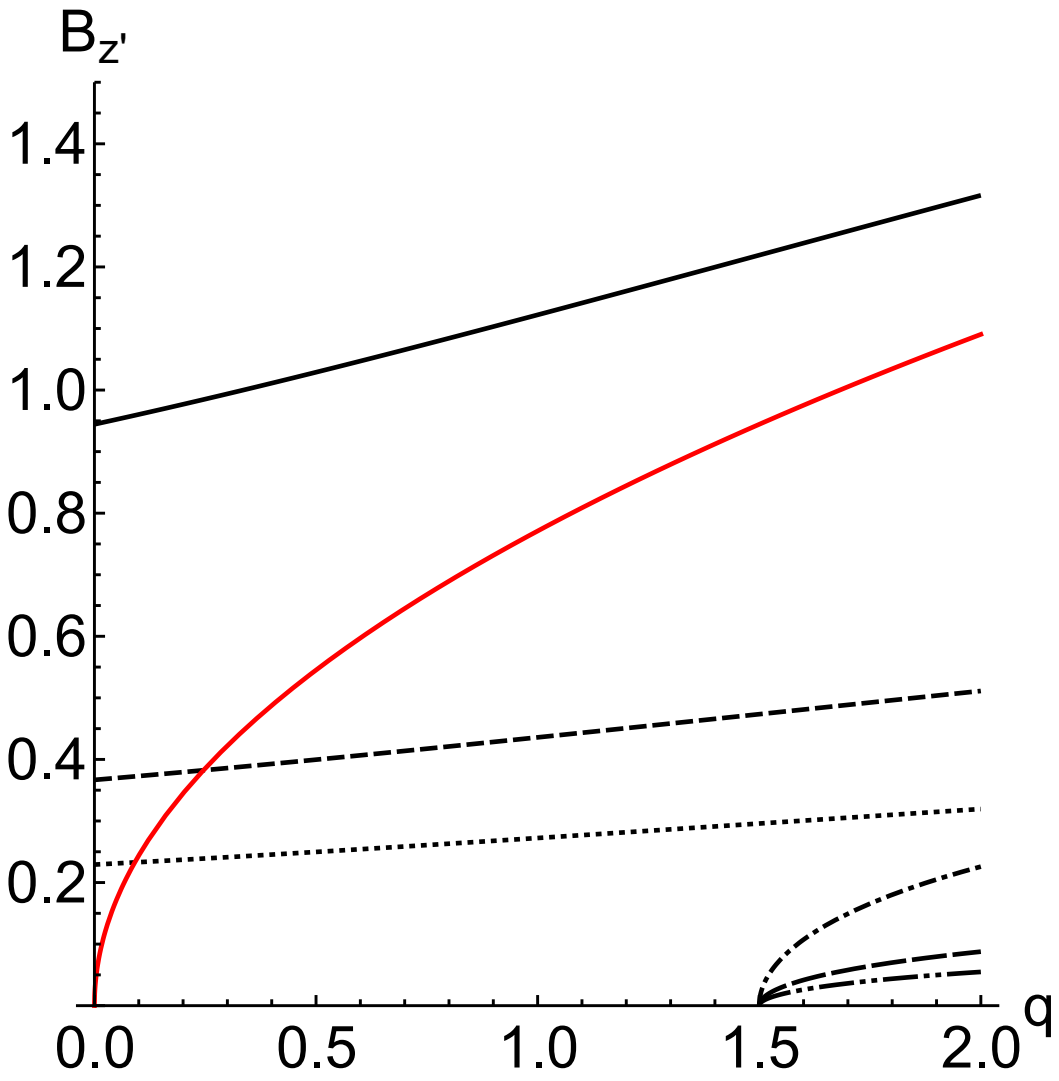

Fig. 3.6: The Alfvénic-epicyclic resonances in the q-$B_{z'}$ plane. The first three slow resonances are the top three nearly straight lines in this figure. The bottom three curves, with a common meeting point at $q = 3/2$ for the hydrodynamic case, are the first three fast Alfvénic-epicyclic resonances. The MRI stability curve is shown in red.

3.4.3 Interpretation of a Divergent Q_3 Coefficient

We have seen that at the Alfvénic-epicyclic resonances the magnitude of the internal flows, and hence the internal torque, are divergent. One may wonder if these results are physical, and if not, how should they be interpreted.

This peculiarity is not new; indeed it was present in the hydrodynamic study of Ogilvie & Latter (2013a) and an interpretation was offered in sections 1.4.2 and 1.7.1 of chapter 1. The magnetised case is only unique insofar as the single resonance between the vertical oscillation mode and the epicyclic mode at $q = 3/2$ is replaced by a series of potential resonances between the vertical oscillation mode and each individual Alfvénic-epicyclic mode. The warped shearing box assumes an implicit separation of scales such that the internal torque is effectively static (see (1.26)). This assumption breaks down in the resonant case, and one must use an alternative approach (see chapter 4).

3.4.4 Effects of the Magnetorotational Instability (MRI)

The MRI in an accretion disc can be expected to exist for a range of magnetic field strengths $B_{min} < B_{z'} < B_{max}$. The upper limit of the MRI-unstable region B_{max} may be found by a standard analysis of the ideal MHD equations as first derived in Balbus & Hawley (1991). It is informative to note the connection between their analysis and the analysis presented here. While investigations of the MRI are primarily focused on the unstable normal modes of a magnetised accretion disc, the chief focus of this work has been the resonant forcing of stable modes. However, when the natural frequency of a stable Alfvénic-epicyclic mode transitions from a real to an imaginary number, that mode becomes unstable corresponding to the onset of the MRI. From equation (3.77) one can deduce that this transition will occur when

$$\mu_1 B_{z'}^2 = 2q, \tag{3.86}$$

where μ_1 is the smallest of the eigenvalues defined by equation (3.67). In the case of a vertical magnetic field and a Keplerian disc, we can conclude that

$$B_{max}^2 = \frac{q}{1.68}. \tag{3.87}$$

Though formulated slightly differently, this corresponds exactly to the result found by Gammie & Balbus (1994) for isothermal discs[1]. Given that the resonance associated with the lowest order eigenfunction of equation (3.67) occurs for a Keplerian disc at $B_{z'} \approx 1.22$ while the MRI is expected below $B_{z'} \approx 0.94$, one can see that a large-scale magnetic field may have a significant effect on disc dynamics even in the MRI stable region. This is an important result because if it was discovered that the resonances discussed in the previous chapters only existed in the MRI unstable region $B_{z'} < B_{max}$, one would be uncertain as to whether these resonances are likely to exist once the effects of the MRI are taken into account.

There are a few shortcomings with the analysis above. Firstly, we found an identical MRI stability condition to that found by Gammie & Balbus (1994). This is unsurprising as the MRI has emerged as an instability in our linear perturbation of an unwarped disc state. Non-linear warped disc solutions may not have the same MRI stability conditions and require a non-linear analysis beyond the scope of this work. Secondly, the value of B_{max} found is only valid for the particular vertical magnetic field configuration considered in this section. We analyse the MRI stability condition for a disc with an equilibrium bending magnetic field ($B_{x0} \neq 0$) in the following chapter.

For small magnetic field strengths, the question is significantly more complicated. The value of B_{min} is related to the non-ideal behaviour of the disc, and therefore is beyond the scope of this analysis. It is unclear at this stage what effects MRI turbulence would have on disc structure or warp propaga-

[1] We are in agreement with the general form for the Alfvén velocity at the midplane, $V_{0z}^2 > 2q\Omega_0^2 H^2/E_1$, as well as the lowest order non-zero eigenvalue $E_1 \approx 1.34$. However, we do not agree on the exact stability condition $V_{0z}^2 > 0.45c_s^2$ that they quote for $q = 3/2$.

tion.

3.4.5 Comparison with Hydrodynamic Warped Discs

It is instructive to consider briefly how the magnetised warped disc considered here relates to the hydrodynamic warped disc discussed in Ogilvie & Latter (2013a).

The distinctive characteristics of a hydrodynamic warped disc are largely due to the unbalanced pressure gradient in the radial equation of motion due to the warped geometry. Internal flows therefore must exist in a warped hydrodynamic disc. More specifically, linear flows were shown to be valid solutions. These flows will be resonantly driven for a Keplerian disc owing to the coincidence of the epicyclic and orbital frequencies. This leads to the rapid diffusion of the warp at small viscosities.

In contrast to a hydrodynamic disc, such simple linear flows are no longer solutions for the internal disc structure of a magnetised warped disc. The presence of the magnetic field adds some stiffness to the fluid, detuning the epicyclic frequency from the orbital frequency and thereby lifting the resonance. In more detail, it was found that there are a number of fast and slow Alfvénic-epicyclic modes present with no analogue in the hydrodynamic disc. These modes may resonate if their natural frequency coincides with the orbital frequency, effectively driving a resonant response.

In an ideal inviscid disc the only non-zero internal torque coefficient is Q_3. The properties of Q_3 may be dramatically different from those of the corresponding hydrodynamic problem, reflecting the far richer structure of the magnetised warped disc. It is also expected that due to the detuning of the epicyclic and orbital frequencies in a warped magnetised disc, the anomalously large values of Q_2 found in the hydrodynamic Keplerian case will be reduced.

At progressively weaker field strengths (see Figure 3.3(a)) the difference between the MHD solution and the corresponding hydrodynamic solution becomes negligible except when the disc is very close to an Alfvénic-epicyclic resonance. Near these resonances the internal structure is very sensitive to small changes in parameters and the magnetohydrodynamic perturbations may have a significant effect on disc structure. This is of some physical relevance as a hydrodynamic Keplerian disc corresponds to one such resonance, and consequently may be sensitive to the introduction of a relatively weak magnetic field. Further investigation is required to probe the weak field limit and the effects of the MRI or a finite viscosity.

3.5 Numerical Solutions

3.5.1 Solution via Numerical ODE Solver

In the previous section we described in detail a semi-analytical solution to the ideal MHD equations of a warped disc without mass outflow in the specific case where, at large distances, the external magnetic field is perpendicular to the disc surface. In this section we outline a numerical method for solving for the internal structure of an accretion disc. There are two motivations for this. Firstly, this provides a check on the semi-analytical results outlined in the previous section. Secondly, it would allow us to solve for the structure of the disc for a more general equilibrium magnetic field configuration and with more general boundary conditions. The method developed is outlined below.

In section 3.2.2, we derived a set of six first-order ordinary differential equations for the six first-order variables; these are given by equations (3.52)–(3.57). The six necessary boundary conditions were also given in equations (3.58)–(3.63). In section 3.3.1 we derived three first-order equations for structure of the unwarped equilibrium disc, along with the three associated boundary conditions.

Owing to symmetry considerations our range of integration may be re-

stricted to $0 < z' < z_h$, where z_h is the effective upper surface of the disc and is some number of scale heights above the midplane. z_h was chosen to be small enough such that the numerical methods described remain feasible, yet large enough to be considered exterior to the disc for all practical purposes. All results were tested at various values of z_h to ensure that its value did not have a significant impact.

The boundary conditions were satisfied via the shooting method. The nine variables were integrated from the midplane to the upper surface of the disc. Four of the nine boundary conditions fix the value of a variable at the midplane, requiring the value of the five remaining variables at the midplane to be guessed. The Newton-Raphson method was employed to refine these five initial value guesses and satisfy the five boundary conditions at the upper surface. All results were found to be insensitive to subsequent iterations of the Newton-Raphson method and all boundary conditions were satisfied to an acceptable degree of error, leading to the conclusion that the Newton-Raphson method had converged on a valid solution.

There are four free parameters in this numerical system. One is $B_{z'}$, a constant which determines the relative strength of the magnetic field in the system. The remaining three are the boundary conditions on the magnetic field which specify the connection between the magnetic field within the disc region and the magnetic field of the disc exterior. The first is $B_{x0}(z_h)$, determining the angle of the equilibrium poloidal field to the disc surface. The remaining two are $B_{x1}(z_h)$ and $B_{y1}(z_h)$, the first-order radial and toroidal magnetic fields external to the disc. These four free parameters must be specified to solve for the internal structure of the disc.

As discussed in section 3.3.2, one of the boundary conditions on this system of equations was the imposition of a rigid lid corresponding to equation (3.63). Based on a far-field analysis of the linear MHD equations, it was found that the results in the high-density region of the disc should be insensitive to

the exact value of the outflow velocity. This was tested by varying the outflow velocity at the upper surface. We confirmed that the rigid lid had little effect on our solutions.

All numerical results found via this method were consistent with the results of the semi-analytical calculation described in section 3.4 to a reasonable degree of accuracy.

3.5.2 The Corrugated Sheet Model

As an alternative to the approach outlined here, one may also consider a standard shearing box model within which all perturbed variables vary sinusoidally with radius at a specified wavenumber k (giving a thin disc the appearance of a corrugated sheet). For very small k this corresponds exactly to the model presented above, where the warping is assumed to be independent of the radius. A numerical setup similar to the Runge-Kutta ODE solver outlined above was used for this corrugated sheet model. This model is informative because it allows us to investigate the dispersion relation $\omega(k)$ of radial bending waves. While the details of this model and its numerical method will be discussed in the following chapters, we quote here the results relevant to this chapter.

The torque coefficient Q_3 can be found from the quadratic dispersion relation of the normal modes of the unwarped magnetised disc. In an unwarped disc there exists a normal mode with frequency $\omega(0) = \Omega$ (where Ω is the orbital frequency) corresponding to vertical oscillations of the disc. For small but non-zero radial wavenumber k, the frequency of this mode is related to Q_3 via

$$\omega(k) = \Omega + Q_3 \frac{c_s^2}{\Omega} k^2. \tag{3.88}$$

It was found that the torque coefficients Q_3 obtained by this numerical method were consistent with the semi-analytical calculations presented in section 3.4

in the non-resonant case, providing a valuable check on our results. We also find that the dispersion relation transitions from quadratic to linear near the critical points in the $(B_{z'}, q)$ plane corresponding to resonance. This transition implies a qualitative change in the disc behaviour associated with enhanced warp propagation at these points. This result, described in more detail in the following chapters, finds a direct hydrodynamic analogy in the dispersionless bending waves of inviscid Keplerian discs.

3.6 Summary and Discussion

Using the warped shearing box framework set out by Ogilvie & Latter (2013a), the local ideal MHD equations were found for warped magnetised thin discs. These equations were expanded to terms linear in the warping parameter ψ. While more general solutions are discussed in later chapters, the case of an external magnetic field oriented normal to the disc surface is relatively simple and can be solved semi-analytically via a spectral method. The results of this analysis were verified by the use of a numerical ODE solver. Many of the distinct characteristics of warped magnetised discs may be illuminated by this rather simple model.

In a hydrodynamic disc it was found that the coincidence of the epicyclic and orbital frequencies causes a resonance in thin Keplerian accretion disc models. This resonance results in fast internal flows and torques acting within the disc, resulting in the rapid propagation of the warp.

In the presence of a magnetic field this resonance is removed. The magnetic tension adds a stiffness to the epicyclic oscillations, detuning the epicyclic frequency from the orbital frequency. Therefore at low viscosities the presence of even a relatively weak magnetic field may dramatically alter the internal structure of a Keplerian or very nearly Keplerian warped disc and evolution of the warp.

In magnetised warped discs there exists a series of normal modes which

we have called Alfvénic-epicyclic modes. These are the normal modes of the magnetised accretion disc, each with a fixed vertical structure and phase relationship between the density, velocity and magnetic field perturbations. For a vanishing magnetic field, the fast Alfvénic-epicyclic modes all oscillate at the orbital frequency while the slow modes are static ($\omega = 0$), thereby recovering the results found by Ogilvie & Latter (2013a). The frequencies of the Alfvénic-epicyclic modes depend on the shear rate q, the magnetic field strength and the inclination of the equilibrium magnetic field.

The warped geometry of the accretion disc creates a pressure gradient in the radial direction that acts as an inhomogeneous forcing term. This system is consequently analogous to a forced oscillator. When the frequency of an Alfvénic-epicyclic mode coincides with the orbital frequency, that particular mode is resonantly forced resulting in large internal torques and rapid warp propagation. Warp propagation in magnetised discs consequently has a surprisingly subtle and rich dependence on the magnetic field strength and shear rate. This mechanism may be critical to understanding and modelling warp propagation in magnetised discs.

In this chapter we have assumed that there is no jet outflow from the disc. The effect of disc warping on jet outflows is not well understood and could be studied using the framework set out in this chapter. The solutions investigated in the latter half of this chapter have neglected the MRI. Consequently, the results of those sections are expected to be of greatest validity in highly magnetised discs ($\beta \approx 1$). The MRI, and especially the interplay between the MRI and the warped magnetised accretion disc dynamics outlined in this chapter, could also be investigated using the formalism developed here.

The resonances between the vertical oscillation mode and an Alfvénic-epicyclic mode result in a divergence of Q_3. This is not a 'true' divergence, but rather an indication that an underlying assumption of the model has failed; namely the time derivative of the internal torque, $\frac{\partial \boldsymbol{G}}{\partial t}$ is non-negligible and the

warp may not be considered static. In the following chapter we present an alternative model, the corrugated disc model, to better investigate the dynamics of a warped disc near resonance.

4. THE CORRUGATED DISC MODEL OF WARP PROPAGATION

4.1 Introduction

In the previous chapter we investigated the internal structure of a magnetised disc using the warped shearing box formalism. It was found that the disc behaved analogously to a forced oscillator, the forcing term originating from the warped geometry. When the vertical oscillation frequency coincided with a horizontal oscillation mode (or an 'Alfvénic-epicyclic' mode) the internal flows and corresponding torque were divergent. Several questions, however, remained unanswered. Our results were often interpreted through the Q_3 coefficient; yet the familiar notion of a warp propagating with a particular wavelength and wave speed is certain to be more tangible to most researchers. How then does the warped shearing box model and the concept of Q_3 translate to the propagation of a warp of a given length-scale? What meaning can be assigned to the divergences of the internal torque in the warped shearing box? Is there any alternative formulation of the problem that avoids the ambiguity in the magnetic boundary condition that we encountered in the previous chapter? In an effort to resolve these issues we present an alternative perspective on warp propagation by solving for the wave modes of a sinusoidal corrugation of the disc, hereby called the 'corrugated disc model'.

We begin in the following section by considering a simple 2D toy model that highlights the non-local aspect of the warped disc dynamics and the connection between the disc interior and disc exterior. We then define the 3-D corrugated disc model and linearise the ideal MHD equations for small warps in section 4.3. An expansion of the MHD equations in the long wavelength limit is dis-

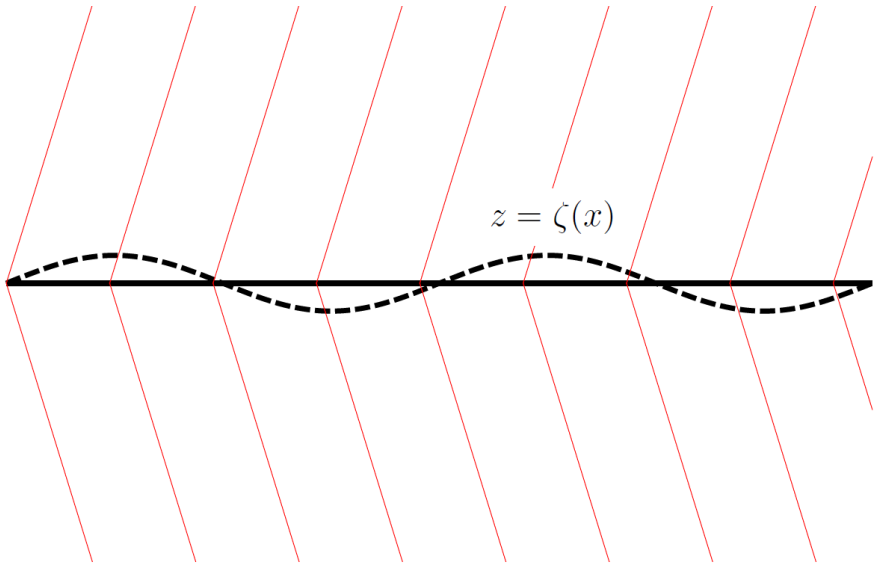

Fig. 4.1: A 2-D cut in the x-z plane of the corrugated sheet. The unperturbed disc (thick black line) lies at $z = 0$ and is threaded by an inclined magnetic field (shown in red). A small corrugation $z = \zeta(x)$ (dashed line) with characteristic wavenumber k is then introduced.

cussed in section 4.4. By considering the asymptotic long-wavelength limit (section 4.5), the corrugated sheet model is shown in section 4.6 to be (within certain caveats) equivalent to the shearing box model discussed in chapter 3. In section 4.7 and 4.8 we provide a description of the dispersion relation for the normal modes of the corrugated disc in general and in the asymptotic limit of long wavelength modes. A numerical scheme for calculating the wave modes in a corrugated disc numerically is then described in section 4.9. Implications of bending field equilibria for the MRI are discussed in section 4.10.

4.2 The Corrugated Sheet Model

We begin by considering a static uniform sheet of infinitesimal thickness such that the sheet initially lies in the $z = 0$ plane. Let there be a bending magnetic field anchored within this disc as shown in Figure 4.1. Note that this is a two dimensional model; effectively $B_y = 0$ and $\nabla \cdot \mathbf{B} = 0$. We wish to investigate

the interplay of the magnetic field and a static corrugation of the sheet, defined such that the z-position of the sheet is given by $\zeta(x)$. At any point on the sheet, the normal to the sheet surface is then

$$\mathbf{n} = \frac{\mathbf{e}_z - \frac{d\zeta}{dx}\mathbf{e}_x}{\sqrt{1 + (\frac{d\zeta}{dx})^2}} \tag{4.1}$$

Just as in chapter 2, we wish to find an appropriate solution via perturbation expansion for the magnetic field in the case of small warps. In this context, what is meant by a 'small' warp? This may be elaborated more fully in the following section, but we define it rather intuitively to mean that the sheet remains very nearly normal to the direction vector $\boldsymbol{e}_z$. Examination of the above implies that that this is satisfied if $d\zeta/dx \ll 1$. This motivates a scaling of the problem

$$\zeta(x) = \epsilon\eta(x) \tag{4.2}$$

where the small dimensionless parameter ϵ may be interpreted as the ratio of the corrugation magnitude ζ and some characteristic wavelength of the corrugation – the only two length-scales present in the problem. Consequently $d\eta/dx$ is of order unity while $\epsilon \ll 1$.

In order to have a well-defined physical problem, we must make some assumptions about the magnetic field. We assume that the magnetic field is anchored within the disc and there is negligible material outflow from the disc. Hence the field is effectively force-free far from the disc surface and the magnetic field in the region external to the disc can by found by solving Laplace's equation with appropriate boundary conditions as discussed in chapter 2. Let the magnetic potential be defined as $\Phi(x, z)$, such that $\mathbf{B} = \nabla\Phi$. Again let us expand $\Phi(x, z)$ in orders of ϵ,

$$\Phi = \Phi_0 + \epsilon\Phi_1 + \cdots \tag{4.3}$$

The simplest such zeroth-order solution may be written as

$$\Phi_0(x,z) = B_{x0}x + B_{z0}z \tag{4.4}$$

where B_{x0} and B_{z0} are the unperturbed radial and vertical magnetic field strengths at the disc surface, and indeed in the entire upper half plane.

4.2.1 Deformation and the Conservation of Flux

Consider a small element of surface as ϵ is increased from zero to some small quantity. Throughout this process, in the absence of any internal flows within the disc, the flux through this surface element of the sheet should remain constant. The normal to the surface is now however

$$\mathbf{n} = \mathbf{e}_z - \epsilon\frac{d\eta}{dx}\mathbf{e}_x. \tag{4.5}$$

(Note that normalisation of this vector is of order $O(\epsilon^2)$ and hence has been omitted). The conservation of flux can hence be expressed as

$$\mathbf{n}\cdot\nabla\Phi = B_{z0} \tag{4.6}$$

in the unperturbed state, which must be equal to

$$\mathbf{n}\cdot\nabla\Phi = (\mathbf{e}_z - \epsilon\frac{d\eta}{dx}\mathbf{e}_x)\cdot\nabla\Phi|_{z=\epsilon\eta}. \tag{4.7}$$

The warping of the sheet has two distinct consequences for the equation above. Firstly, we must expand the magnetic potential appropriately in powers of ϵ. Secondly we note that the condition of flux conservation is now evaluated not at $z = 0$ but at $z = \epsilon\eta$, the disc surface. Using the expansion of Φ, we have

$$\mathbf{n}\cdot\nabla\Phi = (\mathbf{e}_z - \epsilon\frac{d\eta}{dx}\mathbf{e}_x)\cdot(\nabla\Phi_0 + \epsilon\nabla\Phi_1 + ...)|_{z=\epsilon\eta} \tag{4.8}$$

or

$$\mathbf{n}.\nabla\Phi = B_{z0} + \epsilon\left(-\frac{d\eta}{dx}B_{x0} + B_{z1}(x,\epsilon\eta)\right) + O(\epsilon^2) \tag{4.9}$$

from which, we conclude that

$$\frac{d\eta}{dx}B_{x0} = B_{z1}(x,\epsilon\eta) \tag{4.10}$$

to order ϵ.

In principle we are now equipped to solve for the magnetic potential Φ_1 given a general function $\eta(x)$. We have identified, to first order, what the normal derivative of the magnetic potential is on the boundary of the corrugated sheet and thus have sufficient boundary conditions to solve Laplace's equation in this region. However, such a problem may be quite difficult in general as this boundary condition must be evaluated at the sheet surface, an arbitrary function of x.

4.2.2 Solution to Laplace's Equation for Sinusoidal Corrugation

We now assume a simple corrugation of the sheet of the form

$$\zeta(x) = \zeta_0 e^{ikx} \tag{4.11}$$

Under such a prescription we set $\epsilon = k\zeta_0$ and assume $\epsilon \ll 1$, reflecting the smallness of the warp. If we assume this functional dependence for all perturbed variables, Laplace's equation gives

$$-k^2\Phi_1 + \frac{d^2}{dz^2}\Phi_1 = 0. \tag{4.12}$$

Let us first consider the region above the disc surface. The only physically plausible solution, decaying appropriately as z tends to infinity, is

$$\Phi_{1+}(x,z) = A_+ e^{ikx}e^{-|k|z}. \tag{4.13}$$

This problem would be simplified considerably if we were ably to apply a boundary condition at the $z = 0$ plane rather than the sheet surface defined by $z = \zeta(x)$. An alternative method is to consider what set of boundary conditions on the $z = 0$ plane surface would result in those same boundary conditions being satisfied at the actual sheet surface. As the difference between $B_{z1}(x, \epsilon\eta)$ and $B_{z1}(x, 0)$ is, by inspection of (4.13), of order ϵ we may substitute $B_{z1}(x, 0)$ into (4.10) without loss of accuracy to first order in ϵ.

If we constructed a solution Φ_{trial} such that Φ_{trial} satisfied Laplace's equation above the surface $z = 0$ and with flux $B_{z1}(x, 0) = B_{x0}$ at the $z = 0$ surface, boundary condition (4.10) of the true magnetic potential solution will be satisfied to first order in ϵ. Therefore a solution for the magnetic potential external to the disc surface may be found by solving Laplace's equation under the condition that $B_{z1}(x, 0) = \frac{d\eta}{dx} B_{x0}$.

The boundary condition $B_{z1}(x, 0) = \frac{d\eta}{dx} B_{x0}$ can now be satisfied by letting

$$A_+ = -\frac{1}{|k|} B_{x0}. \tag{4.14}$$

An equivalent derivation in the region below the disc surface implies

$$\Phi_{1-}(x, z) = A_- e^{ikx} e^{|k|z} \tag{4.15}$$

where in fact $A_- = A_+$. Therefore the magnetic field perturbations decay vertically on a length scale of $1/k$ where k is the wavenumber of the radial perturbation. Note that B_{z1} and B_{x0} are odd functions of z while B_{z0} and B_{x1} are even functions of z; this is consistent with the symmetry properties found in the related warped shearing box model. The magnetic field perturbation $\boldsymbol{B}$ is shown in Figure 4.2. Further, we note that

$$B_{z1} = i \frac{k}{|k|} B_{x1} \tag{4.16}$$

at the upper disc surface and

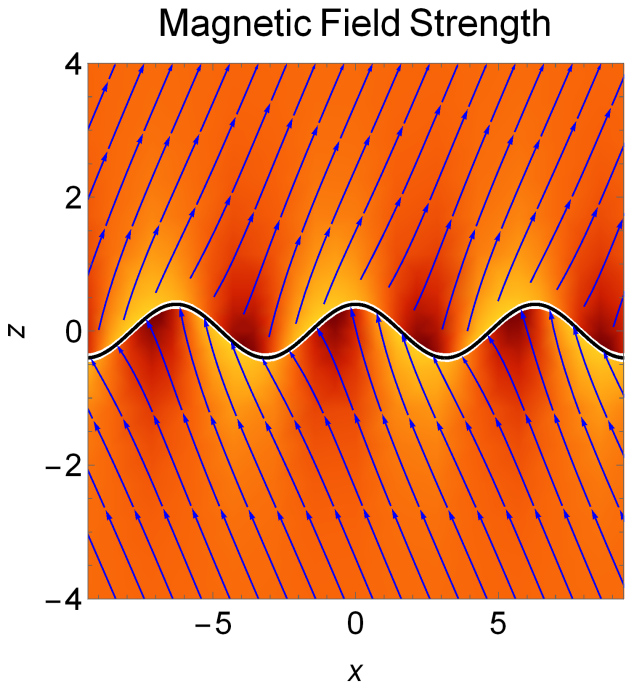

Fig. 4.2: An exaggerated representation of the magnetic field in the vicinity of a corrugated sheet. The field lines are shown in blue, while the background shading indicates the magnitude of the magnetic field - a lighter shading indicates a stronger field at that region, while a darker shading indicates a weaker field. Note that the magnetic perturbations decay vertically on the length-scale of the corrugation. Far from the sheet surface the field is approximately undisturbed from its equilibrium state.

$$B_{z1} = -i\frac{k}{|k|}B_{x1} \tag{4.17}$$

at the lower disc surface. These relations will serve to provide boundary conditions for the later work of this chapter.

4.2.3 Oscillation Modes of the Corrugated Sheet

We now consider the vertical forces acting upon the corrugated sheet and its associated response. Let us consider a small vertical column of the sheet. The vertical force due to the Maxwell stress acting on the sheet may be written as

$$F_z = \int (\mathbf{T} \cdot d\mathbf{S})_z. \tag{4.18}$$

This consists of a magnetic stress and pressure acting on the upper and lower surfaces of the disc as well as a non-negligible shear stress acting on the radial boundaries. The force per unit area

$$F_z = \frac{1}{2\mu_0}[B_z^2 - B_x^2]_-^+ - \int \partial_x (B_x B_z) dz \tag{4.19}$$

can, with proper attention paid to the integration across the thin sheet and the boundary conditions of the magnetic field, be shown to simply be

$$F_z = -\frac{\epsilon}{\mu_0}[B_{x0} B_{x1}]_-^+ = -\frac{2\epsilon B_{x0} B_{x1+}}{\mu_0}. \tag{4.20}$$

All the work we have performed thus far has been performed in an infinite two-dimensional static sheet. Yet a similar analysis may be performed in a local co-rotating Cartesian frame in an infinitely thin disc subject to a radial corrugation without much difficulty; in this case there is simply an additional restoring force due to the gravity of the central object. If the vertical position of the disc is given by $\zeta(x,t) = \zeta_0(t) e^{ikx}$, then $\epsilon = k\zeta_0$ and we find

$$\Sigma \partial_t^2 \zeta_0 = -\Sigma \Omega^2 \zeta_0 - \frac{2|k| B_{x0}^2 \zeta_0}{\mu_0} \tag{4.21}$$

which implies the following dispersion relation

$$\omega^2 = \Omega^2 + \frac{2|k| B_{x0}^2}{\Sigma \mu_0}. \tag{4.22}$$

In the limit of long wavelength warps, we find that

$$\frac{\omega(k)}{\Omega} = 1 + \frac{B_{x0}^2}{\Omega^2 \Sigma \mu_0} |k| + O(k^2) \tag{4.23}$$

4.2.4 Discussion

The dispersion relation (4.23) for the vertical oscillation modes of the infinitely corrugated sheet is linear in $|k|$ and the group velocity $d\omega/dk$ is only

non-zero as $k \to 0$ if the field is a 'bending' field ($B_{x0} = 0$). This result indicates the warp is being propagated non-locally by magnetic stresses, in some sense communicating angular momentum across magnetic field lines. Both the physical interpretation and the mathematical form of the dispersion curve have an analogy in self-gravitating discs, where the non-local gravitational interaction between non-neighbouring rings results in a linear contribution to the dispersion curve of the form $|k|$. This result had been previously found via a similar analysis by Terquem & Papaloizou (2000) and Agapitou, Papaloizou, & Terquem (1997).

It is worth noting the implicit assumptions in the working above. In order to treat the disc as a razor-thin sheet, the characteristic length scale of the vertical decay in magnetic field strength (and equivalently the radial warping length scale) must be large compared to the disc thickness. In addition the radial length scale R of the disc itself must be much longer than the wavelength of the corrugation. Hence there is an separation of scales given by

$$H \ll \frac{1}{k} \ll R. \tag{4.24}$$

The equilibrium magnetic potential Φ_0 may be considered to represent a local approximation to a more general magnetic potential determined by some radial distribution of flux within a real disc; if so, the approach outlined above remains valid if the radial length-scale of the equilibrium flux distribution is far longer than the length-scale of the corrugation. This distinguishes the corrugated sheet (and corrugated disc models) from the work of the previous two chapters. In chapters 2 and 3, the assumption of self-similarity did not allow for a separation between the warp and the flux distribution length-scales. The only way in which the magnetic boundary conditions could be determined is via the solution of the global external field, either explicitly as demonstrated in chapter 1 or parametrised as unknowns in equations (3.58)–(3.59) of chapter 2. In contrast, the assumption that the corrugation wavelength is small relative to the equilibrium field structure allows us to, through purely local considerations, specify the magnetic perturbation.

This simple toy model serves two purposes. Firstly, it gives a clear idea of the magnetic field behaviour far from the disc surface. Secondly, it provide some insight as to how the magnetic stresses above and below the disc, caused by the disc deformation, modify the vertical oscillation frequency and hence warp propagation. However, we must remain sceptical of the reliability of this model; just like the early hydrodynamic warp theorists, we ignore the internal flows of the disc at our own peril. In the following section we expand upon the simple model presented here and consider in a more rigorous manner the internal structure of a warped disc. More specifically, we aim to verify the transport of angular momentum by a bending field as well as consider the effect of internal flows on warp propagation. This could be cast as a relaxation of the condition $H \ll 1/k$ as we probe the connection between the two regimes.

4.3 Ideal Magnetohydrodynamics in a Corrugated Disc

4.3.1 The Physical Equations in the Shearing Box

We now turn our attention to a warped disc of finite thickness. Let us construct a standard Cartesian coordinate system centred around a test particle in a reference orbit at radius r and angular velocity Ω about the central object (Figure 4.3). The magnetohydrodynamic equation of motion is

$$\rho\left(\frac{D\mathbf{u}}{Dt} + 2\Omega\mathbf{e}_z \wedge \mathbf{u}\right) = -\rho\nabla\Phi - \nabla p + \mathbf{J} \wedge \mathbf{B} \tag{4.25}$$

where the Lorentz force in ideal MHD is given by

$$\mathbf{J} \wedge \mathbf{B} = \frac{1}{\mu_0}(\mathbf{B}\cdot\nabla)\mathbf{B} - \frac{1}{2\mu_0}\nabla\mathbf{B}^2. \tag{4.26}$$

The effective potential due to gravitational effects and the rotating frame is:

$$\Phi = \frac{1}{2}\Omega^2(z^2 - 2qx^2). \tag{4.27}$$

The continuity equation may be given by

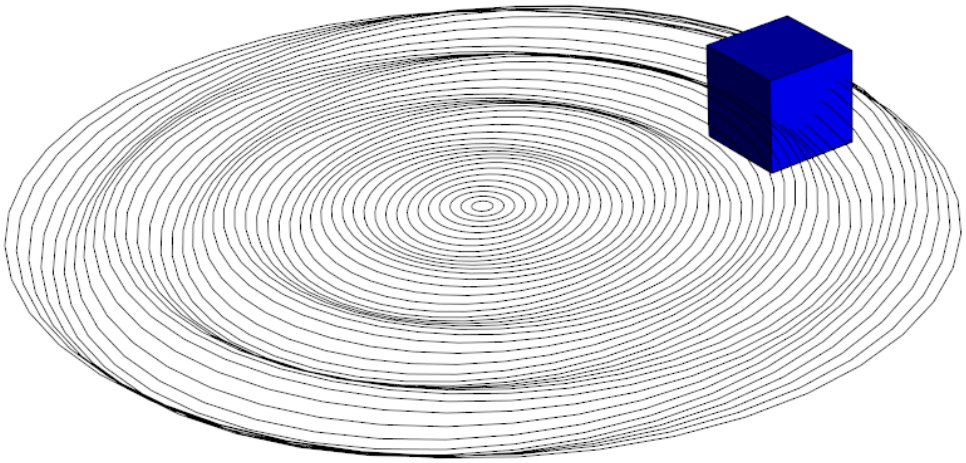

Fig. 4.3: An untwisted warped disc, viewed as a collection of tilted rings subjected to a sinusoidal corrugation. A co-rotating local Cartesian model may be constructed at some reference orbit as represented by the blue box.

$$\frac{\partial \rho}{\partial t} + \nabla \cdot (\rho \mathbf{u}) = 0 \tag{4.28}$$

while the induction equation implies

$$\frac{\partial \mathbf{B}}{\partial t} = \nabla \wedge (\mathbf{u} \wedge \mathbf{B}) = \mathbf{B} \cdot \nabla \mathbf{u} - \mathbf{u} \cdot \nabla \mathbf{B} - \mathbf{B}(\nabla \cdot \mathbf{u}), \tag{4.29}$$

completing the system of ideal magnetohydrodynamic equations.

In order to understand in the simplest possible scenario the effect of a large scale magnetic field on the disc structure and in direct analogy to the corrugated sheet model discussed in section 2, we first consider a horizontally homogeneous isothermal circular disc with a poloidal bending magnetic field. We then seek linear perturbations to this equilibrium state of the form $e^{ikx-i\omega(k)t}$, corresponding to a radial corrugation of the sheet of wavelength k. The result is linear one-dimensional system of equations for the vertical structure of the disc and the dispersion relation $\omega(k)$ of bending waves within the disc.

For simplicity we consider the following dimensionless scaled quantities

$$\widehat{t} = \Omega t, \tag{4.30}$$

$$\widehat{z'} = \frac{z'\Omega}{c_s}, \tag{4.31}$$

$$\widehat{x} = \frac{x\Omega}{c_s}, \tag{4.32}$$

$$\widehat{v_i} = v_i/c_s, \tag{4.33}$$

$$\widehat{\rho} = \frac{\rho c_s}{\Sigma\Omega}, \tag{4.34}$$

$$\widehat{B_i} = \frac{B_i}{\sqrt{\mu_0 \Sigma c_s \Omega}}, \tag{4.35}$$

$$\widehat{\omega} = \frac{\omega}{\Omega}, \tag{4.36}$$

and

$$\widehat{k} = \frac{k c_s}{\Omega}, \tag{4.37}$$

where c_s is the isothermal sound speed, Σ is the vertically integrated surface density of the disc, and all other terms maintain their previous definitions. This scaling is nearly identical to that of chapter 3, with only a slight change of convention for the magnetic field components. From this point onwards all physical quantities will be assumed to be scaled in this way and the widehats will be removed. The full set of scaled MHD equations may then be expressed as

$$\frac{Dv_x}{Dt} - 2v_y = -\frac{1}{\rho}\partial_x p + \frac{1}{\rho}(B_z\partial_z B_x - B_y\partial_x B_y - B_z\partial_x B_z), \tag{4.38}$$

$$\frac{Dv_y}{Dt} = -(2-q)v_x + \frac{1}{\rho}(B_x\partial_x B_y + B_z\partial_z B_y), \tag{4.39}$$

$$\frac{Dv_z}{Dt} = -z - \frac{1}{\rho}\partial_z \rho + \frac{1}{\rho}(B_x\partial_x B_z - B_x\partial_z B_x - B_y\partial_z B_y), \tag{4.40}$$

$$\frac{\partial \rho}{\partial t} + \partial_x(\rho v_x) + \partial_z(\rho v_z) = 0, \tag{4.41}$$

$$\frac{\partial B_x}{\partial t} = B_z\partial_z v_x - v_x\partial_x B_x - v_z\partial_z B_x - B_x\partial_z v_z, \tag{4.42}$$

$$\frac{\partial B_y}{\partial t} = B_x\partial_x v_y + B_z\partial_z v_y - qB_x - v_x\partial_x B_y - v_z\partial_z B_y - B_y\partial_x v_x - B_y\partial_z v_z, \tag{4.43}$$

$$\frac{\partial B_z}{\partial t} = B_x\partial_x v_z - v_x\partial_x B_z - v_z\partial_z B_z - B_z\partial_x v_x, \tag{4.44}$$

$$\partial_x B_x + \partial_z B_z = 0. \tag{4.45}$$

Note that we have omitted all y derivatives for simplicity as the disc is assumed to be locally azimuthally invariant.

4.4 Perturbation Analysis

This problem inherently may contain a wide array of length scales, only some of which can or should be investigated in great detail. As a first step in our analysis we consider the limiting case of small warps. What precisely is a 'small' warp in this context? We have four distinct length-scales in this problem: the wavelength of the corrugation $2\pi/k$, the radial length-scale R, the vertical length-scale H and the amplitude of the corrugation ζ. By analogy with the toy problem considered in section 4.2, we could define a small warp to be one such that the small dimensionless quantity

$$\epsilon = k\zeta \ll 1. \tag{4.46}$$

From a physical perspective this may be derived by enforcing the condition that the disc surface is very nearly normal to the $\boldsymbol{e}_z$ axis as we had argued above. Equivalently we may say that a small warp is a warp such that horizontal variation of the physical variables is much smaller than the vertical variation. For example, the density in an unwarped disc varies vertically by an amount of order unity (in scaled units) on the length-scale H. The position of the midplane varies horizontally by an amount of order ζ on the length-scale $1/k$. Consequently in order for the disc to remain approximately vertically stratified such that the density gradient is approximately vertical, we require $1/H \gg \zeta k/H$, or $k\zeta \ll 1$.

Yet such a scaling would imply that, if $\zeta \gg H$, the disc would perform vertical oscillations far greater in extent than the scale-height of the disc. A perturbation analysis could be performed in principle, but would require shifting to a reference frame that follows the vertical oscillation; such a method essentially underlies the warped shearing box formalism, with all its advantages and drawbacks.

Instead we impose a more severe condition, $\zeta/H \ll 1$, so that the vertical oscillation may be considered a perturbation to the equilibrium disc. If we define the dimensionless quantity

$$\xi = \frac{\zeta}{H} \tag{4.47}$$

we may perform a perturbation expansion in ξ safe in the knowledge that such an expansion will be convergent.

The ideal MHD equations found in the previous section may be linearised about a reasonable equilibrium solution providing a linear theory for the structure of warped magnetised discs. More formally, we seek solutions for the internal structure of the disc under the following expansion

$$A(x, y, z; t) = A_0(z) + \xi A_1(z) e^{i(kx-\omega t)} + O(\xi^2) \tag{4.48}$$

corresponding to a radial corrugated structure akin to that investigated in section 2 for the infinitely thin sheet.

4.4.1 The Equilibrium Solution

We assume the equilibrium state of the disc to be axisymmetric and radially invariant in the shearing box, though we allow the disc to have a bending poloidal field. This is equivalent to the equilibrium state used in chapter 3. In such a case we have $v_{x0} = v_{z0} = B_{y0} = 0$, and B_{z0} is independent of z and t.

$$2v_{y0} + \frac{B_{z0}}{\rho_0} d_z B_{x0} = 0 \tag{4.49}$$

$$z + \frac{1}{\rho_0} d_z \rho_0 + \frac{1}{\rho_0} B_{x0} d_z B_{x0} = 0 \tag{4.50}$$

$$B_{z0} d_z v_{y0} - q B_{x0} = 0 \tag{4.51}$$

Just as in chapter 3, the following three boundary conditions must also be satisfied.

$$B_{x0}(\infty) = B_{xs} \tag{4.52}$$

$$B_{x0}(0) = 0 \tag{4.53}$$

and

$$\int_{-\infty}^{\infty} \rho_0(z') dz = 1 \tag{4.54}$$

where B_{xs} is limiting value of B_x far above the disc and is conceptually consistent with B_{x0} as defined in the corrugated sheet analysis of the previous

section.

4.4.2 The Perturbation Solution

An expansion of the ideal MHD equations (4.38)–(4.45) to first order in the small parameter ξ yields the following one dimensional linear equations for the internal structure of the disc.

$$-i\omega v_{x1} - 2v_{y1} = -\frac{ik}{\rho_0}\rho_1 + \frac{1}{\rho_0}\left(B_{z0}\partial_z B_{x1} + B_{z1}\partial_z B_{x0} - ikB_{z0}B_{z1}\right) - \frac{\rho_1}{\rho_0^2}\left(B_{z0}\partial_z B_{x0}\right) \tag{4.55}$$

$$-i\omega v_{y1} + v_{z1}\partial_z v_{y0} = -(2-q)v_{x1} + \frac{1}{\rho_0}(B_{x0}ikB_{y1} + B_{z0}\partial_z' B_{y1}) \tag{4.56}$$

$$-i\omega v_{z1} = -\frac{1}{\rho_0}\partial_z\rho_1 + \frac{\rho_1}{\rho_0^2}\partial_z\rho_0 + \frac{1}{\rho_0}\left(ikB_{x0}B_{z1} - B_{x1}\partial_z B_{x0} - B_{x0}\partial_z B_{x1}\right) + \frac{\rho_1}{\rho_0^2}\left(B_{x0}\partial_z B_{x0}\right) \tag{4.57}$$

$$-i\omega\rho_1 + ik\rho_0 v_{x1} + \rho_0\partial_z v_{z1} + v_{z1}\partial_z\rho_0 = 0 \tag{4.58}$$

$$-i\omega B_{x1} = B_{z0}\partial_z v_{x1} - v_{z1}\partial_z B_{x0} - B_{x0}\partial_z v_{z1} \tag{4.59}$$

$$-i\omega B_{y1} = ikB_{x0}v_{y1} + B_{z0}\partial_z v_{y1} - qB_{x1} \tag{4.60}$$

$$-i\omega B_{z1} = ikB_{x0}v_{z1} - ikB_{z0}v_{x1} \tag{4.61}$$

$$ikB_{x1} + \partial_z B_{z1} = 0 \tag{4.62}$$

There are 8 equations for 7 variables; however, note that (4.61) has no vertical derivative . This is therefore a seventh order system of equations – one of the physical variables is in a sense degenerate to the remaining seven and can in principle be eliminated. Whether it is practical to do so depends on one's objectives.

4.4.3 Boundary Conditions

Examination of the ideal equations to first order in the corrugation amplitude implies there are two solution classes which may be labelled as 'even' or 'odd', dependent on the symmetry properties of the mode under the transformation $z \to -z$, just as in chapter 3. Again we restrain our analysis to the 'odd' solutions such that B_{x1}, v_{z1} and B_{y1} are even in z while $\rho_1, B_{z1}, v_{y1}, v_{x1}$ are odd in z. These solutions alone correspond to a vertical displacement of the centre of mass of the fluid in the co-rotating local frame, and hence could be reasonably described as 'warping' modes. The neglected 'even' modes could physically be described as vertical breathing modes - symmetric vertical compressions and rarefactions of the disc that are not relevant to this study.

As a result of these symmetry considerations we obtain four boundary conditions at the disc mid-plane where $z = 0$. Three additional boundary conditions are therefore required to ensure a well-defined solution.Informed by the analysis of the corrugated sheet model, we set the combination $B_{z1} - i\frac{k}{|k|}B_{x1} = 0$ to ensure that, far from the mid-plane, the magnetic field perturbation matches the expected exponential decay. The limiting value of the azimuthal magnetic field is set to zero; the development of a large-scale toroidal field from an untwisted warp would raise difficult questions about physical interpretation.

Perhaps this could best be understood by looking at the force equations (4.38)–(4.40) after multiplying through by ρ. In the low-density regions, assuming quite reasonably that the velocities satisfy $\rho v \to 0$ as $z \to \infty$, the

magnetic force terms must vanish. For the poloidal equations of motion this can be satisfied by a mutual exponential decay of B_x and B_z in z towards their unwarped equilibrium values; this concept is at the heart of section 4.2. Equation (4.39), the toroidal equation of motion, however carries a different implication: the magnetic force may vanish if $\mathbf{B} \cdot \nabla B_y = 0$, or if B_y is constant along a field line. This reflects in the local model the more general fact that an axisymmetric force-free field satisfies $\mathbf{B} \cdot \nabla(rB_\phi) = 0$. A non-zero B_y here is related to a poloidal current (via its gradient) or a magnetic torque communicated from local region to some point far beyond the computational domain. This might happen if, for example, the magnetic field line threading the disc were anchored to the central stellar object or some other portion of the disc. These 'winding' solutions are vastly more complicated, violate our assumption that the magnetic field perturbations occur on a much smaller scale than the global magnetic field structure (see the discussion of 4.2.4), and fundamentally emphasize different physics to the remainder of this thesis; they are therefore excluded.

Mathematically we require one additional boundary condition in order to close this system of equations. Physically, since we are looking at free modes, we must somehow determine the amplitude of the mode. Both of these objectives are accomplished by setting the vertical velocity perturbation at both the mid-plane and the upper boundary to 1. In the absence of a magnetic field and in the long-wavelength limit, the corresponding mode is just a vertical oscillation at the orbital frequency of unit amplitude, making this a natural choice of scaling. It is worthy of note that, just as in chapter 3, the solutions are generally insensitive to the value of the vertical velocity at the upper boundary - this boundary condition is chiefly required to exclude pathological solutions.

4.5 Wavenumber Expansion

The above equations for the internal structure of a corrugated disc may be solved numerically (see section 4.9) and the dispersion relation $\omega(k)$ may be calculated numerically. In this section we perform a analytical expansion of the linear free modes discussed in the previous section with respect to wavenumber k. The reasons for this are threefold. Firstly, such an expansion provides a check on the numerical solver, ensuring accuracy. Secondly, the expansion suggests a physical interpretation for the different factors influencing bending wave propagation in a magnetised warped disc. Thirdly, a long-wavelength expansion provides a connection between the corrugated disc model and the related warped shearing box model of chapter 3. More specifically, a slightly adapted warped shearing box model can be shown to correspond to the corrugated disc model when the wavelength of the corrugation is long.

Before delving into the perturbation expansion, it is worth taking a moment to appreciate the broader perspective. This model contains four distinct length-scales: the corrugation magnitude ζ, the wavelength of the corrugation $1/k$, the disc thickness H, and the radial length-scale of the disc R, assumed to be much larger than the former three. The assumption that the warp is small implies $\zeta/H \ll 1$. Recall that the corrugated sheet model of section 4.2 assumed $kH \ll 1$, while the disc model has relaxed this condition. The work of this section may therefore be understood as an analysis of the asymptotic limit as we reimpose the condition $kH \ll 1$, or when the wavelength of the warp is long relative to the disc scale height. This is not only of physical interest (there are many systems in which the warp length-scale is thought to be larger than the disc thickness), but also provides a correspondence between the corrugated sheet model and the corrugated disc model.

4.5.1 Expansion in k: Zeroth Order

There exists a free vertical translational mode of the entire disc that is of zeroth order in wavenumber. The solution to the disc equations to zeroth order in k and first order in ξ may be written as

$$v_{z1(0)} = 1 \tag{4.63}$$

$$(\rho_1/\rho_0)_{(0)} = -i\frac{d_z\rho_0}{\rho_0} \tag{4.64}$$

$$v_{y1(0)} = -id_z v_{y0} \tag{4.65}$$

$$B_{x1(0)} = -id_z B_{x0} \tag{4.66}$$

$$B_{y1(0)} = 0 \tag{4.67}$$

$$B_{z1(0)} = 0 \tag{4.68}$$

$$v_{x1(0)} = 0 \tag{4.69}$$

with mode frequency $\omega_0 = 1$. This is simply the free vertical oscillation of fluid elements in a standard unwarped accretion disc. The form of the mode is such that the Lagrangian perturbations of the density, pressure and magnetic field vanish – hence the Eulerian perturbations are simply proportional to the gradients of those quantities. Such a mode has no radial structure and consequently the presence of the bending poloidal field, along with the mixing of the vertical and horizontal equations of motion, has no impact on the oscillation frequency.

4.5.2 Expansion in k: First Order

The expansion of equations (4.55)–(4.62) to first order in radial wavenumber k is given by

$$d_z v_{p1} = -i\left(\frac{\omega_1 B_{x1(0)} + \omega_0 B_{x1(1)}}{B_{z0}}\right) \tag{4.70}$$

$$d_z v_{y1(1)} = q\frac{B_{x1(1)}}{B_{z0}} - i\omega_0\frac{B_{y1(1)}}{B_{z0}} - i\frac{B_{x0}}{B_{z0}}v_{y1(0)} \tag{4.71}$$

$$d_z v_{z1(1)} = -2\frac{B_{x0}}{B_{z0}}v_{y0}v_{z1(1)} + i\omega_1\left(\frac{\rho_1}{\rho_0}\right)_{(0)} + i\omega_0\left(\frac{\rho_1}{\rho_0}\right)_{(1)} + v_{z1(1)}z \tag{4.72}$$

$$\begin{aligned} B_{z0}d_z B_{x1(1)} = 2\frac{B_{z1(1)}}{B_{z0}}\rho_0 v_{y0} + i\rho_0(\frac{\rho_1}{\rho_0})_{(0)} - 2\rho_0 v_{y1(1)} \\ -2\rho_{1(1)}v_{y0} - i\omega_0\rho_0 v_{x1(1)} \end{aligned} \tag{4.73}$$

$$\begin{aligned} B_{z0}d_z B_{y1(1)} = -iB_{x0}B_{y1(0)} + (2-q)\rho_0 v_{x1(1)} + q\frac{B_{x0}}{B_{z0}}\rho_0 v_{z1(1)} - \\ i\omega_1\rho_0 v_{y1(0)} - i\omega_0\rho_0 v_{y1(1)} \end{aligned} \tag{4.74}$$

$$d_z B_{z1(1)} = -iB_{x1(0)} \tag{4.75}$$

$$\begin{aligned} d_z(\frac{\rho_1}{\rho_0})_1 = 2\frac{B_{x1(1)}}{B_{z0}}v_{y0} + i\omega_1 v_{z1(0)} + i\omega_0 v_{z1(1)} \\ +\frac{B_{x0}}{B_{z0}}\left(-i(\frac{\rho_1}{\rho_0})_{(0)} - 2\frac{B_{z1(1)}}{B_{z0}}v_{y0} + 2v_{y1(1)} + i\omega_0 v_{x1(1)}\right) \end{aligned} \tag{4.76}$$

where $v_p \equiv (B_{z0}v_x - B_{x0}v_z)/B_{z0}$ is proportional to the velocity perpendicular to the equilibrium magnetic field. Note that if $d_z B_{z1(1)} = -iB_{x1(0)}$ and $d_z B_{x1(0)} = -d_z B_{x0}$, then:

$$d_z B_{z1(1)} = -d_z B_{x0} \tag{4.77}$$

or, using the appropriate symmetry properties,

$$B_{z1(1)} = -B_{x0} \tag{4.78}$$

We may begin to notice a connection between the problem of the long wavelength corrugated disc and the warped shearing box. Recall that, by the definition of this perturbation expansion, $B_z = B_{z0} + \xi(e^{i\omega t} B_{z1} k + O(k^2)) + O(\xi^2)$. Therefore

$$B_z = B_{z0} - \xi k B_{x0} e^{i\omega t} + O(k^2) \tag{4.79}$$

Comparison with

$$B_z = B_{z'} - \psi \cos(t) B_x \tag{4.80}$$

from chapter 3 in the warped shearing box suggests a potential connection between the two perspectives of a warped disc,

$$\psi = \xi k \tag{4.81}$$

or equivalently $\psi = k\zeta$ in unscaled units. We investigate this connection in the following section.

4.6 The Connection to the Warped Shearing Box

The problem considered here is somewhat similar to the warped shearing box model of chapter 3. In this section we outline the conceptual and practical connections between the two approaches to warped disc dynamics.

The warped shearing box model analysed the dynamics of a warped disc on a radial length scale far shorter than that of the warp itself. The warped geometry forced oscillations within the disc at the orbital frequency, resonantly driving the disc response under certain conditions. Conversely, in this

section we have been analysing the spectrum of the free oscillation modes of a corrugated disc with some characteristic radial wavenumber k. One would expect the two models to be in agreement as the wavelength of the corrugation becomes very large in comparison to the scale height of the disc, as conceptually the warped shearing box could be viewed as little more than the long-wavelength limit of a corrugated disc.

This can immediately be verified in the case of a vertical equilibrium magnetic field by direct comparison of equations (4.70)–(4.76) with the the linearised equations of motion (3.52)–(3.57) from chapter 3. To see this, note that in the vertical field case $v_{y1(0)} = B_{x1(0)} = 0$ and $-id_z\rho_0/\rho_0 = iz$.

What does this correspondence tell us about the underlying models? In both cases, one may begin with an equilibrium disc of order ψ^0 and $\epsilon^0 k^0$ in scaled units. In the warped shearing box, the warp is built into the coordinate system, acting as a forcing term for a perturbation of order ψ^1. In contrast, the corrugated sheet has no explicit forcing term; rather, a radially invariant vertical oscillation introduced at order ξk^0 induces a response of order ξk. One can thereby deduce by equating orders that $\psi = \xi k$ in scaled units, or $\psi = \zeta k$ in unscaled units. Note that, as expected, ψ is defined to be independent of disc thickness and indeed can be derived by applying the definition of ψ to a corrugated sheet. Also note that this definition of ψ corresponds to ϵ as defined in the corrugated sheet.

This correspondence is somewhat more subtle in the case of a bending field. The reason for this can be most clearly seen as an extension of the work in section 4.2 - namely, the deformation of a corrugated sheet results in a net vertical stress above and below the disc, causing a slight modification to the vertical equation of motion of a magnitude proportional to B_{x0}^2 (see equation (4.21)). If this additional vertical acceleration term is included in the warped shearing box equation of motion, there is again a perfect correspondence between the long-wavelength corrugated disc equations of section

4.5.2 and the warped shearing box. This term has been included in all numerical implementations of the warped shearing box in which there is a bending field (e.g. Figure 4.4). If this extra term is neglected, there is an unbalanced vertical force and the Newton-Raphson numerical method of section 3.5 fails to converge.

There is one additional subtlety that needs to be considered before it is possible to conclude that the two perspectives are indeed in perfect agreement. In chapter 3 there were three free boundary conditions on the magnetic field. The first simply specified the inclination angle of the equilibrium magnetic field with respect to the disc surface B_{xs}; this must also be specified in the corrugated disc model. The remaining two parameters specified the limiting values of the radial and aximuthal magnetic field perturbations; neither could be immediately prescribed through theoretical argument. For the corrugated disc however, the sinusoidal corrugation results in an exponentially decaying magnetic field perturbation with a specified wavenumber k as seen in section 4.2. Therefore in order for the warped shearing box to correspond to the corrugated sheet in the long wavelength limit, particular boundary conditions on the magnetic field must be chosen.

A comparison of the numerical results of both the warped shearing box model and the corrugated disc model confirm that, having taken the appropriate steps defined above, the two models of warp propagation give identical predictions in the long-wavelength limit. This is demonstrated in Figure 4.4, in which the vertical structure of the radial magnetic field is calculated in the warped shearing box for a series of bending field equilibria (the coloured curves). The radial magnetic field component in the corrugated disc to first order in wavenumber, $B_{x1(1)}$, was also calulated under the same equilibrium conditions and plotted in black. This was achieved by solving equations (4.55)–(4.62) for a small value of k (here $k = 0.01$, though the result is insensitive to the exact value) and subtracting off the $O(k^0)$ contribution. The sets of coloured and black curves are so close as to be virtually indistinguishable,

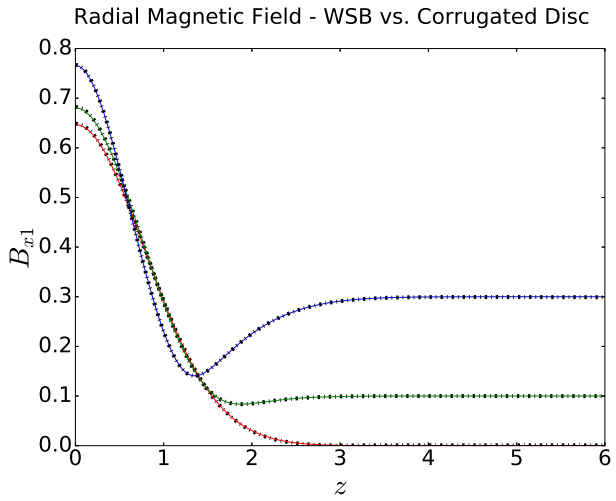

Fig. 4.4: The radial perturbation to the magnetic field B_{x1} calculated numerically using the warped shearing box for different bending field configurations, $B_{xs} = 0$ (red), $B_{xs} = 0.1$ (green) and $B_{xs} = 0.3$ (blue). Also shown in dashed black is $B_{x1(1)}$, found numerically using the corrugated disc model in all three cases.

demonstrating the equivalence between the warped shearing box and the corrugated sheet formalisms in the long wavelength limit.

There are two important consequences to this finding. The first is that the internal consistency of these models provides a check on the numerical schemes used, and hence lends some confidence to the results. The second, perhaps more conceptually interesting consequence is that to some extent warp propagation may be understood purely through the warped shearing box formalism. More specifically, the warped shearing box model is equivalent to finding the internal structure of the warped corrugated disc to order $O(k)$. The penalty of treating a corrugated disc via a warped shearing box expansion is a truncation error of order $O(k^2)$ for the internal structure of the disc and $O(k^3)$ in the dispersion relation $\omega(k)$.

4.7 The Dispersion Relation and the Vertical Momentum Equation

In the previous sections we have defined the corrugated disc model and performed a perturbation expansion of the equations of motion both in warp amplitude and in the wavenumber of the corrugation k. We now turn our attention towards the dynamics of these wave modes; in particular, we attempt in this section to find a general relationship between the frequency of free modes of oscillation in the corrugated sheet model and the torques acting upon the disc.

Consider the vertical momentum equation, which can be derived from the vertical force equation,

$$\partial_t(\rho v_z) + \nabla \cdot (\rho v_z \mathbf{v}) = -\Omega^2 z\rho + \partial_z(p) + M_z, \tag{4.82}$$

where M is the z-component of the Lorentz force and p is the pressure, and the continuity equation

$$\frac{\partial \rho}{\partial t} + \nabla \cdot (\rho \mathbf{v}) = 0. \tag{4.83}$$

We may multiply the continuity equation by z, vertically integrate it and take its time derivative in order to derive the relation

$$\int z\partial_t^2 \rho + \partial_t \left(z\nabla \cdot (\rho \mathbf{v})\right) dz = 0. \tag{4.84}$$

As there is assumed to be no vertical material flux out of the disc, we may integrate this relation by parts to find:

$$\int \partial_t(\rho v_z) dz = \int z\partial_t^2 \rho + \partial_{t,x}(z\rho v_x) dz \tag{4.85}$$

This expression for the time derivative of the vertically integrated vertical momentum may be substituted into the vertical integral of equation (4.82). After removing all total derivative terms related to the flux of material at the boundaries (assumed to be zero), the resulting expression may be written as

$$(\partial_t^2 + \Omega^2)\mathcal{F} + \partial_x \mathcal{R} = \mathcal{M} \tag{4.86}$$

where

$$\mathcal{F} = \int z\rho dz \tag{4.87}$$

is the integrated first moment of the density,

$$\mathcal{R} = \int (z\partial_t + v_z)\rho v_x dz \tag{4.88}$$

is related to the horizontal flux of vertical momentum, and

$$\mathcal{M} = \int M_z dz \tag{4.89}$$

is the vertically integrated vertical component of the Lorentz force. An alternative form that perhaps more clearly shows expresses the effect of the boundary terms of the magnetic stress tensor is:

$$(\partial_t^2 + \Omega^2)\mathcal{F} + \partial_x \mathcal{R}^* = [T_{zz}]_-^+. \tag{4.90}$$

where T_{ij} is the magnetic stress tensor and

$$\mathcal{R}^* = \int \left((z\partial_t + v_z)\rho v_x - T_{xz}\right) dz \tag{4.91}$$

is the horizontal flux of vertical momentum with the magnetic contribution included.

Expression (4.90) captures some of the fundamental physics of bending waves within magnetized discs. There is a natural vertical oscillation mode at the orbital frequency that may be modified by internal flows as is familiar for hydrodynamic discs. Additionally, in the case of a net vertical flux magnetic field, differential magnetic stresses above and below the disc will also modify the solution.

We may contrast equation (4.90) with (4.21), the corresponding relation

for the corrugated sheet. They both share the same magnetic source term caused by the imbalance of magnetic stresses far above and below the disc surface, which for the corrugated sheet implied the propagation of waves at a speed related to the horizontal component of the external magnetic field. Yet the corrugated sheet (4.21) does not take into account the internal flux of momentum, $\mathcal{R}^*$ that may be critical in driving disc warping. In this sense (4.90) may be seen as a bridge between hydrodynamic theory and earlier theoretical studies of magnetised warped discs (Terquem & Papaloizou, 2000).

Expression (4.90) relates the time derivative of the first moment of the density (analogous to a 'warp amplitude') to the radial flux of vertical momentum. In order to close these equations analytically, we must look at the horizontal motions; this problem is of greater complexity and is considered in greater depth in the following chapter.

4.8 An Asymptotic Analysis of the Dispersion Relation

Having shown the correspondence between the warped shearing box and the corrugated disc model, there are several questions that remain unanswered. What is the dispersion relation for the wave modes in a magnetised warped disc? To what extent does the corrugated disc model correspond with the corrugated sheet model discussed at the start of this chapter? Is the value of Q_3 derived in chapter 3 reliable or applicable to the corrugated disc model? Although some of these topics we must relegate to chapter 5, we may answer many of these questions by performing an asymptotic expansion of (4.90) in wavenumber k.

4.8.1 Wavenumber Expansion

Let the oscillation frequency be expanded in powers of wavenumber k, such that

$$\omega = \omega_0 + \omega_1 k + \omega_2 k^2 + \cdots \tag{4.92}$$

By combining the analysis of section 4.5 with (4.90), we may gain some understanding of the free mode frequencies in the long-wavelength limit.

Zeroth Order

To zeroth order in k, (4.90) gives

$$(1 - \omega_0^2) \int z\rho_{1(0)} dz = -[B_{x0} B_{x1(0)}]_-^+ \tag{4.93}$$

Recalling the zeroth order mode solution, we note that $B_{x1(0)} = -id_z B_{x0}$ and is therefore radially invariant as well as negligible at the upper and lower boundaries far from the mid-plane. Another way to describe this is that the magnetic field becomes constant in the low-density region.

Conversely, $\rho_{1(0)} = -id_z \rho_0$, and so integrating by parts we find:

$$(1 - \omega_0^2) \int \rho_0 dz = 0 \tag{4.94}$$

Clearly this is only possible if $\omega_0 = 1$ as expected.

First Order

To first order we have

$$\begin{aligned} (1 - \omega_0^2) \int z\rho_{1(1)} dz - 2\omega_0\omega_1 \int z\rho_{1(0)} dz + \omega_0 \int \rho_0 z v_{x1(0)} dz \\ = i \int B_{x0} B_{z1(0)} dz - [B_{x0} B_{x1(1)}]_-^+. \end{aligned} \tag{4.95}$$

The first term vanishes quite clearly. If we note that $v_{x1(0)} = 0$ (there is no horizontal transport of momentum in this vertical oscillation mode), that

$B_{z1(0)} = 0$ (as can be seen by the divergence of magnetic field) and that again $B_{x1(0)} = -id_z B_{x0}$, then

$$-2\omega_0\omega_1 \int z\rho_{1(0)}dz = \int B_{x0}d_z B_{z0}dz - [B_{x0}B_{x1(1)}]^+_-. \tag{4.96}$$

Integrating by parts, we have

$$-2i\omega_1 \int \rho_0 dz = -[B_{x0}B_{x1(1)}]^+_-. \tag{4.97}$$

To find the value of this last term, consider that from the corrugated sheet analogy we determined an appropriate boundary condition

$$(B_{z1} - iB_{x1})|_\infty = 0 \tag{4.98}$$

or equivalently that the radial and vertical magnetic field components are of equal magnitude and in antiphase. Therefore we deduce

$$\omega_1 = B_{xs}^2 \tag{4.99}$$

which may be compared with (4.23). We may thus confirm that our analysis is consistent with the predictions of the corrugated sheet in the long-wavelength limit. The dispersion curves plotted at various values of B_{xs} are shown in Figure 4.5. Note that while this asymptotic approximation appears valid at very small wavenumbers, the quadratic (and higher) terms are quite significant when $kH \approx 0.1$. This quadratic component represents the transport of angular momentum via an internal torque. The fact that this contribution is non-negligible demonstrates, in contradiction to the assumptions of prior theorists, the importance of internal flows in the propagation of warps in magnetised discs. Such internal torques may only be expected to play a larger role in resonant scenarios (see chapter 5).

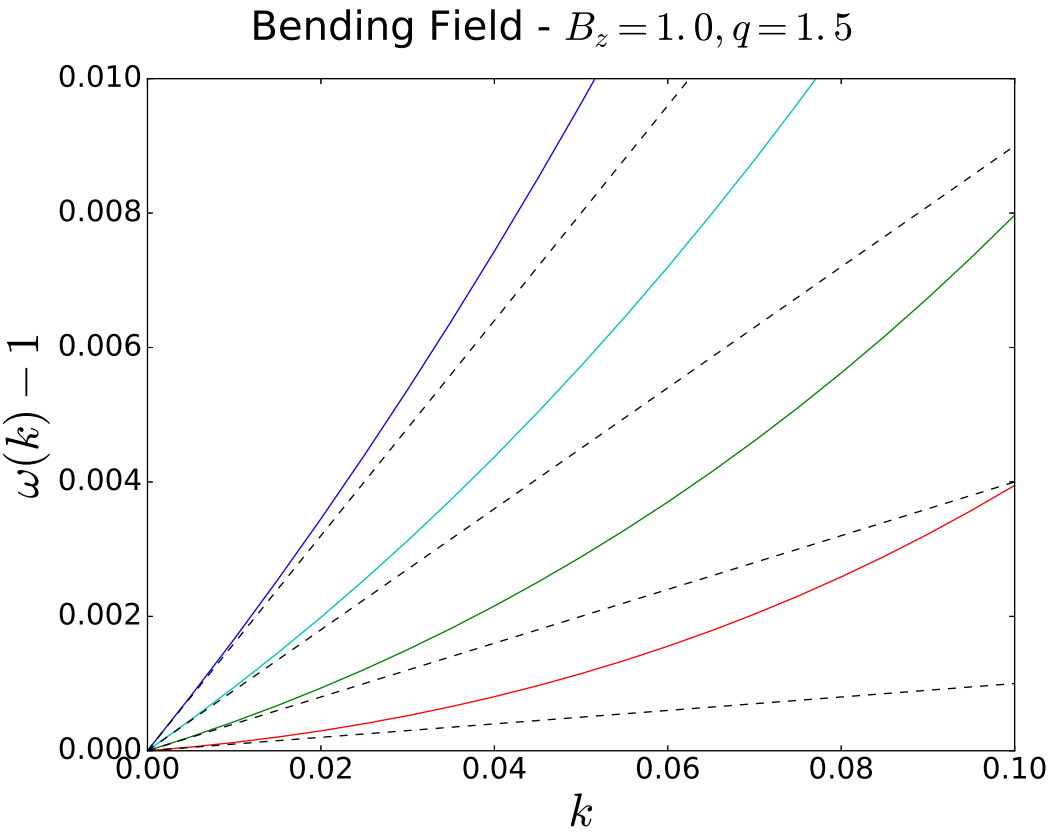

Fig. 4.5: Numerical dispersion curves $\omega(k)$ calculated at $q = 1.5$, $B_z = 1$ with different bending field equilibria. Shown are curves corresponding to $B_{xs} = 0.1$ (red), $B_{xs} = 0.2$ (green), $B_{xs} = 0.3$ (cyan) and $B_{xs} = 0.4$ (blue). The theoretical asymptotic linear components of the dispersion curves as per (4.99) are indicated by dashed black lines.

Second Order

If we carry out the same procedure to second order, we find

$$\begin{aligned}(-2\omega_0\omega_2-\omega_1^2)\int z\rho_{1(0)}dz-2\omega_0\omega_1\int z\rho_{1(1)}dz+\omega_0\int\rho_0 z v_{x1(1)}dz\\ =\int iB_{x0}B_{z1(1)}dz-[B_{x0}B_{x1(2)}]_-^+.\end{aligned}\tag{4.100}$$

Rearranging, we find

$$i(-2\omega_2-B_{x0}^4)-2B_{x0}^2\int z\rho_{1(1)}dz+\int\rho_0 z v_{x1(1)}dz=\int iB_{x0}B_{z1(1)}dz-[B_{x0}B_{x1(2)}]_-^+\tag{4.101}$$

or:

$$(2\omega_2+B_{x0}^4)=2iB_{x0}^2\int z\rho_{1(1)}dz-i\int\rho_0 z v_{x1(1)}dz-\int B_{x0}B_{z1(1)}dz-i[B_{x0}B_{x1(2)}]_-^+\tag{4.102}$$

We expect the corrugated disc to match with the results of the warped shearing box in the limit of small k; consequently the shearing box is really just an alternate and simpler method of calculation the first order quantities in k. Therefore if ω_2 depends only on variables that are first order in k, the shearing box will be capable of predicting the dispersion relation of these vertical modes to second order in k.

All terms with the exception of $B_{x1(2)}$ are the first order quantities in k. We can work around the final term by again noting the boundary condition on the magnetic field. $B_{x1(2)}=-iB_{z1(2)}$. Due to divergence of the magnetic field, we can deduce that $d_zB_{z1(2)}=-iB_{x1(1)}$. Consequently, by recasting $[B_{x0}B_{x1(2)}]=B_{x0}\int d_zB_{x1(2)}dz$, we obtain

$$[B_{x0}B_{x1(2)}]=-B_{x0}\int B_{x1(1)}dz\tag{4.103}$$

Therefore as we would hope, the wave frequency can indeed be calculated to

second order in k using only the shearing box model.

4.8.2 The Case of the Vertical Field

The only case explicitly studied in the chapter 3 was that of a vertical field such that $B_{xs} = 0$.

The magnetic torque acting on the disc is:

$$\mathcal{M} = i\left(\int B_{x0}\partial_x B_{z1} dz - [B_{x0}B_{x1}]\right). \tag{4.104}$$

For a vertical field $B_{x0} = 0$; there is no magnetic torque acting on the disc to first order in the corrugation amplitude ξ. Hence $\omega_1 = 0$ and the dispersion relation is quadratic. This quadratic term is given by

$$\omega_2 = -\frac{i}{2}\int \rho_0 z v_{x1(1)} dz. \tag{4.105}$$

Despite a slight change in notation, this corresponds to expression (3.83) for the torque coefficient Q_3 discussed in the previous chapter. As $\omega(k) = \Omega + Q_3\frac{c_s^2}{\Omega}k^2$ in unscaled units, it is encouraging that the two expressions for ω_2 have similar forms. A comparison between the numerical dispersion curve in the vertical field case and the dispersion curve predicted using Q_3 as described here is shown in Figures 4.6 and 4.7. Note that while there is very good agreement at small values of wavenumber, verifying the asymptotic limit we have derived, the agreement becomes considerably worse at larger wavenumbers.

It should also be noted that although the explicit magnetic torque does not appear in this expression, it is incorrect to assert that the magnetic field has no effect on the torque. In the previous chapter it was shown that the presence of the magnetic field leads to a complex set of resonances where ω_2, naively evaluated, may be divergent. This problem is investigated in far greater detail in the following chapter.

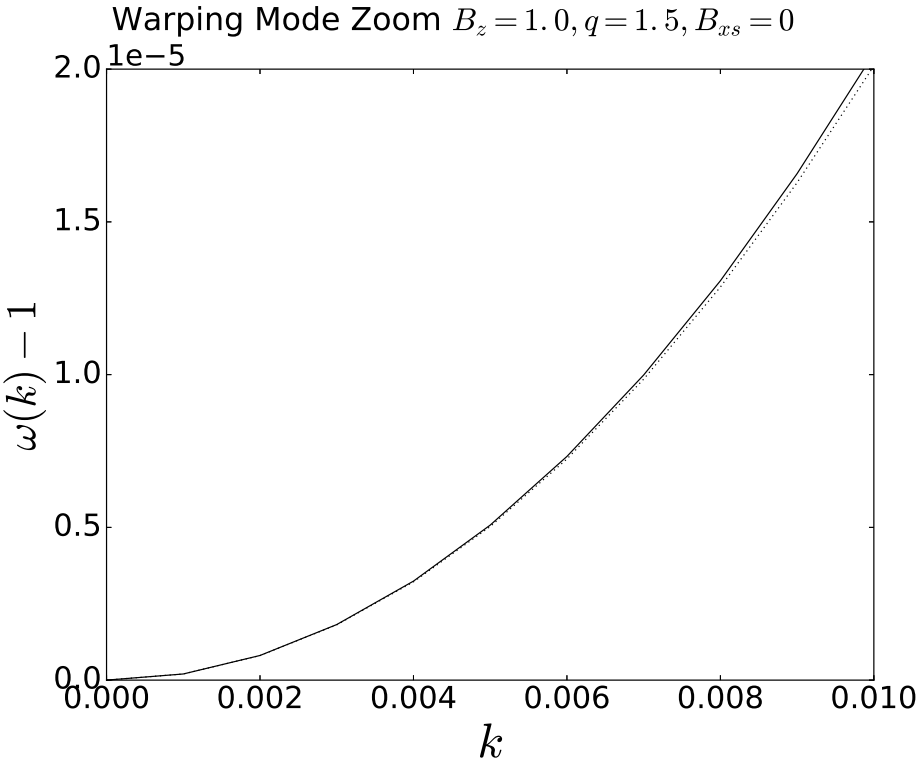

(a) $B_z = 1.0$

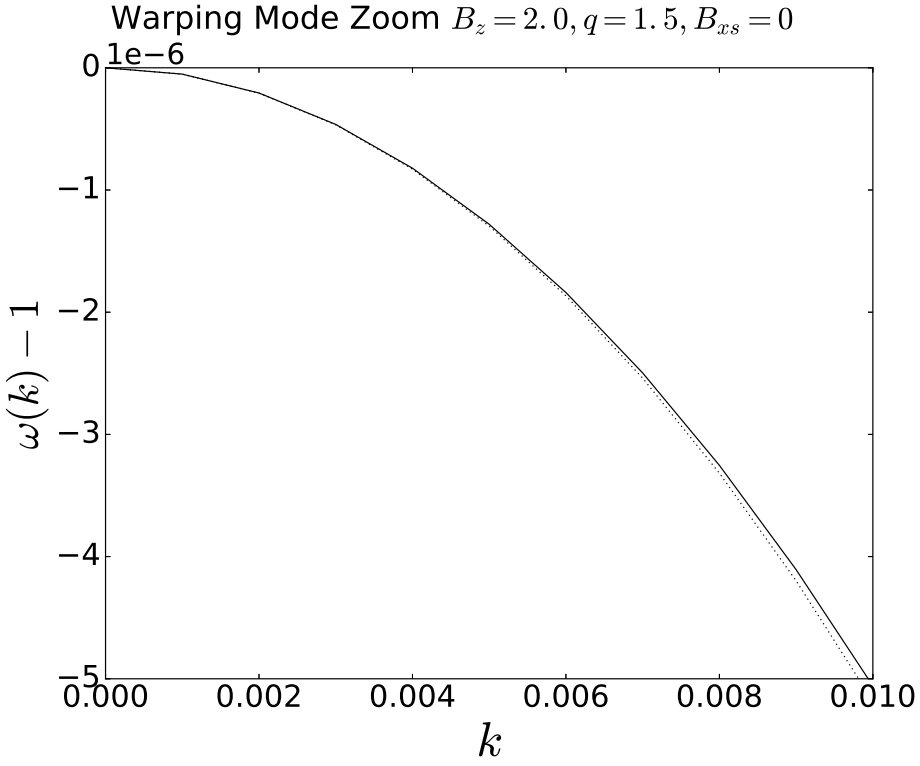

(b) $B_z = 2.0$

Fig. 4.6: Dispersion curves calculated numerically (black solid lines) and theoretically via the Q_3 coefficient of equation (3.83) at different magnetic field strengths. The equilibrium field is vertical and the wavenumbers extend to $kH = 0.01$.

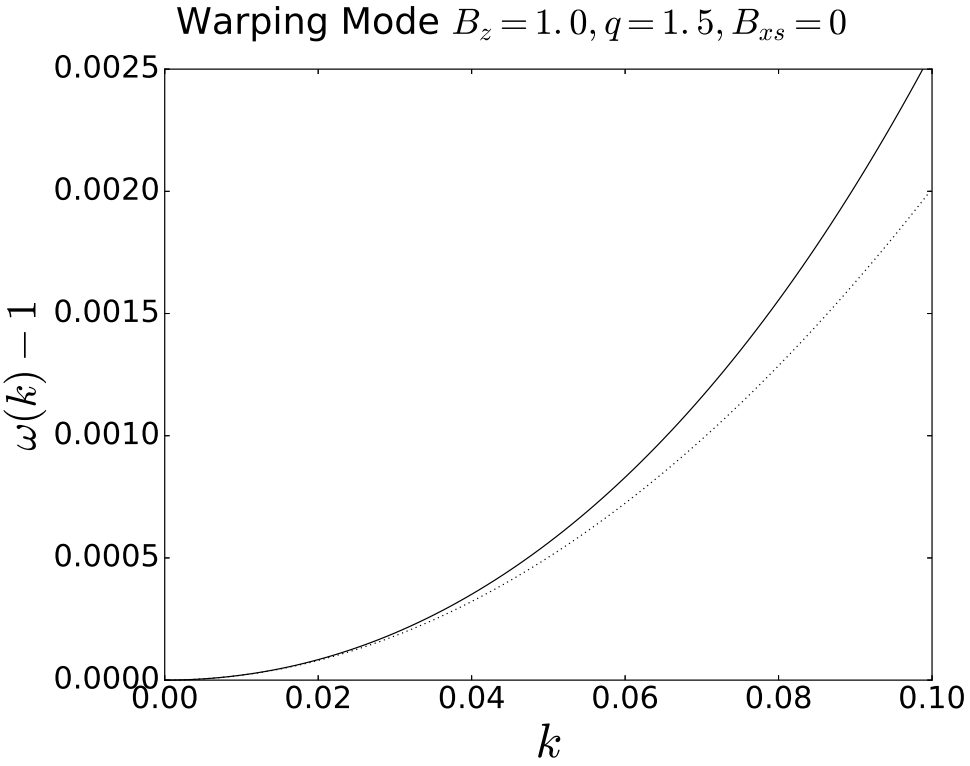

(a) $B_z = 1.0$

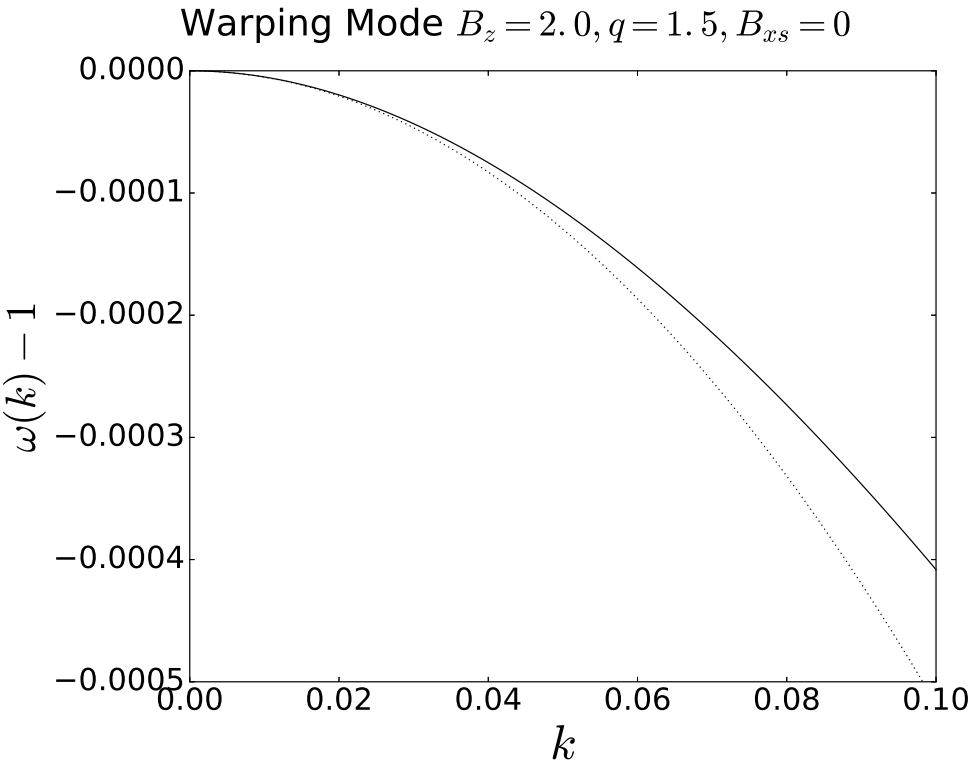

(b) $B_z = 2.0$

Fig. 4.7: Dispersion curves as presented in Figure 4.6, but the range of wavenumbers extend to $kH = 0.1$. The theoretical fit is a poorer approximation at larger values of kH.

4.9 Numerical Method

The free wave modes at a given wavenumber k were found using a formally 1-D fourth order Runge-Kutta differential equation solver to solve over the vertical extent of the disc. More precisely, we solved the set of 1-D equations as defined in section 4.4.2, using the shooting method to satisfy the boundary conditions set out in section 4.4.3 at a surface roughly 6 scale heights above the disc midplane. The principle of this numerical scheme is in many ways very similar to the numerical method defined in the previous chapter; however, there are several critical differences that I will outline below.

In the warped shearing box we considered the response of a disc to a forcing term at the orbital frequency due to the warped geometry as parametrised by the warp amplitude ψ. The warping was assumed to be horizontally invariant with no explicit horizontal length-scale and ambiguous magnetic boundary field conditions. Conversely, in the corrugated disc model, we seek for free wave modes of a magnetised disc. We have an additional input parameter - namely the wavelength of the warp relative to the scale height of the disc - in addition to the shear rate q and the poloidal magnetic field strength at the disc surface B_{xs} and B_{z0}. As discussed in section 4.2, there is an implied magnetic boundary condition due to the assumption that the field decays towards its unperturbed equilibrium sufficiently far from the disc on the lengthscale $1/k$.

Whereas in the warped shearing box model the solution one would get is well-defined, the numerical scheme described above may select one of many different branches of the dispersion curve. While it is trivial to confirm that the numerical code has converged correctly onto a particular branch of the dispersion curve, it is not a priori clear what initial parameters (or "guesses") in the shooting method will converge upon a particular dispersion curve branch.

There are three general rules of thumb for finding a particular dispersion curve branch. Firstly, if one were looking for a mode at a particular frequency, that frequency should be used as the initial guess for the wave frequency. Sec-

ondly, the choice of normalization should reflect the wave mode you are looking for; normalise $v_{z1} = 1$ to select for modes with predominantly vertical oscillation mode behaviour, and normalise $B_{x1} = 1$ to select for Alfvénic-epicyclic or largely horizontal mode behaviour. Finally, there is a notion of parameter continuity - if a set of initial guesses $\boldsymbol{\lambda}_0$ is the solution for a particular branch of the dispersion curve at a given value of a parameter (like magnetic field strength or wavenumber k), then that guess $\boldsymbol{\lambda_0}$ will very likely select the same dispersion curve when those parameters are slightly varied. In this way, once one finds a particular dispersion curve branch, one can with some effort trace that dispersion curve as the magnetic field strength, q or the wavenumber are slowly varied.

In practice, difficulty in selecting a particular dispersion curve branch only truly appears when there is a form of crossing or resonance between two distinct wave modes. At these crossings, the two modes have very similar frequency and often very similar characteristics; consequently, it is non-trivial to select a particular wave mode. Figure 4.8 demonstrates a complete spectrum of modes one may encounter. Note the presence of both Alfvénic-epicyclic modes, with frequencies given by equations (3.76)– (3.77) at $k = 0$, and vertical oscillation modes at $\omega = \sqrt{n}$ for odd integers n at $k = 0$. The following chapter will discuss many features of this figure in far greater detail.

4.10 The MRI Stability Boundary in Discs with Net Flux

In the previous section we discussed how one could select a dispersion curve branch at a particular frequency for a given set of parameters (q, B_{z0}, B_{x0}, k). One could conversely ask for what set of parameters (q, B_{z0}, B_{x0}, k) is the frequency of the wave mode zero? The presence of a zero frequency wave mode in this case implies the transition from a real to an imaginary mode frequency, and consequently the onset of the MRI. Therefore the numerical method described for looking at wave modes may be used to investigate the MRI stability condition in a variety of initial magnetic field conditions.

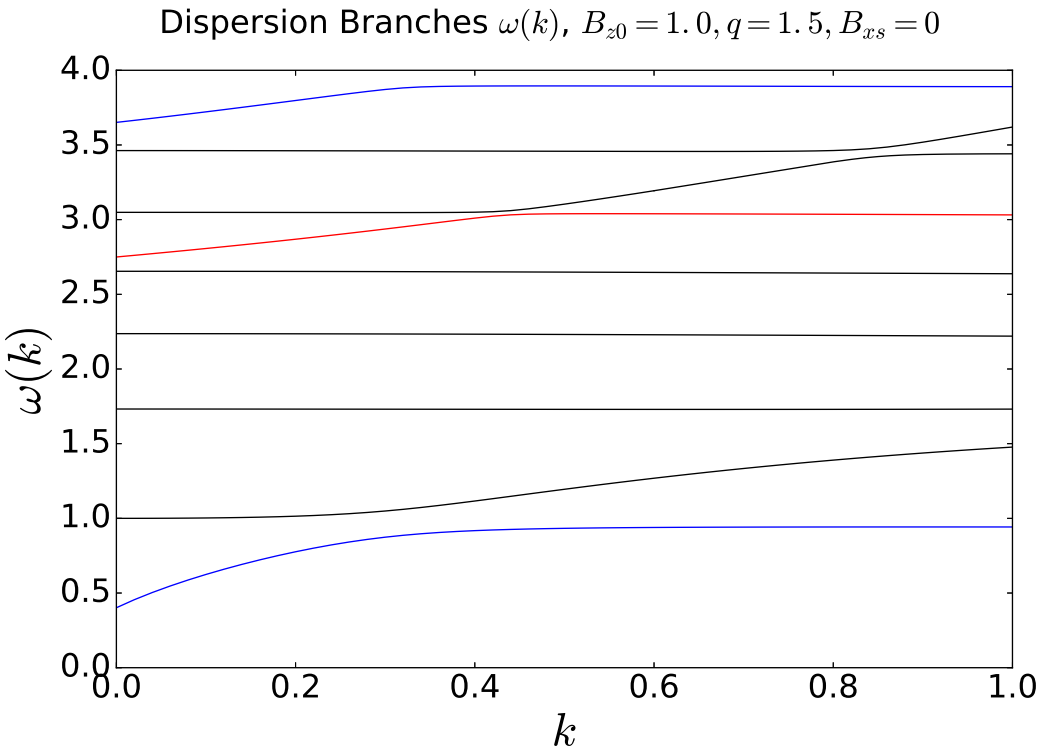

Fig. 4.8: Dispersion curves plotted with parameters $B_{z0} = 1.0$, $q = 1.5$, $B_{xs} = 0$ (vertical field). The first and second slow Alfvénic-epicyclic modes are shown in blue, while the first fast Alfvénic-epicyclic mode is shown in red. In black are the vertical oscillation modes.

Firstly, it is worth of note that the only wave modes that may exhibit the MRI are the primarily horizontal Alfvénic-epicyclic modes. As these modes generally speaking monotonically increase with wavenumber, it is sufficient to look only at the $k = 0$ mode frequencies. Further, as the Alfvénic-epicyclic frequencies (see equations (3.76)–(3.77)) are monotonically increasing with mode number, we need only investigate the point when the first slow Alfvénic-epicyclic mode becomes unstable. This implies that we need not worry about our boundary conditions selecting only odd AE modes - any even Alfvénic-epicyclic mode would necessarily have a higher frequency than the first odd Alfvénic-epicyclic mode, and hence the inclusion of even Alfvénic-epicyclic modes is not necessary to find the MRI stability boundary.

The case of a vertical magnetic field is well-known in the literature (see Gammie & Balbus (1994) and section 3.4.4). Our numerical scheme allows us to add another dimension to the parameter space by investigating the extent to which the magnetic field configuration - more specifically, the amount of radial 'bending' in the equilibrium poloidal field state - affects the MRI stability condition. As can be seen in Figure 4.9, the presence of a poloidal bending field modestly enhances the MRI, allowing the instability to present itself at higher field strengths at a given shear rate.

It is worth noting that this conclusion appears different from the stability analysis of polytropic magnetized discs by Ogilvie (1998) (Figure 7 of that work). The reason for this is probably that the units in which the magnetic field is expressed in that paper (eq. 4.23 of that work) depend on the polytropic constant and the thickness of the disc, rather than the surface density (as in this thesis). In asking whether the bending of the field increases or decreases the stability of the disc, we need to say what is held constant (e.g. thickness or surface density). At a fixed surface density and B_{z0} increasing the bending decreases the thickness.

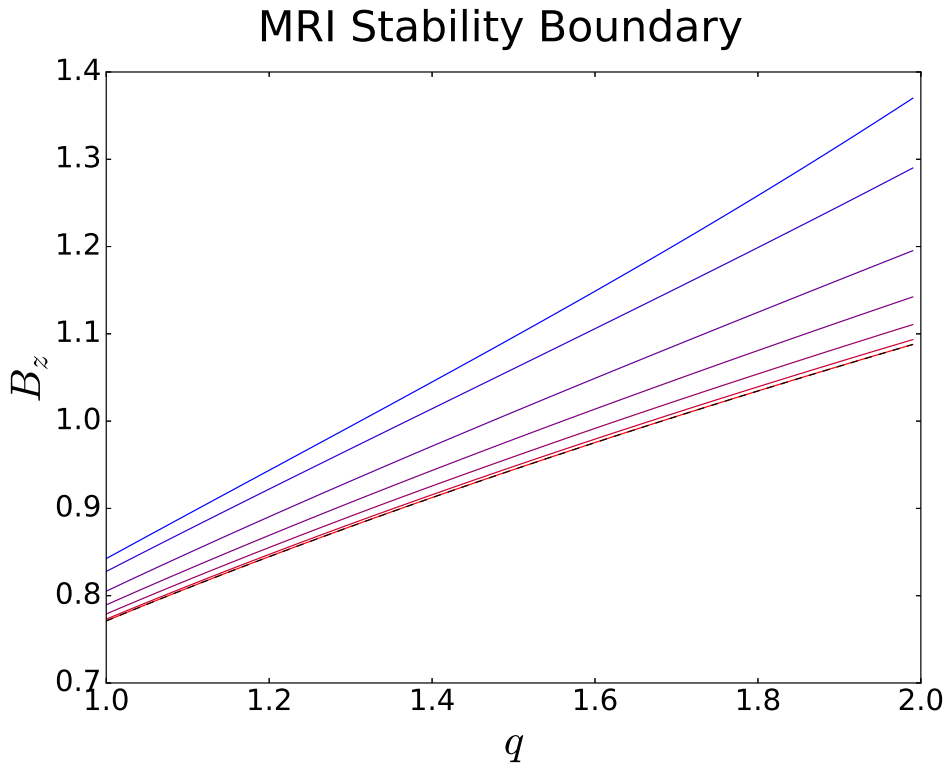

Fig. 4.9: The numerically derived MRI stability boundary in (B_z, q) space at varying degrees of field inclination. The theoretical stability boundary for a vertical field configuration, $\mu_1 B_{z0}^2 = 2q$ (Gammie & Balbus, 1994), is shown by the dotted black line. The ratio between the radial and vertical magnetic field components at the surface are, from the lower red line to the upper blue line, $B_{xs}/B_{z0} = 0, 0.1, 0.2, 0.3, 0.4$, and 0.5 respectively. These correspond to values of inclination angle $\theta_{mag} = 0°$, $5.7°, 11.3°, 16.7°, 21.8°$, and $26.6°$ respectively.

4.11 Summary and Discussion

In this chapter we have presented an alternative perspective on warped discs to complement the warped shearing box of chapter 2.

We first introduced the toy problem of an infinitely thin sheet threaded by a bending magnetic field and subject to a sinusoidal corrugation. The structure of the magnetic field some distance away from the disc surface was inferred under the assumption that the length-scale of the corrugation was short compared to the radial length-scale. Further, it was found that the corrugation was propagated non-locally by the external field in a dispersionless manner, analogous to a self-gravitating disc, with a wave-speed dependent on the radial magnetic field strength in the equilibrium state.

The corrugated disc model was then presented, similar to the corrugated sheet but capable of modelling the fluid mechanics of the disc interior. The non-linear ideal MHD equations were presented within this model, as well as a series of linearised expansions in both the magnitude and wavenumber of the corrugation. The connection between the corrugated disc and the warped shearing box of chapter 3 was discussed, and the equivalence between the warped shearing box and the asymptotic limit of the corrugated disc at large wavelengths was proven.

A brief analysis of the dispersion curve was presented in which we outlined the physical quantities influencing warp propagation in the corrugated sheet. Notably the oscillation frequency is affected by the local flux of angular momentum as well as a non-local magnetic contribution. It was shown that the linear component of the dispersion curve was identical to that of the corrugated sheet, while the quadratic term was (in the vertical field case) equivalent to Q_3.

The numerical method used to investigate the wave modes of the corrugated disc was adapted to probe the MRI stability boundary in a disc with

a poloidal bending field. It was found that the presence of a bending field increases the minimum magnetic field strength needed to quench the MRI.

5. THE ASYMPTOTIC WAVE MODES IN A MAGNETISED WARPED DISC

5.1 Introduction

In the previous chapter we introduced the corrugated disc model in order to examine the free modes of a warped disc threaded by a magnetic field. The numerical method of section 4.9 provided a means by which we could probe the free modes in a wide variety of scenarios, and the behaviour of the primary mode associated with disc warping was investigated via a perturbation expansion in orders of k in the non-resonant case.

Yet several questions remain unanswered. Equation (4.90) described how the internal flows may advect angular momentum, but does not describe the generation of these flows by the warp; it is, in some sense, incomplete. The analysis of section 4.4 implicitly assumes that there is no resonance between the vertical oscillation mode and the Alfvénic-epicyclic oscillations. Is there a noticeable change in the wave-speed of the warp due to this resonance, and can this effect be predicted by theoretical argument? Does the presence of a bending field significantly alter these results? In this chapter we hope to answer these questions and provide a more complete understanding of the wave modes in a magnetised warped disc.

This chapter is, conceptually, split into two broad sections. In the first half of the chapter we present an analysis in the long-wavelength limit of the Alfvénic-epicyclic modes and the vertical oscillation mode in both resonant and non-resonant scenarios in the vertical field case, synthesising the semi-analytical method of chapter 3 with the corrugated disc formalism of

the previous chapter. In the second half we discuss and interpret our numerical results. In those regimes where the theoretical analysis is applicable, we discuss the correspondence between the two approaches. When the numerics probe regimes beyond the scope of our theoretical analysis, we offer an interpretation informed by that analysis.

In section 5.2 the linearised corrugated sheet equations are examined and a new mathematical formalism is introduced in order to better investigate the asymptotic behaviour of the free modes. The vertical and horizontal motions are treated as two separate weakly interacting systems of equations. In section 5.3 the solutions to the decoupled ($k = 0$) systems of equations are discussed). In section 5.4 we examine the asymptotic behaviour of both the Alfvénic-epicyclic modes and the vertical oscillation mode in the non-resonant case. In section 5.5 we examine the resonant case and provide analytical expressions for the asymptotic behaviour of the dispersion branches at resonance. In section 5.6 we present numerical results that extend the discussion of this chapter to general bending magnetic field equilibria before concluding our discussion in section 5.7.

5.2 Framework for the Analysis

We begin by considering the following linearised equations (see section 4.4.2) for perturbations to the structure of a magnetised disc when the equilibrium magnetic field is constant and vertical. Just as in chapter 4, we assume a radial corrugation with wavenumber k and seek free oscillation modes of frequency ω.

The set of equations for the first order scaled perturbations of the disc are presented below. For simplicity, all quantities are assumed to be perturbed quantities unless explicitly stated otherwise using a '0' subscript. In these cases, the perturbed quantity is indicated with a '1' subscript. All magnetic field values are scaled by the equilibrium magnetic field strength, B_{z0}.

$$\partial_t v_x - 2v_y = -\partial_x(\frac{\rho_1}{\rho_0}) - \frac{B_{z0}^2}{\rho_0}(-\partial_z B_x + \partial_x B_{z1}) \tag{5.1}$$

$$\partial_t v_y = -(2-q)v_x + \frac{B_{z0}^2}{\rho_0}\partial_z B_y \tag{5.2}$$

$$\partial_t v_z = -z - \partial_z(\frac{\rho_1}{\rho_0}) \tag{5.3}$$

$$\partial_t \rho_1 + \rho_0 \partial_x v_x + \partial_z(v_z \rho_0) = 0 \tag{5.4}$$

$$\partial_t B_x = \partial_z v_x \tag{5.5}$$

$$\partial_t B_y = \partial_z v_y - qB_x \tag{5.6}$$

$$\partial_t B_{z1} = -\partial_x v_x \tag{5.7}$$

$$\partial_x B_x + \partial_z B_{z1} = 0 \tag{5.8}$$

5.2.1 A Conceptual Division

We divide these equations into a subset for the horizontal motion

$$\partial_t v_x - 2v_y + \frac{B_{z0}^2}{\rho_0}(-\partial_z B_{x1} + \partial_x B_{z1}) = -\partial_x(\frac{\rho_1}{\rho_0}) \tag{5.9}$$

$$\partial_t v_y + (2-q)v_x - \frac{B_{z0}^2}{\rho_0}\partial_z B_{y1} = 0 \tag{5.10}$$

$$\partial_t B_x - \partial_z v_x = 0 \tag{5.11}$$

$$\partial_t B_y - \partial_z v_y - qB_x = 0 \tag{5.12}$$

$$\partial_t B_{z1} + \partial_x v_x = 0 \tag{5.13}$$

$$\partial_x B_x + \partial_z B_{z1} = 0 \tag{5.14}$$

and a subset for the vertical motion

$$\partial_t \rho_1 + \partial_z (v_z \rho_0) = -\partial_x v_x \rho_0 \tag{5.15}$$

$$\partial_t v_z + \partial_z (\frac{\rho_1}{\rho_0}) = 0. \tag{5.16}$$

This leads to a fairly clear conceptual scheme that can be used to investigate both the vertical and horizontal motions in the long-wavelength limit:

$$(\partial_t + \widehat{\mathbf{O}}_{AE})\mathbf{v}_{AE} = -\partial_x \mathbf{f}_v \tag{5.17}$$

and

$$(\partial_t + \widehat{\mathbf{O}}_{v})\mathbf{v}_{v} = -\partial_x \mathbf{f}_{AE} \tag{5.18}$$

where

$$\widehat{\mathbf{O}}_{AE} = \begin{bmatrix} 0 & -2 & -\frac{B_{z0}^2}{\rho_0}\partial_z & 0 & \frac{B_{z0}^2}{\rho_0}\partial_x \\ (2-q) & 0 & 0 & -\frac{B_{z0}^2}{\rho_0}\partial_z & 0 \\ -\partial_z & 0 & 0 & 0 & 0 \\ 0 & -\partial_z & -q & 0 & 0 \\ \partial_x & 0 & 0 & 0 & 0 \end{bmatrix},$$

,

$$\widehat{\mathbf{O}}_v = \begin{bmatrix} 0 & (\partial_z - z) \\ \partial_z & 0 \end{bmatrix}, \mathbf{v}_{AE} = \begin{bmatrix} v_x \\ v_y \\ B_x \\ B_y \\ B_z \end{bmatrix}, \mathbf{v}_v = \begin{bmatrix} \rho_1/\rho_0 \\ v_z \end{bmatrix}, \mathbf{f}_{AE} = \begin{bmatrix} v_x \\ 0 \end{bmatrix}, \mathbf{f}_v = \begin{bmatrix} \rho_1/\rho_0 \\ 0 \\ 0 \\ 0 \\ 0 \end{bmatrix}.$$

where $\widehat{\mathbf{O}}_{AE}$ and $\widehat{\mathbf{O}}_v$ are two linear operators associated with the Alfvénic-epicyclic and vertical oscillation modes respectively, $\mathbf{v}_{AE}$ and $\mathbf{v}_v$ are vectors of the respective perturbed variables, and $\mathbf{f}_{AE}$ and $\mathbf{f}_v$ are vectors providing coupling when $k \neq 0$. We express the dynamical equations in this form to emphasise that the vertical and horizontal oscillation modes may be treated, if the wavelength k is small, as two distinct weakly coupled linear systems. The wavenumber k acts as a coupling constant; if $k = 0$, the two systems are totally independent, and the solutions are the Alfvénic-epicyclic (AE) modes and the vertical oscillation modes respectively. We may therefore apply a perturbation analysis to each system in turn, making full use of the linear algebraic formalism implied by the problem and partially utilised in chapter 3. This central idea underlines the analytical portion of this chapter.

5.2.2 Reduction to Equations in One Variable

Rather than consider the five and two dimensional problems above, it will prove to be convenient to reduce both the horizontal and vertical systems to a one-dimensional problem.

The vertical case is considerably simpler. Taking the time derivative of equation (5.15) and substituting from (5.16), one derives

$$\partial_t^2 \frac{\rho_1}{\rho_0} + z\partial_z \frac{\rho_1}{\rho_0} - \partial_z^2 \frac{\rho_1}{\rho_0} = -\partial_{x,t} v_x \tag{5.19}$$

The original pair of equations were of first order in time and z; it is therefore

unsurprising the resultant 1-D equation is second order in both these quantities. The quantity ρ_1/ρ_0 will come up quite often in this analysis, so for convenience we will adopt the convention $\rho_1/\rho_0 = r$ for the remainder of this chapter; in this case the above becomes

$$\partial_t^2 r + z\partial_z r - \partial_z^2 r = -\partial_{x,t} v_x. \tag{5.20}$$

The horizontal case is somewhat more complex. By taking the time derivative of equation (5.9) and substituting in $\partial_t B_x$ from equation (5.11) and $\partial_t B_{z1}$ from equation (5.13)), we have:

$$\left(\partial_t^2 - \frac{B_{z0}^2}{\rho_0}(\partial_z^2 + \partial_x^2)\right) v_x - 2\partial_t v_y = -\partial_{x,t} r. \tag{5.21}$$

Similarly, by taking two time derivatives of equation (5.10), we may eliminate the magnetic perturbations and find

$$\partial_t \left(\partial_t^2 - \frac{B_{z0}^2}{\rho_0}\partial_z^2\right) v_y - q\left(\partial_t^2 - \frac{B_{z0}^2}{\rho_0}\partial_z^2\right) v_x + 2\partial_t^2 v_x = 0. \tag{5.22}$$

If we make the substitution $\widehat{\mathbf{P}} = \partial_t^2 - \frac{B_{z0}^2}{\rho_0}\nabla^2$ and $\widehat{\mathbf{O}} = \partial_t^2 - \frac{B_{z0}^2}{\rho_0}\partial_z^2$, the two above equations may be written in the simpler form

$$\widehat{\mathbf{P}} v_x - 2\partial_t v_y = -\partial_{x,t}(r) \tag{5.23}$$

and

$$\partial_t(\widehat{\mathbf{O}} v_y) - (q\widehat{\mathbf{O}} - 2\partial_t^2) v_{x1} = 0. \tag{5.24}$$

Finally, if we apply the operator $\widehat{\mathbf{O}}$ to the top equation and substitute with the lower equation, we find

$$(\widehat{\mathbf{O}}\widehat{\mathbf{P}} - 2(q\widehat{\mathbf{O}} - 2\partial_t^2)) v_x = -\partial_{x,t}(\widehat{\mathbf{O}} r). \tag{5.25}$$

This reduced equation is a fourth order differential equation in both time and z. While this may appear surprising coming from a first order differential

system of five variables, one of the variables was in fact degenerate – an aspect of the problem we had encountered in the previous chapter (section 4.4.2).

5.2.3 General Boundary Conditions

We have split the problem into a coupled fourth order problem and second order problem. Hence we require six boundary conditions in order to ensure the problem is well-defined. As this is an eigenvalue problem, we have an additional degree of freedom and must therefore have a total of seven boundary conditions. These were discussed in section 4.4.3, but we briefly discuss them here again for convenience.

By symmetry we concluded that v_x, v_y, B_z and ρ_1 are odd functions of z, and hence vanish at the mid-plane. This gives three boundary conditions to be enforced at the disc midplane. A value of v_z was imposed on the boundary to act as a rigid lid, though the solution was found to be insensitive to the exact value one used. By analogy with the corrugated sheet model, we deduced that the poloidal magnetic field should decay on the lengthscale $1/k$ while the toroidal field should decay on the length-scale of the disc density. While these boundary conditions remain unchanged from their definition in chapter 4, in this reduced notation involving only v_x and ρ_1/ρ_0 these may be more difficult to express.

We adopt the convention that a prime refers to a derivative taken with respect to z. Trivially we note that

$$v_x(0) = 0 \tag{5.26}$$

and

$$r(0) = 0. \tag{5.27}$$

The condition $v_y(0) = 0$, using the above two conditions and equation (5.23),

may be cast as

$$v_x''(0) = 0. \tag{5.28}$$

Equations (5.11) and (5.13) suggest that if the poloidal magnetic perturbations decays to zero far from the disc surface, so too does the radial velocity. This may be expressed as

$$v_x'(L) = -kv_x(L) \tag{5.29}$$

where L is some sufficiently large distance above the disc chosen as a suitable upper boundary.

The 'rigid lid' may be quite easily applied, looking at equation (5.16), by

$$r'(L) = \Lambda \tag{5.30}$$

where Λ is some constant that in principle should not affect the solution in any meaningful way.

The boundary condition setting B_y to zero (or more precisely, forcing it to become negligible on the length-scale of the disc height as opposed to the longer $1/k$ scale height) requires considerably more effort. Looking at equations (5.11)–(5.12), we can deduce that

$$\partial_t^2 B_y = \partial_z(\partial_t v_y - q v_x).$$

Substituting $\partial_t v_y$ from (5.23), we derive

$$2\partial_t^2 B_y = \partial_z((\widehat{\mathbf{P}} - 2q)v_x + \partial_{x,t} r) = 0$$

at $z = L$. Assuming a sinusoidal corrugation and a free mode, this implies

$$\left(\frac{B_{z0}^2}{\rho_0} v_x''\right)' = -\left(\omega^2 + 2q + k^2 \frac{B_{z0}^2}{\rho_0}\right) v_x'(L) + \omega k r'(L)$$

Using the above two conditions, we may further simplify this to

$$\left(\frac{B_{z0}^2}{\rho_0}v_x''\right)' = k\left(\omega^2 + 2q + k^2\frac{B_{z0}^2}{\rho_0}\right)v_x(L) + \omega k\Lambda. \tag{5.31}$$

Formally, as we are dealing with free modes we also require a condition that sets the size of the mode. However as this is arbitrary in a linear analysis, we will select an ad hoc scaling suitable for our purposes.

Notation convention

In order to avoid over-cluttering the equations, we will adopt certain naming conventions. B_{z0} is used to scale the magnetic field; it will be convenient to simply label this quantity B. Further we will almost always be dealing, from this point on, with the radial velocity field v_x. This will be represented by simply v unless otherwise specified.

5.2.4 Bra-ket Formalism and an Eigenfunction Basis

We choose to use the bra-ket notation, familiar from quantum mechanics, such that functions of z may be mapped to vectors in a Hilbert space that may be transformed by the action of differential operators. While this may initially appear quite cumbersome, it serves to simplify our notation and emphasizes the linear algebraic nature of the analysis. This formalism is useful largely due to the frequent occurrence of the differential operator $(1/\rho_0)\partial_z^2$. We had discussed the eigenvalue spectrum of this operator in chapter 3; notably we demonstrated that it was of Sturm-Liouville form, with a spectrum of eigenfunctions u_i (see Figure 3.2) and eigenvalues μ_i such that

$$\frac{d^2u_i}{dz^2} = -\rho_0\mu_i u_i \tag{5.32}$$

A natural inner product is defined such that

$$\langle f(z)|g(z)\rangle = \int_0^\infty f(z)\rho_0(z)g(z)dz \tag{5.33}$$

Note that we normalize the eigenfunctions $u_i(z)$ such that

$$\langle u_i|u_i\rangle = 1 \tag{5.34}$$

In this notation the wave modes of the disc may be described as the solutions to

$$\widehat{\mathbf{H}}\,|v\rangle \equiv (\widehat{\mathbf{O}}\widehat{\mathbf{P}} - 2(q\widehat{\mathbf{O}} - 2\partial_t^2))\,|v\rangle = -\partial_{x,t}\widehat{\mathbf{O}}\,|r\rangle\,. \tag{5.35}$$

and

$$\widehat{\mathbf{L}}\,|r\rangle \equiv (\partial_t^2 + z\partial_z - \partial_z^2)\,|r\rangle = -\partial_{x,t}\,|v\rangle\,. \tag{5.36}$$

We will be using the eigenfunction basis $\{u_i\}$ in much of the work of this chapter. It will be convenient to discuss here some of the key features of this basis. The projection of each of the eigenvectors onto the function $f(z) = z$ will recur often in this chapter, and was defined to be (see equation (3.73))

$$\langle u_i|z\rangle = c_i. \tag{5.37}$$

Each of the normalised eigenfunctions u_i tends to a constant value far from the midplane as can be seen in Figure 3.6. This value will enter our analysis through the application of boundary condition (5.29). This value, $u_i(L)$ at some large vertical height L, may be expressed in terms of the parameters c_i and μ_i; to see this, consider the overlap integral,

$$c_i \equiv \langle u_i|z\rangle = \int z\rho_0 u_i dz. \tag{5.38}$$

We know that $u_i'' = -\mu_i u_i \rho_0$, hence we may write

$$c_i = -\frac{1}{\mu_i}\int z u_i'' dz. \tag{5.39}$$

Integrating by parts, and bearing in mind the boundary conditions on u_i –

namely that they are odd in z and have zero derivative at large z, we find

$$u_i(L) = \mu_i c_i. \tag{5.40}$$

Finally, note that the normalisation of the density $\int_0^\infty \rho_0 dz = 1/2$ implies, for example, that $\sum_i c_i^2 = 1/2$ or equivalently $\langle z|z\rangle = 1$.

5.2.5 Wavenumber Expansion

We are primarily interested in the long-wavelength asymptotic form of the solutions. Therefore we perform an expansion in wavenumber, just as in chapter 4, for all quantities f such that

$$f(k) = f_0 + f_1 k + f_2 k^2 + \cdots \tag{5.41}$$

Note that this expansion applies not only to physical variables but also to the wavenumber $\omega(k)$. Hence the operators $\widehat{\mathbf{H}}$, $\widehat{\mathbf{L}}$ and $\widehat{\mathbf{O}}$ all have their own unique expansions in wavenumber. The differential operators $\widehat{\mathbf{O}}$ and $\widehat{\mathbf{P}}$ differ by a term of order k^2. This term will be subdominant in all the cases considered in this chapter and we may let $\widehat{\mathbf{P}} = \widehat{\mathbf{O}}$ without loss of accuracy for the remainder of this chapter.

5.3 Decoupled Equations

When $k = 0$, the horizontal and vertical motions are completely decoupled. The solutions to these two separate problems may be found in the specific case under consideration, namely that of a vertical equilibrium field in an isothermal disc. While these results had been found previously, we derive them again within this framework for clarity.

5.3.1 The Vertical Motion

To solve for the vertical modes we must solve

$$\widehat{\mathbf{L}}_0 \left| r_0 \right\rangle = (-\omega^2 + z\partial_z - \partial_z^2) \left| r_0 \right\rangle = 0. \tag{5.42}$$

This equation has two solutions for integer ω_0; one complementary function is related to a Hermite polynomial, while the other is a hypergeometric function that grows very rapidly with z (faster than the inverse of the density). It can be easily verified that the Hermite solution corresponding to $\omega_0 = 1$ gives $\frac{\rho_1}{\rho_0} = z$, as we had shown in section 4.5.1. This is not the only solution; one can clearly see several vertical oscillation branches corresponding to $\omega_0 = \sqrt{n}$ for a series of odd integers n in Figure 4.8 (the boundary condition at $z = 0$ filters out all even Hermite polynomials). However, the mode continuous with $\omega_0 = 1$ is the most relevant when considering a slowly evolving warp and so is the subject of most of our analysis.

The boundary condition (5.30) at large z is largely irrelevant, as it only serves to constrain the hypergeometric complementary function. This spurious solution is significant only at the very edge of the domain, and hence has a negligible effect on the disc interior yet matches almost any reasonable value of vertical velocity at the upper boundary.

5.3.2 Horizontal Motion

We must solve the set of equations

$$\widehat{\mathbf{H}}_0 \left| v_0 \right\rangle = (\widehat{\mathbf{O}}_0^2 - 2(q\widehat{\mathbf{O}}_0 - 2\partial_t^2)) \left| v_0 \right\rangle = 0. \tag{5.43}$$

Recalling that the eigenfunction expansion of chapter 3 was defined by the relation:

$$\frac{B_{z0}^2}{\rho_0}\partial_z^2 u_i = -\lambda_i u_i \tag{5.44}$$

where $\lambda_i = \mu_i B_{z0}^2$, as in chapter 3, we may deduce that

$$\widehat{\mathbf{O}} u_i = (-\omega^2 + \lambda_i) u_i \tag{5.45}$$

If we seek solutions of the form $|v_0\rangle = \sum_i a_i |u_i\rangle$, equation (5.43) becomes

$$\Sigma_i a_i((-\omega_0^2 + \lambda_i)^2 - 2(2-q)\omega_0^2 - 2q\lambda_i)u_i = 0. \tag{5.46}$$

Nontrivial solutions in which some $a_i \neq 0$ may be found if

$$(-\omega_0^2 + \lambda_i)^2 - 2(2-q)\omega_0^2 - 2q\lambda_i = 0 \tag{5.47}$$

The solutions to this equation are

$$\omega^2_{i(fast)} = \lambda_i + 2 - q + \sqrt{4\lambda_i + (2-q)^2} \tag{5.48}$$

$$\omega^2_{i(slow)} = \lambda_i + 2 - q - \sqrt{4\lambda_i + (2-q)^2} \tag{5.49}$$

which can be cross-referenced with the fast and slow AE mode frequencies (equations (3.76)–(3.77)) found in chapter 3. We therefore conclude again that the normalised Alfvénic-epicyclic modes are given by $|v_0\rangle = u_i(z)$.

5.4 The Asymptotic Form of the Dispersion Curve - The Non-resonant Case

We now extend our analysis to higher orders in the wavenumber k. We have two distinct regimes we may consider: the resonant case and the non-resonant case. In this section we look at the asymptotic limit of the dispersion curves in the non-resonant case.

Before we begin, we must answer the question: how do we mathematically differentiate the non-resonant and the resonant regimes? When we perform an expansion in orders of wavenumber k, we must expand from some $O(k^0)$ mode. In the non-resonant case, this mode will be either purely horizontal or vertical with a specified wave-frequency ω_0. In the context of this work, typically this implies either $|r_0\rangle \neq 0$ or $|v_0\rangle \neq 0$. Therefore we must expand from an order $O(k^0)$ solution – either the vertical oscillation mode or one of the Alfvénic-epicyclic modes.

In the resonant case by contrast, there are two distinct modes at $k = 0$ with the same frequency ω_0. The equilibrium state that forms the basis of our expansion must be considered a linear combination of both modes (in the context of our work, an AE mode and the vertical oscillation mode), the proportions of which must be deduced. We shall see an example of this in section 5.5. This may be considered an example of degenerate perturbation theory and may be more familiar to the reader in a quantum mechanical context.

5.4.1 The Vertical Oscillation Branch

There is a branch of the dispersion curve with frequency $\omega = 1$ at $k = 0$ corresponding to a pure vertical oscillation mode. We might consider the perturbation to the $\omega = 1$ dispersion branch when some small corrugation is present. As we shall see, this analysis is equivalent to our analysis within the warped shearing box of chapter 3. Looking at equations (5.35)–(5.36),

$$\widehat{\mathbf{H}}\,|v\rangle = -\omega k \widehat{\mathbf{O}}\,|r\rangle\,. \tag{5.50}$$

and

$$\widehat{\mathbf{L}}\,|r\rangle = -\omega k\,|v\rangle\,. \tag{5.51}$$

We may perform an expansion about $k = 0$; at $k = 0$ there is a pure vertical oscillation mode, $r = r_0$ as described in section 5.3.1. By inspection we see that the horizontal components of the solution will therefore be of order k, and the next order contribution to the vertical equation of motion will be of order k^2. More formally, we have to order $O(k^0)$

$$\widehat{\mathbf{L}}_0\,|r_0\rangle = 0. \tag{5.52}$$

which has solutions $\omega_0 = 1$ and $r_0 = z$. To first order in k the vertical equation (5.51) rather dully gives

$$\widehat{\mathbf{L}}_0 |r_1\rangle + \widehat{\mathbf{L}}_1 |r_0\rangle = 0 \tag{5.53}$$

with solution $|r_1\rangle = \omega_1 = 0$; there is no first order density perturbation in k and there is no linear contribution to the dispersion relation in the non-resonant vertical field case.

To first order in k (5.50) gives

$$\widehat{\mathbf{H}}_0 |v_1\rangle = -\omega_0 \widehat{\mathbf{O}}_0 |r_0\rangle . \tag{5.54}$$

In this case we may make relatively easy progress by projecting $|r_0\rangle$ onto the eigenfunction basis $\{|u_i\rangle\}$ – in fact, we performed this exact expansion (and demonstrated its convergence) in chapter 3, where we found $z = \sum_i c_i u_i$ for a set of known constants c_i. Hence we may write

$$|r_0\rangle = \sum_i c_i |u_i\rangle \tag{5.55}$$

The $|u_i\rangle$'s are all eigenfunctions of $\widehat{\mathbf{H}}_0$. This implies we may expand $|v_1\rangle = \sum_i a_i |u_i\rangle$ and equate coefficients.

$$\Sigma_i a_i((-(1)^2+\lambda_i)^2 - 2(2-q)(1)^2 - 2q\lambda_i) |u_i\rangle = -\Sigma_i c_i k(-(1)^2+\lambda_i) |u_i\rangle . \tag{5.56}$$

or

$$a_i = -c_i \frac{\lambda_i - 1}{\lambda_i^2 - 2(1+q)\lambda_i + (2q-3)} \tag{5.57}$$

reproducing result (3.71) of chapter 3.

We may continue to second order in k, in which case (5.51) gives

$$\widehat{\mathbf{L}}_2 |r_0\rangle + \widehat{\mathbf{L}}_0 |r_2\rangle = -\omega_0 |v_1\rangle . \tag{5.58}$$

Left-multiplying by $\langle r_0|$, we have

$$\langle r_0|\widehat{\mathbf{L}}_2|r_0\rangle + \langle r_0|\widehat{\mathbf{L}}_0|r_2\rangle = -\omega_0 \langle r_0|v_1\rangle . \tag{5.59}$$

Let us consider this term by term. The only part of the operator $\widehat{\mathbf{L}}$ that depends on wavenumber k derives from the term $-\omega^2$; therefore $\widehat{\mathbf{L}}_2 = -2\omega_0\omega_2$. The first term therefore gives

$$\langle r_0|\widehat{\mathbf{L}}_2|r_0\rangle = -2\omega_2 \int z^2\rho_0 dz = -\omega_2. \tag{5.60}$$

Let us next consider the inner product

$$\langle r_0|\widehat{\mathbf{L}}_0|r_2\rangle = \int r_0(z)\rho_0(-1 + z\partial_z - \partial_z^2)r_2(z)dz. \tag{5.61}$$

If we first consider only the $z\partial_z$ term, we have, by the relation $\rho_0' = -z\rho_0$:

$$\int r_0\rho_0 z r_1' dz = -[r_0\rho_0 r_1'] + \int (r_0'\rho_0 r_1' + r_0\rho_0 r_1'')\, dz. \tag{5.62}$$

substituting the above back into equation (5.61) we find

$$\langle r_0|\widehat{\mathbf{L}}|r_1\rangle = \int (-\rho_0 r_0 r_1 + \rho_0 r_0' r_1')dz. \tag{5.63}$$

We may integrate by parts again on the rightmost term to return another similar vanishing boundary term, leaving

$$\langle r_0|\widehat{\mathbf{L}}|r_1\rangle = \int r_1(z)\rho_0(-1 + z\partial_z - \partial_z^2)r_0(z)dz = \langle r_1|\widehat{\mathbf{L}}|r_0\rangle . \tag{5.64}$$

In fact, this result is quite general - $\widehat{\mathbf{L}}$ is self-adjoint in the space of any functions that are zero at the mid-plane and well-behaved (vanish when multiplied by the density) far from the mid-plane. In particular $\widehat{\mathbf{L}}\,|r_0\rangle = 0$ and the entire term vanishes.

The final term in expression (5.59) is, by an eigenfunction expansion, simply given by

$$\langle r_0|v_1\rangle = \sum_{i,j} c_i a_j \langle u_i|u_j\rangle = \sum_i c_i a_i. \tag{5.65}$$

Hence we deduce that the perturbation to the frequency is given by

$$\omega_2 = \sum_i c_i^2 \frac{1-\lambda_i}{\lambda_i^2 - 2(1+q)\lambda_i + (2q-3)}. \tag{5.66}$$

This corresponds precisely with the torque coefficient Q_3 we had explicitly calculated in chapter 3 (equation (3.84)). We therefore have re-derived the results of our warped shearing box analysis and clearly demonstrated yet again the equivalence between the warped shearing box and the asymptotic limit of the corrugated disc.

5.4.2 The Horizontal Oscillation Branches

Let us now turn our attention from the vertical oscillation branch to one of the Alfvénic-epicyclic oscillation branches. In the non-resonant case the vertical and horizontal motions are decoupled to zeroth order in k. The horizontal equation of motion implies that, to order $O(k^0)$, we have

$$\widehat{\mathbf{H}}_0 |v_0\rangle = 0 \tag{5.67}$$

The solutions to this equation are the Alfvénic-epicyclic modes discussed in chapter 3 or section (5.3.2) of this chapter. If we wish to perform an expansion, we must first select a particular AE mode at $k = 0$. Let us select $|v_0\rangle$ to be the i^{th} AE mode, either fast or slow, with frequency ω_0 (which will of course differ between the fast and slow mode).

To first order in k, we have from (5.35)

$$\widehat{\mathbf{H}}_0 |v_1\rangle + \widehat{\mathbf{H}}_1 |v_0\rangle = 0 \tag{5.68}$$

Left multiplying by $\langle v_0|$, we find that

$$\langle v_0|\widehat{\mathbf{H}}_1|v_0\rangle = -\langle v_0|\widehat{\mathbf{H}}_0|v_1\rangle\,. \tag{5.69}$$

We must evaluate these two terms. Let us look at the left hand side of equation (5.69) and consider what terms contribute to $\langle v_0|\widehat{\mathbf{H}}_1|v_0\rangle$. These are, by expanding (5.35)

$$\widehat{\mathbf{H}}_1 = 4\omega_0\left(\omega_0^2 + \frac{B^2}{\rho_0}\partial_z^2 + q - 2\right)\omega_1 \tag{5.70}$$

Recalling the eigenfunction properties of $|v_0\rangle$, we have

$$\langle v_0|\widehat{\mathbf{H}}_1|v_0\rangle = 4\,\langle v_0|v_0\rangle\,\omega_0(\omega_0^2 - \lambda_i + q - 2)\omega_1. \tag{5.71}$$

We now turn our attention to $\langle v_0|\widehat{\mathbf{H}}_0|v_1\rangle$. This term is somewhat more difficult to break down; we proceed by noting that $\langle v_1|\widehat{\mathbf{H}}_0|v_0\rangle = 0$ and considering how we may transform the inner product to give this result. This could also be thought of as finding the 'adjoint' of $\widehat{\mathbf{H}}_0$.

For the purposes of transposing the inner product, $\widehat{\mathbf{H}}_0$ contains three distinct types of terms which we will call H_a, H_b and H_c. The first type of term, H_a, are simply constants with respect to z. It is clear by definition that H_a is self adjoint:

$$\langle v_0|H_a|v_1\rangle = \langle v_1|H_a|v_0\rangle\,. \tag{5.72}$$

The second type of term, H_b, are of the form $H_b = \frac{1}{\rho_0}\partial_z^2$.

$$\langle v_0|H_b|v_1\rangle = \int \rho_0 v_0 \frac{1}{\rho_0} v_1'' dz = \int v_0 v_1'' dz \tag{5.73}$$

By parts, this is equivalent to

$$\langle v_0|H_b|v_1\rangle = [v_0 v_1']_0^L - [v_0' v_1]_0^L + \langle v_1|H_b|v_0\rangle\,. \tag{5.74}$$

Boundary condition (5.29) implies that

$$\langle v_0|H_b|v_1\rangle = -(\mu_i c_i)^2 + \langle v_1|H_b|v_0\rangle \tag{5.75}$$

The final type of term, H_c is of the form $\frac{1}{\rho_0}\partial_z^2(\frac{1}{\rho_0}\partial_z^2)$, which arises from the $\widehat{\mathbf{O}}^2$ part of the operator $\mathbf{H}_0$. We wish to find the transpose of

$$\langle v_0|H_c|v_1\rangle = \int v_0(\frac{1}{\rho_0}v_1'')''dz \tag{5.76}$$

By parts one finds

$$\langle v_0|H_c|v_1\rangle = [v_0(\frac{1}{\rho_0}v_1'')'] - [v_0'(\frac{1}{\rho_0}v_1'')] + [v_1'(\frac{1}{\rho_0}v_0'')] - [v_1(\frac{1}{\rho_0}v_0'')'] + \langle v_1|H_c|v_0\rangle\,, \tag{5.77}$$

where the limits have been omitted for simplicity. Again we turn to our boundary conditions and deduce, using (5.29) and (5.31),

$$\langle v_0|H_c|v_1\rangle = (\omega_0^2 + 2q + \lambda_i)\frac{(\mu_i c_i)^2}{B^2} + \langle v_1|H_c|v_0\rangle\,, \tag{5.78}$$

By determining how we may transform each type of term within $\langle v_0|\widehat{\mathbf{H}}_0|v_1\rangle$ into its transpose, we may now transform the inner product in its entirety into its transpose and merely collect all the boundary terms that remain. The operator $\widehat{\mathbf{H}}_0$ may be written as:

$$\widehat{\mathbf{H}}_0 = \omega_0^2(\omega_0^2 - 2(2-q))H_a + \omega_0^2(2+2q)B^2H_b + B^4H_c$$

Hence we conclude

$$\langle v_0|H_0|v_1\rangle = 0 - \omega_0^2(2+2q)B^2(\mu_i c_i)^2 + (\omega_0^2 + 2q + \lambda_i)B^2(\mu_i c_i)^2 + \langle v_1|H_0|v_0\rangle$$

or

$$\langle v_0|H_0|v_1\rangle = (-\omega_0^2 + \lambda_i)B^2(\mu_i c_i)^2. \tag{5.79}$$

Looking again at equation (5.69), we conclude that the AE modes when not

in resonance have a wave speed given by

$$\omega_1 = \frac{B^2(\mu_i c_i)^2}{4\omega_0} \frac{\omega_0^2 - \lambda_i}{\omega_0^2 - \lambda_i + q - 2} \tag{5.80}$$

The accuracy of this expression has been confirmed for several fast and slow AE modes. This expression for the dispersion curve is compared directly with the dispersion curve found numerically in Figures 5.1 and 5.2 for the first fast and slow mode respectively. Their close correspondence at small wavenumbers would appear to support the asymptotic validity of expression (5.80). We also note that this provides an opportunity to test the numerical method outlined in section 4.9 of chapter 4. Encouragingly we see that the discrepancy between our numerical AE mode wave speed and equation (5.80) is largely negligible, but can be further reduced if necessary by increasing the numerical resolution (Figure 5.3).

The asymptotic wave speed of the AE modes (5.80) is a new result and is worthy of discussion. The wave speed depends on the mode number, whether it is a fast or slow mode, the magnetic field strength, and (weakly) on the shear rate. While a fuller discussion of this wave speed is discussed in section 5.5, we note that for $B \approx 1$ the AE mode propagates far faster than the vertical oscillation modes, as can be seen in Figure 4.8. The wave speed of the AE modes generally increases with magnetic field strength, though very nearly MRI unstable slow modes may propagate very rapidly due to the $1/\omega_0$ divergence of expression (5.80).

5.5 The Resonant Case

We now consider the case in which a vertical oscillation mode (most importantly the $\omega = 1$ mode) is resonant with an Alfvénic-epicyclic mode. We proceed in a very similar manner to the previous section. The zeroth order modes are in fact largely the same, with one key difference - while in the non-resonant case, a solution either had non-zero horizontal or vertical com-

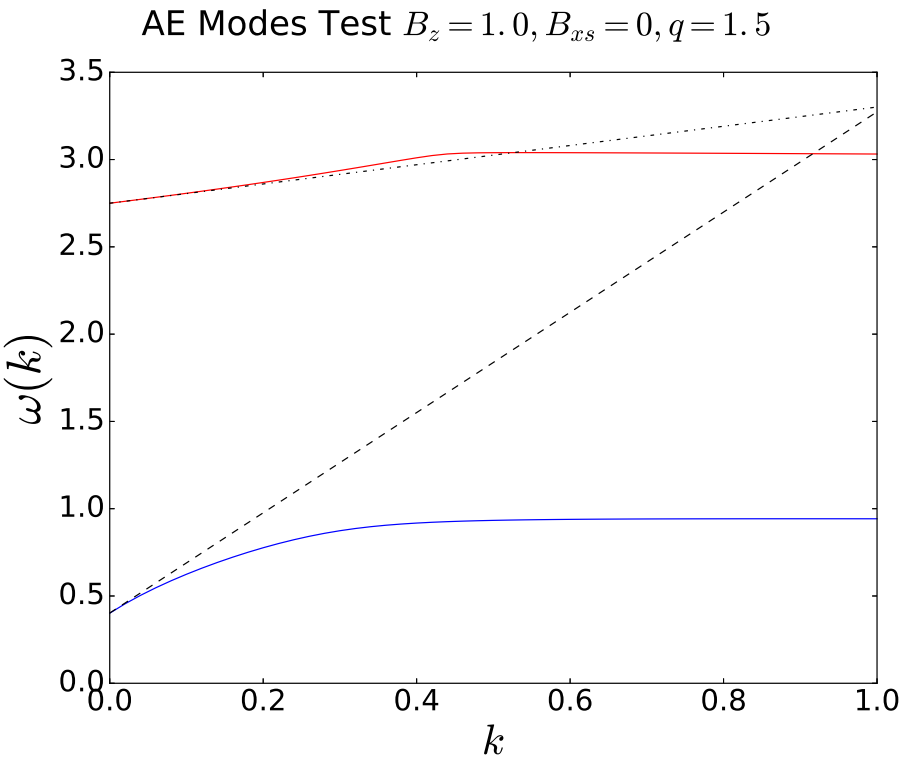

Fig. 5.1: The first fast(red) and slow (blue) AE modes, along with their asymptotic gradients according to equation (5.80). Note that though the linear regime appears to be quite small, comparison with Figure 4.8 demonstrates the linear behaviour is transferred to another mode at an avoided crossing.

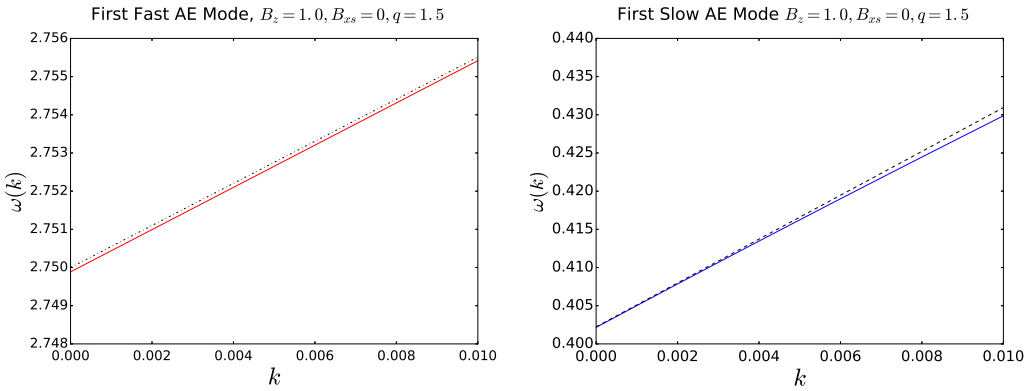

(a) First fast AE mode *(b)* First slow AE mode

Fig. 5.2: The frequencies of the first fast and slow AE modes at small wavenumber k with magnetic field strength $B_{z0} = 1$. The asymptotic expression (5.80) is shown by the dotted line.

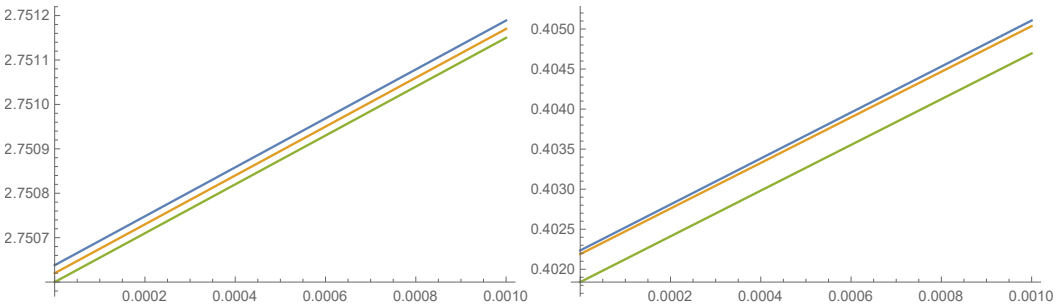

(a) First fast AE mode *(b)* First slow AE mode

Fig. 5.3: The dispersion curves of the first fast and slow AE modes. Very small wavenumbers are chosen to emphasise the discrepancy between the numerical and theoretical results in the asymptotic long-wavelength limit. In blue is the semi-analytical solution derived in this document. In green are the results from the corrugated disc numerical model of section 4.9. Yellow shows the results of another higher resolution run. Generally speaking, increasing the numerical resolution translates the dispersion curve vertically towards the semi-analytical solution.

ponents, in the resonant case there may exist a non-interacting mixture of both vertical and horizontal oscillation components in any proportion. We must bear this in mind as we proceed with our analysis.

5.5.1 The Resonant Condition

Before we continue, we briefly note what conditions lead to resonance. Resonances between AE modes and vertical oscillation modes will occur when, for a given fast or slow AE mode, $\omega_i^2 = 1$. Recall that

$$\omega_i^2 = \lambda_i + 2 - q \mp \sqrt{4\lambda_i + (2-q)^2} \tag{5.81}$$

where the $\pm$ differentiates the fast from the slow modes. Setting this equal to 1, the warping mode frequency, leads to the condition on λ_i

$$\lambda_i = 1 + q \mp \sqrt{4 + q^2}. \tag{5.82}$$

Recall that $\lambda_i \equiv B^2\mu_i$, where μ_i is the unscaled eigenvalue of the problem $u_i'' = -\mu_i\rho_0 u_i$. Therefore the condition on the magnetic field to achieve resonance between the i^{th} AE mode and the vertical oscillation mode is

$$B^2 = \frac{1 + q \mp \sqrt{4 + q^2}}{\mu_i} \tag{5.83}$$

for some i. As the eigenvalues are roughly quadratic in i, the parameter space becomes increasingly dense with resonances as B is tended to zero.

For $q < 3/2$, the numerator of (5.83) is negative; there is no value of B^2 such that resonance is satisfied. Hence fast AE modes cannot be resonant if the disc is sub-Keplerian. This can be seen in Figure 3.6 of chapter 3. If $q = 3/2$, we similarly deduce that all fast modes are resonant if $B_{z0} = 0$. This pile-up of resonances is connected to the hydrodynamic limit in a way that will be further explored later on in section 5.5.6.

5.5.2 First Order

Again we begin with the paired equations

$$\widehat{\mathbf{H}}\,|v\rangle = -\omega k \widehat{\mathbf{O}}\,|r\rangle\,, \tag{5.84}$$

$$\widehat{\mathbf{L}}\,|r\rangle = -\omega k\,|v\rangle\,. \tag{5.85}$$

As was mentioned at the start of section 5.4, the resonance between the vertical oscillation mode and an AE mode implies that, as per degenerate perturbation theory, we must expand from a $k = 0$ state that contains some as of yet unspecified combination of $|v_0\rangle$ and $|r_0\rangle$. We are free to pick a normalisation to the problem such that $\langle v_0|v_0\rangle = 1$. The first order problem gives

$$\widehat{\mathbf{H}}_1\,|v_0\rangle + \widehat{\mathbf{H}}_0\,|v_1\rangle = -\omega_0 \widehat{\mathbf{O}}\,|r_0\rangle \tag{5.86}$$

and

$$\widehat{\mathbf{L}}_1\,|r_0\rangle + \widehat{\mathbf{L}}_0\,|r_1\rangle = -\omega_0\,|v_0\rangle\,. \tag{5.87}$$

Taking appropriate inner products, we find

$$\langle v_0|\widehat{\mathbf{H}}_1|v_0\rangle + \langle v_0|\widehat{\mathbf{H}}_0|v_1\rangle = -\omega_0\,\langle v_0|\widehat{\mathbf{O}}|r_0\rangle \tag{5.88}$$

and

$$\langle r_0|\widehat{\mathbf{A}}_1|r_0\rangle + \langle r_0|\widehat{\mathbf{L}}|r_1\rangle = -\omega_0\,\langle r_0|v_0\rangle\,. \tag{5.89}$$

We proceed by finding all the terms in the above expressions (5.88)–(5.89).

Consider the inner product:

$$\langle v_0|\widehat{\mathbf{O}}|r_0\rangle = \int v_0(z)\rho_0 \left(-\omega_0^2 - \frac{B^2}{\rho_0}\partial_z^2\right) r_0(z)dz \tag{5.90}$$

As $|v_0\rangle$ is an eigenfunction of $\widehat{\mathbf{O}}$, we would like to find the transpose of this expression. The constant ω_0^2 term is obviously self-adjoint. We therefore are only concerned with the second derivative term

$$\int v_0 r_0'' dz = [v_0 r_0'] - [v_0' r_0] + \int v_0'' r_0 dz. \tag{5.91}$$

Given the boundary conditions on the problem, this implies

$$\langle v_0|\widehat{\mathbf{O}}|r_0\rangle = -B^2\mu_i c_i \Lambda + \langle r_0|\widehat{\mathbf{O}}|v_0\rangle$$

or

$$\langle v_0|\widehat{\mathbf{O}}|r_0\rangle = -B^2\mu_i c_i \Lambda + (-\omega_0^2 + \lambda_i)\langle r_0|v_0\rangle \tag{5.92}$$

This raises a question - is $\widehat{\mathbf{O}}$ self-adjoint? The answer is, unfortunately and surprisingly, no. The function r_0 does not necessarily have a zero derivative at the upper boundary, causing the operator $\widehat{\mathbf{O}}$ to not be self-adjoint. This is related to the imposition of a rigid lid on the disc at some scale height. As we shall see, our result is indeed insensitive to the value of Λ and to all intents and purposes it may be ignored.

Next, consider the inner product

$$\langle r_0|\widehat{\mathbf{L}}_0|r_1\rangle = \int r_0(z)\rho_0(-1 + z\partial_z - \partial_z^2)r_1(z)dz \tag{5.93}$$

We already encountered a similar term in section 5.4.1 and proved that $\widehat{\mathbf{L}}$ is self-adjoint. Hence $\langle r_0|\widehat{\mathbf{L}}|r_1\rangle = \langle r_1|\widehat{\mathbf{L}}|r_0\rangle$ and therefore vanishes.

Next, we consider

$$\langle r_0|\widehat{\mathbf{L}}_1|r_0\rangle = -2\omega_0\omega_1\langle r_0|r_0\rangle \tag{5.94}$$

We are almost done, given that most of the other terms in (5.88)–(5.89) were already discussed in the non-resonant case (section 5.4.2). There is, however, one subtlety that should not be neglected. In the resonant case, the bound-

ary term on B_y provides a contribution to the $\langle v_0|\widehat{\mathbf{H}}_0|v_1\rangle$ term of magnitude $-\omega_0(\mu_i c_i)B^2\Lambda$. This in fact exactly cancels the same term that appeared in $\langle v_0|\widehat{\mathbf{O}}|r_0\rangle$ discussed above. In short, the imposition of a rigid lid at the upper boundary has little impact on the dispersion relation.

5.5.3 Putting it All Together

We therefore have found all the terms in the set of paired equations (5.88)–(5.89). Before we dive into the algebra, let us try to see the 'big picture'.

Every term in the pair of equations (5.88)–(5.89) may be reduced to a numerical factor multiplied by one of three inner products: $\langle v_0|v_0\rangle$,$\langle v_0|r_0\rangle$ or $\langle r_0|r_0\rangle$. We chose, by freedom of normalization, to set $\langle v_0|v_0\rangle = 1$. We know that $r_0 \propto z$, so let write that $|r_0\rangle = b\,|z\rangle$, such that $\langle z|z\rangle = 1/2$. b takes the role of a 'mixing parameter', a number that determines the ratio of the vertical motion amplitude relative to the horizontal motion amplitude in the $k = 0$ state. Fortunately from the work of chapter 3, we know that $\langle v_0|z\rangle = c_i$, the projection of z onto each of the AE mode eigenfunctions. From all this we may deduce that

$$\langle r_0|r_0\rangle = \frac{b^2}{2} \tag{5.95}$$

and

$$\langle v_0|r_0\rangle = bc_i. \tag{5.96}$$

With this simplification, we may write the paired set of equations (5.88)–(5.89) as

$$A\omega_1 + C = Dbc_i \tag{5.97}$$

and

$$b\omega_1 = c_i, \tag{5.98}$$

where

$$A = 4\omega_0(\omega_0^2 - \lambda_i + q - 2) \tag{5.99}$$

$$C = (-\omega_0^2 + \lambda_i)B^2(c_i\mu_i)^2 \tag{5.100}$$

$$D = \omega_0(\omega_0^2 - \lambda_i) \tag{5.101}$$

Combining these two equations by eliminating for b gives

$$A\omega_1^2 + C\omega_1 = Dc_i^2 \tag{5.102}$$

The solution to this quadratic is

$$\omega_1 = \frac{-C}{2A} \pm \frac{\sqrt{C^2 + 4ADc_i^2}}{2A} \tag{5.103}$$

The AE modes when not in resonance satisfy $A\omega_1 + C = 0$, implying that $\omega_1 = -\frac{C}{A}$. In some cases, notably when there is very weak coupling between the vertical and horizontal motions, it might make sense to look at the resonant problem as a small alteration to the non-resonant problem; in that case, we may rewrite our solution above as

$$\omega_1 = \frac{-C}{2A}\left(1 \pm \sqrt{1 + \frac{4ADc_i^2}{C^2}}\right) \tag{5.104}$$

or

$$\omega_1 = \frac{\omega_{AE}}{2}\left(1 \pm \sqrt{1 + \xi}\right). \tag{5.105}$$

This form of the solution perhaps makes it clear that when $\xi \equiv \frac{4AD}{C^2} \ll 1$, the AE mode frequency is only slightly modified and the bending wave mode picks up a small linear contribution to its dispersion relation. ξ takes the role of a coupling constant between the vertical oscillation mode and the resonant AE mode.

5.5.4 Analysis of the Linear Contribution to the Dispersion Relation

In the previous section we derived an expression for the first order perturbation to the dispersion relation ω_1 in the resonant case. In this section we offer some analysis of this expression in various cases.

Understanding the terms in the dispersion relation

Let us look at the term $\frac{-C}{A}$ which appears in our expression. This is in fact the original AE non-resonant result found earlier (equation (5.80)),

$$\omega_{AE} = \frac{-C}{A} = \frac{B^2(\mu_i c_i)^2}{4\omega_0} \frac{\omega_0^2 - \lambda_i}{\omega_0^2 - \lambda_i + q - 2}. \tag{5.106}$$

In the resonant case however, these terms are not all independent - we know that $\omega_0 = 1$, and λ_i must have a specific dependence on q in order to achieve resonance as discussed in section 5.5.1. Putting this all together, we have

$$\omega_{AE} = \frac{B^2(\mu_i c_i)^2}{4} \frac{q \pm \sqrt{4+q^2}}{2 \pm \sqrt{4+q^2}}. \tag{5.107}$$

The term $\frac{q \pm \sqrt{4+q^2}}{2 \pm \sqrt{4+q^2}}$ will appear quite often and is virtually always very well-behaved and of order unity, offering very little interesting behaviour or dependencies. From this point onwards I call it a form factor $f_\pm(q)$ to simplify the algebra, where $f_+(q)$ applies to the slow mode and $f_-(q)$ applies to the fast mode. Hence

$$\omega_{AE} = \frac{B^2(\mu_i c_i)^2}{4} f_\pm(q). \tag{5.108}$$

The other term that appears in the dispersion relation, the coupling constant ξ, is given by

$$\xi = \frac{16}{f_\pm(q)} \frac{1}{\lambda^2(q)(\mu_i c_i)^2}. \tag{5.109}$$

Hence we may write the first order perturbation to the dispersion relation at resonance as

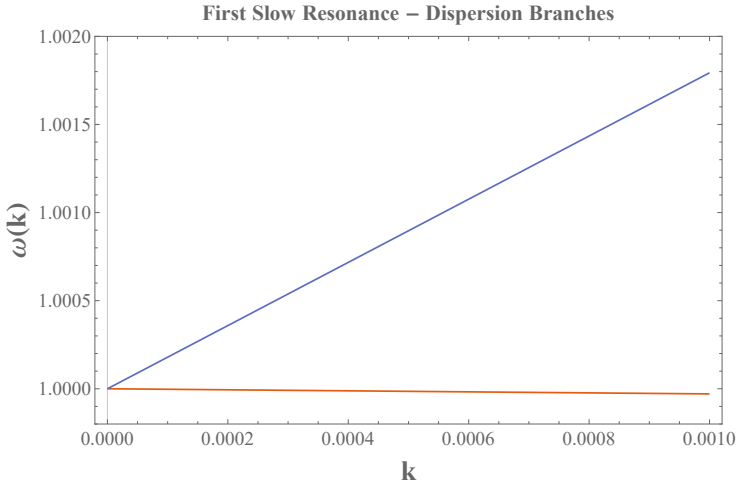

Fig. 5.4: The theoretical dispersion curve when the first slow AE mode is resonance with the vertical oscillation mode. The upper, steeper branch has a much stronger AE mode character while the lower branch is predominantly a vertical oscillation mode.

$$\omega_1 = \frac{f_\pm(q)}{8}\lambda_i(q)\mu_i c_i^2 \left(1 \pm \sqrt{1 + \frac{16}{f_\pm(q)}\frac{1}{\lambda^2(q)(\mu_i c_i)^2}}\right). \tag{5.110}$$

We have attempted to corroborate this expression with relevant numerical results from the corrugated box 1D numerical solver. This is non-trivial - while a resonance is very easy to analyse theoretically, the numerical dispersion curve is quite sensitive and perfect resonance is impossible to achieve in practice. Consequently, the numerical dispersion curves are never quite as steep as (5.110) would imply. Yet the numerical results, seen in Figures 5.4 and 5.5b (as well as Figure 5.11 that we shall discuss later) provide sufficient evidence of the validity of expression (5.110).

Let us investigate equation (5.110). By enforcing the condition of resonance, we no longer are able to tune the magnetic field strength. Rather, the only parameters in this equation are the mode number i and the shear rate q. Let us investigate ω_i for different modes when $\lambda_i(q)$ is of order unity, the generic case (so either looking at slow modes or fast modes when $q > 3/2$). In

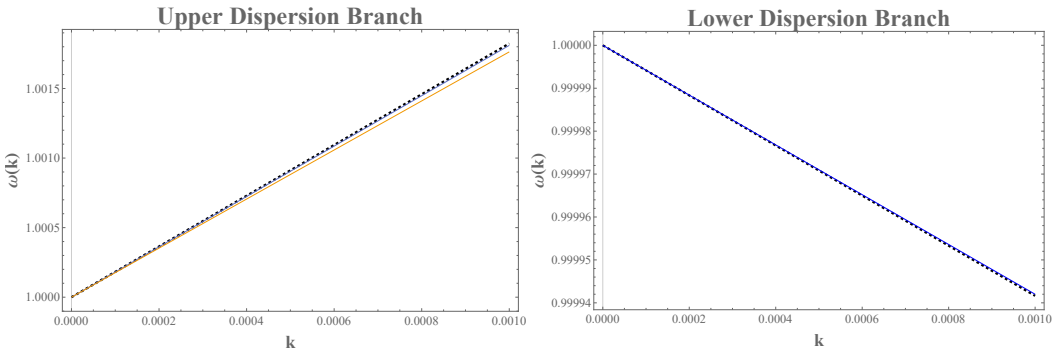

(a) Upper branch *(b)* Lower branch

Fig. 5.5: A comparison of the theoretical and numerical frequencies on the upper lower branches of the dispersion curve at the resonance between the first slow mode and the vertical oscillation mode shown in Figure 5.4. The theoretical result according to (5.105) is shown in dashed black, the numerical result in blue, and the theoretical dispersion branch in the absence of resonance (the frequency of the pure AE mode excluding all vertical motion) is shown in yellow for the upper branch.

this case, we see that at higher and higher modes, μ_i increases and the square root in equation (5.110) tends to unity. Hence we obtain limiting forms of $\omega_1 = \omega_{AE}$ and $\omega_1 = 0$ – the horizontal and vertical modes are effectively decoupled.

What is the physical rationale behind this result? At higher and higher mode numbers, the magnetic field must become ever weaker in order to achieve resonance with the $\omega = 1$ vertical mode. Hence the coupling between the vertical and horizontal motions becomes steadily weaker, and in the limit $B \to 0$ or $i \to \infty$, we recover essentially decoupled horizontal and vertical modes. The vertical mode dispersion curve becomes quadratic, and the horizontal modes behave just as they did in the non-resonant case.

How strong is the coupling between the slow AE modes and the vertical oscillation mode? In ascending order of mode number, the coupling constant ξ is found to be

$$\xi = \{0.134, 0.068, 0.046, 0.0032, \dots\} \tag{5.111}$$

This in turn implies that the resonance changes the wave speed of the AE mode by an amount

$$\frac{\Delta\omega_1}{\omega_{1,AE}} = \{3.4\%, 1.6\%, 1.2\%, 0.8\% \dots\} \tag{5.112}$$

Of course the coupling is not the only thing that changes as we look at different AE modes – the wave speed of each AE mode also varies with mode number. These wave speeds at resonance are:

$$\omega_{1,AE} = \{1.764, 0.520, 0.300, 0.214, \dots\} \tag{5.113}$$

The fact that these wave speeds decrease with increasing mode number can be physically understood as a consequence of the fact that higher order resonances occur at lower and lower values of magnetic field strength. As these are Alfvénic modes, it is unsurprising that their wave speed would diminish with the magnetic field strength.

These results in conjunction imply that the resonance most likely to impact the propagation of the warp is the first slow mode. This mode has the greatest wave speed and the greatest coupling with the vertical oscillation mode. In real terms, this means that the first slow mode AE wave speed is changed from 1.76 to 1.82 c_s by the resonance, while the warping mode travels at a wave speed of 0.06 c_s. Though this is not insignificant, it is far from extraordinary.

Thus far we have only looked at the slow AE modes. Is it possible that the fast modes might provide more interesting coupling? Indeed the coupling between the vertical oscillation mode and the fast AE modes may become very large, as we discuss in the following section! However, these fast modes suffer from requiring weak magnetic field strengths to achieve resonance, meaning there is very limited potential for enhanced warp propagation. In fact, as we shall see, this large coupling only serves to reproduce the hydrodynamic resonance.

There is one way in which we could perhaps salvage the idea of enhanced warp transport through resonance. This analysis has thus far been predicated on the assumption that the equilibrium field is purely vertical, effectively decoupling the vertical and horizontal equations of motion. Could an inclined equilibrium magnetic field better couple the AE modes to the warping mode and thereby enhance the effects of resonance? We explore this idea in section 5.6.

5.5.5 Resonant Fast Modes

We discussed the resonance between the warping mode and the slow AE modes in the previous section. In this section we turn our attention to the fast AE modes. The resonant condition gives (see section 5.5.1)

$$\lambda_i = 1 + q - \sqrt{4 + q^2}. \tag{5.114}$$

for fast AE modes. By tuning the shear rate q, this value of λ_i can become very small, independently of the mode number i. Hence, it is possible for the term inside the square root of (5.110) to, rather than tend to unity, become very large leading to very strong coupling and qualitatively different behaviour altogether! To see this, let $q = 3/2 + \delta$ such that $\delta \ll 1$. Then

$$\lambda_i(q) = \frac{2}{5}\delta + O(\delta^2) \tag{5.115}$$

Let us now consider what happens to ω_1 as we let q tend towards $3/2$ for a resonant fast mode i. The form factor f_- is very well-behaved and tends towards the value

$$f_-(q) \to f_-(3/2) = 2 \tag{5.116}$$

Plugging this into expression (5.110) above for the frequency perturbation ω_1, we have

$$\omega_1 = \frac{\delta}{5}\mu_i c_i^2 \left(1 \pm \sqrt{1 + \frac{50}{\delta^2 (c_i \mu_i)^2}}\right). \tag{5.117}$$

We see that there is a form of competition between δ and $\mu_i c_i$. At higher and higher mode numbers, $\mu_i c_i$ becomes very large. However, for every mode i we may always tend q to 3/2 in such a way that $\delta^2(\mu_i c_i)^2 \ll 1$ by tending δ to zero. By expressing the above as

$$\omega_1 = \frac{\delta}{10}\mu_i c_i^2 \left(1 \pm \frac{5\sqrt{2}}{\delta \mu_i c_i}\sqrt{1 + \frac{\delta^2 (\mu_i c_i)^2}{50}}\right). \tag{5.118}$$

we see that in the limit of small δ, ω_1 becomes independent of δ and has two solutions equal and opposite in sign

$$\omega_1 = \pm \frac{c_i}{\sqrt{2}} \tag{5.119}$$

This certainly looks somewhat like the hydrodynamic resonance, but the sound speed we derive contains an additional factor of c_i. This analysis is incomplete; in the following section we present a corrected version of this result.

5.5.6 The Hydrodynamic Resonance

In the above working, we looked at the implications of resonance on the dispersion relation near the hydrodynamic resonance ($B = 0$ and $q = 3/2$). However, this does not account for the fact that as we approach the hydrodynamic resonance, the vertical oscillation mode is not resonant with a **single** fast AE mode, but rather is resonant with **every** fast AE mode. In fact, this problem is exactly soluble and we examine the solution below.

At $B = 0$, $q = 3/2$, and $k = 0$ every fast AE mode and the vertical oscillation mode have frequency $\omega_0 = 1$. When $k \neq 0$ we expect to find a solution to the perturbed problem of the form:

$$|v\rangle = \sum_i a_i \, |v_{i,0}\rangle + k \, |v_1\rangle \tag{5.120}$$

and

$$|r\rangle = |r_0\rangle + k \, |r_1\rangle \tag{5.121}$$

where $|v_{i,0}\rangle$ is the i^{th} AE mode solution.

The unique aspect of this set-up is that, unlike in the previous cases, rather than the $k = 0$ state being a mixture of a **particular** AE mode and the vertical oscillation mode, the $k = 0$ state is a linear combination of **all** the fast AE modes since they are all resonant with the vertical oscillation mode when $B = 0$, $q = 1.5$.

We proceed as before, taking an expansion in k and taking the inner product of each AE term by its respective AE mode $\langle v_{i,0}|$:

$$\forall_i : a_i(\langle v_{i,0}|\widehat{\mathbf{H}}_1|v_{i,0}\rangle + \langle v_{i,0}|\widehat{\mathbf{H}}_0|v_1\rangle) = -\langle v_{i,0}|\widehat{\mathbf{O}}|r_0\rangle \, . \tag{5.122}$$

due to the orthogonality of the $|v_{i,0}\rangle$'s and

$$\langle r_0|\widehat{\mathbf{A}}_1|r_0\rangle + \langle r_0|\widehat{\mathbf{L}}|r_1\rangle = -\omega_0 \sum_i a_i \, \langle r_0|v_{0,i}\rangle \, . \tag{5.123}$$

Note that this is identical the the method used in section (5.5) with the exception that we've chosen to normalise $|r_0\rangle$ to unity rather than the v_i's and that we must include the contribution from multiple AE modes rather than a single AE mode.

The upper equation gives, using the obvious extensions to A, C and D from equation (5.102):

$$\forall_i : a_i(A_i\omega_1 + C_i) = Dc_i \tag{5.124}$$

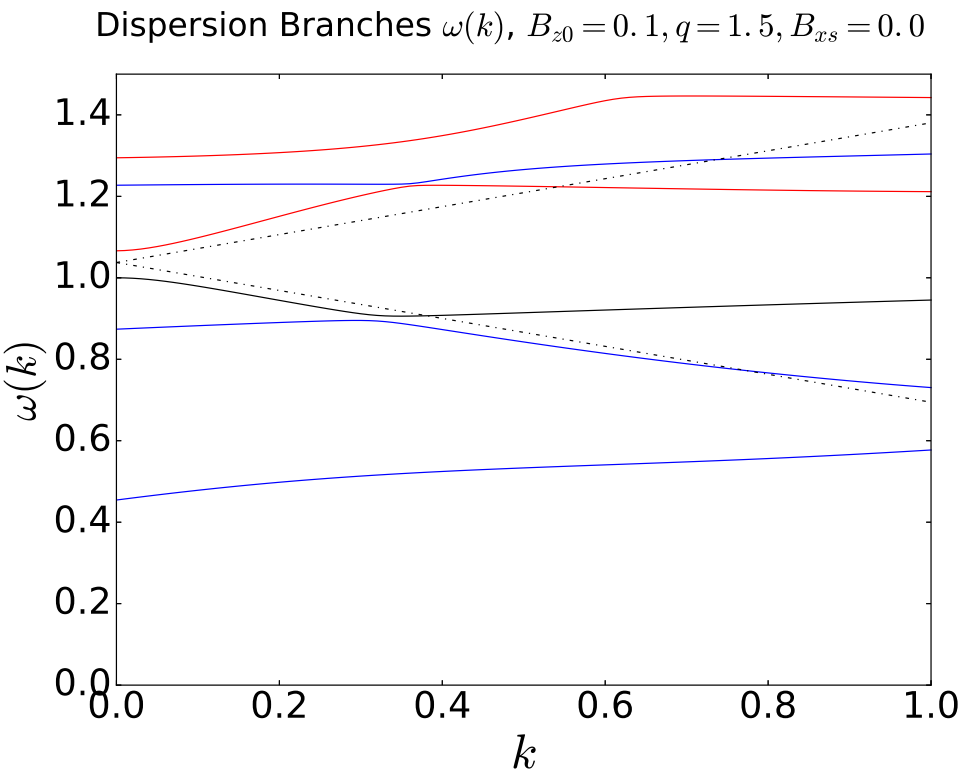

Fig. 5.6: Dispersion curves at $B_z = 0.1$. The fast modes (red) are beginning to cascade downwards towards $\omega(k) \approx 1$. The dotted lines represent waves travelling at half the sound speed. The hydrodynamic resonance is beginning to occur.

and

$$-\omega_1 = -\sum_i a_i c_i. \tag{5.125}$$

Substituting for a_i, we find that

$$\omega_1 = \sum_i \frac{D_i}{A_i\omega_1 + C_i} c_i^2. \tag{5.126}$$

At the hydrodynamic resonance, $A_i = 2$, $C_i = 0$ and $D_i = 1$, implying that:

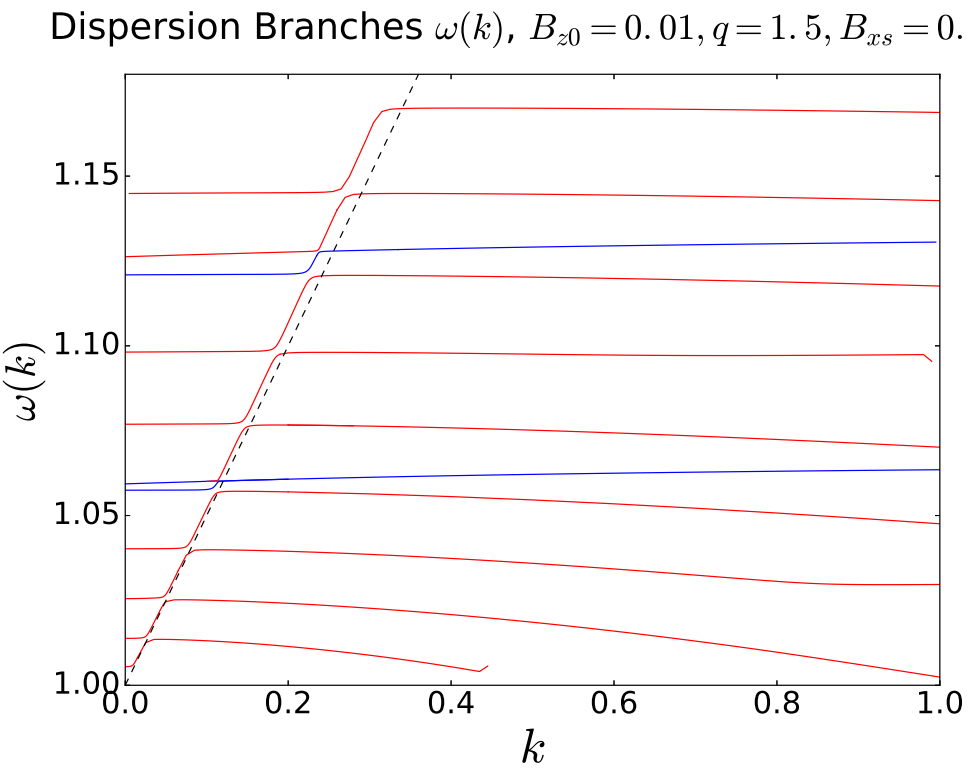

Fig. 5.7: Dispersion curves at $B_z = 0.01$. The first 10 fast modes (red) are densely packed at frequencies just above 1. The dotted line represents a travelling wave at half the sound speed. The hydrodynamic resonance has been achieved for the entire range of wavenumbers shown.

$$\omega_1 = \sum_i \frac{1}{2\omega_1} c_i^2 \tag{5.127}$$

or

$$\omega_1^2 = \sum_i \frac{1}{2} c_i^2 \tag{5.128}$$

By the normalisation of c_i, this evaluates to:

$$\omega_1 = \pm\frac{1}{2} \tag{5.129}$$

as expected.

We may also use equation (5.124) to note that:

$$a_i = \pm c_i \tag{5.130}$$

given that c_i is the overlap between the velocity eigenfunctions and the vertical density perturbation, we conclude that

$$|v_0\rangle = \sum_i a_i \, |v_{i,0}\rangle = \pm \sum_i \langle r_0 | v_{i,0} \rangle \, |v_{i,0}\rangle = \pm \, |r_0\rangle \, . \tag{5.131}$$

In other words, the radial velocity perturbation is equal to the density perturbation and thus is a linear function of z – a well-known feature of the hydrodynamic equations.

It should be noted that this result is not unexpected. By looking at the hydrodynamic limit, we are investigating the case where the fast AE modes are all in a sense degenerate. Hence, splitting the horizontal velocity into a

sum of these eigenmodes is, while perfectly valid, also somewhat arbitrary and it is not too surprising (though a good test of internal consistency) that we recover the traditional hydrodynamic result.

A numerical investigation into the hydrodynamic limit is shown in Figure 5.6 and Figure 5.7. In Figure 5.6, the magnetic field strength is $B = 0.1$ and we see that the first and second fast AE modes in red are close to $\omega = 1$. Although the resonance is far from perfect, a rough correspondence can be drawn between the gradients of the dispersion curves and the hydrodynamic prediction of dispersionless waves travelling at half the sound speed shown by the dotted lines. In Figure 5.7, the field is weakened to $B = 0.01$ and the resonance is far more visible. The first ten fast AE modes can be seen, all very closely spaced just above $\omega = 1$. A clear line can be traced hurtling between dispersion curve branches with a gradient of roughly $1/2$; the hydrodynamic resonance has largely been achieved.

5.6 Beyond the Vertical: The Effect of a Bending Field

The analytical investigation presented in this chapter correctly predicted the effect of resonance between an Alfvénic-epicyclic mode and the vertical oscillation mode on the wave speed of the warp in the vertical field case. However, it was found that the effect of resonance – though significant and measurable – was somewhat modest, allowing the warp to travel as a dispersionless wave at less than a tenth of the sound speed.

This weak coupling could partially be explained by the use of a vertical equilibrium magnetic field, which allows the vertical and horizontal modes to be largely decoupled. The work of this section attempts to determine whether a bending equilibrium field might be capable of providing a stronger coupling between the Alfvénic-epicyclic modes and the vertical oscillation mode at resonance, thereby enhancing the wave speed of the warp.

5.6.1 Bending Field Dispersion Curves

In Figure 5.8 the dispersion branches of the warped disc can be seen at various field inclinations. Note that as as the inclination is increased the minimum slow mode frequency is decreased until, at roughly $B_{xs} = 0.4$, the mode frequency drops to zero indicating the onset of the MRI. This can be compared with Figure 4.9, which demonstrates the same phenomenon – the MRI is enhanced by the presence of a bending field.

We also note that while it makes sense to distinguish the vertical oscillation modes and the AE modes in the vertical field case, this distinction becomes murkier as the bending poloidal field couples the horizontal and vertical equations of motion. We colour each curve using some notion of continuity, based on the the idea that a given branch would correspond to either a purely vertical or a purely horizontal mode if the field inclination were gently reduced back to zero.

Most importantly for our purposes, the avoided crossing between the warping mode near $\omega = 1$ and the first slow mode qualitatively changes at larger values of B_{xs}. For nearly vertical fields, the avoided crossing takes place over a relatively narrow region. Conversely the avoided crossing is considerably more dramatic in subfigures (e) and (f). This could be interpreted as an indication of greater coupling between the slow mode and the vertical oscillation mode.

5.6.2 Direct Numerical Investigation of Resonance with a Bending Field

In this section we present a direct numerical investigation of the resonance between the first slow AE mode and the warp. This problem contains various subtleties that must be taken into account. We first examine an analogous hydrodynamic resonance in order to aid the reader's understanding.

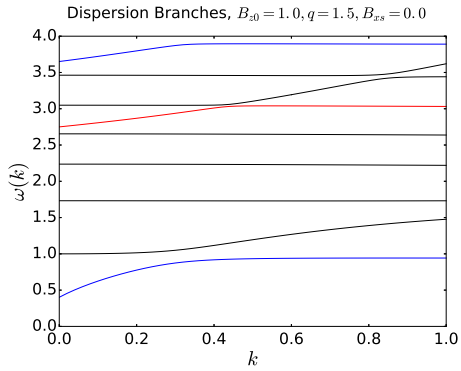

(a) $B_{xs} = 0$

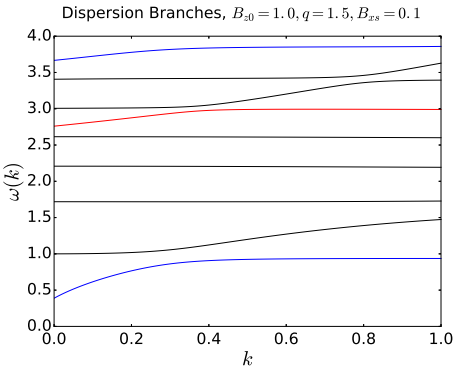

(b) $B_{xs} = 0.1$

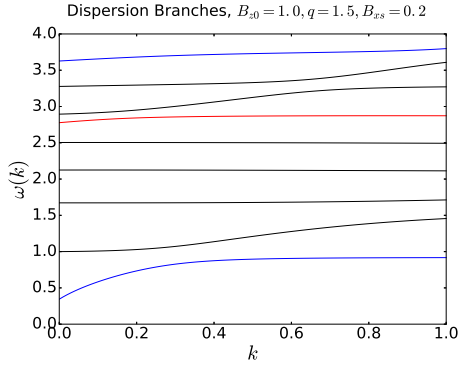

(c) $B_{xs} = 0.2$

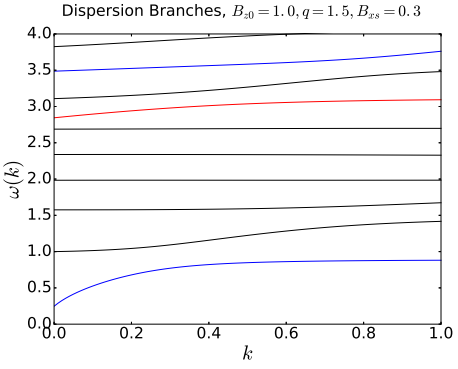

(d) $B_{xs} = 0.3$

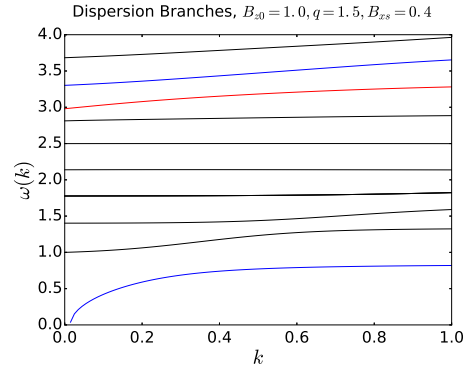

(e) $B_{xs} = 0.4$

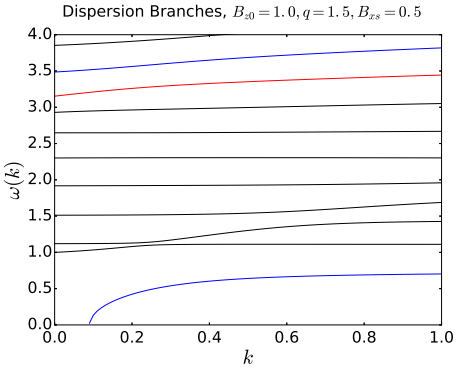

(f) $B_{xs} = 0.5$

Fig. 5.8: Dispersion branches at various field inclinations. $B_{z0} = 1$, $q = 1.5$ in all cases.

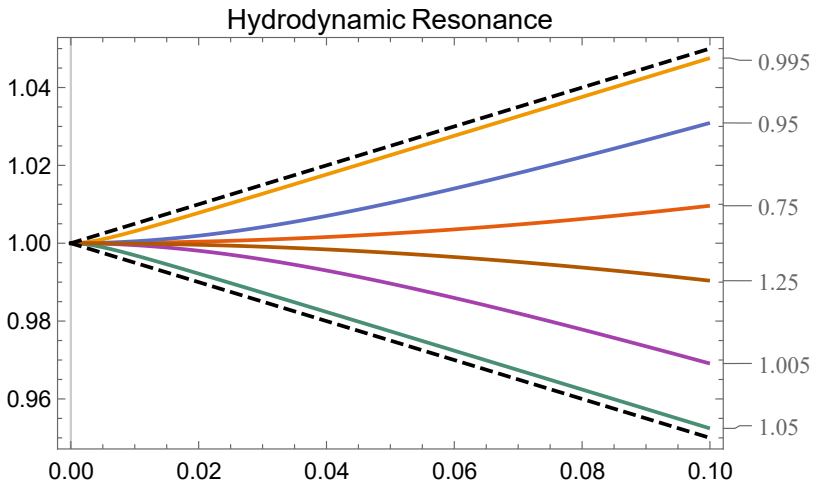

Fig. 5.9: The dispersion branch meeting the y axis at $\omega(0) = \Omega$ in a hydrodynamic disc at various values of epicyclic frequency κ (indicated on the right). The ratio of the epicyclic frequency to the orbital frequency is labelled for each curve. Shown in dashed black are curves of $\omega = \Omega \pm \frac{1}{2} c_s k$.

Hydrodynamic analogy

Consider the dispersion branches of a hydrodynamic slightly non-Keplerian disc, as shown in Figure 1.6. If one were to plot only the dispersion branch originating at $\omega/\Omega = 1$ at various values of epicyclic frequency κ, one would obtain a plot similar to Figure 5.9. When the epicyclic frequency $\kappa = 0.75$, the disc is far from resonance and the dispersion curve is quadratic. As the epicyclic frequency is raised towards $\kappa = \Omega$, the dispersion curve becomes nearly linear with a gradient of $1/2$, corresponding to the hydrodynamic resonance. When the epicyclic frequency exceeds the orbital frequency, the epicyclic branch of the dispersion curve now lies above the vertical oscillation branch, and one achieves an approximately linear curve with a gradient of nearly $-1/2$. As the epicyclic frequency is further increased, the quadratic character of the dispersion branch is re-established. In this way the hydrodynamic resonance – including the predicted dispersionless wave speed of a half the sound speed – may be probed numerically.

In Figure 5.10 we have shown a very similar plot but reduced the range

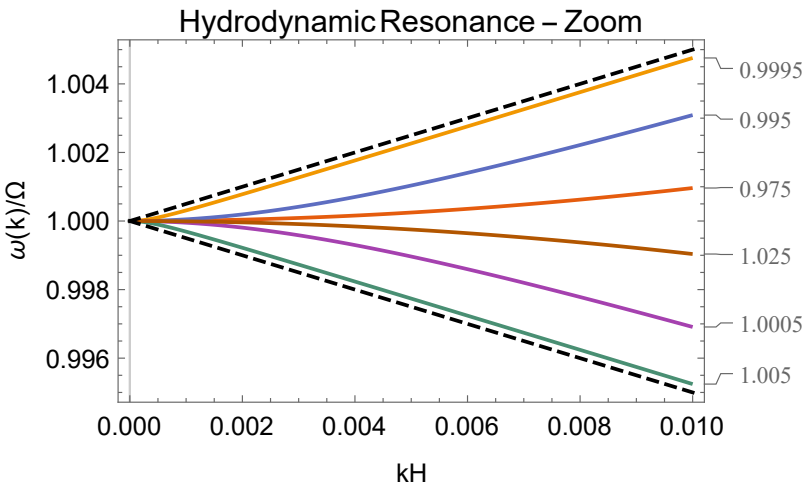

Fig. 5.10: A similar plot to 5.9, but over a smaller range of wavenumbers. Note that the epicyclic frequency must be more finely tuned in order to achieve resonant behaviour.

of wavenumbers by an order of magnitude. Note that in order to achieve resonance at this length-scale, the epicyclic frequency must be significantly (in fact, roughly ten times) closer to the orbital frequency. The purpose of this plot is to demonstrate that the presence or absence of resonant behaviour is dependent on the length-scale of the corrugation, as we discussed in section 1.4.2.

The vertical field case

Having demonstrated our method in the hydrodynamic case, we will now present equivalent results in magnetised warped discs. Rather than varying the epicyclic frequency however, we will be varying the magnetic field strength near its resonant value – the value at which the first slow AE frequency is equal to the vertical oscillation frequency.

The first slow resonance in the vertical field case is shown in Figure 5.11. The vertical field case is of particular importance – we have developed a quite comprehensive theoretical understanding of the resonance that must now be

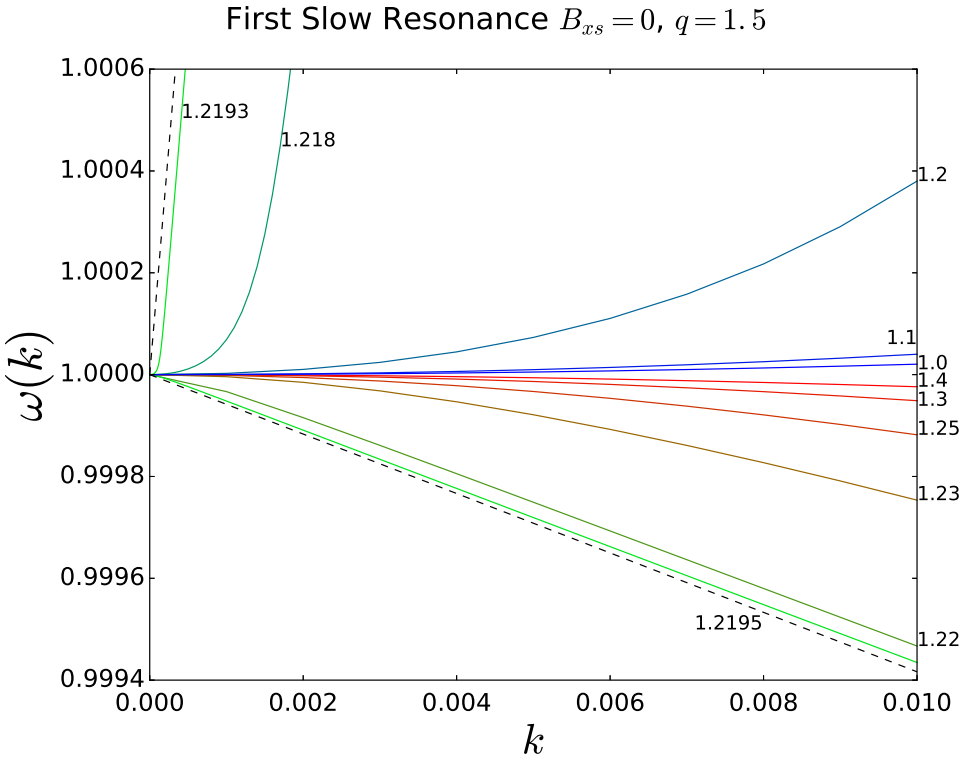

Fig. 5.11: The dispersion branch continuous with $\omega = 1$ at $k = 0$ at various values of magnetic field strength B for a Keplerian disc. Larger field values are coloured red, while weaker values are coloured in blue. The resonance, shown in green, occurs at $B_{z0} = 1.219$, consistent with our predictions. The theoretical dispersion curve of equation (5.105) are shown by the dashed black lines.

tested. Equation (3.78) would suggest that the resonance should occur at $B_{z0} = 1.2193$ – indeed, looking at Figure 5.11 this seems to be true. Just as in the hydrodynamic case, the behaviour of the dispersion curve is largely quadratic far from resonance but becomes linear as resonance is approached. The dashed lines represent the dispersionless wave speeds predicted at resonance by equation (5.105). Such close correspondence would seem to validate the analysis of this chapter.

Bending field configurations

We now present a similar analysis for bending poloidal fields, $B_{xs} \neq 0$. There is a slight complication – recall from section 4.2 and Figure 4.5 that bending fields may propagate angular momentum non-locally via the external field. Therefore the warping mode already has a linear contribution to its dispersion curve of magnitude B_{xs}^2. This not only makes comparison of the resonance between models with different inclination angles somewhat difficult, but also obscures the key physics we are investigating in this chapter – the importance of internal flows in magnetised discs.

We circumvent this issue by subtracting this linear contribution due to the external field from the dispersion curve. The result for $B_{xs} = 0.3$, corresponding to an inclination angle of 16.7°, is shown in Figure 5.12. After subtracting off the external field contribution, one finds that far from resonance the dispersion curve is quadratic as expected. The resonance occurs at $B_{z0} = 1.263$, a higher value than in the vertical field case. Most importantly, the 'wave speed anomaly' – the contribution to the linear component of the dispersion curve due to the internal flows at resonance – is considerably larger than in the vertical field case, corresponding to a wave speed of $-0.2c_s$ As we had speculated, it appears that a bending wave may provide a stronger coupling between the AE mode and the vertical oscillation mode, enhancing the angular momentum transport at resonance.

The original dispersion curve, without subtracting off the non-local linear magnetic term, is shown in Figure 5.13. Far from resonance equation (4.99) approximates the dispersion curve well; the internal torque only makes a minor quadratic contribution. At resonance the internal torque is greater than the external magnetic torque, dramatically and qualitatively changing the behaviour of the wave mode.

The dispersion anomaly is plotted for other values of B_{xs} in Figure 5.14, though the interpretation largely remains unchanged. The greater the bending

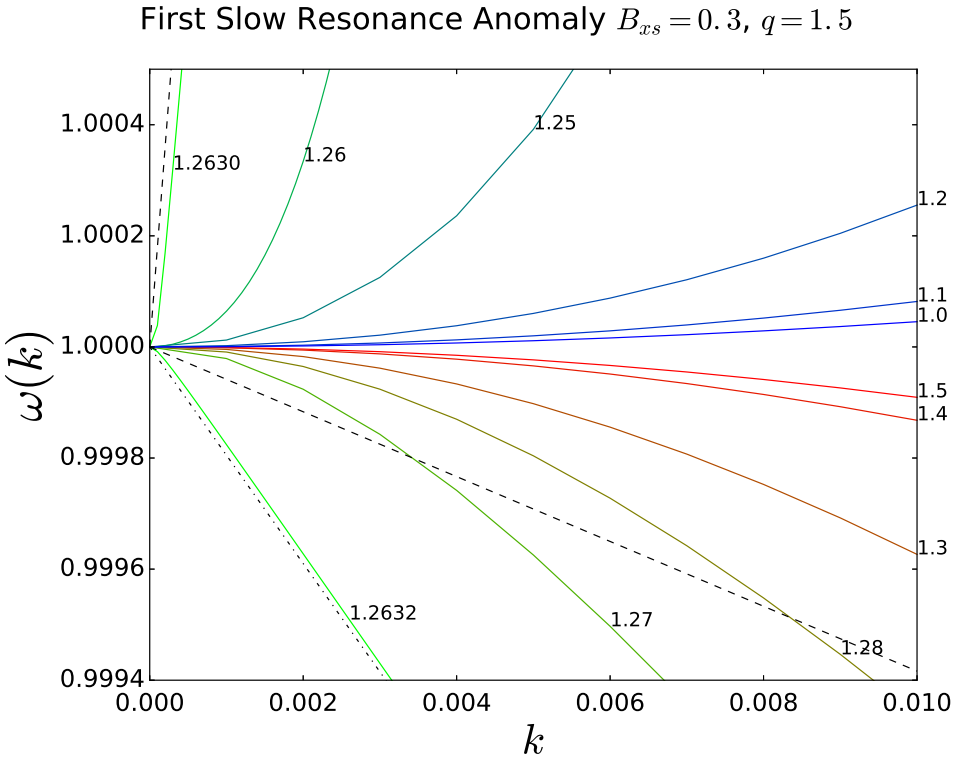

Fig. 5.12: Resonance between the vertical oscillation mode and the first slow AE mode for a Keplerian disc with a bending field of $B_{xs} = 0.3$, or an inclination angle of 16.7°. The dashed line represents the dispersion curve at resonance in the vertical field case. The dash-dot line is an empirical estimate of the dispersion curve at resonance.

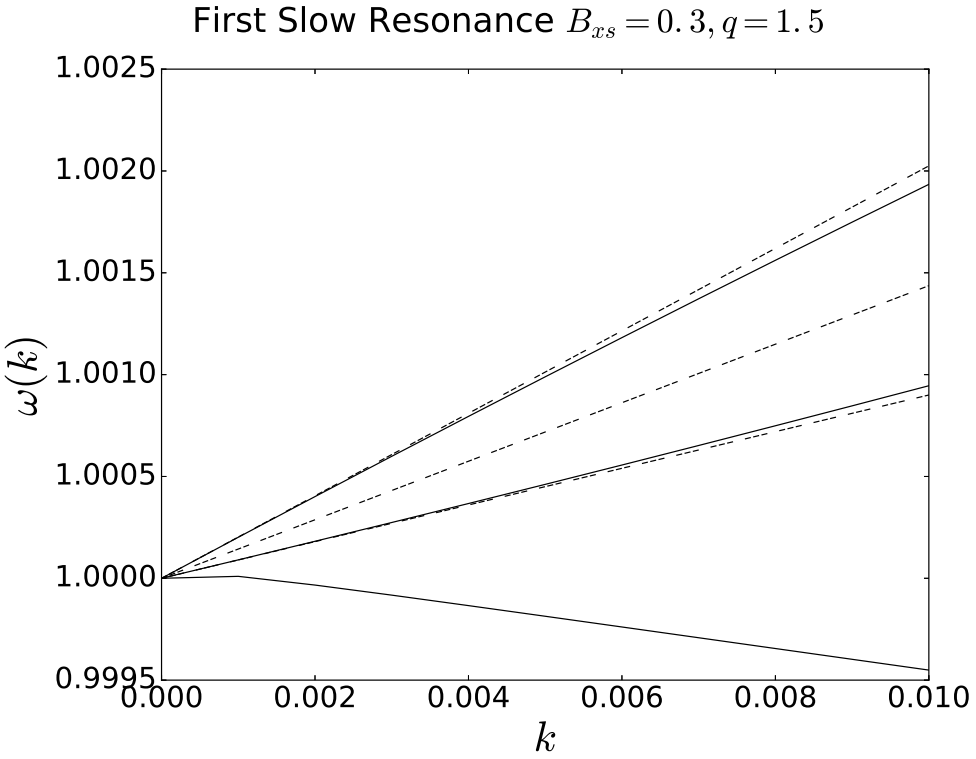

Fig. 5.13: Resonance between the vertical oscillation mode and the first slow AE mode for a Keplerian disc $B_{xs} = 0.3$. The dashed lines, from top to bottom represent the linear contribution due to the external field at $B_{z0} = 1.5, 1.264$ and 1.0 respectively. For $B_z = 1.0$ and $B_z = 1.5$, the dispersion curve shows only slight quadratic deviation. At $B_z = 1.264$ however, the wave speed is substantially altered by the internal torque.

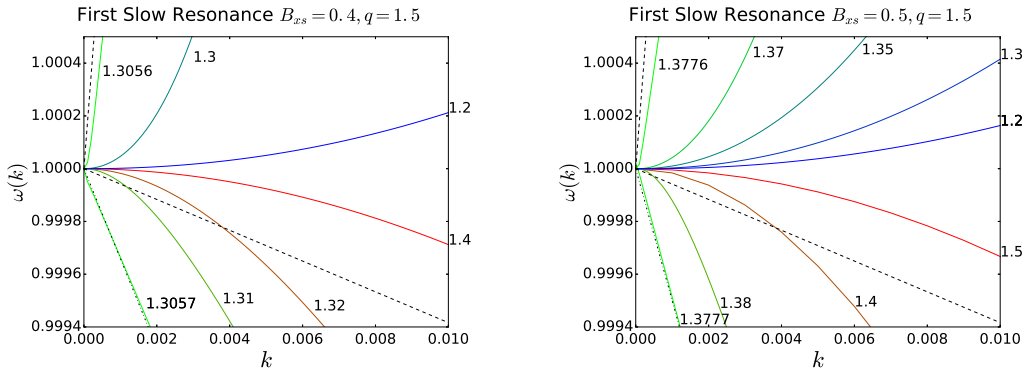

(a) $B_{xs} = 0.4$ (b) $B_{xs} = 0.5$

Fig. 5.14: Similar to Figure 5.12, the dispersion branches at the resonance between the first slow AE mode and the vertical oscillation mode at different values of magnetic field strength B (labelled along each curve) and bending field inclination B_{xs}.

in the poloidal field, the stronger the coupling between the vertical oscillation mode and the greater the influence of the internal torque at resonance. By finding the gradients of the dispersion curve anomalies near resonance, as we discussed in the case $B_{xs} = 0.3$, we may quantify a 'wave speed anomaly' – the change in the implied wave speed of the vertical oscillation mode due to the resonance. The wave speed anomaly is shown in Figure 5.15.

5.7 Summary and Discussion

In this chapter we synthesised the semi-analytical approach of chapter 3 with the corrugated sheet formalism of chapter 4 to examine both the vertical oscillation mode and the Alfvénic-epicyclic modes in both the resonant and non-resonant regimes. Using this mathematical scheme we were able to re-derive the results of chapter 3. Semi-analytical expressions were found for the asymptotic long-wavelength behaviour of the Alfvénic-epicyclic modes. An analytical expression was also found for the dispersion curves in the resonant case. The hydrodynamic resonance of inviscid Keplerian discs was re-derived in the weak field limit, in which case the vertical oscillation mode becomes resonant with many fast Alfvénic-epicyclic modes. In all cases, the analytical

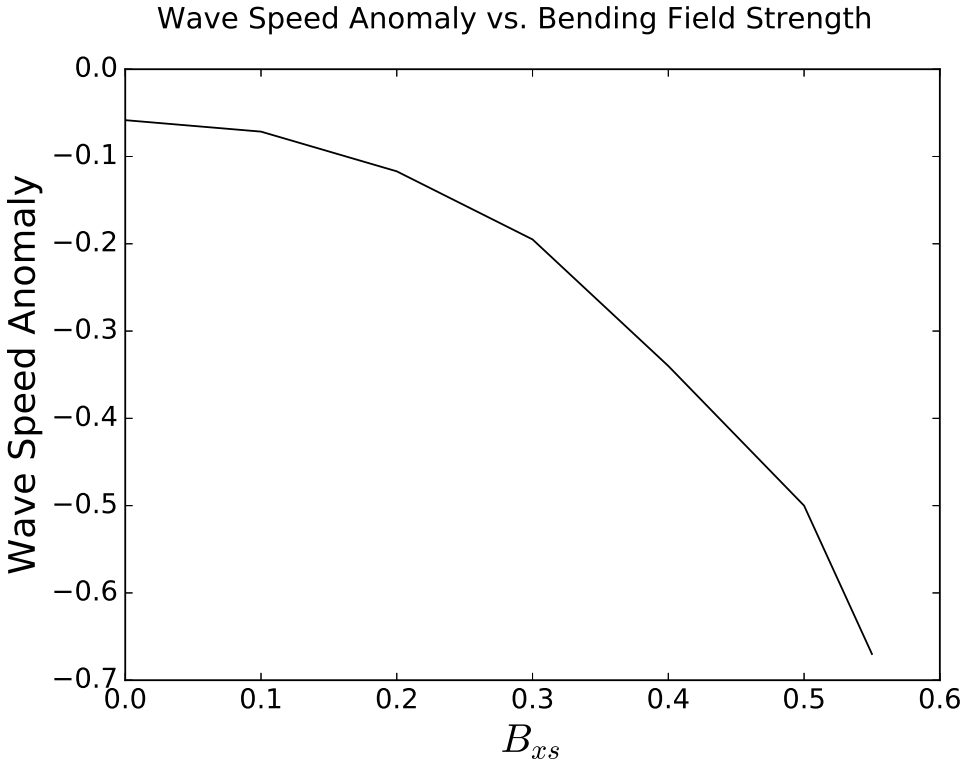

Fig. 5.15: The wave speed anomaly – the contribution to the wave speed as $k \to 0$ due to the internal torque when the vertical oscillation mode is resonant with the first slow AE mode – for various values of radial field strength B_{xs}. Note that stability against magnetocentrifugal outflows implies that $B_{xs} < 1/\sqrt{3}$.

results were strongly supported by the numerical method discussed in chapter 4.

It was found that while the warp propagation can be enhanced by resonance, in the vertical field case the effect is relatively weak. In the asymptotic limit of small k, the warp would be expected to travel as a dispersionless wave at no more than $0.06c_s$.

A numerical investigation of the bending field regime was also presented. The bending field couples the vertical and horizontal oscillation modes, enhancing the effects of resonance. At inclination angles greater than 20°, the warp may travel at an anomalous speed greater than half the sound speed. We therefore conclude that the resonance between the Alfvénic-epicyclic modes and the vertical oscillation mode may indeed qualitatively and significantly alter the propagation of the warp, though a bending field greatly enhances this effect.

In real discs many of the relevant parameters such as magnetic field strength, density, inclination angle and shear rate may vary with radius. It is difficult at this stage to make any sweeping comments about warp propagation through an inhomogeneous medium. However, given the spectrum of Alfvénic-epicyclic resonances and the non-local transport of angular momentum by the magnetic field, a wide variety of interesting and unexpected phenomena may be possible such as the pile-up or trapping of bending waves (potentially even driving a fragmentation event). This is of course speculative; it is my hope that the work of this chapter might be used to interpret the behaviour of future simulations of bending waves in magnetised discs. In the next chapter we take a tentative first step in this direction.

At this point we have established both a numerical and theoretical understanding of warp propagation in magnetised discs within certain regimes and under certain simplifying assumptions. In the following chapter we discuss the

application of the theory we have developed to simulations. We also present and interpret a set of introductory simulations of a magnetised warped disc using a customized grid-based code Athena++.

6. APPLICATION TO SIMULATIONS

6.1 Introduction

In the previous chapters we developed various approaches to investigate the wave modes of a warped magnetised disc. It was noted with some relief that the numerical and semi-analytical methods presented appear to be in agreement. However, thus far the methods presented in this thesis have been restricted to the analysis of abstracted models and the numerical results of one-dimensional ODE solvers. How should the key concepts of this thesis be applied to warped disc simulations? How accurate in practice are the numerical methods and theoretical predictions that have been proposed? In this chapter we present an analysis of various warped disc simulations using the grid-based MHD code Athena++. In the process we hope to bridge the divide between theory and practice as well as demonstrate the utility of the methodology we have developed.

In the following section we discuss the details of our simulation, including a few technical caveats regarding the boundary conditions. In section 6.3 we present a series of fiducial simulations of hydrodynamic warped discs. In section 6.4 we discuss the structure of the magnetised warped disc. We also calculate and compare the wave frequencies of the normal modes contributing to its motion with the results of previous chapters. In section 6.5 we put briefly discuss how our results fit within the theoretical discussion developed over the previous few chapters.

6.2 Details of the Simulation

In order to perform our simulations we use a customized version of the grid-based MHD code Athena++ (White, Stone & Gammie, 2016), the recent successor to Athena. Athena++ solves the equations of compressible, ideal MHD in conservative form by a finite-volume method. It is a higher-order Godunov scheme that computes the fluxes of conserved variables by solving a Riemann problem at each cell interface. The divergence-free condition on the magnetic field is maintained by the constrained transport algorithm, which updates the magnetic fluxes through cell interfaces according to the electromotive forces around their edges. The code runs in parallel on multiple cores using MPI.

We wish to simulate a magnetised warp disc in a very simple test case that will be both physically interesting and easily understandable. For this reason we consider a disc threaded by a purely vertical magnetic field in a two-dimensional shearing box subject to a small initial velocity perturbation, $v_z = \zeta_0 \cos(kx)$. Our plan is to initialise this disc by applying this small vertical perturbation at $t = 0$ and simply allowing the disc to evolve in time.

If we are interested in warps, why are we looking at vertical oscillations in a local shearing box? As we discussed in earlier chapters (e.g. chapter 3), a vertical oscillation at the orbital frequency in the local fluid frame corresponds to a static tilt of the disc in a global inertial frame. Radial variation of this vertical oscillation in the local frame thus corresponds to a static warp in the global frame. Notably any deviation of the oscillation frequency from the orbital frequency in the shearing box would correspond to the time evolution of the warp in a global inertial frame. We may therefore interpret any deviation from a perfect vertical oscillation in this simulation as indicative of warp evolution.

The disc is assumed to be isothermal and vertically stratified; an appropriate vertical gravitational force is added to the code and the disc is initialised

with an appropriate Gaussian density profile. The standard horizontal boundary conditions of the shearing box are periodic in y and shearing-periodic in x. For simplicity we seek axisymmetric solutions that are independent of y; the boundary conditions then simplify to being periodic in x. In order to study long-wavelength warps, the box needs to radially extended. This necessarily implies that the radial extent of the box should be some integer number of wavelengths; in practice this is always one.

The vertical boundary conditions are somewhat more challenging. Often outflow boundary conditions are applied to the primitive variables to imitate the free outer boundary of the disc; however, we have found them to be unsuitable because the vertical oscillation tends to evacuate the disc over several orbits and contributes to numerical instability of the solution. The imposition of a density floor was also found to promote instability, and so was avoided. In practice we found that periodic boundary conditions on the primitive hydrodynamic variables best suited our problem. The magnetic boundary conditions however were more subtle. We wished to, in analogy to the discussion of chapter 4, allow the poloidal magnetic field to decay on the lengthscale $1/k$ related to the horizontal wavelength of the corrugation. This corresponds to matching the magnetic field onto a force-free (in fact, potential) field beyond the computational domain (if the corrugation wavelength is sufficiently small relative to the radial length-scale of the disc). We will discuss how this was achieved in the following section.

The computational difficulties of this problem when compared to its hydrodynamic counterpart, alluded to in section 1.6, are to be emphasized. Far from the disc mid-plane the density becomes very low due to the density stratification; this in conjunction with a strong net vertical field leads to an extremely large Alfvén speed near the disc boundary – and a correspondingly small time-step. The MHD warped disc simulations described in this section are three to four orders of magnitude slower than the corresponding hydrodynamic problem. In addition, several simulations are required in order to

explore the dependence of the disc evolution on parameters such as magnetic field strength and choice of boundary condition. Consequently every effort was made to be frugal while running the simulation.

Box parameters were chosen that strike a balance between computational efficiency and utility. The resolution of our disc is relatively poor – The shearing box is 10 scale heights vertically and 40 scale heights in the radial direction, and our resolution is (640x160) in all runs unless otherwise specified. We note however that there is no implicit viscosity or MRI turbulence in our simulation. We are primarily concerned with the large-scale mean flows, and have no need to resolve smaller scales. All structures worthy of note remain well-resolved throughout our runs.

The box width of 40 scale heights implies, if we fit a single wavelength into the box, a minimum wavenumber k equal to $\pi/20 \approx 0.157$. While we would like to probe the long-wavelength limit, increasing the radial box length would make the computational cost more prohibitive. Similarly, our choice of 10 scale heights in the vertical direction was based on a balance between minimising computational cost while ensuring reasonable physical fidelity. Typically the MHD simulations are allowed to run for tens of orbits, which shall be sufficient for the purposes of this investigation. Sadly due to computational limitations we are only able to investigate a few distinct simulations, probing only a small but meaningful region of parameter space.

Results were outputted at intervals $\Delta t = 0.01$ in units such that the orbital frequency is 1. Consequently a single orbit takes approximately 6.14 time units or 614 cycles. Occasionally results may be outputted at intervals $\Delta t = 0.05$ units for various reasons; we will highlight when this is relevant and adjust all plots accordingly. The ROE approximate Riemann solver was used in all runs and the Courant number was set to 0.3 to determine the time-step, ensuring the Courant-Friedrichs-Lewy (CFL) condition always remained satisfied.

6.2.1 The Vertical Boundary Condition on the Magnetic Field

We seek a boundary condition to be applied on the poloidal magnetic field components that will allow them to match a force-free solution outside the computational domain as described in chapter 4. The boundary condition used in our previous numerical approaches, equation (4.17), is unfortunately too simplistic because it assumes that only one wavenumber k is present. To adapt it for a nonlinear numerical simulation, we begin with the divergence condition

$$\partial_z B_z + \partial_x B_x = 0. \tag{6.1}$$

Performing a Fourier transform in radial coordinate x and assuming an appropriate decaying vertical solution, gives

$$\tilde{B}_x = -i\ s(k)\tilde{B}_z \tag{6.2}$$

where $s(k)$ is a shorthand for the sign function $s(k) = k/|k|$. We attempt to find a prescription or a kernel that allows one to fill the ghost zones for B_x given a surface distribution B_z on the vertical boundary.

Periodic boundary conditions have been imposed in the x-direction with a computational domain between $-L/2$ and $L/2$, where L is the radial extent of the box. We wish to find what the above result in Fourier space implies in real space in this particular situation. One method is to take the Fourier transform of equation (6.2), revealing the $1/(x - x')$ nature of the kernel in real space. Using the Poisson summation formula, the periodic nature of the boundary conditions implies that this kernel can be represented as an infinite sum. Careful consideration of the sum implies that the kernel is of the form

$$B_x(x) = \int_{-L/2}^{L/2} \left(B_z(x') \cot(\frac{\pi(x - x')}{L}) \right) dx' \tag{6.3}$$

This term is formally divergent when $x = x'$ - a feature that is often encountered in the analogous problem of a self-gravitating disc. Fortunately Athena++ evaluates the magnetic field at the cell faces, implying that B_x and B_z are evaluated on grid cells staggered by half a cell width. There is therefore no divergence and (6.3) may be used with impunity. The discretised form may be written as

$$B_x(i, j_g) = \frac{1}{N_x} \sum_m (B_z(m, j_e) - B_{av}) \cot(\frac{\pi(i - m - 0.5)}{N_x}) \tag{6.4}$$

where i is the grid cell along the x-direction, j_e is the value of the z-direction cell coordinate j at the upper (or lower) boundary, j_g is the value of j corresponding to a ghost cell, N_x is the number of cells in the x-direction, and B_{av} is the average value of B_z at the upper boundary. Expression (6.4) enables us to fill the ghost zones in such a manner consistent with an exponentially decaying magnetic field perturbation as described in chapter 4.

We therefore customized the Athena++ code by writing a subroutine to provide a user-defined set of boundary conditions. This implements periodic vertical boundary conditions on the hydrodynamic variables, but instead implements the non-local boundary condition (6.4) on the magnetic field component B_x, which corresponds to matching the computed interior solution to a potential exterior field. B_z was copied into the ghost zones directly from the boundaries, while B_y was set to zero in the ghost zones as per the analysis of chapter 4.

6.3 Hydrodynamic Simulations

We begin with a brief summary of a few relevant hydrodynamic warped disc simulations. The hydrodynamic case not only provides a point of reference for our later MHD simulations, but also introduces the methodology we will apply to MHD discs in a setting that is more familiar to most readers.

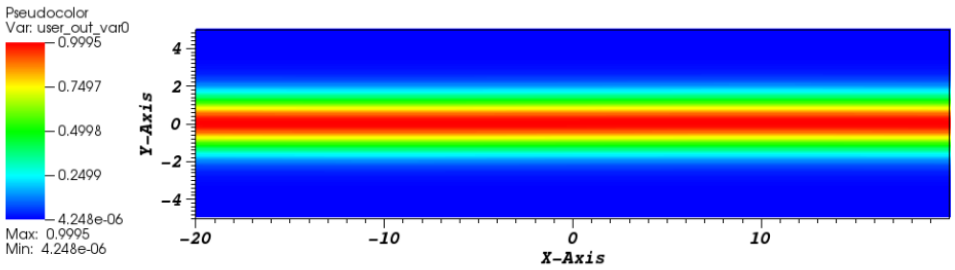

Fig. 6.1: The density of a warped disc with $\zeta_0 = 0.01$ within the warped shearing box. The warp is too small to be seen by eye.

We present three distinct models: a Keplerian disc in a standard box ($k = \pi/20$), a non-Keplerian disc with shear rate $q = 1.6$, and a Keplerian disc in an elongated box ($k = \pi/100$). The first two simulations are intended to display the effects of resonance on the output, while the third demonstrates the effect of box size.

The density and radial velocity are shown in Figures 6.1 and 6.2. The warping induces radial flows within the disc with the expected phase relation and characteristic linear vertical structure (Figure 6.2 (b)).

Our primary interest lies in the connection between the time evolution of these discs and the free wave modes of the system. If the value of the vertical velocity at a particular point in the shearing box is plotted as shown in Figure 6.3(b), one notices a peculiar beat pattern. This may be understood by considering the dispersion branches of the hydrodynamic disc. For inviscid Keplerian discs, the relevant waves travel in a dispersionless manner at half the sound speed; notably at $k = \pi/20$ (see the outer vertical lines of Figure 6.3(a)) there are two solutions with positive k – namely $\omega_+ = 1 + \pi/40$ and $\omega_- = 1 - \pi/40$. We will not go into too much detail, but by symmetry the initial warp is projected with equal weighting upon both modes. Their different frequencies generate a 'beat', which in this case can be shown to be at the frequency $\omega_{beat} = \pi/20$. Using a box five times longer should in theory

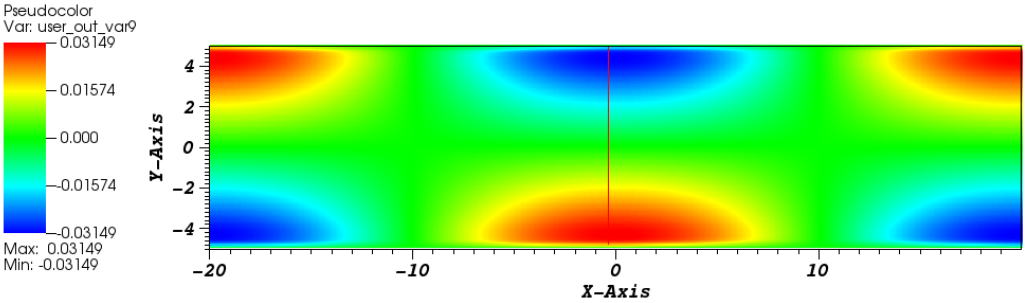

(a) Radial velocity v_x within the shearing box. Note that the x and y axes of the simulation correspond to the x and z axes of our model.

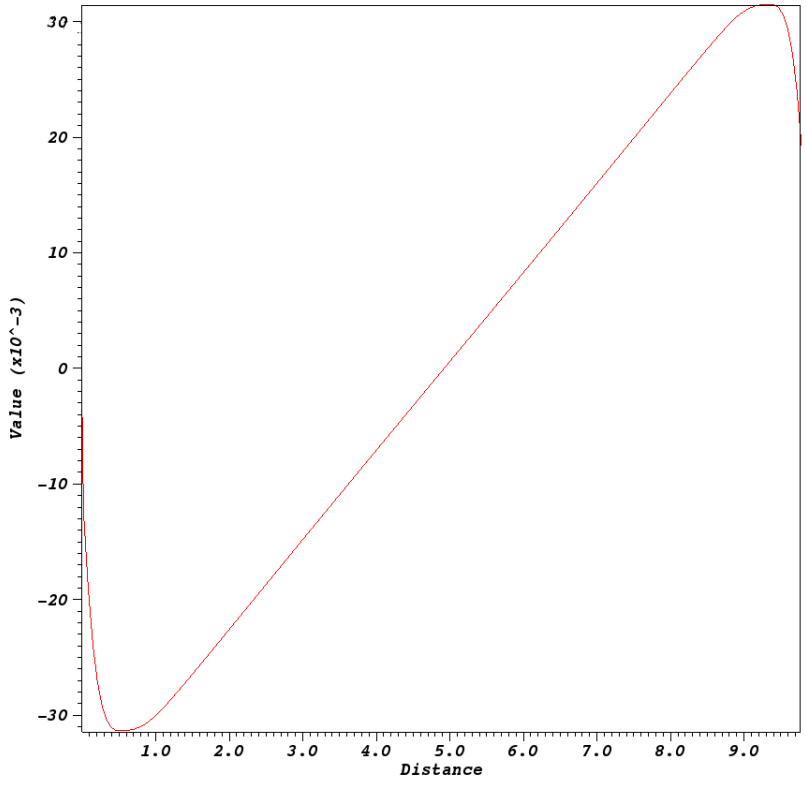

(b) vertical profile of v_x, with the disc midplane defined in this plot to be at 5.0 on the x-axis.

Fig. 6.2: Radial velocity in a hydrodynamic warped disc. The velocity profile is cosinusoidal in x and is linear in z, though the periodic boundary condition alters this near the boundaries.

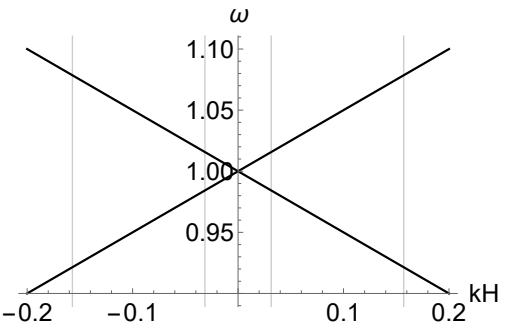

(a) Dispersion relation for a hydrodynamic Keplerian disc. Grey vertical lines indicate the wavenumbers associated with the long and short box simulations.

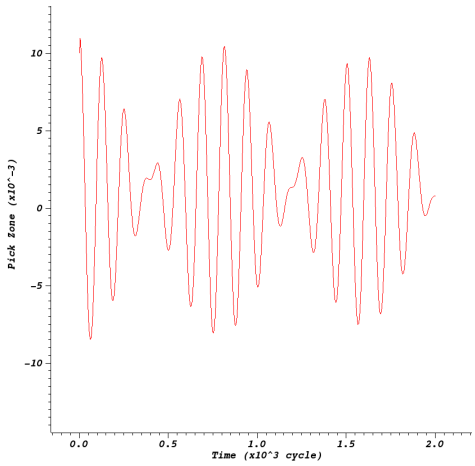

(b) v_z at a particular grid-point in time in a $q = 1.5$, $k = \pi/20$ run.

Fig. 6.3: Verical velocity v_z at a representative point in the shearing box for the Keplerian small box run. The warp is projected equally onto the two modes with frequencies shown in the left hand panel at where the outer vertical lines cross the dispersion curve. A beat frequency is established, corresponding to the relative phase relations of the two components.

produce a beat frequency five times slower (the inner vertical lines of Figure 6.3); this is indeed borne out by simulation.

The non-resonant case is similar in principle. The warping of the disc has coupled the vertical and epicyclic modes, and our initial warp – which lacked any horizontal motion whatsoever – must again be projected onto some combination of the warping branch of the dispersion curve and the epicyclic branch of the dispersion curve, as shown in Figure 6.4(a). In this case, however, the projection is not equally weighted, and the vertical oscillation branch dominates the motion. The warping mode dominates the vertical velocity profile as shown in Figure 6.4(b), but the epicyclic contribution constructively and destructively interferes, modulating the amplitude.

The radial velocity is initialised to zero; this forces a particular weighting of the vertical oscillation mode and the epicyclic mode, and this weighting

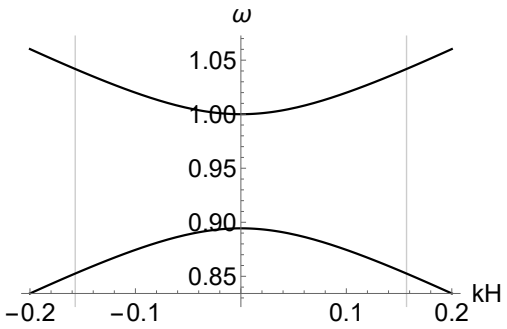

(a) Dispersion relation for a hydrodynamic non-Keplerian disc. Grey vertical lines indicate the wavenumbers associated the short box simulation.

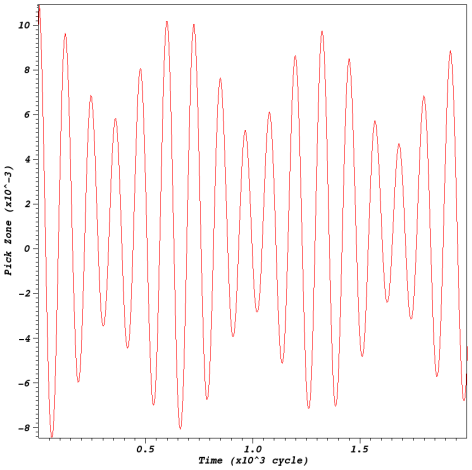

(b) v_z at a particular grid-point in time.

Fig. 6.4: The same setup as Figure 6.3, but for a non-Keplerian simulation ($q = 1.6$).

does not change with time. Hence the radial velocity amplitude oscillates in time like the vertical velocity, but unlike the vertical velocity profile the horizontal profile will always contain equal contributions (at different frequencies) from both modes. Figure 6.5(a) shows the amplitude of the radial velocity at a representative point in the shearing box simulation with $q = 1.6$ plotted through time. Figure 6.5(b) is a model constructed by assuming that the radial velocity has two components of equal magnitude from the vertical oscillation branch and the epicyclic branch, but at different frequencies given by (1.31). Notably, at $q = 1.6$, the vertical oscillation branch has frequency $\omega_w = 1.042$ and $\omega_e = 0.853$. As the waveform is very sensitive to the frequencies involved, matching waveforms to unknown frequencies is a powerful and useful tool for identifying wave mode frequencies using only a few orbits. We use this technique in a MHD context in the next section.

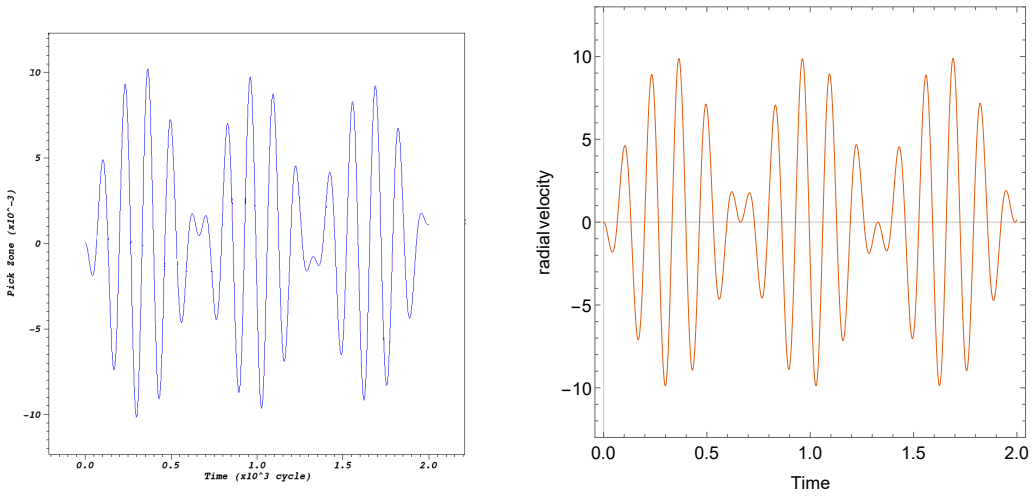

(a) Simulation *(b)* Model

Fig. 6.5: Radial velocity in a non-resonant hydrodynamic warped disc. In the left panel is the radial velocity at an representative point in the box, plotted through time. On the right is the output of a simple model assuming equal contributions from one oscillation at the warping mode frequency and another at the epicyclic frequency.

6.4 MHD Simulations

Five simulations are presented in this section. All models are of Keplerian discs at different values of magnetic field strength: $B_{z0} = \{0.947, 1.219, 1.26, 2.53, 6.32\}$[1]. The simulation run at $B_{z0} = 0.947$ is only marginally MRI stable (see Figure 6.11). $B_{z0} = 1.219$ corresponds to a disc in which the vertical oscillation frequency is predicted to be resonant with the first slow AE mode. $B_{z0} = 1.26$ is a near-resonant disc, while $B_{z0} = 2.53$ and $B_{z0} = 6.32$ begin to probe the strong-field limit. The warp in all cases was initialised via a sinusoidal perturbation to v_z. Some models were run at $\zeta = 0.01$, while others were run at $\zeta = 0.001$; qualitatively little difference was found beyond a uniform scaling of all parameters.

[1] Due to a discrepancy in disc mass normalisation by a factor of $\sqrt{2\pi}$, in code units these magnetic field strengths correspond to $B_{z0} = \{1.5, 1.93, 2.0, 4.0, 10.0\}$. I have have adjusted these values to be consistent with the mass normalisation convention used in the remainder of this thesis.

6.4.1 Vertical Structure

The work of chapters 3–5 makes explicit predictions about the relative phases and vertical structures of the physical quantities. For example, the radial velocity perturbation and the field perturbation should be phase shifted by $\pi/2$ (for example, see section 3.3.2). These relations are found to be preserved in the simulations. We may take linear vertical slices of the physical quantities and compare them to our results of the previous chapters. The radial velocity and magnetic field[2] are plotted, along with the equivalent results derived at $k = \pi/20$ using the numerical method of section 4.9. Note that we have adjusted the z-axis to be measure the distance along the vertical slices shown in part (a) of the figures in order to ease direct comparison.

Overall there is very good qualitative and quantitative agreement between the numerical method of section 4.9 and the simulation results as can be seen in Figures 6.6 and 6.7. The radial velocity profile may be understood as $u_i(z)$ (Figure 3.2), but amended to match with a decaying velocity profile on the corrugation length-scale.

It is interesting to note the appearance of higher order mode structures at the nodes of the dominant mode as shown in Figure 6.8. These structures are smaller than the dominant mode by a factor of order of the corrugation amplitude and have twice the radial number; most likely they herald the onset of non-linearities.

6.4.2 Determination of the Wave Frequencies

We propose here a method of determining the wave frequencies of the modes contributing to the motion of the disc. By observing the value through time of v_z at a particular point (chosen to be at the point of greatest amplitude),

[2] The magnetic field strengths plotted here are in the code units, which differ from the convention of this thesis. The plotted values are therefore $(2\pi)^{1/4}$ larger than they should be.

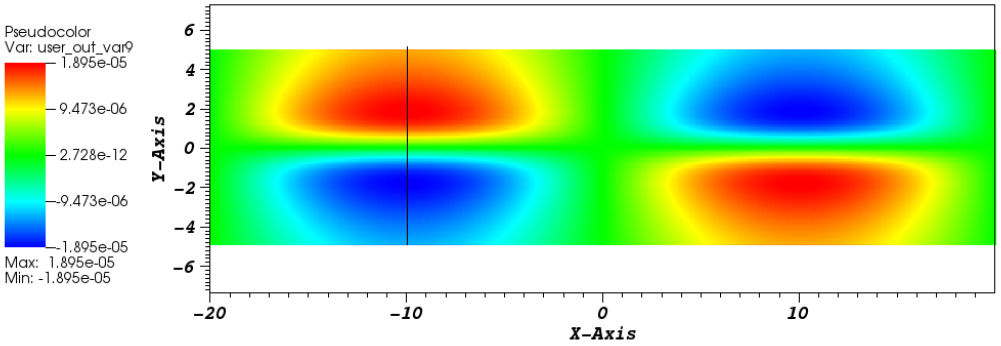

(a) Radial velocity v_x within the shearing box in the $B_{z0} = 2.53$ run, taken at $t = 314$ cycles or half an orbit.

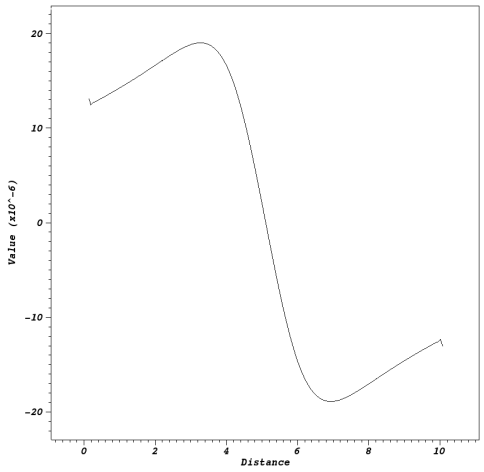

(b) v_x along the black line shown in part (a)

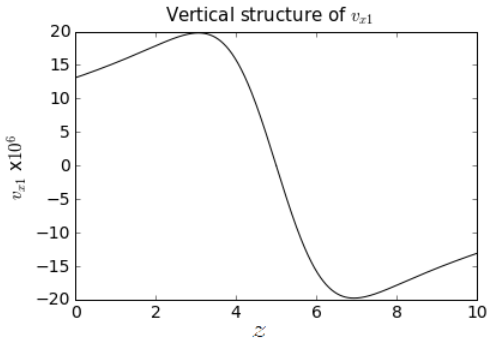

(c) v_{x1} calculated using the numerical section of section 4.9

Fig. 6.6: Radial velocity in a magnetised warped disc. The velocity profile is cosinusoidal in x and increases linearly in z before decaying on the corrugation length-scale. There is good agreement between the vertical profile observed in simulation and using the one-dimensional solver of section 4.9.

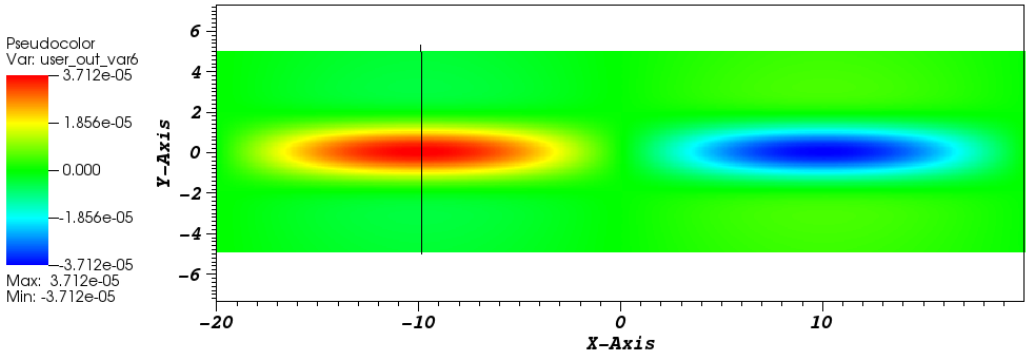

(a) Radial magnetic field B_x within the shearing box in the $B_{z0} = 2.53$ run, taken at 471 cycles or $3\pi/2$ phase.

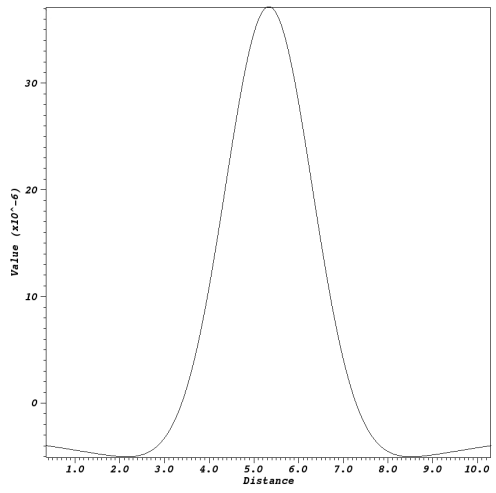

(b) B_x along the line shown in part (a)

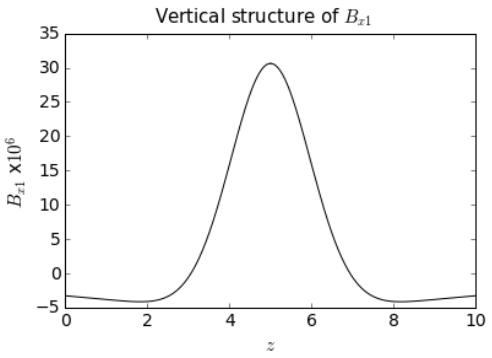

(c) B_{x1} calculated using the numerical section of section 4.9

Fig. 6.7: Radial magnetic field in a magnetised warped disc. The field profile is sinusoidal in x and decays on the corrugation length-scale.

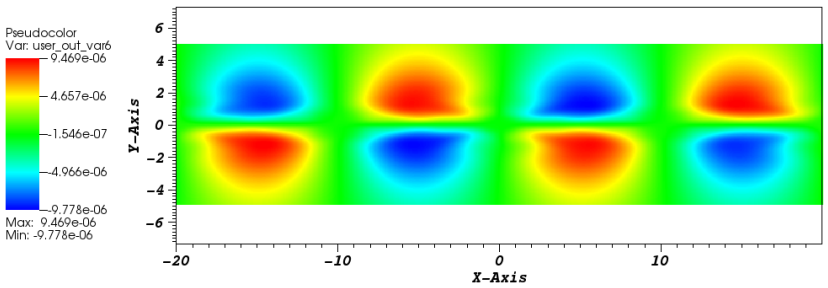

Fig. 6.8: The radial magnetic field at t=1569 cycles or phase 5π in the $B_{z0} = 6.32$ model, corresponding to a node in the dominant oscillation shown in Figure 6.7(a). The structures shown here are smaller than the dominant mode by roughly a factor of the corrugation amplitude.

one can observe a clear single frequency with slight modulation. We are able to determine the frequency of this dominant contribution to within a reasonable degree of accuracy over many orbits. We label this frequency $\omega_{w(sim)}$, the frequency of the warping mode inferred from simulation, and have listed these values in Table 6.1.

The error estimates were determined in the following way. We are able to identify the maximum or minimum of the signal with an accuracy of a cycle, or 0.01 in the time units of the problem. If we assume the existence of a single wave mode of constant unknown frequency close to 1, then after ten orbits we may estimate the value of ten times the period, approximately 20π time units, with an error of 0.02 time units. Naively this gives an error bound of 0.0005 for the wave frequency. In practice however the disc is modulated, and the period between successive extrema may vary by as much as a percent. Yet these variations are themselves periodic and average away to zero. After consideration it was established that the error may be conservatively estimated at 0.001.

The radial velocity in time at a given point in the box (again chosen to be the point of maximal amplitude) was plotted as shown in the left hand side of Figure 6.10. Let us assume that there are only two relevant modes; the warping mode and some other a priori unknown mode, which we will see

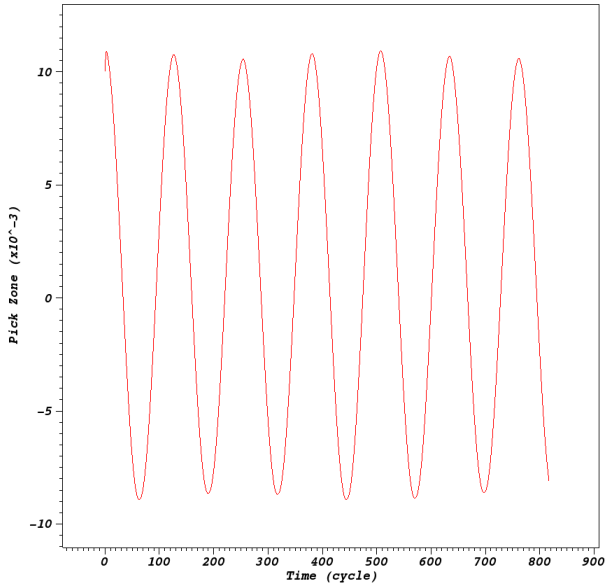

Fig. 6.9: The vertical velocity against time at a particular representatitive point in the $B_{z0} = 1.219$ simulation of the resonant case. A small but noticeable modulation of the oscillation can be observed.

is the nearest AE branch of the dispersion curve. In that case, the initialisation of the disc implies that there will be equal and opposite contributions to the radial velocity from the warping mode, now of known frequency, and the unknown AE mode branch of unknown frequency. By tuning this unknown frequency to match the profile of the response, we may obtain an estimate of the AE mode frequency. This method is quite sensitive and thus provides a surprisingly accurate estimate of the wave frequencies. This process is demonstrated in the right hand panel of Figure 6.10 using the calculated values $\omega_{AE(sim)}$ values of Table 6.1. Note that while small contributions from higher order modes are evident in left hand plots of Figure 6.10, the broad outline of the radial velocity amplitude can be determined purely from this two-mode model. This would suggest that we are somewhat justified in our assumption that a single AE mode branch dominates the solution.

The values of the warping mode branch frequency and the nearest AE

Field Strength	Simulation	Model
$B_{z0} = 0.947$	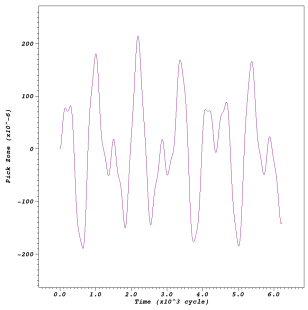	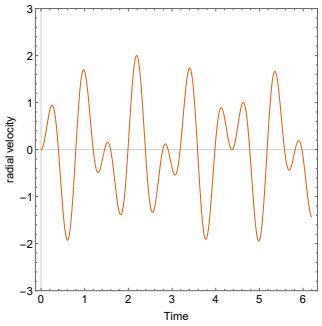
$B_{z0} = 1.219$	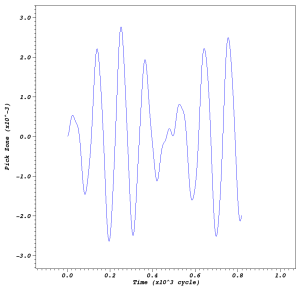	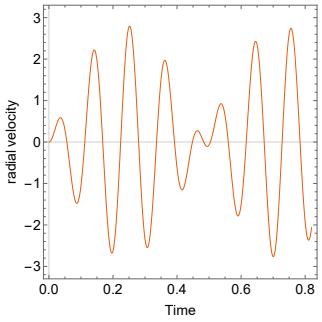
$B_{z0} = 1.26$	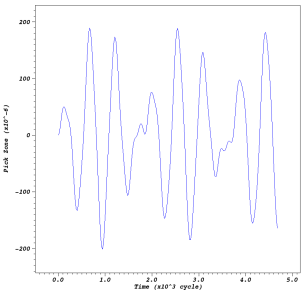	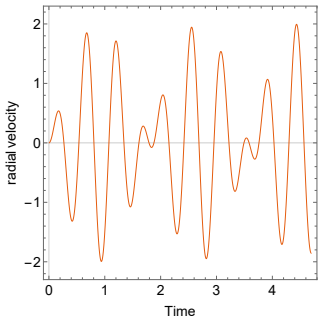
$B_{z0} = 2.5$	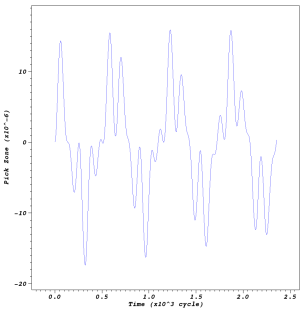	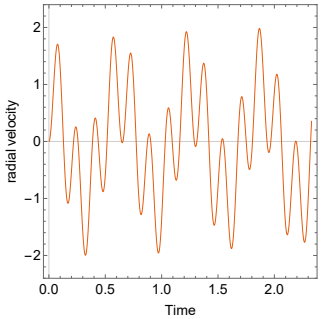
$B_{z0} = 6.3$	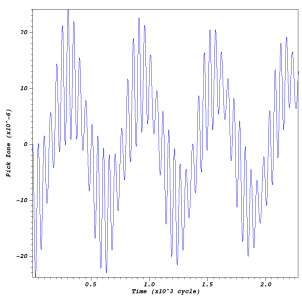	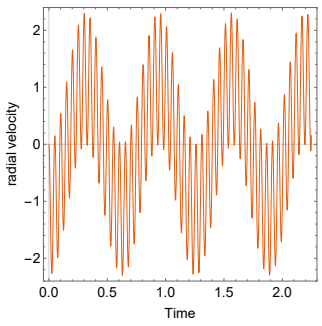

Fig. 6.10: The amplitude of the radial flows in time at a particular representative point in the shearing box. On the left is the output directly from the simulation. On the right is a simple two-mode model in which one of the frequencies, $\omega_{AE(sim)}$, is fitted.

B_z	$\omega_{w(th)}$	$\omega_{AE(th)}$	$\omega_{w(num)}$	$\omega_{AE(num)}$	$\omega_{w(sim)}$	$\omega_{AE(sim)}$
0.947	1.004	1.86*	1.0051	0.5725	1.0055 ± 0.001	0.573 ± 0.005
1.219	0.9908	1.286	0.9919	1.252	0.991 ± 0.001	1.251 ± 0.002
1.26	0.972**	1.3707	0.9942	1.3466	0.994 ± 0.001	1.345 ± 0.005
2.53	0.9993	3.918	0.9995	3.872	1.000 ± 0.001	3.8 ± 0.1
6.32	0.99990	11.336	0.99993	11.092	1.000 ± 0.001	12.46 ± 0.02
6.32	0.99990	13.214	0.99993	13.495	1.000 ± 0.001	12.46 ± 0.02

Tab. 6.1: A table illustrating the frequency of the warping mode branch ω_w and the frequency of the nearest interacting AE mode branch, ω_{AE}, at various field strengths and calculated by different methods. $\omega_{(th)}$ are frequencies calculated using the asymptotic theory of chapter 5, $\omega_{(num)}$ are found directly using the numerical model of section 4.9 and $\omega_{(sim)}$ are the frequencies derived from the Athena++ simulations of this chapter.

mode frequency may also be directly calculated via the numerical method of section 4.9 and are presented as $\omega_{w(num)}$ and $\omega_{AE(num)}$. We note the very strong agreement between the fitted parameters and the numerically derived wave frequencies. Although in this limited suite of simulations we are unable to directly track a dispersion curve or measure a wave speed, this excellent agreement strongly suggests that the dispersion curves derived using the corrugated disc numerical scheme are accurate and relevant to the dynamics of simulated warped discs. It further suggests that our local boundary condition (6.4) is useful and accurate for local simulations of warped discs.

We may also test the predictions of the asymptotic theory, shown by $\omega_{w(th)}$ and $\omega_{AE(th)}$. This is slightly different in each case; in the non-resonant cases the warping mode frequency is derived using either our expression for Q_3 (equation (3.83)) or equivalently our expression for ω_2. The frequency of the nearest AE modes is found using expressions (5.80) and (3.76)–(3.77). In the resonant case, both frequencies are found via the two solutions of expression (5.105). We see that these expressions, while often qualitatively correct, are only a rough approximation to the numerical solutions. This is unsurprising:

$k = 0.157$ cannot be said to be within the asymptotic regime.

There are a few datapoints in this table worthy of further commentary. The value of $\omega_{AE(th)}$ for the $B_{z0} = 0.947$ run is wildly off; this is because the relevant AE mode is only marginally stable and its dispersion branch is highly non-linear at $k = 0$ (See Figure 6.11). The prediction $\omega_{w(th)}$ for the $B_{z0} = 1.26$ run is also particularly poor; this is because we have naively applied the non-resonant equation for Q_3 (3.83), when in fact for wavenumbers as large as $k = 0.157$, $B_{z0} = 1.26$ is quite close to resonance. Finally, the final row has been doubled with two distinct predictions for the AE mode frequency, neither of which matches our result from the simulation. It just so happens that at $B_{z0} = 6.32$ the fast and slow AE modes are relatively close together, and the warp is significantly projected onto both modes. This violates our assumption that only one AE mode significantly interacts with the warp, and in our fitting of Figure 6.10 an intermediate frequency between the two contributing frequencies was found (see Figure 6.12).

6.5 Theoretical Discussion

6.5.1 Resonant Case

As per our discussion in chapter 5, at resonance there are two distinct branches originating from $\omega = 1$ and linear in k, though with very different gradients. When a warp is initialised, it projects primarily (in the limit of small k) onto those two branches. In fact we may estimate in this case how much the warp is projected onto each branch. Recall from section 5.5.3 that there is a mixing ratio b such that the $O(k^0)$ modes are some mixture of $|r_0\rangle$ and $|v_0\rangle$, the bending and (resonant) AE mode as per degenerate perturbation theory. If we let $|+\rangle$ represent the state continuous with the upper branch of the curve and $|-\rangle$ be the state continuous with the lower branch, we have

$$|+\rangle = |v_0\rangle + b_+ |r_0\rangle \tag{6.5}$$

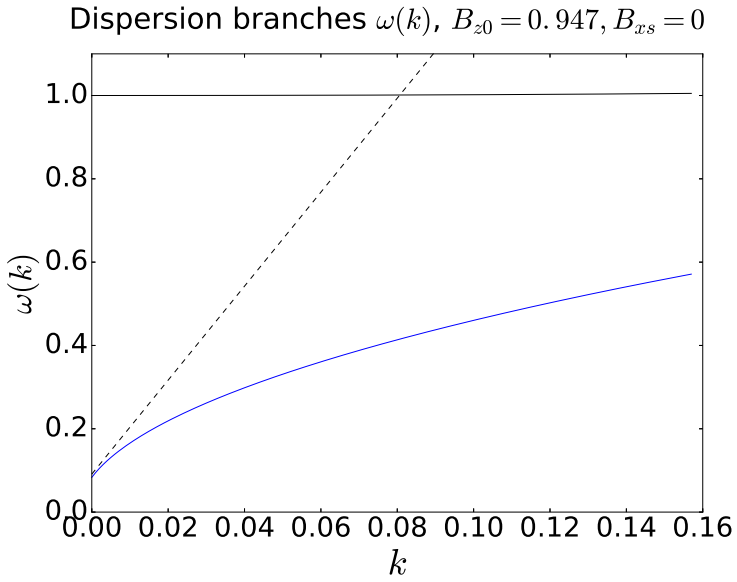

Fig. 6.11: The dispersion branches of the vertical oscilation mode (black) and the first slow AE mode (blue) at $B_{z0} = 0.947$, plotted from $0 < k < \pi/20$ using the numerical method of section 4.9. The slow mode is marginally MRI stable and a linear approximation (dashed line) leads to the erroneous prediction $\omega_{AE(th)}$.

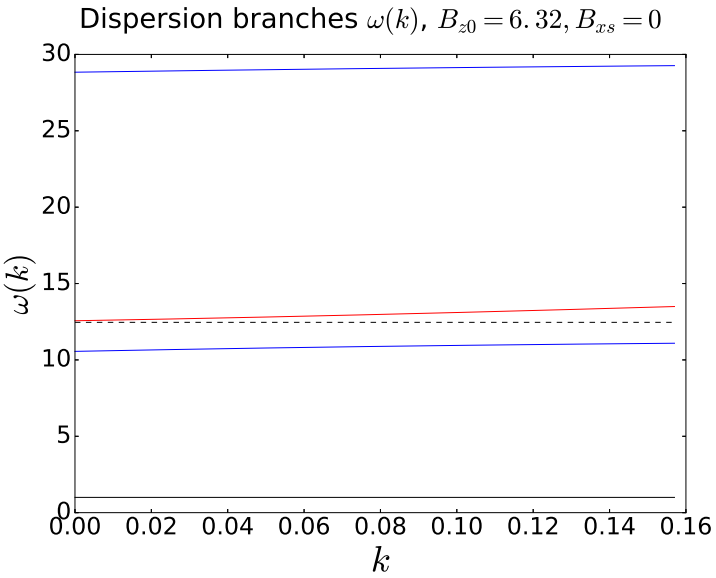

Fig. 6.12: The dispersion branches of the vertical oscilation mode (black), the first fast AE mode (red) and the first and second slow AE modes (blue) at $B_{z0} = 6.32$, plotted from $0 < k < \pi/20$ using the numerical method of section 4.9. The value of $\omega_{AE(sim)}$ is indicated by the black dashed line.

and

$$|-\rangle = |v_0\rangle + b_- |r_0\rangle \,. \tag{6.6}$$

We know from equation (5.98) that

$$b_\pm = \frac{c_i}{\omega_{1\pm}} \tag{6.7}$$

where we emphasise the fact that the two branches have different wave speeds – notably, $\omega_{1+} = 1.8$ and $\omega_{1-} = -0.057$. Consequently $b_- \gg b_+$, which confirms that the lower branch has far more a warping character than the upper branch.

Our initial condition mandates that there is an initial purely vertical motion. This can be achieved by initialising the state of the system, $|s\rangle$, to be some linear combination of these branches

$$|s\rangle = A_+ |+\rangle + A_- |-\rangle \tag{6.8}$$

such that, looking at coefficients of $|v_0\rangle$,

$$A_+ + A_- = 0 \tag{6.9}$$

and of $|r_0\rangle$,

$$A_+ b_+ + A_- b_- = 1 \tag{6.10}$$

with solutions

$$A_- = -A_+ = \frac{1}{b_- - b_+}. \tag{6.11}$$

In short, our warp projects equally and oppositely onto both branches of the dispersion curve. Having found the weightings $A_\pm$ we now see that the time evolution of the system as a whole is

$$|s(t)\rangle = A_+ |+\rangle \, e^{i\omega_{1+}t} + A_- |-\rangle \, e^{-i\omega_{1-}t} \tag{6.12}$$

or

$$|s(t)\rangle = (A_+ b_+ e^{-i\omega_{1+}t} + A_- b_- e^{-i\omega_{1-}t}) \, |r_0\rangle + (A_+ e^{-i\omega_{1+}t} + A_- e^{-i\omega_{1-}t}) \, |v_0\rangle \tag{6.13}$$

Given equations (6.9)–(6.10), this implies that the horizontal motions should be made up of two modes of equal magnitude but differing frequency, as we have seen. In contrast, the vertical oscillation mode will begin at its maximum of 1 and have a minimum when the modes are in antiphase, leading to the beat structure observed in Figure 6.9. The ratio of the amplitude minimum to maximum is given by

$$A_- b_- - A_+ b_+ = \frac{\omega_{1+} - \omega_{1-}}{\omega_{1+} + \omega_{1-}} = 0.94 \tag{6.14}$$

In short, the vertical oscillations should vary in amplitude by about six percent

at resonance. We may compare this with Figure 6.9; it is difficult to make a determination, but the amplitude of the modulation appears to be about three percent, somewhat less than what we might expect. This discrepancy could perhaps be attributed to the fact that we are using an asymptotic analysis at $k = 0.157$. We can see from table 6.1 that the resonant asymptotic values of ω deviate from simulations by roughly ten percent, so it is not surprising this asymptotic result too is inaccurate. Yet the analysis presented in this section at least is able to predict the order of magnitude of the modulation.

6.5.2 Non-Resonant Case

We may use the formalism we developed in the previous chapter to better understand the projection of the warp onto the normal modes of the disc in the non-resonant case as well. We saw from equation (5.57) that if we perform a perturbation expansion in orders of k about the vertical oscillation mode, horizontal motions are induced to first order in k.

$$k\,|v_1\rangle = \sum_i k a_i\,|u_i\rangle \tag{6.15}$$

Like in the resonant case the disc is initialised without any horizontal flows, yet the vertical oscillation mode branch necessarily includes horizontal flows due to the warp. We may resolve this paradox by simply adding $-ka_i$ amounts of every AE mode. Therefore by creating a corrugated warp we project onto the AE modes by an amount proportional to the wavenumber k and a_i. Typically a_i is only significant for a particular mode i that is closest to the vertical oscillation branch. This would imply that the evolution of the warped disc should be able to be reconstructed from knowledge of the dispersion branches and may be dominated by a single nearby mode, as we have demonstrated.

A similar analysis to the resonant case may be performed in order predict the projection of the warp onto the various wave mode branches. That lies beyond the scope of this chapter and contributes relatively little to the interpretation of our results, and so is omitted.

6.6 Summary and Discussion

In this chapter we have presented several simulations of warped magnetised discs using Athena++. We have described and successfully implemented a boundary condition that may be used to match the magnetic perturbations to a force-free decaying solution beyond the computational domain. A method to deduce the wave frequencies of the vertical oscillation mode and the dominant contributing AE mode was described. These results were found to be consistent with the frequencies found using the numerical method of section 4.9. The asymptotic analytical expressions achieved only modest success; this is due to the relatively large wavenumber $k \approx 0.157$ used in this analysis.

This has been only an exploratory investigation; indeed there is much else that can be done using this framework. The effect of bending fields, believed to be so important based on the work of the last chapter, has yet to be examined. Bending field equivalents to the simulations discussed in this chapter could confirm the non-local linear contribution to the warping mode frequency as discussed in section 4.2. In addition, one would expect far more dramatic results in resonant cases owing to the enhanced coupling between the vertical and horizontal AE modes as discussed in section 5.6. The effects of viscosity, non-linearities and the MRI (or the local instabilities as studied by Ogilvie & Latter (2013b) and Paardekooper & Ogilvie (2019)) are all obvious candidates for further investigation.

The remarkable consistency between the results of these simulations and the numerical predictions of section 4.9 provides strong evidence that the wave modes discussed in this thesis are not mere abstraction, but demonstrably present in this rather generic warped disc simulation.

7. CONCLUSION

Discussion

The work of this thesis began as an open-ended investigation into the dynamics of warped discs in the presence of net magnetic fields. That investigation has taken several twists and turns that we have endeavoured to describe in the chapters of this thesis.

Chapter 2 outlined a brief sortie into the problem of solving for the magnetic field structure external to a warped disc under a series of simplifying assumptions. Notably an expression was found for the Laplacian in the warped coordinate system of Ogilvie (1999). The solutions we derived provided useful context for the local models presented in the latter chapters of this thesis. Additionally the naive application of our solutions to the Blandford and Payne outflow criterion suggests that the presence of even a relatively small warp may have dramatic consequences for the outflow, both in terms of its existence and azimuthal variability. This interplay between disc warping and jet-variability may, subject to further investigation, suggest a connection between jet ejection events and quasi-periodic oscillators in X-ray binaries.

Yet we readily concede that this self-similar external field model is a heavily abstracted toy model. The assumption of self-similarity, while perhaps valid as some intermediate asymptotic, will inevitably break down. The assumption that the field is anchored within the disc raises several questions about the role of the stellar magnetic field when applied to real systems. Our results are only valid for small-amplitude warps, and perhaps most importantly the presence of outflows is totally neglected.

The latter chapters focused on the internal dynamics of the warped disc and have in many ways simply offered different perspectives of a single idea: warp propagation in magnetised discs is qualitatively distinct from its hydrodynamic analogue. Given the ubiquity of magnetised accretion systems in nature this result is of no small consequence, and researchers would do well to be cognizant of the differences when interpreting observations or simulations.

In a hydrodynamic disc the coincidence of the epicyclic and orbital frequencies causes a resonance in thin inviscid Keplerian accretion disc models. This resonance results in fast internal flows and torques acting within the disc, resulting in the rapid propagation of the warp.

In the presence of a magnetic field this resonance is removed. The magnetic tension adds a stiffness to the epicyclic oscillations, detuning the epicyclic frequency from the orbital frequency. Therefore at low viscosities the presence of even a relatively weak magnetic field may dramatically alter the internal structure of a Keplerian or very nearly Keplerian warped disc and the evolution of the warp.

In magnetised warped discs there exists a series of normal modes which we have called Alfvénic-epicyclic modes. These are the normal modes of the magnetised accretion disc, each with a fixed vertical structure and phase relationship between the density, velocity and magnetic field perturbations. The frequencies of the Alfvénic-epicyclic modes depend on the shear rate q, the magnetic field strength and the inclination of the equilibrium magnetic field. In the case of a very weak magnetic field, the fast Alfvénic-epicyclic modes all oscillate at the orbital frequency; the simultaneous resonance of the fast Alfvénic-epicyclic modes with the vertical oscillation mode results in the dispersionless propagation of the warp at half the sound speed, thereby recovering the hydrodynamic resonance of inviscid Keplerian discs.

The warped geometry of the accretion disc creates a pressure gradient in the radial direction that acts as an inhomogeneous forcing term. This system is consequently analogous to a forced oscillator. When the frequency of an Alfvénic-epicyclic mode coincides with the orbital frequency, that particular mode is resonantly forced resulting in large internal torques and rapid warp propagation. This occurs at particular values of the magnetic field strength (normalised in a way that depends on the local angular velocity, sound speed and surface density). In addition, the warp may also be communicated non-locally via the external magnetic field in a manner analogous to self-gravitating discs. Warp propagation in magnetised discs consequently has a surprisingly subtle and rich dependence on the magnetic field strength, geometry and shear rate. This mechanism may be critical to understanding and modelling warp propagation in magnetised discs.

We have come to this conclusion using a myriad of distinct models and methods, all of which give consistent answers to a reasonable degree of accuracy. In chapter 3 we made use of the warped shearing box, a generalisation of the classic shearing box to warped discs. Using this framework we presented both semi-analytical and numerical solutions for the horizontally invariant solutions for the vertical structure and the internal torque when the magnetic field threads the disc vertically.

In chapters 4 and 5 we developed the corrugated disc model in which the warp was not self-similar (and hence of constant warp amplitude) but rather varied sinusoidally with radius. Using this framework we developed both a numerical (for general bending fields) and semi-analytical (in the case of a vertical equilibrium field) scheme to solve for the normal modes, or wave modes, of the corrugated disc. Notably both numerical and semi-analytical expressions were found for the wave speed of long-wavelength warps in thin discs in both resonant and non-resonant scenarios. The warped shearing box was shown to, with slight and physically motivated amendment, be consistent with the asymptotic limit of the corrugated disc when the wavelength of the

perturbation was long relative to the disc thickness.

In chapter 6 the application of the theory developed in the previous chapters to both physical warps and simulations were discussed. Simulations using Athena++ of a warped magnetised disc within a shearing box provide tentative confirmation of our numerical and analytical findings. Namely the magnetised warp disc was shown to have a vertical structure consistent with theory, and the free mode frequencies were determined to be in line with those predicted by our analytical and prior numerical models. The hydrodynamic resonance for Keplerian inviscid discs did not appear in the magnetically threaded disc, and evidence was found for an alternative resonance with the first slow Alfvénic-epicyclic mode in line with our predictions.

Future Work

We conclude this thesis by highlighting several exciting and potentially fruitful avenues of inquiry through which the work of this thesis may be extended. These avenues may be divided into a few broad categories that we discuss below.

In chapter 2 the topic of jet-warp interaction was discussed. Due to the simplicity of our model we could not make any definitive statements regarding the interaction between outflows and jets; however, we argued that there is reason to believe variation of the inclination angle due to disc warping may introduce asymmetries to the jet. Such a model could be tested at varying levels of abstraction, potentially even using the warped shearing box formalism in a manner analogous to other two-dimensional wind studies (e.g. Ogilvie & Livio (2001)).

Due to the inherent mathematical complexities of magnetised warped discs in contrast to their hydrodynamic counterparts and the virginal nature of the field, the work of this thesis has satisfied itself with a linear analysis (in warp

amplitude) for the most part. Although a non-linear theory of magnetised warped discs may prove to be cumbersome, the numerical methods outlined in this thesis (among others) could at least numerically probe the non-linear regime. The likely presence of magnetic fields in many scenarios in which disc fragmentation is expected to occur (e.g. Doğan et al., (2015)) as well as reports of significant non-linearities in recent MHD warped disc simulations (Hawley & Krolik, 2018) provide ample motivation for an exploration of the non-linear regime.

In chapter 6 the results of several simulations of magnetised warped discs using Athena++ were presented; however, these only represented a fraction of the potential simulations that could be in principle performed. A more extensive suite of simulations might be able to better resolve the resonance between the vertical oscillation mode and the first slow AE mode. Simulations using a bending initial poloidal field would be able to test our predictions regarding the non-local transport of angular momentum via the field itself. A suite of simulations using different box sizes would provide a better direct measure of the dispersion curve, while larger boxes would better probe the asymptotic theory we have developed in chapter 5 for long-wavelength warps. In all cases the computational costs will be restrictive, but considerably less so than a conventional global simulation.

Nearly the entirety of the work of this thesis has been performed assuming an untwisted warp. Extension of the theory to twisted warped discs would certainly be of great interest, and at present I cannot speculate as to what new physical effects such a study might reveal.

Perhaps the most pertinent criticism of this thesis is the neglect of an explicit viscosity (via a parameter α) or MRI effects. We have proceeded on the assumption that introduction of a small-scale viscosity will not significantly alter the mean flow. Much of the theory presented here (and of course the numerical methods) could be amended to include the effects of some isotropic

viscosity α. However, if the viscosity is believed to be related to the MRI, this approach may be inferior to simply simulating a magnetised warped disc (potentially using the Athena++ code of chapter 6) in the MRI unstable regime. Whether the theory outlined in this thesis – including the potential resonance of the vertical oscillation mode with the higher order Alfvénic-epicylic modes – survives the onset of MRI turbulence will determine whether the results of this thesis are applicable only to MRI stable discs or magnetised discs more broadly.

There are more discs in the heavens than are dreamt of in our philosophy; this appears to hold doubly true for this thesis. We humbly admit that this work dimly illuminates but a small region of the vast parameter space inherent to the problem. Yet it is the fervent hope of the author that this faint flicker of light may one day serve to help someone else find their way.

BIBLIOGRAPHY

Agapitou V., Papaloizou J. C. B., Terquem C., 1997, MNRAS, 292, 631

Agapitou V., Papaloizou J. C. B., 1996, ApLC, 34, 363

Aly J. J., 1980, AA, 86, 192

Bai X.-N., Stone J. M., 2013, ApJ, 767, 30

Balbus S. A., Gammie C. F., Hawley J. F., 1994, MNRAS, 271, 197

Balbus S. A., Hawley J. F., 1991, ApJ, 376, 214

Balbus S. A., Hawley J. F., 1998, RvMP, 70, 1

Bardeen J. M., Petterson J. A., 1975, ApJ, 195, L65

Blandford R. D., Payne D. G., 1982, MNRAS, 199, 883

Bouvier J., Grankin K., Ellerbroek L. E., Bouy H., Barrado D., 2013, AA, 557, A77

Bouvier J., et al., 2007, AA, 463, 1017

Brandenburg A., Nordlund A., Stein R. F., Torkelsson U., 1995, ApJ, 446, 741

Campbell C. G., 2010, MNRAS, 401, 177

Cao X., Spruit H. C., 1994, AA, 287, 80

Cao X., Spruit H. C., 2013, ApJ, 765, 149

Casassus S., 2016, PASA, 33, e013

Casassus S., 2017, RMxAC, 11, RMxAC..49

Casassus S., et al., 2018, MNRAS, 477, 5104

Christiaens V., et al., 2018, AA, 617, A37

Clarkson W. I., Charles P. A., Coe M. J., Laycock S., 2003, MNRAS, 343, 1213

Cuello N., et al., 2018, ArXiv e-prints, arXiv:1810.10186

Curtis H. D., 1918, PLicO, 13, 9

Doğan S., Nixon C., King A., Price D. J., 2015, MNRAS, 449, 1251

Fabian A. C., Rees M. J., 1979, MNRAS, 187, 13P

Facchini S., Lodato G., Price D. J., 2013, MNRAS, 433, 2142

Foulkes S. B., Haswell C. A., Murray J. R., 2006, MNRAS, 366, 1399

Foulkes S. B., Haswell C. A., Murray J. R., 2010, MNRAS, 401, 1275

Fragile P. C., Anninos P., 2005, ApJ, 623, 347

Fragile P. C., Blaes O. M., Anninos P., Salmonson J. D., 2007, ApJ, 668, 417

Fragile P. C., Lindner C. C., Anninos P., Salmonson J. D., 2009, ApJ, 691, 482

Fragner M. M., Nelson R. P., 2010, AA, 511, A77

Fromang S., Papaloizou J., 2007, AA, 476, 1113

Fromang S., Latter H., Lesur G., Ogilvie G. I., 2013, AA, 552, A71

Gammie C. F., Balbus S. A., 1994, MNRAS, 270, 138

Gammie C. F., Goodman J., Ogilvie G. I., 2000, MNRAS, 318, 1005

Gerend D., Boynton P. E., 1976, ApJ, 209, 562

Ghosh P., Lamb F. K., 1979, ApJ, 232, 259

Goldreich P., Lynden-Bell D., 1965, MNRAS, 130, 125

Gingold R. A., Monaghan J. J., 1977, MNRAS, 181, 375

Guilet J., Ogilvie G. I., 2012, MNRAS, 424, 2097

Hatchett S. P., Begelman M. C., Sarazin C. L., 1981, ApJ, 247, 677

Hawley J. F., 2000, ApJ, 528, 462

Hawley J. F., Gammie C. F., Balbus S. A., 1995, ApJ, 440, 742

Hawley J. F., Krolik J. H., 2018, ApJ, 866, 5

Herrnstein J. R., Greenhill L. J., Moran J. M., 1996, American Astronomical Society Meeting Abstracts #188, 188, 16.03

Heyvaerts J., Norman C., 1989, ApJ, 347, 1055

Heyvaerts J., Priest E. R., Bardou A., 1996, ApJ, 473, 403

Hjellming R. M., Rupen M. P., 1995, Natur, 375, 464

Ivanov P. B., Zhuravlev V. V., Papaloizou J. C. B., 2018, MNRAS, 481, 3470

Katz J. I., 1973, NPhS, 246, 87

Kotze M. M., Charles P. A., 2012, MNRAS, 420, 1575

Krolik J. H., Hawley J. F., 2015, ApJ, 806, 141

Kuiper G. P., 1941, ApJ, 93, 133

Lai D., 1999, ApJ, 524, 1030

Larwood J. D., Nelson R. P., Papaloizou J. C. B., Terquem C., 1996, MNRAS, 282, 597

Larwood J. D., Papaloizou J. C. B., 1997, MNRAS, 285, 288

Latter H. N., Fromang S., Gressel O., 2010, MNRAS, 406, 848

Latter H. N., Papaloizou J. C. B., 2012, MNRAS, 426, 1107

Lesur G., Ferreira J., Ogilvie G. I., 2013, AA, 550, A61

Lewis B. T., Bate M. R., Price D. J., 2015, MNRAS, 451, 288

Lewis B. T., Bate M. R., 2017, MNRAS, 467, 3324

Lodato G., Pringle J. E., 2007, MNRAS, 381, 1287

Lodato G., Price D. J., 2010, MNRAS, 405, 1212

Low B. C., 1986, ApJ, 310, 953

Lubow S. H., Ogilvie G. I., 2000, ApJ, 538, 326

Lubow S. H., Papaloizou J. C. B., Pringle J. E., 1994, MNRAS, 267, 235

Lucy L. B., 1977, AJ, 82, 1013

Lovelace R. V. E., Romanova M. M., Bisnovatyi-Kogan G. S., 1995, MNRAS, 275, 244

Lovelace R. V. E., Romanova M. M., 2014, EPJWC, 64, 05003

Lynden-Bell D., Pringle J. E., 1974, MNRAS, 168, 603

Marino S., Perez S., Casassus S., 2015, ApJ, 798, L44

Martin R. G., Tout C. A., Pringle J. E., 2008, MNRAS, 387, 188

McKinney J. C., Tchekhovskoy A., Blandford R. D., 2013, Sci, 339, 49

Miyoshi M., Moran J., Herrnstein J., Greenhill L., Nakai N., Diamond P., Inoue M., 1995, Natur, 373, 127

Moll R., 2012, A&A, 548, A76

Morales Teixeira D., Fragile P. C., Zhuravlev V. V., Ivanov P. B., 2014, ApJ, 796, 103

Morales Teixeira D., Avara M. J., McKinney J. C., 2018, MNRAS, 480, 3547

Murray J. R., Chakrabarty D., Wynn G. A., Kramer L., 2002, MNRAS, 335, 247

Narayan R., Igumenshchev I. V., Abramowicz M. A., 2003, PASJ, 55, L69

Nealon R., Nixon C., Price D. J., King A., 2016, MNRAS, 455, L62

Nelson R. P., Papaloizou J. C. B., 1994, MNRAS, 270, 1

Nelson R. P., Papaloizou J. C. B., 1993, MNRAS, 265, 905

Nelson R. P., Papaloizou J. C. B., 1999, MNRAS, 309, 929

Nelson R. P., Papaloizou J. C. B., 2000, MNRAS, 315, 570

Nixon C. J., King A. R., 2012, MNRAS, 421, 1201

Nixon C., 2015, MNRAS, 450, 2459

Ogilvie G. I., 1997, MNRAS, 288, 63

Ogilvie G. I., 1999, MNRAS, 304, 557

Ogilvie G. I., Dubus G., 2001, MNRAS, 320, 485

Ogilvie G. I., 2003, MNRAS, 340, 969

Ogilvie G. I., 2006, MNRAS, 365, 977

Ogilvie G. I., 2012, MNRAS, 423, 1318

Ogilvie G. I., Latter H. N., 2013, MNRAS, 433, 2403

Ogilvie G. I., Latter H. N., 2013, MNRAS, 433, 2420

Ogilvie G. I., Livio M., 2001, ApJ, 553, 158

Paardekooper S.-J., Ogilvie G. I., 2019, MNRAS, 483, 3738

Papaloizou J. C. B., Pringle J. E., 1983, MNRAS, 202, 1181

Papaloizou J. C. B., Lin D. N. C., 1995, ApJ, 438, 841

Parkin E. R., Bicknell G. V., 2013, MNRAS, 435, 2281

Petterson J. A., 1977, ApJ, 216, 827

Petterson J. A., 1977, ApJ, 218, 783

Petterson J. A., 1978, ApJ, 226, 253

Prendergast K. H., Burbidge G. R., 1968, ApJ, 151, L83

Price D. J., et al., 2017, ascl.soft, ascl:1709.002

Pringle J. E., 1992, MNRAS, 258, 811

Pringle J. E., Rees M. J., 1972, AA, 21, 1

Pudritz R. E., Ouyed R., Fendt C., Brandenburg A., 2007, prpl.conf, 277, prpl.conf

Riols A., Ogilvie G. I., Latter H., Ross J. P., 2016, MNRAS, 463, 3096

Rosenfeld K. A., et al., 2012, ApJ, 757, 129

Ross J., Latter H. N., 2018, MNRAS, 477, 3329

Salvesen G., Simon J. B., Armitage P. J., Begelman M. C., 2016, MNRAS, 457, 857

Shakura N. I., 1972, AZh, 49, 921

Shakura N. I., Sunyaev R. A., 1973, AA, 500, 33

Sheikhnezami S., Fendt C., 2015, ApJ, 814, 113

Simon J. B., Beckwith K., Armitage P. J., 2012, MNRAS, 422, 2685

Sorathia K. A., Krolik J. H., Hawley J. F., 2013, ApJ, 777, 21

Sorathia K. A., Krolik J. H., Hawley J. F., 2013, ApJ, 768, 133

Spruit H. C., 1996, ArXiv e-prints, astro–ph/9602022

Spruit H. C., 2010, Lecture Notes in Physics, Berlin Springer Verlag, 233, LNP...794

Stapelfeldt K. R., Krist J. E., Ménard F., Bouvier J., Padgett D. L., Burrows C. J., 1998, ApJ, 502, L65

Tananbaum H., Gursky H., Kellogg E. M., Levinson R., Schreier E., Giacconi R., 1972, ApJ, 174, L143

Terquem C., Papaloizou J. C. B., 2000, A& A, 360, 1031

Torkelsson U., Ogilvie G. I., Brandenburg A., Pringle J. E., Nordlund Å., Stein R. F., 2000, MNRAS, 318, 47

Uchida Y., Shibata K., 1985, PASJ, 37, 515

Xiang-Gruess M., Papaloizou J. C. B., 2013, MNRAS, 431, 1320

Xiang-Gruess M., 2016, MNRAS, 455, 3086

Xiang-Gruess M., Ivanov P. B., Papaloizou J. C. B., 2016, MNRAS, 463, 2242

Xiang-Gruess M., Kroupa P., 2017, MNRAS, 471, 2334

White C. J., Stone J. M., Gammie C. F., 2016, ApJS, 225, 22

Wijers R. A. M. J., Pringle J. E., 1999, MNRAS, 308, 207

Zhuravlev V. V., Ivanov P. B., Fragile P. C., Morales Teixeira D., 2014, ApJ, 796, 104